Doctoral theses at NTNU, 2021:87

Davide Proserpio

Isogeometric Phase-Field Methods for Modeling Fracture in Shell Structures

NTNU
Norwegian University of
Science and Technology

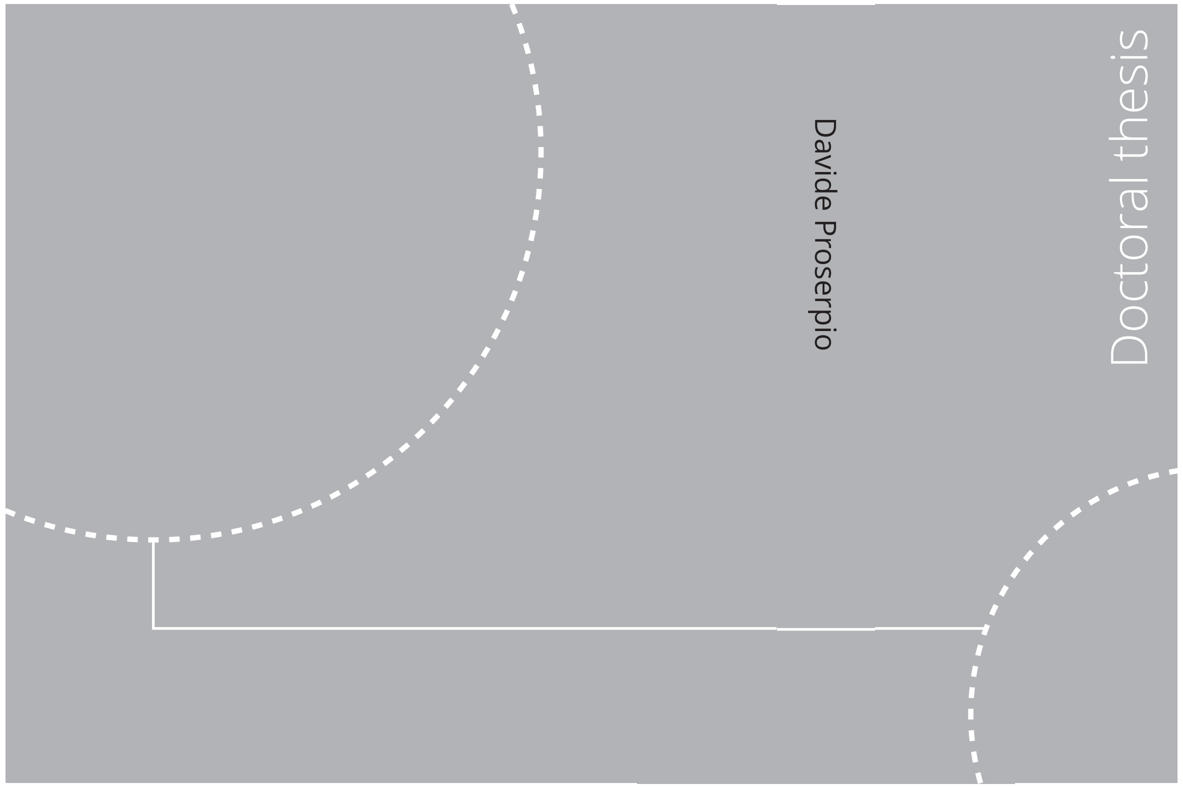

Doctoral thesis

Davide Proserpio

Doctoral theses at NTNU, 2021:87

NTNU

NTNU
Norwegian University of
Science and Technology
Thesis for the degree of
Philosophiae Doctor
Faculty of Engineering
Department of Marine Technology

ISBN 978-82-326-5830-5 (printed ver.)
ISBN 978-82-326-5177-1 (electronic ver.)
ISSN 1503-8181 (printed ver.)
ISSN 2703-8084 (electronic ver.)

NTNU
Norwegian University of
Science and Technology

Davide Proserpio

Isogeometric Phase-Field Methods for Modeling Fracture in Shell Structures

Thesis for the degree of Philosophiae Doctor

Trondheim, March 2021

Norwegian University of Science and Technology
Faculty of Engineering
Department of Marine Technology

NTNU
Norwegian University of
Science and Technology

NTNU
Norwegian University of Science and Technology

Thesis for the degree of Philosophiae Doctor

Faculty of Engineering
Department of Marine Technology

ISBN 978-82-326-5830-5 (printed ver.)
ISBN 978-82-326-5177-1 (electronic ver.)
ISSN 1503-8181 (printed ver.)
ISSN 2703-8084 (electronic ver.)

Doctoral theses at NTNU, 2021:87

PRINTED IN
NORWAY
NO - 1598

NORDIC SWAN ECOLABEL
Printed matter
2041 0731

Printed by Skipnes Kommunikasjon AS

Abstract

The simulation of the fracture of engineering structures is a challenging topic that requires accurate and efficient numerical models. This thesis focuses on the modeling of brittle and ductile fracture in thin shell structures employing the phase-field approach. A rotation-free isogeometric Kirchhoff-Love shell model is therefore adopted and combined with brittle and ductile phase-field fracture formulations. For the modeling of complex structures, a penalty-based approach is employed for coupling the structural and phase-field behaviors in correspondence of patch interfaces. All the penalty parameters involved in the model are controlled by a single dimensionless penalty coefficient, independently of the type and setup of the problem. The efficiency of the solution algorithm is improved by adopting a predictor-corrector algorithm for adaptive local refinement of the mesh based on Locally Refined Non Rational B-Splines, an adaptive time-stepping scheme, and a strongly coupled staggered solution scheme for the solution of the nonlinear system of equations. The presented formulation is qualitatively and quantitatively evaluated through several numerical tests and validated against experimental benchmarks involving complex shell geometries, thus opening for the application of the model to real-world structures.

Preface

This thesis is submitted to the Norwegian University of Science and Technology (NTNU) for partial fulfillment of the requirements for the degree of Philosophiae Doctor (PhD).

This doctoral work has been performed at the Department of Marine Technology (IMT), NTNU Trondheim, with Professor Josef Kiendl as main supervisor and Professor Sigmund Kyrre Ås as co-supervisor.

Acknowledgments

The PhD has been a long journey that made me grow as a person, as an engineer, and as a researcher. It has been full of commitment, sparks of enthusiasm, but also stressful moments. Being close to the end of it, I have a long list of thanks to everybody that helped me reach this point.

I would like to thank sincerely my supervisor, Professor Josef Kiendl, for his guidance and for showing me a great example of how to conduct research work. During the last years, he supervised my work being always available for valuable discussions and suggestions, leaving me freedom and flexibility in organizing my work. This has been truly appreciated. Furthermore, I would like to thank him for letting me finalize my PhD work at the Bundeswehr University in Munich. A great thank you goes also to Professor Laura De Lorenzis and to Marreddy Ambati for their collaboration, willingness to share ideas, and for hosting me twice at the Technische Universität Braunschweig. I would like to thank also NTNU and the Department of Marine Technology for the possibility of joining the PhD program and Professor Sigmund Kyrre Ås for his co-supervision.

I want to deeply thank my love and future wife Nora: you are an endless source of support and motivation and you transmitted to me even more passion for research! I would like to thank my family for supporting me with the not easy decision of moving to Trondheim for the PhD. They taught me the value of work and constant commitment that allowed me to reach this point. Even at distance, their encouragement was felt as they were here. Grazie di cuore! A final thanks also to all my friends, met before or during this journey, with whom I spent wonderful moments outside the working life.

December 2020, Davide Proserpio

List of attached papers

The following papers are reported in Appendix A:

Paper 1

Austin J. Herrema*, Emily L. Johnson*, Davide Proserpio*, Michael C.H. Wu, Josef Kiendl, Ming-Chen Hsu

Penalty coupling of non-matching isogeometric Kirchhoff-Love shell patches with application to composite wind turbine blades

Computer Methods in Applied Mechanics and Engineering, 2019; 346 (810-840)

*These three authors contributed equally to this work.

Paper 2

Davide Proserpio, Josef Kiendl, Marreddy Ambati, Laura De Lorenzis, Kjetil André Johannessen, Trond Kvamsdal

Simulation of brittle fracture in shells using a phase-field approach and LR B-splines

7th GACM Colloquium on Computational Mechanics for Young Scientists from Academia and Industry, Stuttgart, 2017

Paper 3

Davide Proserpio, Marreddy Ambati, Laura De Lorenzis, Josef Kiendl

A framework for efficient isogeometric computations of phase-field brittle fracture in multipatch shell structures

Computer Methods in Applied Mechanics and Engineering, 2020; 372, (113363)

Paper 4

Davide Proserpio, Marreddy Ambati, Laura De Lorenzis, Josef Kiendl

Phase-field simulation of ductile fracture in shell structures

Submitted to Computer Methods in Applied Mechanics and Engineering

Contents

List of Figures

1 Introduction

1.1 Motivation

The simulation of the fracture of mechanical and civil structural members plays an important role in many engineering applications, for understanding the behavior of structures and avoiding their failure. The simulations can be performed at the design step or during the in-service life of the structures for monitoring, through inspections and simulations, the evolution of possibly found defects or cracks, and therefore assessing the residual life of already damaged parts. Structural analysis can be also performed for avoiding expensive and time-consuming experimental campaigns.

Plate and shells are structures having one dimension (the thickness) relatively small compared with the other two dimensions. They are very common structural parts in many engineering fields, including marine and offshore industries, automotive and aerospace sector, and civil engineering. Specific structural models are required for efficiently describing their behavior.

Depending on the way the failure develops, two types of fracture are usually identified for uniform isotropic materials. Brittle fracture occurs suddenly and it is preceded by almost no inelastic deformation. Ductile fracture follows instead extensive plastic deformation. Depending on the conditions (for example temperature), both the fracture types can happen in structural materials like metals. Designers are mostly interested in the maximum load that a structure can withstand, after which fracture develops and the functionality of the structure can be partially or fully compromised. For both the brittle and ductile case, the description of the propagation of cracks can be useful for understanding the development of fracture, identifying the weak members of a structure, or assessing a *fail-safe* design type, according to which a structure should retain sufficient structural integrity even if individual parts of it fail.

The term Computed Aided Engineering (CAE) refers to all the tools involving the use of computer software (commercial or non-commercial) employed in the engineering practice. Among these, CAE structural analysis is considered for determining the ultimate strength and the failure behavior of structures. In order to perform these type of simulations, reliable and efficient structural and fracture numerical models are needed.

1.2 Research context

The Finite Element Method (FEM) is currently the most used numerical tool for performing CAE structural analysis simulations. Besides its huge versatility and potential, one of the most important weak points of the method is represented by the time-consuming process necessary for generating the FE mesh on the geometries to be analyzed, which usually are originated through Computer Aided Design (CAD) software. Hughes and coworkers [1,2] introduced Isogeometric Analysis (IGA) with the original objective of bridging the gap between CAD and structural analysis. The main feature of IGA is the adoption of Non Uniform Rational B-Splines (NURBS) as basis functions for the discretization of the geometry and for the (structural) analysis. Since NURBS are the basis functions used for the description of the geometry in CAD software, the adoption of IGA greatly reduces the time devoted to the meshing of the models and allows performing analyses on the exact geometry of the structure. The smoothness of the basis functions and the continuity across element boundaries results in optimal accuracy and convergence rate with respect to exact solutions of structural problems. In addition, the high continuity of the shape functions fosters the implementation of shell models or higher-order formulations. In this context, a variety of approaches have been proposed, including isogeometric formulations for solid shells [3–7], Kirchhoff-Love [8–11] and Reissner-Mindlin [12–15] shells and plates, as well as hierarchic shells [14, 16]. Since the focus of this thesis work is on the simulation of thin shell structures, a technology for coupling the behavior of Kirchhoff-Love shell patches is needed. Besides the penalty formulation [11, 17, 18], that is adopted in this work, the bending strip method [19, 20], the mortar method [21, 22] and the Nitsche's method [23, 24] have been proposed.

The numerical formulations for the description of the fracture process typically implemented in the FE framework may be categorized as discrete or continuum models. FEM remeshing [25] allows for the description of discrete crack as discontinuities in the FE geometry. The XFEM [26] technology embeds the crack discontinuity through the definition of enriched shape functions based on the partition of unity method. Both these approaches require the definition of *ad hoc* criteria for crack initiation and propagation and present numerous implementation challenges, especially in the three-dimensional setting. The cohesive zone modeling approach [27] is based on the insertion of interface elements in correspondence to the fracture location. However, the application becomes problematic in the case of unknown crack paths. Continuum approaches for modeling fracture (see [28] for an extensive review) employ the use of a damage parameter that modifies the material stiffness according to the damage level. Damage models may suffer from strong mesh sensitivity problems in case of local formulations, meaning that the material behavior is described at specific locations independently of the surrounding continuum. In order to overcome this problem, non-local damage formulations including a length scale parameter and a gradient term for the damage have been introduced [29, 30].

The phase-field approach has emerged in the last decade as a promising tool for the simulation of fracture. The formulation employs a continuous scalar variable, the so-called ”phase-field” order parameter, which is described over the whole domain of the analysis and whose smooth variation approximates sharp cracks. One of the main advantages of the approach consists in its flexibility, since all the fracture process is controlled by the minimization of the energy functional of the system and no *ad hoc* criteria need to be assumed for crack initiation or growth. No *a priori* knowledge of the fracture path is required. The crack is tracked by the evolution of the phase-field parameter and the model can describe arbitrarily complex fracture patterns, including the branching or merging of cracks without additional implementation contribution. The extension of the model from the unidimensional to the three-dimensional setting is straightforward. The approach refers indirectly to the original description of brittle fracture by Griffith [31], later presented in a variational formulation by Francfort and Marigo [32] and then regularized by Bourdin et al. [33]. From this point, a variety of applications of the approach and contributions to the original phase-field model have been presented both for brittle and ductile fracture formulations, see for example the extensive review works [34–36]. In addition, the phase-field approach has been applied to the description of fracture in anisotropic materials [37–40] or heterogeneous media [41, 42]. Recently, applications to the description of fatigue failure have been introduced, see [43–46] among many others. Furthermore, the applicability and usability of the phase-field formulation have been enhanced by implementations in the commercial finite element software Abaqus [47–50]. Phase-field formulations for fracture have been discretized with standard finite elements as well as with isogeometric analysis (IGA). Borden et al. [51] were the first to exploit the continuity properties of isogeometric discretizations in this context and proposed a higher-order phase-field formulation for fracture, which can be adopted thanks to the higher continuity of the NURBS basis functions.

A crucial point regarding the research related to the phase-field method for fracture is the assessment of the accuracy and reliability of the formulation with respect to the comparison with experimental benchmarks. Several works are focused on the validation of the approach through the comparison of the results of numerical simulations with experimental tests, such as [34, 52–55] for the brittle case. For ductile fracture, the works from Wick et al. [56] and Borden et al. [57], which report qualitative results for the fracture of screws and of a bolted plate, respectively, are recalled. A quantitative comparison, showing good agreement between the results of ductile fracture phase-field simulations and experiments, is reported by Ambati et al. [58].

1.3 Research objectives

The phase-field method has shown great potential due to its flexibility and relatively easy implementation with respect to other methodologies for the simulation of fracture. Nevertheless, very few applications to real-world structures have been presented up to now. For this reason, the focus of the work of this thesis is on the application of the method to complex shell structures, which can be found in many engineering fields, firstly for simulating brittle and then for ductile fracture. An approach for combining the phase-field ductile fracture model with an isogeometric Kirchhoff-Love formulation is to be defined, based on the one already existing for the brittle case. A penalty-based technology is formulated for patch coupling and for imposing structural continuity across the interfaces between the shells, in order to simulate multipatch structures. The methodology is to be extended for enforcing the required continuity of the phase-field across patches, for fracture simulations. In order to perform these analyses with a reasonable computational cost, different algorithmic techniques, i.e. space and time adaptivity and different staggering schemes, need to be adopted and their efficiency is to be evaluated.

Finally, in order to evaluate the accuracy of the phase-field approach, results from simulations and experimental tests, both in the brittle and fracture context, are to be compared and discussed.

The work is restricted to quasi-static simulations (no dynamic fracture) for uniform isotropic shells, considering only the Kirchhoff-Love formulation. Nevertheless, the available literature suggests that potentially good results can be obtained also for complex structures including thick shells or anisotropy in the elastic properties or in the fracture formulation.

1.4 Thesis structure

The first part of the thesis reviews the most important features of the adopted structural and phase-field formulations for simulating the brittle and ductile fracture in multipatch shell structures (Section 2). Section 3 is focused on the algorithmic aspects which have been studied in order to improve the efficiency of the simulations. In Section 4, three numerical examples that have not been published but are considered relevant for the reader are proposed and discussed.

Since the thesis is paper-based, meaning that it is constituted by the compendium of articles published during the PhD period, all the relevant results, numerical tests and discussions are included in the attached papers in Appendix A (see the following section for further details).

1.4.1 Outline of the papers and contributions

- **Paper 1:** the work presents a penalty based formulation for weakly imposing displacement and rotational continuity between interfaces of isogeometric Kirchhoff-Love shell patches so that linear and nonlinear analyses of multipatch shell structures can be effectively conducted. The proposed method requires only a single penalty coefficient for both the coupling terms, thus alleviating the problem-dependency of penalty parameters. The accuracy and stability of the formulation, as well as the choice of the global penalty coefficient, are tested through numerous benchmarks and through the modeling of the realistic structure of a wind turbine blade.
  The candidate contributed to the implementation of the numerical approach for determining the optimal value of the penalty coefficient and for perform-

ing the nonlinear benchmark studies, above drafting the dedicated sections of the manuscripts.

- **Paper 2:** the work presents the first results of the use of Locally Refined NURBS for the local pre-refinement of shell geometries in the context of phase-field brittle fracture simulations, for improving the efficiency of the analyses.
  The candidate contributed with the implementation of the phase-field approach for brittle fracture for shells with discretization based on Locally Refined NURBS, performed all the simulations, and drafted the paper.

- **Paper 3:** the work is devoted to the simulation of brittle fracture in thin shell structures by employing the phase-field approach in the IGA framework. The penalty coupling formulation presented in Paper 1 is extended to the enforcement of the required continuity of the phase-field between patches, assuming a standard or a higher-order phase-field formulation. Also for this case, all the penalty terms are controlled by a single dimensionless parameter. A multistep predictor-corrector adaptive mesh refinement algorithm based on Locally Refined NURBS is presented and adopted, together with a strongly coupled staggering scheme. The improvement in the computational efficiency due to the adaptive local refinement, the strongly coupled staggering scheme, and the higher-order phase-field formulation for the simulation of brittle fracture is demonstrated. The effectiveness of the patch coupling technology for phase-field analyses is tested through different benchmarks and numerical tests on complex structures.
  The candidate contributed with the development of the penalty-based approach for imposing phase-field continuity between patches and with the development of the adaptive local refinement technique, including the transfer of the solution from coarse to refined mesh. Then, he was responsible for the implementation of the approach in a newly-established in-house code, performed all the simulations, and drafted the paper.

- **Paper 4:** the work presents a formulation for the simulation of ductile fracture in complex shell structures. The isogeometric thin shell formulation is combined with a phase-field ductile fracture model at finite strains based on a local formulation of plasticity. For this reason, the mesh sensitivity of the model is investigated and it is shown that the adaptive local refinement algorithm presented in Paper 3 can safely be adopted also in the ductile fracture context. Moreover, the adaptive mesh refinement allows for capturing important features typical of ductile fracture, as cracking along shear bands, while reducing the computational cost of the analyses. The strongly coupled staggering scheme and an adaptive time-stepping strategy are also adopted for improving the efficiency of the simulations. The same formulation used in Paper 3 for structural and phase-field patch coupling is adopted for the description of realistic structures. Then, the numerical model is employed for simulating the results of an experimental indentation tests performed on complex structures consisting of stiffened steel plates, originally carried out for evaluating the consequences of grounding on ship hulls.

The candidate contributed with the adaptation of the penalty patch coupling, of the space and time adaptive schemes, and of the staggered solution scheme, to the phase-field ductile fracture context for shells, and to the implementation of the approach. The candidate performed all the simulations and drafted the paper.

2 Formulation

The focus of this work is on the simulation of brittle and ductile fracture in complex shell structures with the phase-field approach. Firstly, the structural model and the chosen isogeometric discretization are presented. Then, the phase-field model for brittle and ductile fracture is introduced, with special attention to the combination of the phase-field approach with the shell formulation. In view of simulating the failure of multipatch shell structures, the penalty approach adopted for coupling the structural and phase-field behaviors across the patch interfaces is presented. Finally, a penalty formulation for the simulation of frictionless contact conditions between surfaces, adopted in Paper 4, is briefly presented.

2.1 Isogeometric formulation for Kirchhoff-Love shells

The main hypothesis of the Kirchhoff-Love shell theory, in which plates are included as a special case, consists in assuming that segments, which are perpendicular to the shell midsurface in the undeformed configuration, remain straight and perpendicular also in the deformed configuration. As a consequence, transverse shear strains are neglected and assumed to be null and the description of the shell kinematics is reduced to the description of the midsurface displacement field. An isogeometric rotation-free Kirchhoff-Love shell formulation [8] is considered, whose main features will be exposed in this section.

The adopted notation comprises Greek indices α, β assuming the values $\{1, 2\}$ for the in-plane components, and Latin indices i, j that take the values $\{1, 2, 3\}$. The notation $\overset{\circ}{(\cdot)}$ indicates the undeformed configuration of the geometric variables. For the description of the shell kinematics, a curvilinear reference system is considered, constituted by the parametric coordinates θ^1 and θ^2 for the midsurface and by the coordinate $\theta^3 \in [-t/2, +t/2]$ for the thickness direction, with t indicating the shell thickness. Considering a point $\mathbf{r}(\theta^1, \theta^2)$ on the middle surface of the shell, a covariant coordinate system can be considered by defining the tangent base vectors $\mathbf{a}_\alpha$ as:

$$\mathbf{a}_\alpha = \frac{\partial \mathbf{r}}{\partial \theta^\alpha}. \tag{2.1}$$

For the sake of brevity, the partial derivatives with respect to θ^α will be indicated as $(\cdot)_{,\alpha} = \partial(\cdot)/\partial\theta^\alpha$, so that equation (2.1) can be simply rewritten in the form $\mathbf{a}_\alpha = \mathbf{r}_{,\alpha}$. A contravariant coordinate system on the shell midsurface can be defined by considering the dual contravariant base vectors $\mathbf{a}^\alpha \cdot \mathbf{a}_\beta = \delta^\alpha_\beta$, where δ^α_β is the Kronecker delta. The unit normal vector in thickness direction is computed as follows:

$$\mathbf{a}_3 = \frac{\mathbf{a}_1 \times \mathbf{a}_2}{\|\mathbf{a}_1 \times \mathbf{a}_2\|}. \tag{2.2}$$

Therefore, the position vector $\mathbf{x}$ of a point in the shell continuum can be determined by the corresponding point on the midsurface $\mathbf{r}$ and the fiber director $\mathbf{a}_3$:

$$\mathbf{x} = \mathbf{r} + \theta^3 \mathbf{a}_3. \tag{2.3}$$

It is possible to define as $\mathbf{g}_i = \mathbf{x}_{,i}$ a set of covariant base vectors at any point $\mathbf{x}$ of the shell continuum. More specifically, distinguishing between in-plane and out-of-plane components:

$$\mathbf{g}_\alpha = \mathbf{a}_\alpha + \theta^3 \mathbf{a}_{3,\alpha}, \qquad \mathbf{g}_3 = \mathbf{a}_3. \tag{2.4}$$

Also in this case, the dual contravariant coordinates system base vectors can be computed by the relation $\mathbf{g}^i \cdot \mathbf{g}_j = \delta^i_j$.

According to the Kirchhoff-Love shell hypothesis, only in-plane strain components are considered. The Green-Lagrange strain tensor $\boldsymbol{\varepsilon}$ is defined, at any point of the shell continuum, as the sum of the membrane and bending contributions:

$$\boldsymbol{\varepsilon}(\theta^3) = \boldsymbol{\varepsilon}^m + \theta^3 \boldsymbol{\kappa}. \tag{2.5}$$

The covariant components of the membrane strain tensor $\boldsymbol{\varepsilon}^m = \varepsilon^m_{\alpha\beta}\, \mathbf{a}^\alpha \otimes \mathbf{a}^\beta$ are retrieved as:

$$\varepsilon^m_{\alpha\beta} = \frac{1}{2}\left(\mathbf{a}_\alpha \cdot \mathbf{a}_\beta - \mathring{\mathbf{a}}_\alpha \cdot \mathring{\mathbf{a}}_\beta\right). \tag{2.6}$$

The bending part of the strain tensor varies linearly through the shell thickness and depends on the curvature change tensor $\boldsymbol{\kappa} = \kappa_{\alpha\beta}\, \mathbf{a}^\alpha \otimes \mathbf{a}^\beta$, whose covariant components are computed as:

$$\kappa_{\alpha\beta} = \mathring{\mathbf{a}}_{\alpha,\beta} \cdot \mathring{\mathbf{a}}_3 - \mathbf{a}_{\alpha,\beta} \cdot \mathbf{a}_3. \tag{2.7}$$

Equations (2.5) and (2.6) are nonlinear strain measures which imply large deformations. In the small displacement framework, it is possible to adopt their linearized version:

$$\varepsilon^{m}_{\alpha\beta,\,lin} = \frac{1}{2}(\mathbf{a}_\beta \cdot \mathbf{u}_{,\alpha} + \mathbf{a}_\alpha \cdot \mathbf{u}_{,\beta}\,), \tag{2.8}$$

$$\begin{aligned}\kappa_{\alpha\beta,\,lin} = -\mathbf{a}_3 \cdot \mathbf{u}_{,\alpha\beta} + &\frac{1}{\|\mathbf{a}_1 \times \mathbf{a}_2\|}\cdot \\ \cdot \Big[(\mathbf{r}_{,\alpha\beta} \times \mathbf{a}_2) \cdot \mathbf{u}_{,1} + (\mathbf{a}_1 \times \mathbf{r}_{,\alpha\beta}\,) \cdot \mathbf{u}_{,2} + \mathbf{r}_{,\alpha\beta} \cdot \mathbf{a}_3 &\big((\mathbf{a}_2 \times \mathbf{a}_3) \cdot \mathbf{u}_{,1} + (\mathbf{a}_3 \times \mathbf{a}_1) \cdot \mathbf{u}_{,2}\,\big)\Big],\end{aligned} \tag{2.9}$$

$\mathbf{u}$ being the midsurface displacement field. The linearized formulation of the strain measures is adopted for the simulations of brittle fracture, for which it is appropriate to consider only small deformations (Paper 2 and Paper 3).

Considering a linear elastic material, the stress-strain relationship reads:

$$\mathbf{S} = \mathbb{C}\boldsymbol{\varepsilon}, \tag{2.10}$$

where $\mathbb{C}$ is a constitutive material tensor and $\mathbf{S} = S^{ij}\mathring{\mathbf{g}}_i \otimes \mathring{\mathbf{g}}_j$ is the second Piola-Kirchhoff stress tensor, energetically conjugated to the Green-Lagrange strain tensor. The effective stress resultants, for axial force and bending respectively, are computed by through-thickness integration of the stresses:

$$\boldsymbol{n} = \int_{-t/2}^{+t/2} \mathbf{S}\; d\theta^3, \tag{2.11}$$

$$\boldsymbol{m} = \int_{-t/2}^{+t/2} \mathbf{S}\; \theta^3 d\theta^3. \tag{2.12}$$

In the standard linear elastic context, these integrals can be performed analytically.

The variational formulation of the shell structural problem is based on the Virtual Work Principle, corresponding to the weak form of the momentum equation:

$$\delta W = \delta W^{\text{int}} - \delta W^{\text{ext}} = 0, \tag{2.13}$$

where W represents the total work, W^{int} the internal work, W^{ext} the external work and δ indicates their variation with respect to the virtual displacement field

$\delta\mathbf{u}$, so that:

$$\delta W = \frac{\partial W}{\partial \mathbf{u}} \delta \mathbf{u}. \tag{2.14}$$

The internal and external virtual works are defined as:

$$\delta W^{\text{int}} = \int_{\Omega} \delta\boldsymbol{\varepsilon} : \mathbf{S} \, dV = \int_{A} \left(\delta\boldsymbol{\varepsilon}^{m} : \boldsymbol{n} + \delta\boldsymbol{\kappa} : \boldsymbol{m} \right) dA, \tag{2.15}$$

$$\delta W^{\text{ext}} = \int_{A} \delta\mathbf{u} \cdot f \, dA, \tag{2.16}$$

with the quantities $\delta\boldsymbol{\varepsilon}$, $\delta\boldsymbol{\varepsilon}^{m}$ and $\delta\boldsymbol{\kappa}$ computed considering the virtual displacement field $\delta\mathbf{u}$, while f indicates the external load per unit area. The approximation $dV \approx tdA$ is assumed, so that the integral over the three-dimensional undeformed domain Ω can be reduced over the undeformed shell midsurface A.

Considering an isogeometric discretization (see Section 2.1.2) of the presented shell element, the residual force vector $\mathbf{R}_u = \mathbf{F}_u^{\text{int}} - \mathbf{F}_u^{\text{ext}}$ is computed by the variation of the virtual work δW^{int} with respect to the discrete displacement values at the control points u_r. The internal force vector is retrieved as:

$$\mathbf{F}_u^{\text{int}} = \frac{\partial W^{\text{int}}}{\partial u_r} = \int_{A} \left(\frac{\partial \boldsymbol{\varepsilon}^{m}}{\partial u_r} : \boldsymbol{n} + \frac{\partial \boldsymbol{\kappa}}{\partial u_r} : \boldsymbol{m} \right) dA, \tag{2.17}$$

while $\mathbf{F}_u^{\text{ext}}$ represents the external force vector. The linearization of the residual vector $\mathbf{R}_u$ leads to to the tangent stiffness matrix $\mathbf{K}_{PF}$ through the second derivatives of the virtual work with respect to the discrete displacement values:

$$\begin{aligned} \mathbf{K}_u &= \frac{\partial^2 W}{\partial u_r \partial u_s} = \frac{\partial^2 W^{\text{int}}}{\partial u_r \partial u_s} - \frac{\partial^2 W^{\text{ext}}}{\partial u_r \partial u_s} = \\ &= \int_{A} \left(\frac{\partial \boldsymbol{\varepsilon}^{m}}{\partial u_r} : \frac{\partial \boldsymbol{n}}{\partial u_s} + \frac{\partial^2 \boldsymbol{\varepsilon}^{m}}{\partial u_r \partial u_s} : \boldsymbol{n} + \frac{\partial \boldsymbol{\kappa}}{\partial u_r} : \frac{\partial \boldsymbol{m}}{\partial u_s} + \frac{\partial^2 \boldsymbol{\kappa}}{\partial u_r \partial u_s} : \boldsymbol{m} \right) dA, \end{aligned} \tag{2.18}$$

under the hypothesis of no displacement-dependent loads, so that the linearization of the external force vector does not contribute to the computation of the stiffness matrix. So, the linearized version of the equilibrium equation:

$$\mathbf{K}_u \, \Delta\tilde{\mathbf{u}} = \mathbf{R}_u, \tag{2.19}$$

can be solved for $\Delta\tilde{\mathbf{u}}$, the incremental displacement vector at the control points. For details about the variation and the linearization of $\boldsymbol{\varepsilon}^m$ and $\boldsymbol{\kappa}$ with respect to u_r and u_s, the reader is referred to [59].

The shell formulation can be used also for composite materials employing laminated plate theory, see Kiendl [59] and Paper 1 for details. Anyway, the focus of this work is restricted to the fracture of uniform isotropic shell.

2.1.1 Elasto-plasticity formulation for Kirchhoff-Love shells

The Kirchhoff-Love shell model presented in the previous section can be extended to the large strains regime in order to be coupled with three-dimensional nonlinear constitutive models, as done by Kiendl et al. [60] for the case of different hyperelastic materials. In this section, an elasto-plastic material model, which will be employed for the phase-field ductile fracture formulation, is considered.

The adopted approach for plasticity is based on the work from Simo [61] and consists in a standard three-dimensional isochoric von-Mises $J2$ rate-independent plasticity theory at finite strains. In the model, a multiplicative decomposition of the deformation gradient $\mathbf{F} = d\mathbf{x}/d\mathring{\mathbf{x}}$ into its elastic and plastic parts is employed:

$$\mathbf{F} = \mathbf{F}^e\mathbf{F}^p. \tag{2.20}$$

This decomposition can be interpreted as a plastic deformation to a stress-free intermediate configuration combined with a purely elastic deformation. The elastic left Cauchy-Green deformation tensor $\mathbf{b}^e$ can be computed from the elastic deformation gradient as:

$$\mathbf{b}^e = \mathbf{F}^e\mathbf{F}^{eT}. \tag{2.21}$$

The sum of the elastic and plastic energy contributions expresses the total free energy functional:

$$E(\mathbf{b}^e, J^e, \alpha) = \int_\Omega \left[\psi_e(\mathbf{b}^e, J^e) + \psi_p(\alpha)\right] dV. \tag{2.22}$$

in which ψ_e represents the elastic strain energy density and $J^e = \det[\mathbf{F}^e]$ indicates the determinant of the elastic deformation gradient tensor, which is a measure of the elastic change of volume. The term $\psi_p(\alpha)$ is the plastic strain energy density function assuming isotropic hardening, with α being the relative internal hardening variable (corresponding to the equivalent accumulated plastic strain). A neo-Hookean constitutive law of decoupled type for describing the elastic behavior of the material is considered. According to this approach, an additive decomposition of the strain energy density into a volumetric (shape preserving) and a deviatoric (volume preserving) part is performed:

$$\psi_e = \psi_e^{vol} + \psi_e^{dev}. \tag{2.23}$$

The two contributions are computed as:

$$\psi_e^{vol} = \frac{\kappa_0}{2}\left(\frac{J^{e2}-1}{2} - \ln J^e\right), \tag{2.24}$$

$$\psi_e^{dev} = \frac{\mu}{2}\left(\bar{I}_b^e - 3\right), \tag{2.25}$$

with κ_0 and μ representing the bulk and shear modulus of the material, respectively. Moreover, the terms $\bar{I}_b^e = \mathrm{tr}[\bar{\mathbf{b}}^e]$, with $\bar{\mathbf{b}}^e = J^{e-\frac{2}{3}}\mathbf{b}^e$ are employed. For further details regarding the plasticity model, including the formulation of the yield function, the associative flow rule, and the time-integration scheme required for the solution of the elasto-plastic constitutive equations, the reader is referred to Ambati et al. [62].

A stress-based approach is adopted for the formulation of the Kirchhoff-Love shell element in the context of large elasto-plastic deformations. The methodology consists in defining integration points through the shell thickness and applying the considered three-dimensional material model at these points. The stress resultants are then computed by through-thickness integration of the stress components, see equations (2.11) and (2.12). In contrast to linear elastic formulations, these integrals need to be computed numerically. It is highlighted the fact that through-thickness integration does not imply any discretization along the thickness direction. The shell variables relevant for the elasto-plastic model can be retrieved from the shell kinematics. The covariant components of the deformation gradient, expressed in the curvilinear reference system constituted by the contravariant bases in the undeformed configuration $\mathring{\mathbf{g}}^i \otimes \mathring{\mathbf{g}}^j$, can be computed as:

$$F_{ij} = \mathring{\mathbf{g}}_i \cdot \mathbf{g}_j. \tag{2.26}$$

Accordingly, the covariant components of the right Cauchy-Green deformation tensor $\mathbf{C} = \mathbf{F}^T\mathbf{F}$ are evaluated:

$$C_{ij} = \mathbf{g}_i \cdot \mathbf{g}_j. \tag{2.27}$$

The shell formulation presented in the previous section describes only the mid-surface deformation and neglects the thickness deformation. In the large strain regime, instead, the out-of-plane deformation needs to be taken into account. The approach from Kiendl et al. [60] and Ambati et al. [62] is followed, therefore the definition of the thickness base vector is corrected as:

$$\mathbf{g}_3 = \lambda_3 \mathbf{a}_3, \tag{2.28}$$

with λ_3 being the thickness stretch. Accordingly, the corrected components of the deformation gradient are obtained as:

$$F_{i\beta} = \mathring{\mathbf{g}}_i \cdot \mathbf{g}_\beta, \qquad F_{i3} = \lambda_3 \, \mathring{\mathbf{g}}_i \cdot \mathbf{a}_3. \tag{2.29}$$

The correction needs to be applied also to the Cauchy-Green deformation tensor:

$$C_{\alpha\beta} = \mathbf{g}_{\alpha\beta}, \qquad C_{\alpha 3} = 0, \qquad C_{33} = {\lambda_3}^2. \tag{2.30}$$

Since the shell kinematics is only defined by the displacement field of the middle surface of the shell, the thickness deformation cannot be determined directly. Therefore, the plane stress condition $S^{33} = 0$ is employed as an additional constraint and it is enforced in a local iterative manner at each thickness integration point. After the update of the kinematic variable in equations (2.28) and (2.29) according to the new value of the thickness stretch λ_3, the corrected Cauchy-Green deformation tensor can be computed as $\mathbf{C} = \mathbf{F}^T\mathbf{F}$ or as shown in equation (2.30). In the first iteration of the process, the current thickness stretch value is chosen from the last converged step, while $\lambda_3 = 1$ is considered for the first step of the analysis. According to $J2$ plasticity theory [61], the elasto-plastic material tangent tensor $\mathbb{C}$ and the stress tensor $\mathbf{S}$ are recomputed from the corrected $\mathbf{F}$. The linearization of the plane stress condition:

$$S^{33} + \frac{\partial S^{33}}{\partial C_{33}} \Delta C_{33} = S^{33} + \frac{1}{2}\mathbb{C}^{3333} \Delta C_{33} = 0, \tag{2.31}$$

allows us to compute ΔC_{33} and so to update the value of C_{33}, from the just obtained S^{33} and $\mathbb{C}^{3333}$. The corrected value of the thickness stretch is then easily determined according to equation (2.30):

$$\lambda_3 = \sqrt{C_{33}}, \tag{2.32}$$

and used as input for a new iteration, until the plane stress condition is numerically satisfied within a certain tolerance.

2.1.2 Discretization of the geometry with LR NURBS

The considered shell formulation requires at least C^1 continuity of the shape functions of the discretized model in order to compute the curvature expressions in equations (2.7) or (2.9). Isogeometric analysis, thanks to the smoothness of the NURBS (Non-Uniform Rational B-splines) basis functions, provides the required continuity and it is the favorable choice for the discretization.

A univariate B-spline basis functions N_i^p of degree p is defined featuring a parametric coordinate ξ and a knot vector $\Xi = \left\{\xi_1, \xi_2, ..., \xi_{n+p+1}\right\}$, with n being the associated number of control points $\boldsymbol{P}_i$. In this work, only open knot vectors are considered, meaning that the first and last knots have multiplicity equal to $p+1$. The univariate B-splines are computed recursively, with respect to the degree p, by the Cox - de Boor formula, starting from piecewise constants ($p = 0$):

$$p = 0 \qquad N_i^0(\xi) = \begin{cases} 1 & \xi_i \leq \xi < \xi_{i+1} \\ 0 & \text{elsewhere} \end{cases}, \tag{2.33}$$

$$p \geq 1 \qquad N_i^p(\xi) = \frac{\xi - \xi_i}{\xi_{i+p} - \xi_i} N_i^{p-1}(\xi) + \frac{\xi_{i+p+1} - \xi}{\xi_{i+p+1} - \xi_{i+1}} N_{i+1}^{p-1}(\xi). \tag{2.34}$$

B-spline functions are C^∞ continuous between knot spans and have C^{p-k} continuity in the correspondence of knots, with k being the multiplicity of the knot. A B-spline curve $\boldsymbol{C}$ is defined by the linear combination of the B-spline basis functions and of the corresponding control points:

$$\boldsymbol{C}(\xi) = \sum_{i=1}^{n} N_i^p(\xi) \boldsymbol{P}_i. \tag{2.35}$$

By associating to each control point a "weight" w_i, it is possible to define a NURBS curve as:

$$\boldsymbol{C}(\xi) = \frac{\sum_{i=1}^{n} N_i^p(\xi) w_i}{\sum_{k=1}^{n} N_k^p(\xi) w_k} \boldsymbol{P}_i = \sum_{i=1}^{n} R_i^p(\xi) \boldsymbol{P}_i, \tag{2.36}$$

with $R_i^p(\xi)$ representing a univariate NURBS basis function, which has the same continuity properties of B-splines. The parametrization of a surface domain $\boldsymbol{S}$ using NURBS basis functions can be obtained considering two parametric coordinates (ξ, η), two sets of knot vectors ($\Xi = \left\{\xi_1, \xi_2, ..., \xi_{n+p+1}\right\}$ and $\mathcal{Z} = \left\{\eta_1, \eta_2, ..., \eta_{m+q+1}\right\}$), a net of $n \times m$ control points $\boldsymbol{P}_{i,j}$, and a tensor product of univariate B-spline basis functions (N_i^p and M_j^q) of degree p, q:

$$\boldsymbol{S}(\xi, \eta) = \frac{\sum_{i=1}^{n} \sum_{j=1}^{m} N_i^p(\xi) M_j^q(\eta) w_{i,j}}{\sum_{k=1}^{n} \sum_{l=1}^{m} N_k^p(\xi) M_l^q(\eta) w_{k,l}} \boldsymbol{P}_{i,j} = \sum_{i=1}^{n} \sum_{j=1}^{m} R_{i,j}^{p,q}(\xi, \eta) \boldsymbol{P}_{i,j}, \tag{2.37}$$

where the term $w_{i,j}$ represents the weights associated with each control point and $R_{i,j}^{p,q}(\xi, \eta)$ the bivariate NURBS basis functions. The global knot vector net of lines defines the so-called Bézier mesh of the geometry. One of the advantages of the adoption of NURBS basis functions, with respect to B-splines, is the fact that the first ones allow for the exact representation of conical sections and surfaces such as circles, cylinders and similar geometries, which are commonly present in engineering structures.

In the context of phase-field fracture analyses, a fine mesh needs to be adopted at least in the vicinity of the crack area, see Section 2.2.1. Due to their tensor product properties, standard NURBS allow only for a global refinement of the mesh that dramatically increases the element number and so the computational cost of the analyses, in case small elements are required. Various isogeometric techniques have been developed for solving the problem of the local refinement, among all Hierarchical B-splines [63, 64] later developed into Truncated Hierarchical B-splines [65], T-Splines [66, 67] and Hierarchical T-splines [68] can be mentioned. Dokken et al. [69] introduced Locally Refined (LR) B-splines, which have been applied to isogeometric analysis by Johannessen et al. [70]. LR B-splines have also been shown to produce better matrices, in terms of sparsity and condition number, with respect to other technologies developed for the local refinement of splines [71]. The technology of LR B-splines is based on the fact that the support of univariate B-splines includes only a limited number of knot spans, i.e.

$[\xi_i, \xi_{i+p+1}]$, constituting a "local knot vector" Ξ^i. The definition of bivariate LR B-splines implies the product of two univariate LR B-splines defined over local knot vectors Ξ^i and $\mathcal{Z}^j$, as follows:

$$B_{\boldsymbol{\Xi}^k}(\xi, \eta) = N^p_{\Xi^i}(\xi) M^p_{\mathcal{Z}^j}(\eta). \tag{2.38}$$

The bivariate LR B-spline has support over a portion of the domain corresponding to a bivariate local knot vector $\boldsymbol{\Xi}^k$ in parametric space and the tensor product properties are maintained only at the level of the basis functions, allowing for an unstructured configuration of the mesh. The same idea can be adopted for extending the approach to LR NURBS [72]. Therefore, bivariate LR NURBS basis functions can be defined as

$$R^{\gamma}_{\boldsymbol{\Xi}^k}(\xi, \eta) = \gamma_k \frac{B_{\boldsymbol{\Xi}^k}(\xi, \eta) w_k}{\sum_{l=1}^{n_{CP}} B_{\boldsymbol{\Xi}^l}(\xi, \eta) w_l}, \tag{2.39}$$

with the term γ_k is introduced in order to maintain the partition of unity property of the shape functions after the refinement operation. In the context of LR NURBS, surfaces are therefore parametrized as:

$$\boldsymbol{S}(\xi, \eta) = \sum_{k=1}^{n_{CP}} R^{\gamma}_{\boldsymbol{\Xi}^k}(\xi, \eta) \boldsymbol{P}_k, \tag{2.40}$$

where n_{CP} is the number of control points.

An LR mesh can be obtained starting from a uniform isogeometric mesh and by operating successive splits of certain LR B-splines, or LR NURBS, basis functions. This split implies the insertion of new mesh lines over the entire local knot vector of the considered shape function and the generation of a new couple of control points and relative weights (computed in order to maintain the partition of unity property) that replace the split basis function. For details about the algorithms for the local refinement of the mesh, the reader is referred to Johannessen et al. [70]. It is important to recall that different refinement strategies can be adopted. Both the "full span" (Figure 2.1a) and the "minimum span" (Figure 2.1b) approaches rely on the definition of an element to be refined. According to the first strategy, all the shape functions that have support on the chosen element are split by the insertion of two mesh lines, one in each parametric direction. The new mesh lines span from the minimum to the maximum knot included in the support of all the basis functions supported by the element. If the ”minimum span” strategy is adopted, instead, the inserted mesh lines are just long enough in order to split at least one function. This allows for a smaller footprint of the refinement. The ”structured mesh” strategy (Figure 2.1c) is based on the split of all the knot spans of the support of a chosen basis function. Compared to the other approaches, the last one provides a more regular mesh when multiple refinement steps are performed and, moreover, keeps the aspect ratio of the elements in the parametric space constant. For these reasons, it was chosen and adopted in all the works presented, with the difference that Paper 2 is limited to the use of LR B-splines, while Paper 3 and Paper 4 include also LR NURBS.

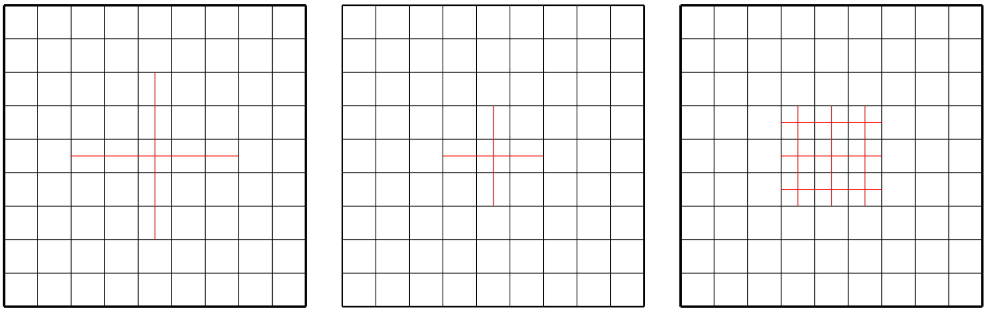

(a) Full span. The selected element to be split is the one in the middle of the mesh.

(b) Minimum span. Since biquadratic NURBS are used, a basis function has support on three knot spans for each parametric direction, and so the inserted mesh lines span over three elements.

(c) Structured mesh. The refined basis function has support over the elements which are split.

Figure 2.1: Comparison between the considered refinement strategies for a biquadratic LR NURBS mesh. Red lines indicate the inserted mesh lines.

2.2 Phase-field approach to fracture

This section presents the main features of the phase-field approach for modeling fracture starting from the brittle case, the first one to be studied and addressed by the scientific community. Some important enhancements to the original model are introduced and briefly discussed. In the last part of the section, the phase-field approach for ductile fracture is presented.

2.2.1 Brittle fracture formulation

The variational formulation of brittle fracture (Francfort and Marigo [32]) directly stems from Griffith's theory [31], according to which the equilibrium of a crack is controlled by a potential strain energy term and a term related to the work required for the creation of new surfaces. The same two terms are present in the energy functional E, whose minimization can describe the entire fracture process:

$$E(\boldsymbol{\varepsilon}, \Gamma) = \int_{\Omega \backslash \Gamma} \psi_e(\boldsymbol{\varepsilon}) \, dV + G_c \int_{\Gamma} d\Gamma. \tag{2.41}$$

In this formulation, the strain energy density ψ_e is integrated over the unbroken domain $\Omega \setminus \Gamma$, while the fracture energy is computed by integrating the material fracture toughness G_c over the discrete domain of the crack $\Gamma \subset \Omega$. The fact that Γ is unknown and evolves during the analysis represents a drawback of the approach. The regularized formulation by Bourdin et al. [33] overcomes the problem by approximating the crack surface energy as:

$$G_c \int_{\Gamma} d\Gamma \approx \int_{\Omega} \psi_s(s, \nabla s) \, dV, \tag{2.42}$$

so that the energy functional can be rewritten in the form:

$$E_\ell(\boldsymbol{\varepsilon}, s) = \int_{\Omega} \big[g(s)\psi_e(\boldsymbol{\varepsilon}) + \psi_s(s, \nabla s) \big] \, dV. \tag{2.43}$$

The term ψ_s, defined over the whole domain Ω, is the so-called fracture energy density and depends on the scalar phase-field variable s. In the phase-field approach, which may be also categorized as a gradient damage model [73, 74], the crack topology is approximated by the continuous variation of s from a value associated with intact material (in this case 1) to a value associated with fully broken material (in this case 0). The width of the smeared crack profile is controlled by the regularization length scale parameter ℓ. For $\ell \to 0$, the approximation theoretically tends, in the sense of Γ convergence, to the sharp crack solution by Francfort and Marigo [75]. Since the length scale parameter needs to be chosen small, a discretization employing fine elements at least in the crack region is needed, in order to correctly resolve the very steep gradient of the smeared crack profile (see Section 2.1.2). A generalized formulation of the fracture energy density is hereby presented:

$$\psi_s(s, \nabla s) = \frac{G_c}{2c_w}\left[\frac{w(s)}{4\ell} + \ell|\nabla s|^2\right]. \tag{2.44}$$

The term $w(s)$ is referred as "dissipation function" and controls the energy dissipation process related to the formation of new cracks. It must fulfill the following properties [76]:

$$w(0) = 1, \qquad w(1) = 0, \qquad w'(s) \leq 0 \text{ for } 0 \leq s \leq 1, \tag{2.45}$$

while the term c_w is computed as:

$$c_w = \int_0^1 \sqrt{w(\delta)}\, d\delta. \tag{2.46}$$

Bourdin et al. [33] adopted a formulation of ψ_s following the so-called "AT2 model" originally proposed by Ambrosio and Tortorelli [77]. In this model, the dissipation function has a quadratic expression in the form $w(s) = (1-s)^2$, and therefore $c_w = 1/2$. According to this choice, the fracture energy density takes the form:

$$\psi_s^{AT2}(s, \nabla s) = G_c\left[\frac{(1-s)^2}{4\ell} + \ell|\nabla s|^2\right]. \tag{2.47}$$

This expression of the fracture energy density is adopted for the work in this thesis and leads to a strong form of the phase-field evolution equation (see equation (2.49)) that contains spatial derivatives of s of the second order, therefore it is termed as "second-order" phase-field theory and it will be indicated as $\psi_{s,2}$ in the rest of the work. This formulation leads to a material model that does not show a perfectly linear elastic behavior, since the phase-field damage starts to accumulate from the beginning of the analysis. An alternative formulation, not adopted in this work, is represented by the "AT1 model", proposed by Pham et al. [73], which employs a linear dissipation function $w(s) = (1-s)$, with $c_w = 2/3$. In the latter case, the fracture energy density expression reads:

$$\psi_s^{AT1}(s, \nabla s) = \frac{3G_c}{4}\left[\frac{1-s}{4\ell} + \ell|\nabla s|^2\right]. \tag{2.48}$$

According to this expression, an initial linear elastic behavior of the material including a clear elastic limit before fracture can be reproduced. Additionally, this formulation avoids another drawback of the AT2 model, namely the fact that, even if the final crack is fully localized, the dissipation during the nucleation phase is spread over a large area.

The term $g(s)$ in equation (2.43) represents a degradation function which couples the phase-field with the elastic field and degrades the properties of the fractured material (see Section 2.2.2.2). The stationarity condition of the energy functional (2.43) with respect to s, considering the AT2 formulation, leads to the strong form of the phase-field evolution equation:

$$\frac{2\,\ell}{G_c} g' \psi_e + s - 4\,\ell^2 \Delta s = 1, \tag{2.49}$$

where $g' = dg(s)/ds$. The driving force of the fracture process in the phase-field equation is the strain energy density ψ_e. The weak form of the previous equation, including δs as a test function for s and considering the usual boundary conditions of the phase-field problem, reads:

$$\int_\Omega \left(\frac{2\,\ell}{G_c} g' \psi_e + s - 1 \right) \delta s \; dV + 4\,\ell^2 \int_\Omega \nabla s \cdot \nabla \delta s \; dV = 0. \tag{2.50}$$

In the IGA discretized framework (see Section 2.1.2), in analogy with the approach adopted for the momentum equation, the variation of expression (2.50) with respect to the discrete value of the phase-field at the control points s_r leads to the residual phase-field vector $\mathbf{R}_{PF}$, whose linearization brings to the tangent stiffness matrix $\mathbf{K}_{PF}$. So, the expression:

$$\mathbf{K}_{PF}\, \Delta\tilde{\mathbf{s}} = \mathbf{R}_{PF}, \tag{2.51}$$

represents the linearized version of the phase-field evolution equation, which is solved for an increment of the vector of the discrete phase-field values at the control points, namely $\Delta\tilde{\mathbf{s}}$.

2.2.2 Enhancements to the phase-field model

2.2.2.1 Tension-compression split

The formulation presented in the previous section (2.43) does not distinguish between fracture behavior in tension and compression and can be referred to as ”isotropic model”, according to which the whole elastic strain energy density is degraded. In order to separate the two behaviors, it is necessary to split the elastic strain energy ψ_e into ”active” and ”inactive” parts (”positive” and ”negative” or ”tension” and ”compression”, referred to as ψ_e^+ and ψ_e^-, respectively), so that fracture under compression and penetration of the crack lips in case of crack closure are prevented. Therefore a specific additive decomposition of the strain energy density is considered:

$$\psi_e = \psi_e^+ + \psi_e^-, \tag{2.52}$$

and it is assumed that the degradation induced by the phase-field acts only on the positive part of the strain energy function. The functional (2.43) and the strong form of the phase-field evolution equation (2.49) are then rewritten as:

$$E_\ell(\boldsymbol{\varepsilon}, s) = \int_\Omega \Big[g(s)\psi_e^+(\boldsymbol{\varepsilon}) + \psi_e^-(\boldsymbol{\varepsilon}) + \psi_s(s, \nabla s) \Big] \, dV, \tag{2.53}$$

and

$$\frac{2\,\ell}{G_c} g' \psi_e^+ + s - 4\,\ell^2 \Delta s = 1. \tag{2.54}$$

A possible approach, proposed by Miehe et al. [78] and adopted in this work for the brittle fracture case (so, in the small strain setting, see Paper 2 and Paper 3), is based on an additive decomposition of the strain tensor

$$\boldsymbol{\varepsilon} = \boldsymbol{\varepsilon}^+ + \boldsymbol{\varepsilon}^-. \tag{2.55}$$

The positive and negative part of $\boldsymbol{\varepsilon}$ are retrieved through a spectral split of the strain tensor:

$$\boldsymbol{\varepsilon} = \sum_{i=1}^{3} \varepsilon_i \, \boldsymbol{n}_i \otimes \boldsymbol{n}_i, \tag{2.56}$$

in which ε_i and $\boldsymbol{n}_i$ represent the eigenvalues and eigenvectors of the strain tensor, respectively. $\boldsymbol{\varepsilon}^+$ and $\boldsymbol{\varepsilon}^-$ are then obtained from the positive and negative principal strains as

$$\boldsymbol{\varepsilon}^\pm = \sum_{i=1}^{3} \langle \varepsilon_i \rangle^\pm \boldsymbol{n}_i \otimes \boldsymbol{n}_i, \tag{2.57}$$

with $\langle x\rangle^{\pm} = (x \pm |x|)/2$. According to this approach, the tension and compression components of the strain energy density and of the stress tensor are obtained as follows

$$\psi_e^{\pm} = \frac{1}{2}\lambda\left(\langle \mathrm{tr}(\boldsymbol{\varepsilon})\rangle^{\pm}\right)^2 + \mu\,\mathrm{tr}\left(\left(\boldsymbol{\varepsilon}^{\pm}\right)^2\right), \tag{2.58}$$

$$\boldsymbol{\sigma}^{\pm} = \lambda\langle \mathrm{tr}(\boldsymbol{\varepsilon})\rangle^{\pm}\,\boldsymbol{I} + 2\mu\,\boldsymbol{\varepsilon}^{\pm}, \tag{2.59}$$

with λ and μ being the Lamé constants and $\boldsymbol{I}$ being the identity tensor. The positive terms ψ_e^+ and $\boldsymbol{\sigma}^+$ are therefore degraded by the degradation function:

$$\psi_e(\boldsymbol{\varepsilon}, s) = g(s)\psi_e^+(\boldsymbol{\varepsilon}) + \psi_e^-(\boldsymbol{\varepsilon}), \tag{2.60}$$

$$\boldsymbol{\sigma}(\boldsymbol{\varepsilon}, s) = g(s)\boldsymbol{\sigma}^+(\boldsymbol{\varepsilon}) + \boldsymbol{\sigma}^-(\boldsymbol{\varepsilon}). \tag{2.61}$$

The driving force of the fracture process in the phase-field equation is now represented by the positive part of the strain energy density.

An alternative approach has been introduced by Amor et al. [79] and it is based on a decomposition of the strain energy into volumetric and deviatoric parts. In the small strains context:

$$\begin{aligned}\psi_e^+(\boldsymbol{\varepsilon}) &= \frac{1}{2}\kappa_0\langle \mathrm{tr}(\boldsymbol{\varepsilon})\rangle^{+2} + \mu\left(\boldsymbol{\varepsilon}_{dev} : \boldsymbol{\varepsilon}_{dev}\right),\\ \psi_e^-(\boldsymbol{\varepsilon}) &= \frac{1}{2}\kappa_0\langle \mathrm{tr}(\boldsymbol{\varepsilon})\rangle^{-2},\end{aligned} \tag{2.62}$$

with $\boldsymbol{\varepsilon}_{dev} = \boldsymbol{\varepsilon} - \mathrm{tr}(\boldsymbol{\varepsilon})\boldsymbol{I}/3$. The approach has been extended to the finite strains setting by Borden et al. [57]:

$$\begin{aligned} J^e < 1 &\begin{cases} \psi_e^+ = \psi_e^{dev}(\bar{\mathbf{b}}^e) \\ \psi_e^- = \psi_e^{vol}(J^e) \end{cases} \\ J^e \geq 1 &\begin{cases} \psi_e^+ = \psi_e^{dev}(\bar{\mathbf{b}}^e) + \psi_e^{vol}(J^e) \\ \psi_e^- = 0 \end{cases} \end{aligned} \tag{2.63}$$

and it is adopted for the ductile fracture case (see Paper 4), since it fits within the considered $J2$ plasticity model, according to which the volumetric and deviatoric contributions of the strain energy are computed in equations (2.24) and (2.25).

Alternative formulations for the tension-compression split have been presented by Freddi et al. [80], based on the symmetric and antisymmetric parts of the strain tensor, and by Steinke and Kaliske [81], who introduced a decomposition of the stress tensor with respect to the crack orientation.

2.2.2.2 Degradation function

The degradation function $g(s)$ controls the transition of the behavior of the material from the intact to the cracked state and has the following characteristics:

$$g(0) = 0, \qquad g(1) = 1, \qquad g'(s) \geq 0 \text{ for } 0 \leq s \leq 1. \tag{2.64}$$

The standard degradation function for phase-field brittle fracture models, adopted also in this work for the brittle case (see Paper 2 and Paper 3), reads:

$$g(s) = (1 - \eta)s^2 + \eta. \tag{2.65}$$

This quadratic degradation function includes a positive small factor $\eta \approx 0$ for avoiding zero stiffness of the material in a fully cracked state. The particular case of the quadratic degradation function in connection with the brittle fracture framework leads to a linear phase-field evolution equation, meaning that the equation can be solved in a single iteration.
Borden et al. [57] introduced a cubic degradation function in the form:

$$g(s) = m(s^3 - s^2) + 3s^2 - 2s^3, \tag{2.66}$$

in which m is chosen as a small positive value ($\approx 10^{-4}$) in order to provide a small but positive slope of the function at $s = 1$ and allow crack nucleation. For $m \to 0$, a perfectly linear stress-strain relationship up to the critical stress is obtained, so that a pure elastic behavior with no softening prior to crack nucleation (typical of brittle fracture) can be observed. In case the cubic degradation function is adopted, the phase-field equation becomes nonlinear and requires an iterative solver. The cubic degradation function has been adopted for the simulation of dynamic brittle fracture of shells by Paul et al. [82] and its influence has been investigated by Bilgen et al. [83]. Kuhn et al. [84] and Sargado et al. [85] proposed and discussed further alternative versions of $g(s)$ for the brittle fracture phase-field formulation.

The phase-field ductile fracture model adopted in this work employs an expression of the degradation function depending on the accumulated plastic strain variable (see 2.2.3 and Paper 4), thus coupling the plastic and fracture behavior of the material and leading, to a nonlinear phase-field evolution equation.

2.2.2.3 Irreversibility of fracture

Another important aspect of the phase-field fracture model is fracture irreversibility, meaning that the crack does not heal if the external loads are removed. The approach adopted in this work is the one introduced by Miehe et al. [78], according to which a history field, corresponding to the maximum of the positive part of the strain energy density up to the current pseudo-time T, is defined:

$$\mathcal{H}(T) := \max_{\tau \in [0,T]} \psi_e^+(\tau). \tag{2.67}$$

This history variable then replaces ψ_e^+ in the strong form of the phase-field evolution equation (2.54), leading to:

$$\frac{2\,\ell}{G_c} g' \mathcal{H} + s - 4\,\ell^2 \Delta s = 1. \tag{2.68}$$

Among others, an alternative approach for ensuring fracture irreversibility based on penalty method has been adopted by Artina et al. [86] and Gerasimov and De Lorenzis [87].

2.2.2.4 Higher-order phase-field model

Borden et al. [51] introduced an alternative expression of the fracture energy density presented in equation (2.47):

$$\psi_{s,4}(s, \nabla s, \Delta s) = G_c \left[\frac{(1-s)^2}{4\ell} + \frac{\ell}{2} |\nabla s|^2 + \frac{\ell^3}{4} \left(\Delta s\right)^2 \right], \tag{2.69}$$

which leads to a ”higher-order” phase-field model (or ”fourth-order”, again referring to the order of the spacial derivatives present in the strong form of the phase-field equation, see equation (2.70)). The higher-order derivatives present in the expression of $\psi_{s,4}$ require at least C^1 continuity of the shape functions between elements, in the discretized framework. Thanks to the smoothness of (LR) NURBS basis functions, the adoption of isogeometric analysis allows for the implementation of the fourth-order phase-field model. The strong form of the phase-field evolution equation employing the higher-order formulation and irreversibility of fracture through the history field reads:

$$\frac{2\,\ell}{G_c} g'\mathcal{H} + s - 2\,\ell^2 \Delta s + \ell^4 \Delta(\Delta s) = 1, \tag{2.70}$$

so that the weak form of the equation is:

$$\int_\Omega \left(\frac{2\,\ell}{G_c} g'\mathcal{H} + s - 1 \right) \delta s \; dV + 4\,\ell^2 \int_\Omega \nabla s \cdot \nabla \delta s \; dV + \ell^4 \int_\Omega \Delta s \cdot \Delta \delta s dV = 0. \tag{2.71}$$

The adoption of the higher-order phase-field formulation allows for a more accurate description of the residual ”cohesive tractions” and residual stresses in the fractured elements and for a higher convergence rate [51]. These features have been investigated in Paper 3, where it was observed that with the adoption of the fourth-order model in connection with a predictor-corrector algorithm for adaptive mesh refinement (see Section 3.3), less staggered iterations and fewer step recomputations are necessary for the converge of the analyses, leading to a reduction of the computational costs.

The analytical solution of the homogeneous phase-field equation in one dimension, after the imposition of the initial condition $s(x = 0) = 0$, brings to the theoretical expression of the unidimensional phase-field profile. Closed form exponential solutions of this profile can be obtained for both the phase-field formulations [51]. For the second-order model:

$$s_2(x) = 1 - e^{-\frac{|x|}{2\ell}}, \tag{2.72}$$

while for fourth-order theory:

$$s_4(x) = 1 - e^{-\frac{|x|}{\ell}} \left(1 + \frac{|x|}{\ell} \right). \tag{2.73}$$

These profiles are shown and compared in Figure 2.2, where it can be noted that the higher-order formulation has a slightly narrower profile, meaning that a smaller region of the domain needs to have a fine mesh in order to correctly resolve the crack. For this and for the abovementioned reasons, the fourth-order phase-field theory can be considered more efficient than the second-order model, although the formulation is more involved. The higher-order model is therefore adopted, whenever possible, for the simulations in this work (see Section 4.2, Paper 3, and Paper 4).

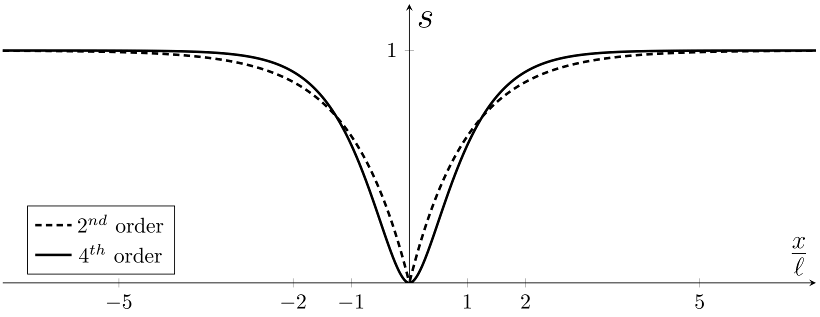

Figure 2.2: Theoretical unidimensional phase-field profiles for second- and fourth-order formulations.

2.2.3 Ductile fracture formulation

The application of the phase-field approach to the simulation of ductile fracture requires a more complex formulation than the one adopted for the brittle fracture case. In addition to the elastic and fracture energy contributions already present in the brittle fracture energy functional (equation (2.47)), an energy dissipation term related to the plastic deformation needs to be included. The main challenge consists in effectively combining the effects of the plasticity-related term and of the fracture term. One of the first proposed formulations can be considered as a ”brittle fracture in elasto-plastic solids” model (Duda et al. [88]), as no coupling is present between the phase-field and the plasticity. As a result, the fracture develops in correspondence with elastic stress concentrations and not in regions that are subjected to high plastic strain, as usually observed in reality. Alessi et al. [89, 90], Borden et al. [57], Kuhn et al. [91], Huang et al. [92], Rodriguez et al. [93] and Miehe et al. [94] (the two latter works including a non-local gradient formulation for plasticity) proposed approaches in which the damage-plastic coupling is achieved through the definition of a degradation function, dependent on the phase-field parameter, not only for the elastic strain energy term, but also for the hardening energy contribution and the plastic dissipated work. Dittman et al. [95] combined the plasticity and fracture behaviors by degrading the critical fracture energy by a function depending on the equivalent plastic strain, in addition to adopting the higher-order phase-field formulation (see Section 2.2.2.4). According to the approach by Ambati et al., at first proposed for the small strains setting [96] and then extended to finite strains [58], the coupling between the two terms is provided by the degradation function of the tensile part of the elastic strain energy, as this function depends on the accumulated plastic strain. This formulation is presented in this section and it is adopted for the work (see Paper 4).

For the ductile fracture case of the phase-field approach, a regularized version of the energy functional that includes elastic, plastic and fracture energy contributions is assumed:

$$E_\ell(\bar{\mathbf{b}}^e, J^e, \alpha, s) = \int_\Omega \left[\psi_e(\bar{\mathbf{b}}^e, J^e, p, s) + \psi_p(\alpha) + \psi_s(s)\right] dV. \tag{2.74}$$

In comparison with the functional assumed for the brittle fracture case (equation (2.47)), the elastic energy term ψ_e is defined according to the finite strains settings and the plastic strain energy term ψ_p is added. The fracture energy density ψ_s can be chosen according to the definitions in equation (2.47) or (2.69), leading to a second or fourth-order phase-field ductile fracture model, respectively. The volumetric-deviatoric split of elastic the strain energy (see Section 2.2.2.1) is adopted in order to reproduce the physical asymmetry of the material behavior in tension and compression, so that only the positive part of ψ_e is degraded through the degradation function $g(s, p)$:

$$\psi_e(\bar{\mathbf{b}}^e, J^e, p, s) = g(s, p)\ \psi_e^+(\bar{\mathbf{b}}^e, J^e) + \psi_e^-(J^e). \tag{2.75}$$

The degradation function accounts for the deterioration of the material due to the nucleation and growth of microcracks and in this formulation takes the following form:

$$g(s, p) = (1 - \eta)s^{2p^m} + \eta, \tag{2.76}$$

with

$$p = \frac{\alpha}{\alpha_{crit}}. \tag{2.77}$$

The term p describes the localization and accumulation of the plastic strains in comparison with the critical value of the hardening variable α_{crit}, and its presence in equation (2.76) couples the plastic behavior of the material with the fracture process. In agreement with the observation that fracture, in elasto-plastic materials, occurs in areas that undergo plasticity, cracks can develop only in regions having significant (i.e. comparable with α_{crit}) plastic strains. In addition, the present formulation implies that, once the fracture starts evolving in a certain area, the plastic strains cease to accumulate, so that the deformations occurring in that region are totally elastic. The expression of $g(s,p)$ can be considered as a generalization of the quadratic degradation function used for brittle fracture, as demonstrated by the fact that, for $\alpha = \alpha_{crit}$ (so, for $p = 1$), equation (2.65) is retrieved. The parameters α_{crit} and m can be considered as material dependent and need to be calibrated through the comparison with experimental results (see [58] or Paper 4). The parameter m can take the values $\{1, 2, 3, ...\}$ and controls the speed of the fracture process. A value of m higher than 1 allows for a slower accumulation of the damage when $p < 1$, and for a faster accumulation when $p > 1$ [96].

The strong form of the phase-field evolution equation for the ductile fracture model reads, for the second- and fourth-order formulations respectively,

$$\frac{2\,\ell}{G_c} g_{,s} \psi_e^+ + s - 4\,\ell^2 \Delta s = 1, \tag{2.78}$$

$$\frac{2\,\ell}{G_c} g_{,s} \psi_e^+ + s - 2\,\ell^2 \Delta s + \ell^4 \Delta(\Delta s) = 1, \tag{2.79}$$

where:

$$g_{,s} = \frac{\partial g(s,p)}{\partial s} = (1-\eta) 2p^m s^{(2p^m - 1)}. \tag{2.80}$$

Unlike the case of brittle fracture with quadratic degradation function, the phase-field equation is nonlinear and therefore requires the use of an iterative solver. Assuming fracture irreversibility through the adoption of the history field (see Section 2.2.2.3):

$$\mathcal{H}^e(T) := \max_{\tau \in [0,T]} \psi_e^+(\bar{\mathbf{b}}^e, J^e, \tau), \tag{2.81}$$

the weak forms of the ductile fracture phase-field equations for standard and higher-order formulation are:

$$\int_\Omega \left(\frac{2\,\ell}{G_c} g_{,s} \mathcal{H}^e + s - 1\right) \delta s \; dV + 4\,\ell^2 \int_\Omega \nabla s \cdot \nabla \delta s \; dV = 0, \tag{2.82}$$

$$\int_\Omega \left(\frac{2\,\ell}{G_c} g_{,s} \mathcal{H}^e + s - 1\right) \delta s \; dV + 2\,\ell^2 \int_\Omega \nabla s \cdot \nabla \delta s \; dV + \ell^4 \int_\Omega \Delta s \cdot \Delta \delta s \; dV = 0. \tag{2.83}$$

2.3 Phase-field fracture modeling for thin shells and plates

A crucial point of the work is the combination of the phase-field model (brittle and ductile) with the presented shell formulation. Special attention is required for the through-thickness distribution of the stress and of the strain energy when reduced-order models, in which the kinematics is based on midsurface variables, are adopted. Various approaches have been introduced for modeling brittle fracture in thin shells and plates with the phase-field method. Areias et al. [97] used two different phase-fields for describing the fracture at the top and bottom shell surfaces. Amiri et al. [98] and Ulmer et al. [99] employed instead a single phase-field variable defined over the shell midsurface. However, in the first approach, the tension-compression split was not considered, while in the second one the split was applied only to the membrane part of the strain tensor. According to Kiendl et al. [100], the tension-compression split, based on the spectral decomposition of the strain tensor, is performed at various points through the shell thickness and numerical integration of the positive and negative strain energy contributions is operated. This approach is adopted in this work (Paper 2, Paper 3 and Paper 4) and presented in the following section, distinguishing between brittle and ductile fracture. A similar approach is presented by Kikis et al. [101] for the modeling of phase-field brittle fracture in Reissner-Mindlin shells and plates. Pillai et al. [102] presented instead a formulation of the phase-field brittle fracture for MITC4+ Reissner-Mindlin degenerated shell elements. Through-thickness integration, but only for the bending part of the strain energy, is employed also by Paul et al. [82], who use a volumetric-deviatoric strain decomposition for modeling the dynamic fracture of Kirchhoff-Love shells. Solid-shell elements were adopted by Reinoso et al. [103], who used, for the phase-field variable, a linear interpolation between the top and bottom surfaces, and by Ambati et al. [104], who used through-thickness isogeometric discretization of the phase-field and of the displacement field. The latter contribution is the first attempt, limited to the small strain framework, of using a phase-field ductile fracture model for shell structures.

2.3.1 Phase-field brittle fracture in thin shells

The adopted approach for modeling phase-field brittle fracture in thin shells consists in reducing the model to the behavior of the midsurface variables, as usually done for Kirchhoff-Love elements. So, the strain energy surface density Ψ_e, which expresses the strain energy per unit area of the midsurface, is defined by through-thickness integration of ψ_e, and its positive and negative parts are computed as:

$$\Psi_e^{\pm} = \int_{-t/2}^{+t/2} \psi_e^{\pm}(\theta^3)\, d\theta^3. \tag{2.84}$$

In plate and shell formulations, due to the bending component related to the curvature change (see equation (2.5)), the strains can vary linearly between tension and compression through the shell thickness t, as depicted for example in Figure 2.3. Considering combined membrane and bending deformation, the spectral split of $\boldsymbol{\varepsilon}$ needs to be performed on the total strain tensor and not on the membrane and bending components separately:

$$\boldsymbol{\varepsilon}^{\pm}(\theta^3) = \left(\boldsymbol{\varepsilon}^m + \theta^3\boldsymbol{\kappa}\right)^{\pm} \neq \boldsymbol{\varepsilon}^{m\pm} + \theta^3\boldsymbol{\kappa}^{\pm}. \tag{2.85}$$

The dependency of the strain tensor on θ^3 and the degradation of the positive part of $\boldsymbol{\sigma}$ lead to a nonlinear through-thickness distribution of the in-plane stress. For this reason, the integral in equation (2.84) needs to be computed by adopting numerical integration and by performing the spectral split of the total $\boldsymbol{\varepsilon}$ at each thickness integration point. The approach, which can be applied regardless of the specific shell formulation (see for example an application to Reissner-Mindlin shells in [101]) allows for describing a nonlinear degradation of stresses and strain energy through the shell thickness (see Figure 2.3), considering only one value of the phase-field variable s and of the degradation function $g(s)$ at the midsurface.

In an analogous way of what presented for Ψ_e, it is possible to define the fracture energy surface density Ψ_s, from the trough-thickness integration of ψ_s.

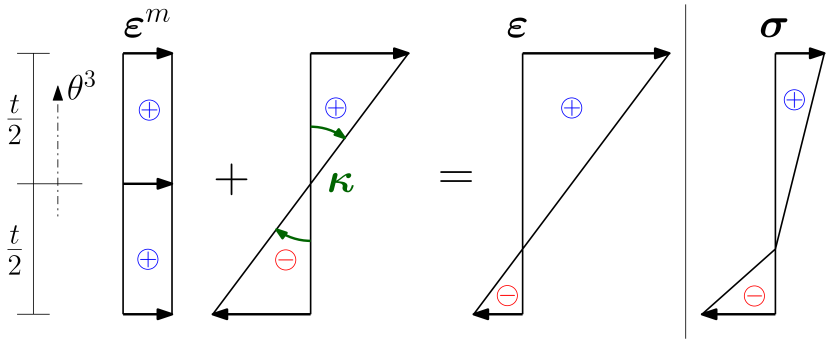

Figure 2.3: Combination of the contributions of membrane and bending strain and total strain over the thickness t for a shell subjected to bending and tension in case of brittle fracture phase-field formulation. Through-thickness stress distribution after degradation of the positive (tensile) component.

Here, for second- and fourth- order phase-field, respectively:

$$\Psi_{s,2} = \int_{-t/2}^{+t/2} \psi_{s,2}(s, \nabla s)\, d\theta^3 = t\, G_c \left[\frac{(1-s)^2}{4\ell} + \ell |\nabla s|^2 \right], \tag{2.86}$$

$$\Psi_{s,4} = \int_{-t/2}^{+t/2} \psi_{s,4}(s, \nabla s, \Delta s)\, d\theta^3 = t\, G_c \left[\frac{(1-s)^2}{4\ell} + \frac{\ell}{2} |\nabla s|^2 + \frac{\ell^3}{4} (\Delta s)^2 \right]. \tag{2.87}$$

The energy functional for brittle fracture problems including the degradation of the positive part of the strain energy density (see equation (2.53)) can be therefore rewritten in a form adapted for thin shells, thus employing surface energy densities:

$$E_\ell(\boldsymbol{\varepsilon}^m, \boldsymbol{\kappa}, s) = \int_A \Big[g(s)\, \Psi_e^+(\boldsymbol{\varepsilon}^m, \boldsymbol{\kappa}) + \Psi_e^-(\boldsymbol{\varepsilon}^m, \boldsymbol{\kappa}) + \Psi_s(s, \nabla s) \Big]\, dA, \tag{2.88}$$

Therefore, the strong form of the phase-field equation for brittle fracture of shells read, for standard and higher-order formulation, respectively:

$$\frac{2\,\ell}{tG_c} g' \Psi_e^+ + s - 4\,\ell^2 \Delta s = 1, \tag{2.89}$$

$$\frac{2\,\ell}{tG_c} g' \Psi_e^+ + s - 2\,\ell^2 \Delta s + \ell^4 \Delta(\Delta s) = 1. \tag{2.90}$$

The history field is defined from the positive part of the surface energy density:

$$\mathcal{H}(T) := \max_{\tau \in [0,T]} \Psi_e^+(\tau), \tag{2.91}$$

and used for enforcing fracture irreversibility (see Section 2.2.2.3) in the weak form of equations (2.89) and (2.90):

$$\int_A \left(\frac{2\,\ell}{tG_c} g' \mathcal{H} + s - 1 \right) \delta s \, dA + 4\,\ell^2 \int_A \nabla s \cdot \nabla \delta s \, dA = 0, \tag{2.92}$$

$$\int_A \left(\frac{2\,\ell}{tG_c} g' \mathcal{H} + s - 1 \right) \delta s \, dA + 2\,\ell^2 \int_A \nabla s \cdot \nabla \delta s \, dA + \ell^4 \int_A \Delta s \cdot \Delta \delta s \, dA = 0. \tag{2.93}$$

2.3.2 Phase-field ductile fracture in thin shells

For the ductile fracture case, the approach for coupling the phase-field model with the structural shell formulation is similar to the one adopted for the brittle fracture. Consequently, the energy functional from equation (2.74) can be rewritten, after through-thickness integration of the energy densities, in the following form

$$E_\ell(\bar{\mathbf{b}}^e, J^e, \alpha, s) = \int_A \left[\Psi_e(\bar{\mathbf{b}}^e, J^e, s, p) + \Psi_p(\alpha) + \Psi_s(s) \right] dA. \tag{2.94}$$

The plastic energy surface density $\Psi_p(\alpha)$ is defined for the integration of $\psi_p(\alpha)$ along t. The nonlinear distribution of the stress tensor along the thickness is a consequence of the plastic behavior of the material and of the degradation of the tensile stresses due to the phase-field fracture formulation, see Figure 2.4. Therefore, numerical integration is again required for computing (2.84). The tension-compression split of the total strain energy is computed at each thickness integration point according to the volumetric-deviatoric formulation at finite strains (see Section 2.2.2.1). Since the correct strain tensor depends both on the membrane and on the bending components, the split needs to be computed on the total strain energy (without separating the membrane and bending parts). Here it is important to recall that the degradation function for ductile fracture (see equation (2.76)) depends not only on the phase-field variable s, but also on the plasticity-related scalar parameter p that, according to the definition in equation

(2.77), depends on the hardening parameter α. Since α is an internal variable assuming different values in any point of the shell continuum, the degradation function can take different values at the various integration points through the shell thickness. So, in this approach, the phase-field parameter, which is defined only on the midsurface, is assumed to be constant through the thickness, but a non-constant degradation function and nonlinear distributions of the stresses along t is obtained (see again Figure 2.4). As a consequence, when the integral in equation (2.84) is computed taking into account the tension-compression split (2.75):

$$\Psi_e = \int_{-t/2}^{+t/2} \left[g(s,p)\psi_e^+(\bar{\mathbf{b}}^e, J^e) + \psi_e^-(J^e) \right] d\theta^3, \tag{2.95}$$

the degradation function term $g(s,p)$ needs to be included in the through-thickness numerical integration. The strong form of the phase-field ductile fracture evolution equation for shells reads:

$$\frac{2\,\ell}{tG_c} \int_t g_{,s}\psi_e^+ \, d\theta^3 + s - 4\,\ell^2 \Delta s = 1, \tag{2.96}$$

$$\frac{2\,\ell}{tG_c} \int_t g_{,s}\psi_e^+ \, d\theta^3 + s - 2\,\ell^2 \Delta s + \ell^4 \Delta(\Delta s) = 1, \tag{2.97}$$

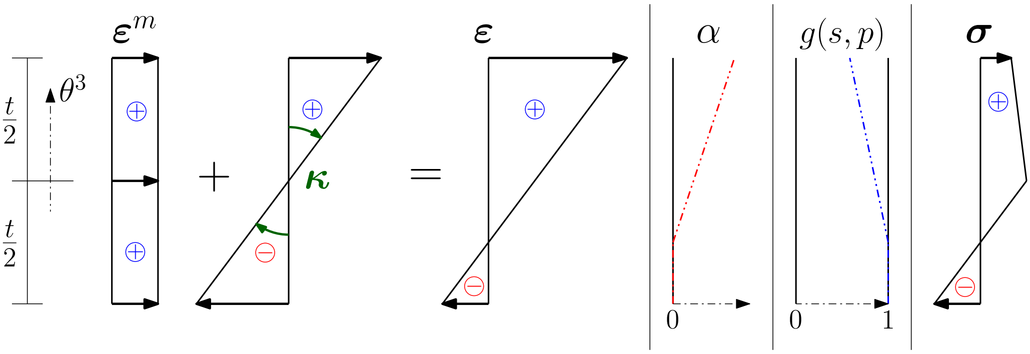

Figure 2.4: Combination of the contributions of membrane and bending strain and total strain $\boldsymbol{\varepsilon}$ over the thickness t for a shell subjected to bending and tension in case of ductile fracture phase-field formulation. Possible distributions of the hardening variable α and of the degradation function $g(s,p)$ along t. As a result, the through-thickness stress $\boldsymbol{\sigma}$ distribution after degradation of the positive (tensile) component is depicted.

with equation (2.96) valid for the second-order formulation and (2.97) for the higher-order model. The weak form of the two previous equations is, therefore:

$$\int_A \left(\frac{2\,\ell}{tG_c} \int_t g_{,s} \mathcal{H}^e d\theta^3 + s - 1 \right) \delta s \; dA + 4\,\ell^2 \int_A \nabla s \cdot \nabla \delta s \; dA = 0, \tag{2.98}$$

$$\int_A \left(\frac{2\,\ell}{tG_c} \int_t g_{,s} \mathcal{H}^e d\theta^3 + s - 1 \right) \delta s \; dA + 2\,\ell^2 \int_A \nabla s \cdot \nabla \delta s \; dA + \ell^4 \int_A \Delta s \cdot \Delta \delta s \; dA = 0. \tag{2.99}$$

The previous equations employ the history field $\mathcal{H}^e$ for enforcing the irreversibility of fracture (see equation (2.81)).

2.4 Penalty-based formulation for patch coupling

In order to simulate the fracture of complex shell structures, an approach for coupling the structural and phase-field behavior across adjacent patch interfaces is proposed. The methodology can impose all the required interface constraints, i.e., displacement and rotational continuity for the structure as well as C^0 and C^1 continuity for the phase-field, with the latter enforced only in the case of the fourth-order phase-field model. The formulation can be applied both to smooth and non-smooth patch connections and to discretizations having matching or non-matching meshes at the interface. The latter feature is crucial when adaptive local refinement is employed, since different mesh densities at two coupled edges might appear, even if the meshes were matching at the beginning of the analysis. The penalty formulation can handle imperfections, such as gaps or intersections between edges, resulting from the use of geometries directly modeled in CAD commercial software. Moreover, the penalty formulations can be used for weakly imposing clamping or symmetry boundary conditions. As shown in Paper 3, the patch-coupling method can also be employed for modeling pre-existing cracks in the form of discontinuities in the structure.

All the penalty parameter involved in the formulation are scaled by the correspondent problem parameters, so that they can be governed by a single global dimensionless penalty parameter α_{glob}. Investigations and results in Paper 1 suggest that setting $\alpha_{glob} = 10^3$ is an adequate choice, independently of the problem parameters. The publication is devoted to the coupling both of isotropic and composite shells modeled with laminated plate theory, but this thesis work is focused only on uniform isotropic material configurations, of which the failure is simulated.

For analyses involving the phase-field approach to brittle and ductile fracture, the structural penalty coupling formulation has been therefore extended for enforcing the required continuity of s across patch interfaces and adopted in Paper 3 and Paper 4. In the following sections, the structural and phase-field penalty coupling method will be reviewed, with a focus on the choice of the penalty parameters.

2.4.1 Structural coupling

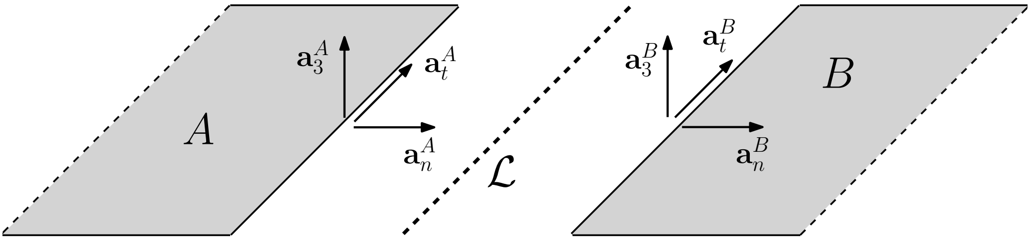

Figure 2.5: Patches A an B coupled along the interface $\mathcal{L}$. Indication of the unitary vectors $\mathbf{a}_t$, $\mathbf{a}_n$ and $\mathbf{a}_3$.

The penalty method for enforcing displacement (C^0) and rotational (C^1) continuity at patch interfaces has been presented in Paper 1 and consists in augmenting the virtual work formulation in equation (2.13) with new contributions:

$$\delta W = \delta W^{\text{int}} - \delta W^{\text{ext}} + \delta W^{\text{pd}} + \delta W^{\text{pr}} = 0. \tag{2.100}$$

The term δW^{pd} represents the virtual work from the penalization of the relative displacement between the coupled patches A and B along the interface curve $\mathcal{L}$ (see Figure 2.5):

$$\delta W^{\text{pd}} = \int_{\mathcal{L}} \alpha_{\text{d}} \left(\mathbf{u}^A - \mathbf{u}^B\right) \cdot \left(\delta\mathbf{u}^A - \delta\mathbf{u}^B\right) d\mathcal{L}. \tag{2.101}$$

The second added term δW^{pr} enforces the rotational continuity between the coupled edges of the patches by penalizing the relative rotations at the interface curve

$\mathcal{L}$:

$$\delta W^{\mathrm{pr}} = \int_{\mathcal{L}} \alpha_{\mathrm{r}} \left(\left(\mathbf{a}_3^A \cdot \mathbf{a}_3^B - \mathring{\mathbf{a}}_3^A \cdot \mathring{\mathbf{a}}_3^B \right) \left(\delta \mathbf{a}_3^A \cdot \delta \mathbf{a}_3^B - \delta \mathring{\mathbf{a}}_3^A \cdot \delta \mathring{\mathbf{a}}_3^B \right) + \right.$$
$$\left. + \left(\mathbf{a}_n^A \cdot \mathbf{a}_3^B - \mathring{\mathbf{a}}_n^A \cdot \mathring{\mathbf{a}}_3^B \right) \left(\delta \mathbf{a}_n^A \cdot \delta \mathbf{a}_3^B - \delta \mathring{\mathbf{a}}_n^A \cdot \delta \mathring{\mathbf{a}}_3^B \right) \right) d\mathcal{L}. \tag{2.102}$$

The terms α_{d} and α_{r} represent the penalty parameters that will be discussed in details in the following section. In equation (2.102), $\mathbf{a}_n$ is the unit vector lying in the plane of the patch and orthogonal to $\mathcal{L}$ which can be computed as:

$$\mathbf{a}_n = \mathbf{a}_t \times \mathbf{a}_3, \tag{2.103}$$

with $\mathbf{a}_t$ being the unit tangent vector of the penalty curve $\mathcal{L}$ (see Figure 2.5). The terms containing $\mathbf{a}_n$ need to be included in equation (2.102) because, without them, it would not be possible to impose rotational continuity of smooth patch connections (in this case, the variation of the terms in the first line of the equation vanishes, see below). Conversely, the terms in the first line are necessary for patches with a 90° angle connection. In this way, instead, the formulation is capable of handling patches forming arbitrary angles at their interface.

For the implementation of the approach in the IGA discretized model and in order to solve the (nonlinear) momentum equation, the variations of the penalty virtual work δW^{pd} and δW^{pr} with respect to the discrete displacement values at the control points u_r need to be added to the internal force vector $\mathbf{R}_u$ (see equation (2.17)):

$$\frac{\partial W^{\mathrm{pd}}}{\partial u_r} = \int_{\mathcal{L}} \alpha_{\mathrm{d}} \left(\mathbf{u}^A - \mathbf{u}^B \right) \cdot \left(\mathbf{u}_{,r}^A - \mathbf{u}_{,r}^B \right) d\mathcal{L}, \tag{2.104}$$

$$\frac{\partial W^{\mathrm{pr}}}{\partial u_r} = \int_{\mathcal{L}} \alpha_{\mathrm{r}} \left(\left(\mathbf{a}_3^A \cdot \mathbf{a}_3^B - \mathring{\mathbf{a}}_3^A \cdot \mathring{\mathbf{a}}_3^B \right) \left(\mathbf{a}_{3,r}^A \cdot \mathbf{a}_3^B + \mathbf{a}_3^A \cdot \mathbf{a}_{3,r}^B \right) + \right.$$
$$\left. + \left(\mathbf{a}_n^A \cdot \mathbf{a}_3^B - \mathring{\mathbf{a}}_n^A \cdot \mathring{\mathbf{a}}_3^B \right) \left(\mathbf{a}_{n,r}^A \cdot \mathbf{a}_3^B + \mathbf{a}_n^A \cdot \mathbf{a}_{3,r}^B \right) \right) d\mathcal{L}. \tag{2.105}$$

The second variation expressions of the penalty virtual works with respect to the discrete displacement values lead to the following terms, that are added to the structural tangent stiffness matrix $\mathbf{K}_u$ (see equation (2.18)):

$$\frac{\partial W^{\mathrm{pd}}}{\partial u_r \partial u_s} = \int_{\mathcal{L}} \alpha_{\mathrm{d}} \left(\mathbf{u}^A_{,s} - \mathbf{u}^B_{,s}\right) \cdot \left(\mathbf{u}^A_{,r} - \mathbf{u}^B_{,r}\right) d\mathcal{L}, \tag{2.106}$$

$$\begin{aligned} \frac{\partial W^{\mathrm{pr}}}{\partial u_r \partial u_s} = \int_{\mathcal{L}} \alpha_{\mathrm{r}} \Bigg(& \left(\mathbf{a}^A_3 \cdot \mathbf{a}^B_3 - \mathring{\mathbf{a}}^A_3 \cdot \mathring{\mathbf{a}}^B_3\right) \left(\mathbf{a}^A_{3,rs} \cdot \mathbf{a}^B_3 + \mathbf{a}^A_{3,r} \cdot \mathbf{a}^B_{3,s} + \mathbf{a}^A_{3,s} \cdot \mathbf{a}^B_{3,r} + \mathbf{a}^A_3 \cdot \mathbf{a}^B_{3,rs}\right) \\ & + \left(\mathbf{a}^A_{3,s} \cdot \mathbf{a}^B_3 + \mathbf{a}^A_3 \cdot \mathbf{a}^B_{3,s}\right) \left(\mathbf{a}^A_{3,r} \cdot \mathbf{a}^B_3 + \mathbf{a}^A_3 \cdot \mathbf{a}^B_{3,r}\right) \\ & + \left(\mathbf{a}^A_n \cdot \mathbf{a}^B_3 - \mathring{\mathbf{a}}^A_n \cdot \mathring{\mathbf{a}}^B_3\right) \left(\mathbf{a}^A_{n,rs} \cdot \mathbf{a}^B_3 + \mathbf{a}^A_{n,r} \cdot \mathbf{a}^B_{3,s} + \mathbf{a}^A_{n,s} \cdot \mathbf{a}^B_{3,r} + \mathbf{a}^A_n \cdot \mathbf{a}^B_{3,rs}\right) \\ & + \left(\mathbf{a}^A_{n,s} \cdot \mathbf{a}^B_3 + \mathbf{a}^A_n \cdot \mathbf{a}^B_{3,s}\right) \left(\mathbf{a}^A_{n,r} \cdot \mathbf{a}^B_3 + \mathbf{a}^A_n \cdot \mathbf{a}^B_{3,r}\right) \Bigg) d\mathcal{L}. \end{aligned} \tag{2.107}$$

For more details regarding the linearization of the quantities in the previous equations, the reader is referred to Paper 1.

For the imposition of symmetric or clamped boundary conditions at the edges of a patch (patch A is assumed), the displacement terms of patch B and its derivatives need to be set to zero in equations (2.104) and (2.106). In case of symmetry, only the components of $\mathbf{u}^A$ (an its derivatives) normal to the symmetry plane are considered. For restraining the rotation in the case of clamped boundary conditions, equations (2.105) and (2.107) can be used but the second line of (2.105) and the last two lines of (2.107) need to be excluded, while $\mathbf{a}^B_3$ and $\mathring{\mathbf{a}}^B_3$ are replaced by $\mathring{\mathbf{a}}^A_n$. For restraining the rotation in the case of symmetry boundary conditions, $\mathbf{a}^B_3$ and $\mathring{\mathbf{a}}^B_3$ are replaced by the normal vector of the symmetry plane. When the displacement and rotation symmetry conditions are enforced, the terms from equations (2.104)-(2.107) are multiplied by a factor equal to 2, in order to correctly represent the contributions from both sides of the symmetry plane.

For the computation of the penalty integrals presented above, the choice of the discretization for the interface curve becomes crucial. If the patches share the same discretization along the coupled edges, this will be assumed also for $\mathcal{L}$. In the case of non-conforming meshes, instead, the discretization of the patch which has the largest number of elements along the connected interface is adopted, and this patch will be considered as patch A. This conservative choice ensures that both edges are entirely considered and avoids that small elements remain unconstrained (this would risk happening if the discretization along the edge with larger elements was chosen). The intersection curve does not necessarily need to correspond to an edge for both the patches. Instead, $\mathcal{L}$ may be an intersection of two NURBS surfaces. In that case, an independent discretization for the interface curve needs to be adopted. If $\mathcal{L}$ does not correspond to one (or both) of the coupled edges, a closest point projection algorithm [105] is adopted in order to find the closest points of the patches, at which evaluate the necessary quantities, from the quadrature points of the interface curve. This allows coupling surfaces that only approximately share a common boundary in the physical space, a possible result of CAD modeling operations.

2.4.1.1 Selection of the structural penalty coupling parameters

For all the penalty formulations, the choice of the penalty parameters is crucial, since they need to be high enough to enforce the satisfaction of the constraints, without creating ill-conditioning in the stiffness matrix. The appropriate value of the penalty parameters is problem-dependent and its choice has a strong influence on the quality of the solution.

The selected approach simplifies the selection of the penalty parameters α_d and α_r by linking them to a global penalty value α_{glob} which is properly scaled by material, geometry and discretization parameters of the model. The scaling terms must maintain dimensional consistency with the momentum equation. Therefore, the penalty parameters α_d and α_r are computed from α_{glob} by scaling it with the membrane and bending shell elastic stiffness values, respectively:

$$\alpha_\mathrm{d} = g(s)\,\alpha_{glob}\frac{E\,t}{h\,(1-\nu^2)}, \tag{2.108}$$

$$\alpha_\mathrm{r} = g(s)\,\alpha_{glob}\frac{E\,t^3}{12\,h\,(1-\nu^2)}, \tag{2.109}$$

with E as the Young's modulus, ν as the Poisson's ratio, and t as the thickness of the shells, while h is the average element length along the coupled edge having the finer discretization (the one along which the integration is performed). For the extension to phase-field fracture analysis, the penalty parameters are further multiplied with the degradation function $g(s)$ to ensure a consistent scaling of structural and penalty stiffness in the cracked areas. This formulation of the penalty parameters is valid for uniform isotropic material configurations, as the ones considered for the phase-field fracture simulations. Paper 1 includes further details regarding the choice of α_d and α_r in case laminated plate theory is employed. The paper includes several simulations and numerous benchmarks involving different analyses types and material properties, which suggest $\alpha_{glob} = 10^3$ as a proper choice for the global penalty parameter. Furthermore, the formulation is employed for simulating a realistic wind turbine structure, as done also in [106].

2.4.2 Phase-field coupling

The penalty approach for ensuring continuity of s across patch interfaces is based on the methodology shown in the previous section for the structural coupling of shells. This method is extended to enforcing the continuity of the phase-field for brittle fracture simulations in Paper 3 and for ductile fracture simulations in Paper 4.

In order to enforce C^0 continuity of the phase-field between the patch interfaces (both for brittle and ductile fracture cases), the following term is added to the left-hand side of the weak form of the phase-field equations (2.92), (2.93), (2.98) and (2.99). Similarly to the approach adopted for the structural coupling, the term penalizes the difference of s between patch A and patch B at the two sides of $\mathcal{L}$:

$$\int_{\mathcal{L}} \alpha_{PF}^{C^0}(s^A - s^B)(\delta s^A - \delta s^B)\, d\mathcal{L}. \tag{2.110}$$

In case the higher-order phase-field formulation is employed, C^1 continuity of s needs to be imposed, in addition to the aforementioned C^0 continuity. This can be achieved by penalizing the relative changes in the directional derivative of the phase-field along $\mathbf{a}_n$ between the two patches. The following term is to be added the the left-hand side of equations (2.93) or (2.99):

$$\int_{\mathcal{L}} \alpha_{PF}^{C^1}(\nabla s^A \cdot \mathbf{a}_n^A - \nabla s^B \cdot \mathbf{a}_n^B)(\nabla \delta s^A \cdot \mathbf{a}_n^A - \nabla \delta s^B \cdot \mathbf{a}_n^B)\, d\mathcal{L}. \tag{2.111}$$

The terms $\alpha_{PF}^{C^0}$ and $\alpha_{PF}^{C^1}$ represent the penalty parameters, whose choice will be discussed in the following section. In equation (2.111), the normal vectors $\mathbf{a}_n^A$ and $\mathbf{a}_n^B$ are assumed to point in the same direction. The proposed approach is applicable to smooth patch interfaces, while it cannot be extended straightforwardly to patch connections forming a kink. In the latter case, the fact that the vectors $\mathbf{a}_n^A$ and $\mathbf{a}_n^B$ belong to two different planes makes the choice of the directional derivative of s to be penalized ambiguous, since the direction of the vectors cannot be chosen univocally. In such situations, where the C^1 continuity of the phase-field cannot be imposed, the second-order phase-field formulation, which requires only C^0 continuity of s, is adopted.

If the ductile fracture phase-field formulation is employed, the nonlinearity of the phase-field evolution equation requires the first variation with respect to the discrete value of the phase-field at the control points s_r of equation (2.110), and of equation (2.111) if applicable, to be added to the residual phase-field vector $\mathbf{R}_{PF}$:

$$\int_{\mathcal{L}} \alpha_{PF}^{C^0}(s^A - s^B)(s^A_{,r} - s^B_{,r})\, d\mathcal{L}, \tag{2.112}$$

$$\int_{\mathcal{L}} \alpha_{PF}^{C^1}(\nabla s^A \cdot \mathbf{a}_n^A - \nabla s^B \cdot \mathbf{a}_n^B)(\nabla s^A_{,r} \cdot \mathbf{a}_n^A - \nabla s^B_{,r} \cdot \mathbf{a}_n^B)\, d\mathcal{L}. \tag{2.113}$$

The second variation expressions need instead to be added to the phase-field tangent stiffness matrix $\mathbf{K}_{PF}$ both for the brittle and ductile fracture formulations:

$$\int_{\mathcal{L}} \alpha_{PF}^{C^0}(s^A_{,s} - s^B_{,s})(s^A_{,r} - s^B_{,r})\, d\mathcal{L}, \tag{2.114}$$

$$\int_{\mathcal{L}} \alpha_{PF}^{C^1}(\nabla s^A_{,s} \cdot \mathbf{a}_n^A - \nabla s^B_{,s} \cdot \mathbf{a}_n^B)(\nabla s^A_{,r} \cdot \mathbf{a}_n^A - \nabla s^B_{,r} \cdot \mathbf{a}_n^B)\, d\mathcal{L}. \tag{2.115}$$

The presented formulation can be used for weakly imposing symmetry conditions at edges by considering, in the previous equations, only the terms relative to patch A.

2.4.2.1 Selection of the phase-field penalty coupling parameters

The penalty parameters are chosen according to the methodology used the structural coupling (Section 2.4.1.1). The global penalty coefficient $\alpha_{glob} = 10^3$ is therefore scaled by terms that maintain dimensional consistency with the phase-field equation and ensure that $\alpha_{PF}^{C^0}$ and $\alpha_{PF}^{C^1}$ are large enough to guarantee the satisfaction of the imposed continuity constraint without creating ill-conditioning in $\mathbf{K}_{PF}$. The history field is the driving force of the fracture process and the term in which it is included becomes numerically predominant, at the points where fracture develops, in the phase-field equation. So, for the imposition of the phase-field continuity, the penalty scaling terms are defined as follows:

$$\alpha_{PF}^{C^0} = \alpha_{glob} \left[\frac{4\ell(1-\eta)\mathcal{H}_{max}}{tG_c} + 1 \right] h, \tag{2.116}$$

$$\alpha_{PF}^{C^1} = \alpha_{glob} \left[\frac{4\ell(1-\eta)\mathcal{H}_{max}}{tG_c} + 1 \right] \ell^2 h. \tag{2.117}$$

$\mathcal{H}_{max}$ corresponds to the current maximum value of the history field over all the integration points of the structure. For the ductile fracture formulation, the penalty parameters remain the same, with $\mathcal{H}^e_{max}$ having the same function as $\mathcal{H}_{max}$. This choice can be justified by the fact that, in fractured regions, the hardening variable reaches levels comparable to α_{crit}, meaning that $p \approx 1$ and so that the quadratic degradation function considered for brittle fracture is approximately retrieved.

2.5 Penalty-based formulation for contact

In Paper 4, a series of experimental tests consisting in different stiffened steel panels being penetrated by an indenter, simulating the consequences of ship grounding, are investigated through phase-field numerical analyses. In order to perform these simulations, a frictionless penalty contact formulation suitable for large deformation problems is adopted and briefly presented in this section.

Also for the contact formulation, the choice of IGA for the spacial discretization presents several advantages, with respect to traditional finite element implementations, including the fact that it is possible to consider the exact geometry of the surfaces in contact and the fact that the higher continuity of the basis functions contributes in improving the performance of the contact algorithms, thanks to the well-posedness of the closest-point projection problems [107]. The adopted approach resembles the one from Dimitri et al. [108], but instead of T-splines, LR NURBS (see Section 2.1.2) are employed for the discretization [109].

The contact between two patches representing the shell midsurfaces is considered. One of them is referred to as *slave* surface and the other as *master* surface. It is assumed that each point $\mathbf{x}^s$ on the slave surface can have only one partner contact point $\mathbf{x}^m$ on the master surface, whose position is computed by a closest point projection [105] of $\mathbf{x}^s$ over the master surface. The normal gap g_N between

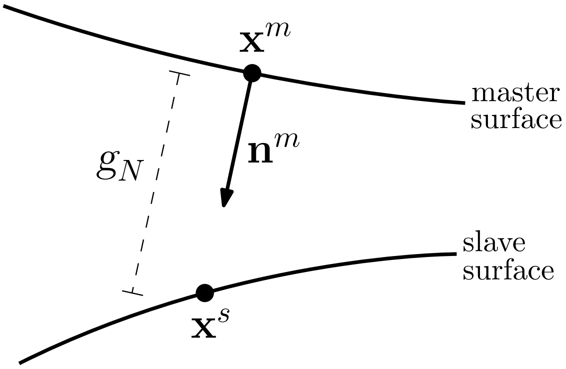

Figure 2.6: Contact formulation, definition of the normal gap.

the two surfaces is computed as:

$$g_N = (\mathbf{x}^s - \mathbf{x}^m) \cdot \mathbf{n}^m, \tag{2.118}$$

with $\mathbf{n}^m$ being the normal unit vector at $\mathbf{x}^m$. The direction of $\mathbf{n}^m$ need to be defined as the one pointing towards the slave surface when no contact occurs (see Figure 2.6), and so it must remain during the analysis, even in case the surfaces come into contact. The definition in equation (2.118), implies that the normal gap is positive if the contact is open, while $g_N < 0$ in case of penetration. For thin shells and plates, instead of defining the contact between the midsurfaces, it is possible to describe the contact between the shell faces by taking into account the slave and master thicknesses, t^s and t^m respectively. In this case, $\mathbf{x}^s$ and $\mathbf{x}^m$ and the relative quantities continue to be defined at the midsurfaces, but contact starts occurring when $g_N < (t^s + t^m)/2$. $\mathbf{T}$ indicates the Piola traction vector and its normal component is the normal contact traction T_N:

$$\mathbf{T} = \mathbf{T}^m = -\mathbf{T}^s = T_N \mathbf{n}^m, \qquad T_N = \mathbf{T} \cdot \mathbf{n}^m. \tag{2.119}$$

The Kuhn-Tucker conditions for impenetrability are defined as follows:

$$g_N \geq 0, \qquad T_N \leq 0, \qquad g_N T_N = 0. \tag{2.120}$$

The penalty formulation allows the regularization of the contact constraint conditions, thus assuming the form:

$$T_N = \alpha_N \langle g_N \rangle^-, \qquad \langle g_N \rangle^- = \begin{cases} g_N & \text{if} \quad g_N < 0 \\ 0 & \text{otherwise} \end{cases} \tag{2.121}$$

with α_N being the penalty parameter related to contact. For $\alpha_N \to \infty$ the exact contact solution can be retrieved, but the use of very large penalty parameters causes ill-conditioning of the stiffness matrix. The frictionless contact contribution to the virtual work of the structure, which needs to be added to equation (2.13), is defined as:

$$\delta W^{\mathrm{N}} = \int_{A^s} T_N \delta g_N \, dA = \alpha_N \int_{A^s} g_N \delta g_N \, dA. \tag{2.122}$$

The integral is evaluated on the slave surface in the reference configuration and δg_N represents the variation of the normal gap. For details regarding the variation and the linearization of the gap function and of the contact virtual work, and their discretization, the reader is referred to [107].

This contact formulation is denoted as Gauss-point-to-surface, since the contributions to the virtual work δW^{N} are computed at each integration point of the slave surface. Contact between patches having non conforming meshes can be managed without any problem, as the master contact point $\mathbf{x}^m$ does not need to be a quadrature point. According to Matzen [110] the non-matching number of the Gauss points and of the degrees of freedom of the contact interface can cause convergence problems due to an over-constrained system. Possible alternatives for alleviating this problem are represented by the choice of Greville, Botella or Chebyshev points for the collocation of the contact equations. Another drawback related to the use of the Gauss-Legendre points is the fact that they are not able to capture contact at edges.

At the beginning of each load-step of analyses including contact, a pre-search algorithm is adopted for excluding, from the computation of the integral (2.122), slave elements which are sufficiently far from the master patch so that they are not affected by penetration, i.e. they do not contribute to δW^{N}. For each not excluded element on the slave surface, the closest element on the master patch is identified, whose center will be the starting point of the search algorithm for finding the contact point $\mathbf{x}^m$ of each integration point belonging to the considered slave element. This pre-computation improves the efficiency of the point search algorithm and prevents it from diverging, i.e. not finding the correct contact point, since the starting point of the search is close to the actual contact point. At this stage, the normal unit vector at $\mathbf{x}^m$ is also computed and the algorithm makes sure that it is oriented in the correct way by inverting its direction, if necessary, so that it can correctly represent $\mathbf{n}^m$. Once the direction of $\mathbf{n}^m$ is determined as the one pointing towards the slave surface (before the contact occurs at $\mathbf{x}^m$), it is kept constant for the rest of the analysis. The contact formulation is also able to handle self-contact of a patch, condition that can be simulated by considering the same surface both as slave and master, see an example in Section 4.3.

When the penalty contact formulation is combined with the phase-field fracture model, an adequate scaling between the structural and the contact penalty stiffness needs to be guaranteed, especially when the regions involved in the contact are also damaged. For this reason, the effect of the phase-field degradation function is added into equation (2.122) through the term $g^{s,m}$, which takes the minimum value of the degradation function between master and slave contact points. Therefore, the elements in the cracked zones have degraded material properties, but they still contribute to the contact penalty terms and, therefore, they provide resistance against penetration. In order to avoid this numerical problem and to remove fully broken elements from the contact computations, zero contact stiffness is guaranteed by setting $g^{s,m} = 0$ if $s < 0.05$ at $\mathbf{x}^s$ or $\mathbf{x}^m$. The virtual work formulation in equation (2.13) is therefore augmented by the following term:

$$\delta W^{\mathrm{N}} = \alpha_N \int_{A^s} g^{s,m} g_N \delta g_N \, dA. \tag{2.123}$$

3 Aspects related to the solution algorithm

This section reviews the algorithmic techniques adopted for improving the efficiency of the phase-field fracture analyses. These techniques have been adopted both for brittle fracture (see Paper 3) and ductile fracture (see Paper 4). Paper 3 contains also the demonstration of the numerical efficiency of the methodologies, through the testing with different benchmarks.

3.1 Staggered solution of the coupled problem

The two governing equations of the phase-field fracture problem, i.e. the momentum and the phase-field evolution equations, are obtained from the stationarity condition of the energy functional (equations (2.88) and (2.94) for brittle and ductile case, respectively) with respect to the displacement field $\mathbf{u}$ and the phase-field s. The numerical solution of the nonlinear system of coupled equation is tackled by employing the staggered solution idea presented by Bourdin et al. [33] and Miehe et al. [78]. Accordingly, the two equations are solved, in their weak form, one after the other at each pseudo-time step of the analysis. The field for which the considered equation is not solved for is kept frozen. The same approach is adopted in this work and the equilibrium of the structure at the end of each load step is ensured by checking the convergence of the solution, with an adequately low tolerance for the residual, after each staggered iteration. The two equations are recomputed, if necessary, until convergence of the staggered iterations is reached. In the brittle fracture context, this choice is crucial because it allows simulating sudden failure by having cracks fully developing in a single load step, with load-displacement curves showing an abrupt drop after the critical load is reached (see the results of the simulations in Paper 3). The analysis presented in Paper 2 was performed without pursuing the convergence of the staggering process, but a maximum fixed number of staggered iterations (10) was instead set for each load step. The result is a load-displacement curve that does not show a

Box 3.1: Loosely and strongly coupled staggering schemes for the ductile fracture system of equations. In case the convergence conditions are not satisfied, the iterations are repeated. For the brittle fracture case, the iteration of the phase-field equation is replaced by the linear solution of the same equation.

Loosely coupled staggering scheme

```
Load step i
  Staggered iterations:
  |
  |  Iterative solution of momentum eq.:
  |  |  Iteration of momentum eq.
  |  |                ↓
  |  |  Check convergence of momentum eq.
  |             ⇓
  |  Iterative solution of phase-field eq.:
  |  |  Iteration of phase-field eq.
  |  |                ↓
  |  |  Check convergence of phase-field eq.
  |             ⇓
  |  Check convergence of stagg. iterations

Load step i + 1
    ...
```

Strongly coupled staggering scheme

```
Load step i
  Staggered iterations:
  |
  |  Iteration of momentum eq.
  |
  |             ⇓
  |
  |  Iteration of phase-field eq.
  |
  |             ⇓
  |
  |  Check convergence of stagg. iterations

Load step i + 1
    ...
```

sudden drop, even if a small step size is used. The fact that brittle cracks may fully develop in a single step is a topic that requires special attention in case an adaptive local mesh refinement technology is adopted, see Section 3.3.

The momentum equation is nonlinear due to the strain energy split, and it requires an iterative solver that finds the equilibrium solution through successive inversion of the structural system. The phase-field equation is linear in the brittle fracture case, therefore a single inversion of the stiffness matrix is sufficient for the solution, and nonlinear in the ductile fracture case, thus requiring an iterative solver. A classical approach, which will be called "loosely coupled" staggering scheme, requires, for each staggered iteration, first the iterative solution of the momentum equation for $\mathbf{u}$ and then the iterative solution of the phase-field equation for s (or the simple linear solution for s in case of brittle fracture). For improving the efficiency of the simulations, the "strongly coupled" staggering scheme is adopted, according to which, in each staggered iteration, a single iteration of the two governing equation is performed (if the approach is applied to the brittle fracture case, the iteration of the phase-field equation is replaced by the linear solution of the equation). Box 3.1 shows a comparison of the two approaches. The strongly coupled staggered scheme requires a higher number of staggered iterations for the solution of the system, but the total number of iterations of the momentum equation is reduced since only one equilibrium iteration is performed in each staggered iteration. Therefore, the reduction of the number of the iterations of the momentum equation, which are computationally more expensive than the linear solution of the phase-field equation, makes the strongly coupled staggering scheme numerically efficient and convenient to adopt. The strong coupling staggering scheme has been effectively applied both to brittle fracture simulations (see Paper 3 for results and considerations about the efficiency of the method) and to ductile fracture simulations (see Paper 4 for results).

3.2 Adaptive time-stepping scheme

As observed by Gerasimov and De Lorenzis [87] for phase-field brittle fracture analyses, if the staggered iterations are recomputed until convergence in each step (see Section 3.1), the use of relatively large pseudo-time steps does not affect the results accuracy and even reduces the computational time, with respect to smaller steps. The use of quite large increments between the steps improves the efficiency of the simulation if this is done when the pure elastic regime dominates, typically in the initial part of the simulations. On the other hand, large steps cannot be used in elasto-plastic analyses when the plasticity starts evolving in the structure, otherwise no convergence of the momentum equation, and so of the staggered iterations, can be achieved. The same applies to the contact formulation, which cannot handle too large step increments that would lead to penetrations at the beginning of the steps too large for allowing the convergence of the equilibrium equation. For these reasons, a simple adaptive step size algorithm is adopted for the elasto-plastic and ductile fracture simulations, some of them also including contact (see Paper 4). The initial step size is chosen as relatively large and it is set as the maximum possible step increment for the analyses. When a load step does not reach convergence, the step is recomputed with an increment reduced by a factor of 2, and the process is repeated until convergence is reached. In order to improve the efficiency of the simulations, increments are obviously intended to be as large as possible. So, each time a step converges, the step size is increased by a factor 1.5 (it was observed that an increase factor equal to the one for step reduction would often lead to non-convergence). The increment cannot, anyway, be larger than the maximum one set at the beginning of the analyses. This approach allows relatively large steps in the initial part of the analyses, while the increment size is reduced when complex deformations occur or contact and phase-field ductile fracture effects dominate the simulation.

3.3 Adaptive local refinement

In phase-field fracture analyses, a fine mesh is required at least in the vicinity of the cracked regions for the correct resolution of the profile of s, see Section 2.2.1. In order to improve the efficiency of the analyses by reducing the total number of elements, the LR NURBS technology presented in Section 2.2.1 is applied to a brittle fracture example in Paper 2. In this case, a pre-refinement of the mesh is performed, as that the crack path is known in advance. If there is not *a priori* knowledge of the crack path, an adaptive local mesh refinement algorithm needs to be adopted.

The use of adaptive mesh refinement for phase-field brittle fracture simulations has been explored with various approaches. Burke et al. [111], Artina et al. [86] and Del Piero et al. [112] showed that local mesh refinement does not affect the propagation of the crack and has little influence both on the energy curves and on the fracture field, justifying the use of adaptive mesh refinement algorithms for saving computational resources when the fracture path is not known in advance. In the first two works, the refinement was controlled by an *a posteriori* error estimate, while the third one used the phase-field value as an indicator for the refinement. The same choice was made by Wick [113] and Heister et al. [114], who focused their attention on a predictor-corrector scheme for the adaptive mesh refinement algorithm, allowing for recomputation of load steps after the refinement. Klinsmann et al. [115] employed an approach for mesh refining or coarsening whose indicator depends on the value of the tension part of the elastic energy, the norm of the phase-field gradient, and the element size. Nagaraja et al. [116] used an adaptive multi-level hp-refinement approach. Adaptive local refinement with T-splines for phase-field fracture simulations in the IGA context was presented by Borden et al. [117] in a simplified version that involved successive runs of the same analysis with meshes refined according to the result of the previous run, thus avoiding the issue of solution transfer between the meshes. Paul et al. [82] used LR NURBS adaptive mesh refinement for simulating dynamic phase-field fracture in thin shells. Adaptive local refinement using Truncated Hierarchical B-splines and Bézier extraction was presented by Kästner and Hennig et al. [118–120], in addition to the possibility of mesh coarsening. These works include detailed discussions about the transfer of the solution between the meshes, distinguishing between quantities related to control and integration points. If only refinement is employed, IGA leads to an error-free projection regarding control point variables, while for the quantities related to the Gauss points, different strategies can be used. The strategy adopted in this work for the transfer of the solution from the coarse to the refined mesh is described in Section 3.3.1.

In the ductile fracture context, additional issues related to the mesh dependency of the adopted elasto-plastic formulation arise and need to be carefully evaluated before applying an adaptive mesh refinement approach. The $J2$ plasticity model (see Section 2.1.1) consists in a local plasticity formulation, meaning that the plastic constitutive equation of the material is evaluated at the integration points of the structure, without including any information about the size of the zone where plastic strains localize, because no length scale parameter is present in the model. As a consequence, the results of the simulations may be sensitive to the elements size in the plastic region, which can localize differently and change dimension in case the mesh is refined [121]. The problem is investigated in details in Paper 4, where it is found that the mesh sensitivity of the ductile failure simulations is reduced thanks to the fact that, in the adopted phase-field formulation (see Section 2.2.3), the localization of the plastic strains ceases at the occurrence of fracture. Moreover, the use of fine meshes allows capturing characteristic features of ductile fracture, such as cracking along shear-bands or cup-and-cone fracture. Adaptive local refinement of the mesh can be safely and effectively employed as long as it is performed before the localization of the plastic strains and the onset of fracture start.

A strategy featuring a multistep predictor-corrector algorithm in order to refine the mesh only where needed, i.e. around the crack area, without *a priori* knowledge of the evolution of the crack is presented. According to the algorithm, which is summarized in Figure 3.1, at the end of each n^{th} step it is evaluated

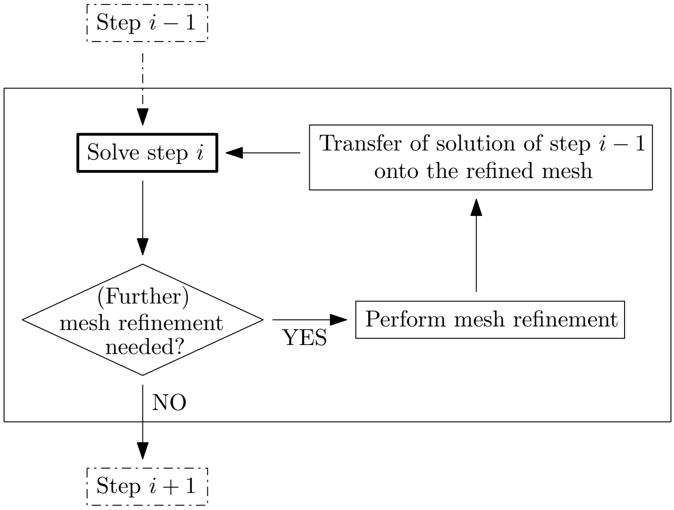

Figure 3.1: Adaptive local refinement algorithm for $n = 1$, meaning that only the current step i is recomputed, if needed.

whether the mesh needs to be refined. If this is the case, the mesh refinement is performed and the current load steps or n load steps, including the current one, need to be recomputed with the refined mesh. For doing so, the solution of the load step preceding the first one to be recomputed needs to be projected onto the refined mesh. If, at the end of the steps recomputation, the crack has grown outside of the region just refined, the mesh is further refined and the procedure is repeated until "convergence of the refinement" is achieved (i.e. there is no need for further refinement). This is the case especially of brittle fracture simulations, which often involve fast-growing cracks that (fully) develop in a single load step (typical examples of unstable crack growth can be found in Section 4.2 and in Paper 3). In ductile fracture simulations, cracks often grow during several steps, meaning that the evolution of the fracture during a single step is relatively limited (even when the convergence of the staggered iterations is achieved). Nevertheless, a refinement step may need to be computed more than once.

For brittle fracture simulations, the value of the phase-field s is used as the indicator for the refinement, similarly to Borden et al. [117]. In this work, it was shown that using the quadratic degradation function (2.65) (as the one adopted), crack nucleation starts at $s = 0.75$, and, therefore, $s_t = 0.75$ was also used as threshold value for refinement. A slightly higher threshold value, namely $s_t = 0.80$, is therefore conservatively adopted for the brittle fracture simulations. In general, one can state that the higher s_t leads to a slightly larger area of refinement, but, on the other hand, it leads to fewer recomputation steps due to crack growth out of the refined zone. In order to check whether an element needs to be refined, the value of the phase-field s measured at the center of the element is compared with s_t. In phase-field ductile fracture analyses, the need for refinement is evaluated according to the fact that cracking is preceded by a concentration of the plastic strains, measured by the hardening variable α. For this reason, the equivalent plastic strain α is chosen as the indicator for the refinement and, at the end of each load step (including recomputed ones), all the elements in which the value of the hardening parameter is higher than a threshold value, i.e. $\alpha > \alpha_t$ at least in one integration point, are marked for refinement. In order to capture the localization of plasticity, that can potentially lead to cracks following shear bands, a conservative approach is adopted so that the mesh is refined before the onset of fracture. Therefore, the value $\alpha_t = 0.25\,\alpha_{crit}$ is chosen.

Regarding the refinement typology, the "structured mesh" refinement strategy (section 2.1.2) is employed, according to which all the knot spans of the support of certain NURBS basis functions are split. These basis functions are selected among all the NURBS having support on each element marked for refinement as the ones which do not include, in their support, any element having already the minimum mesh dimension (see section 3.3.1) for the refinement round. This approach guarantees a regular mesh and a smooth transition between zones with different refinement levels.

The optimal number of steps to be recomputed each time the mesh is refined (n) depends on the type of the problem and the type of solver. When convergence of the staggered iterations is achieved in every step (see Section 3.1), relatively large load steps can be used since their size does not affect the accuracy of the results, but only the frequency in capturing the response of the system. Moreover, the smaller the steps, the higher becomes the computational cost of the analyses, as observed also by Gerasimov and De Lorenzis [87] for brittle fracture analyses. For this reason, "large" load increments are adopted and $n = 1$ is set, both brittle and ductile fracture simulations.

The space-adaptivity algorithm presented in this section is applied to brittle fracture simulations in Paper 3 (where it is investigated how the algorithm improves the efficiency of the analyses) and to ductile fracture problems in Paper 4.

3.3.1 Transfer of variables and fields from coarse to refined mesh

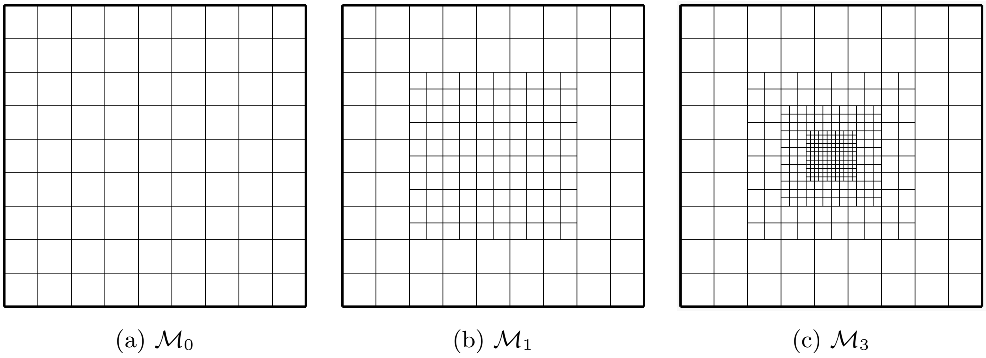
(a) $\mathcal{M}_0$ (b) $\mathcal{M}_1$ (c) $\mathcal{M}_3$

Figure 3.2: Examples of different levels of mesh refinement using the structured mesh strategy.

A critical point of adaptive mesh refinement algorithm consists in the transfer of the solution from the coarse to the refined mesh. This section presents the approach adopted in this work.

Considering an initial non-refined mesh $\mathcal{M}_0$ and m levels of refinement performed, there will be m intermediate refinement rounds producing meshes $\mathcal{M}_1$, $\mathcal{M}_2$, ..., $\mathcal{M}_{m-1}$, $\mathcal{M}_m$, which can be discarded, except for the last one, at the end of the refinement process (see for example Figure 3.2). During each refinement round, the basis functions can be refined only once, i.e. the selected elements can be split only one time per parametric direction. In order to avoid excessive mesh refinement caused by the split of elements that have already been refined during the previous steps of the analysis, a minimum element dimension for the m^{th} refinement round, equal to $h_0/2^m$, is set (h_0 is the characteristic element dimension in the initial non-refined mesh $\mathcal{M}_0$). The evaluation of the element size is performed in the parametric space, so that the mesh distortion does not influence the refinement strategy.

For each refinement round, all the state variables defined over the coarse mesh $\mathcal{M}_m$ need to be transferred to the refined mesh $\mathcal{M}_{m+1}$. For the variables defined at the control points (displacement $\mathbf{u}$ and phase-field s, that are also the unknowns of the coupled problem), the projection occurs according to the same algorithm used for determining the coordinates of the control points in the refined mesh [70]. Regarding the variables stored at the integration points, the transfer is based on the interpolation of the quantities between coarse and refined meshes in a fashion similar to the approached used by Caseiro et al. [6] for transferring strain quantities from integration points to an alternative set of points, see Figure 3.3. For this approach, a distinction needs to be operated between the brittle and the ductile fracture implementation. In the brittle case, the only quantity to consider is the history field $\mathcal{H}$, stored at each quadrature point of the elements of the surface. In ductile fracture case, instead, the history field $\mathcal{H}^e$, the hardening variable α, the thickness stretch λ_3, and the plastic right Cauchy-Green deformation tensors $\mathbf{C}^p = \mathbf{F}^{p^T}\mathbf{F}^p$ are defined and stored at each thickness integration point. The transfer of these quantities, from the integration points of the coarse element to the ones of the refined elements having the same position across the thickness, is performed in the same way as done for $\mathcal{H}$ in the brittle fracture context, as outlined in the following part of the section. For the right Cauchy-Green deformation tensor, the transfer is operated separately for each component.

For each element to be refined, a set of bivariate Bernstein polynomials $\boldsymbol{B}_m$ corresponding to the basis functions of a Bézier element with the same polynomial order of the adopted NURBS parametrization is defined. The value of the history field in a (ξ, η) point of the coarse mesh element can be consequently computed as:

$$\mathcal{H}(\xi, \eta) = \boldsymbol{B}_m(\xi, \eta)\hat{\mathcal{H}}_m, \tag{3.1}$$

where $\hat{\mathcal{H}}_m$ indicates the (unknown) set of the values of the history field at the control points of the Bézier element. If $(\bar{\xi}_m, \bar{\eta}_m)$ indicates the set of the local coordinates of all the quadrature points of the Bézier element, the previous expression can be rewritten as:

$$\mathcal{H}(\bar{\xi}_m, \bar{\eta}_m) = \mathbf{B}_m(\bar{\xi}_m, \bar{\eta}_m)\hat{\mathcal{H}}_m. \tag{3.2}$$

In the latter equation, $\mathbf{B}_m$ collects the values of the Bernstein polynomials in all the integration points. For each of the sub-elements in which the element is split, the coordinates of the integration points in the parametric space of the coarse element are denoted by $(\bar{\xi}_{m+1}, \bar{\eta}_{m+1})$. Analogously to equation (3.2), the projected value of the history field onto the integration points of the refined mesh elements can be found as:

$$\mathcal{H}(\bar{\xi}_{m+1}, \bar{\eta}_{m+1}) = \mathbf{B}_m(\bar{\xi}_{m+1}, \bar{\eta}_{m+1})\hat{\mathcal{H}}_m. \tag{3.3}$$

This expression can be rewritten as:

$$\mathcal{H}(\bar{\xi}_{m+1}, \bar{\eta}_{m+1}) = \mathbf{B}_m(\bar{\xi}_{m+1}, \bar{\eta}_{m+1})\mathbf{B}_m^{-1}(\bar{\xi}_m, \bar{\eta}_m)\mathcal{H}(\bar{\xi}_m, \bar{\eta}_m), \tag{3.4}$$

by employing the inversion of the relation in (3.2). Since the refinement occurs by splitting in half each element along both the parametric directions, the coordinates of the integration points are the same in the Bézier parametric space of each element to be split, and so the term $\mathbf{B}_m(\bar{\xi}_{m+1}, \bar{\eta}_{m+1})\mathbf{B}_m^{-1}(\bar{\xi}_m, \bar{\eta}_m)$ of equation (3.3) is identical for all elements, at each refinement level and at each step of the simulation. Therefore, the projection matrix for the quantities defined at the integration points and can be precomputed at the beginning of the analysis, making the mapping approach computationally inexpensive.

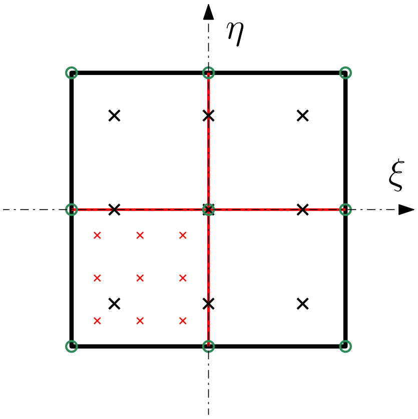

Figure 3.3: Transfer operator for the quantities stored at the integration points for a biquadratic mesh with 3 × 3 Gauss points per element. Black lines indicate the element to be split and black crosses the location of its integration points $(\bar{\xi}_m, \bar{\eta}_m)$, referred to its parametric space. Green circles correspond to the control points of the Bézier element. After the refinement, four elements are generated from the inserted red lines. For one of the newly generated fine elements, the location of the Gauss points $(\bar{\xi}_{m+1}, \bar{\eta}_{m+1})$ is shown.

4 Additional numerical examples

The papers attached in Appendix A contain all the relevant numerical simulations and results obtained in relation to the formulation presented in Section 2. This section includes significant examples that were not published but whose results are worth being mentioned. The first one is a convergence study on the quadrature scheme for the through-thickness integration in the context of the brittle fracture phase-field model for thin plates and shells. The second study includes the comparison of numerical and experimental results for the brittle fracture of notches specimens, while the third consists in a challenging benchmark for the elasto-plastic shell formulation in connection with the adopted model for contact.

4.1 Study on the through-thickness integration scheme for brittle fracture in thin shells

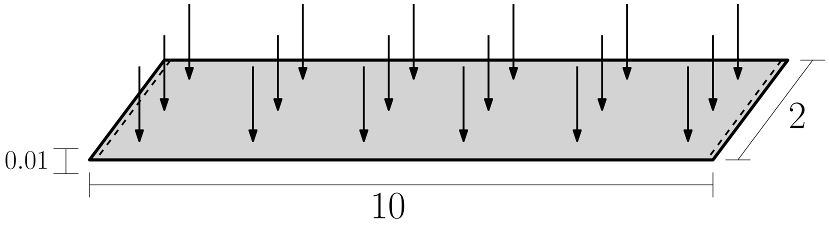

Figure 4.1: Setup of the simulation of the simply supported beam problem (dimensions in mm). Dashed lines indicate supported edges.

In order to investigate the effect of different integration schemes or different numbers of integration points for the through-thickness numerical integration of the positive and negative part of the strain energy density ψ_e (equation (2.84)) for the phase-field brittle fracture approach for thin plates and shells, a model constituted by a simply supported beam subjected to bending due to a uniform pressure in the out-of-plane direction is considered. The geometry and dimensions of the specimen are outlined in Figure 4.1, while the material parameters are Young's modulus $E = 10 \times 10^9$ N/mm^2, Poisson's ratio $\nu = 0$, fracture tough-

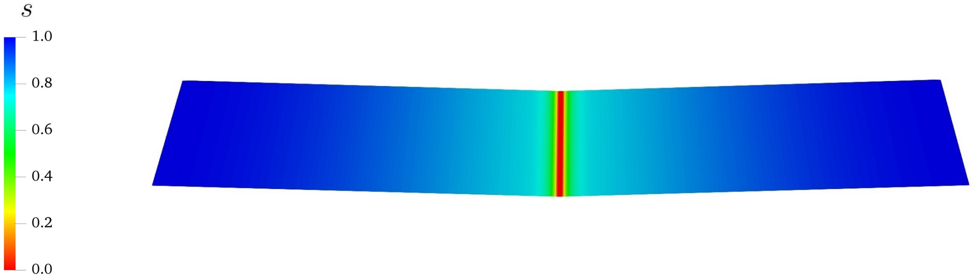

Figure 4.2: Simply supported beam problem, result of the simulation on the deformed structure. The colormap indicates the value of the phase-field variable s.

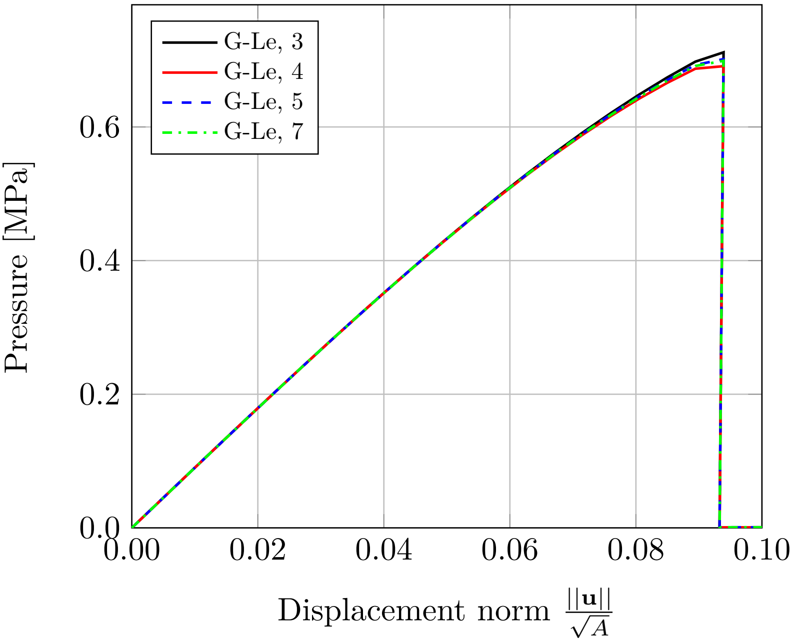

Figure 4.3: Load-displacement curves for the simply supported beam example using Gauss-Legendre (G-Le) through-thickness integration scheme.

ness $G_c = 3$ N/mm and length scale $\ell = 0.04$ mm. Adaptive local refinement (Section 3.3) with 2 levels of refinement from the initial uniform mesh is adopted, so that the minimum element size is equal to $h = \ell/2$. Quadratic LR NURBS with 3×3 Gauss-Legendre integration points per element are employed. A phase-field formulation for brittle fracture considering second-order theory (according to the AT2 model), spectral split, and quadratic degradation function is chosen for this numerical test.

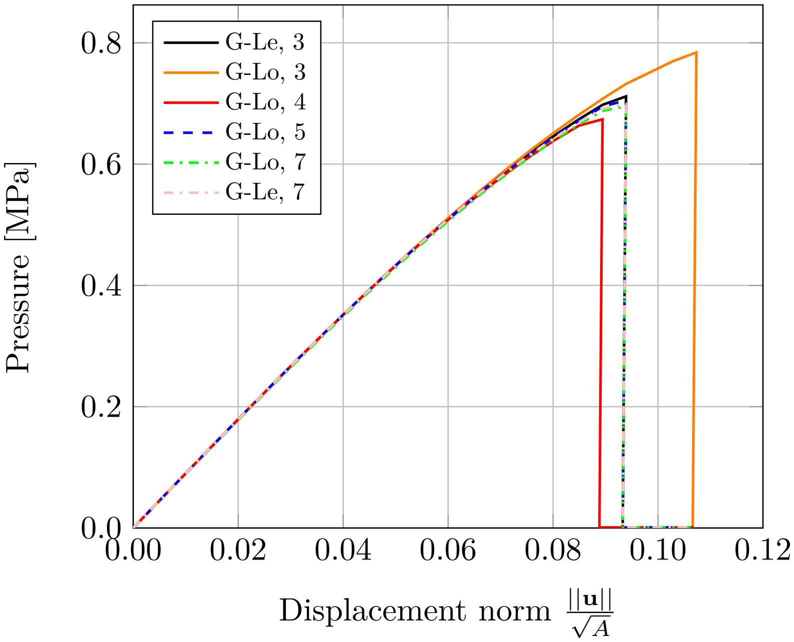

Figure 4.4: Load-displacement curves for the simply supported beam example using Gauss-Lobatto (G-Lo) through-thickness integration scheme, compared with Gauss-Legendre (G-Le) scheme.

Figure 4.2 shows the result of the simulation for the case of traditional Gauss-Legendre through-thickness integration scheme with 3 quadrature points. As expected, the crack nucleates and develops until complete fracture in the middle of the beam (very similar results are obtained also with a different integration scheme or a different number of integration points). The load-displacement curves in Figure 4.3 describe this behavior through a deviation of the curves from the linear elastic branch, as typical for the AT2 formulation due to the widespread dissipation in correspondence with crack nucleation, followed by an abrupt pressure drop corresponding to the full development of the crack, which happens in a single step due to the convergence of the staggered iterations. The different curves in Figure 4.3 correspond to different numbers of thickness integration points according to a traditional Gauss-Legendre scheme, with a predominance of odd numbers, which allow placing an integration point at the shell midsurface. As the results with 7 or 9 points can be considered converged, since the curves are practically overlapping, the result with 3 points can be considered accurate, as it is reasonably close to the converged curves, also in terms of critical load and critical displacement. For the results in Figure 4.4, a through-thickness integration scheme using Gauss-Lobatto quadrature points is adopted. Unlike the Gauss-Legendre rule, this scheme locates integration points at the extremes of the domain to integrate, corresponding, in this case, to the top and bottom surfaces of the plates (or shells). The load-displacement curves show how the Gauss-Lobatto quadrature rule provides less accurate results, when a low number of integration points is considered, with respect to the Gauss-Legendre scheme. Nevertheless, the result with 7 integration points can be considered converged and corresponding to the one using the same number of Gauss-Legendre points. Even if the Gauss-Lobatto integration scheme allows placing quadrature points in correspondence to the location of the maximum and minimum strains and strain energies (typically, top and bottom surfaces), the results of the through-thickness integration are less accurate than the Gauss-Legendre scheme. This might be related to the fact that, for polynomial functions, considering n integration points, it is proven that the Gauss-Legendre rule can integrate exactly functions up to the degree $2n-1$, while this maximum degree is reduced to $2n-3$ for the Gauss-Lobatto scheme. The strain energy density to integrate through the thickness is not necessarily described by a polynomial, but this gives an idea of the higher precision of the first rule with respect to the second one. For these reasons, the Gauss-Legendre quadrature rule is adopted and, according to Figure 4.3, the use of 3 thickness integration points represents the optimal trade-off between accuracy and efficiency of the simulations.

4.2 Simulation of the brittle fracture of V-notched specimens

The brittle fracture of V-notched specimens under mixed-mode I+II loading conditions is simulated according to the experimental setup from Gomez et al. [122]. Different geometries having the notch at the middle of the specimen are considered (see Figure 4.5) The vertical notch specimens with notch angle $\alpha = 30°, 60°, 90°$ are called V30, V60 and V90, respectively. The tilted geometries with notch at 45° and notch angle $\alpha = 30°, 60°, 90°$ are referred as T30, T60 and T90, respectively. The specimens are subjected to three point bending tests with imposed displacement of the upper support, so that also the analyses are performed in imposed displacement mode. The loading condition for the notches, corresponding to mixed mode I (tensile opening mode) and mode II (in-plane shear

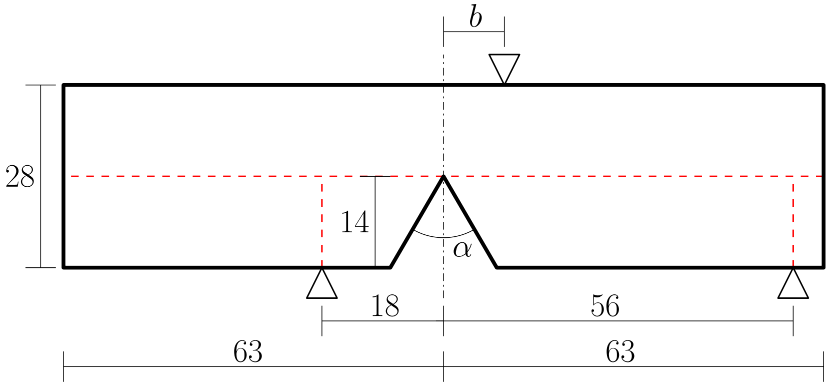

(a) Vertical notch, $\alpha = 30°,\ 60°,\ 90°$

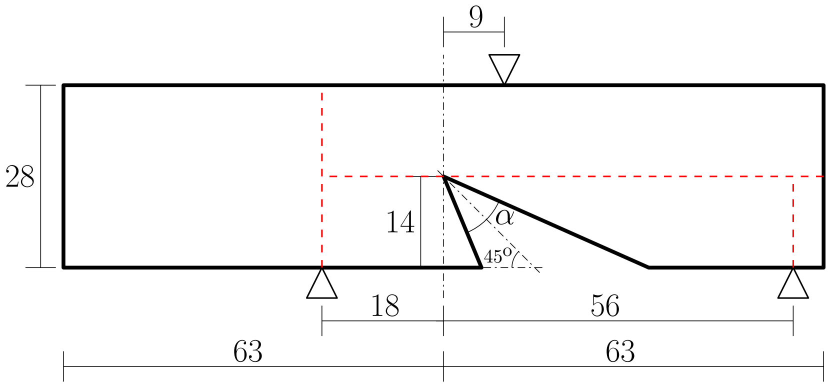

(b) Tilted notch, $\alpha = 30°,\ 60°$

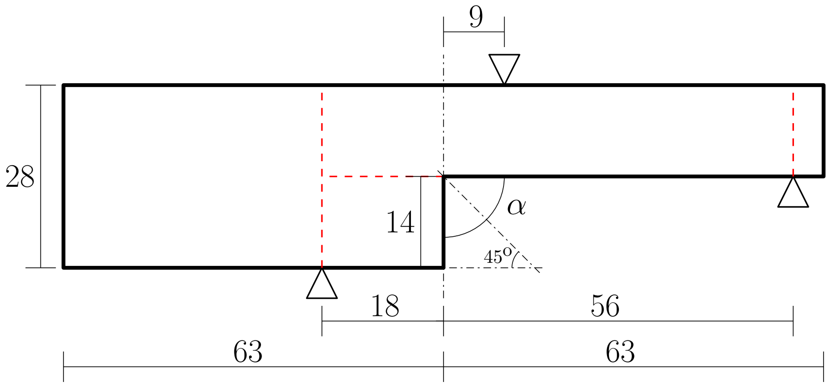

(c) Tilted notch, $\alpha = 90°$

Figure 4.5: Setup of the simulations of the fracture of the V-notched specimens (dimensions in mm). Dashed red lines indicate the division in patches.

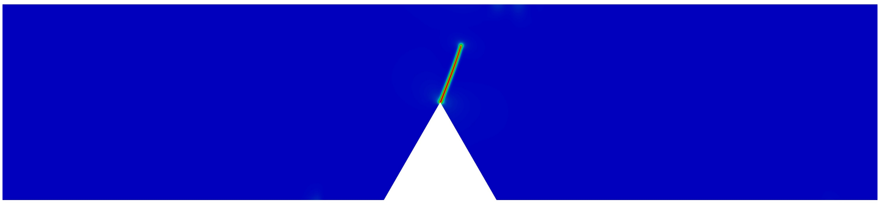

(a) V60 b9 specimen

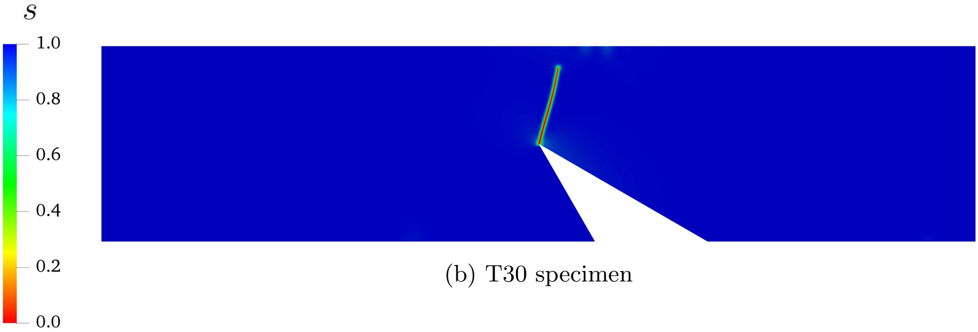

(b) T30 specimen

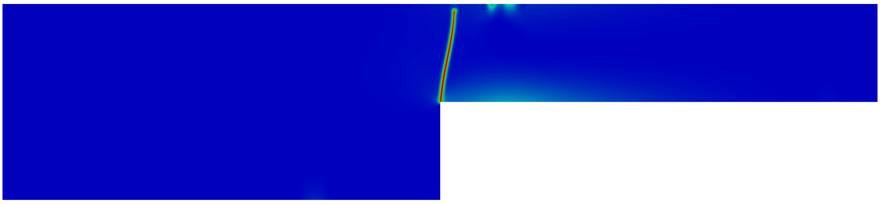

(c) T90 specimen

Figure 4.6: Results of the simulations of the fracture of three V-notched specimens. The colormap indicates the value of the phase-field variable s.

mode), are obtained by placing the supports not symmetrically with respect to the notch. For the vertical notch specimen, two different positions of the upper support are considered ($b = 1$ mm or $b = 9$ mm), in order to simulate different fracture conditions. The penalty-based patch coupling formulation presented in Section 2.4 is used for modeling the geometries without excessive mesh distortion and for imposing the supports in the corrected points of the specimens (see again Figure 4.5 for the patch decomposition of the geometries). The material of the tested specimens was polymethyl-methacrylate (PMMA), an amorphous glassy polymer that shows non-linear behavior at room temperature and linear elastic behavior up to fracture at $-60°$ C. Therefore, the tests were performed at the temperature of $-60°$ C inside an environmental chamber cooled by liquid nitrogen. The average material properties at $-60°$ C, assumed also for the simulations, are

Young's modulus $E = 5.05 \times 10^3$ MPa, Poisson's ratio $\nu = 0.40$, tensile strength $\sigma_c = 128.4$ MPa, and critical stress intensity factor $K_{IC} = 53.76$ MPa$\sqrt{\text{mm}}$. Given the two-dimensional geometry and the thickness of the specimens ($t = 14$ mm), plane strain conditions are assumed. According to Linear Elastic Fracture Mechanics (LEFM) laws [123], it is possible to determine the fracture toughness of the material, needed for the phase-field model, from the available parameters:

$$G_c = \frac{(1-\nu^2){K_{IC}}^2}{E}. \tag{4.1}$$

Given the smooth geometry of the specimens, the fourth-order phase-field model is employed. When trying to predict the results of experimental tests with the phase-field method, the choice of the length scale parameter ℓ is crucial. As stated in Section 2.2.1, ℓ is a regularization parameter for the model controlling the width of the smeared phase-field crack so that the solution tends to the sharp crack one as the length scale parameter is decreased towards zero (however, Γ convergence has not been proven yet for the fourth-order phase-field model). This would imply that, the smaller ℓ, the better the results of the simulations are. On the other hand, the length scale parameter cannot be freely chosen as close to zero, as ℓ controls the element size in the crack region since the discretization has to be able to resolve the phase-field crack profile. Most of the time, in practical contexts, the minimum element size that can be adopted in the simulations influences the choice of the length scale parameter. The adaptive mesh refinement technologies (see Section 3.3) help in making phase-field simulations less computationally expensive, so that smaller minimum element sizes can be used. From the solution of the homogeneous unidimensional phase-field equation in the brittle framework, the following expression is obtained [117,124]:

$$\ell = \left(\frac{9}{16}\right)^2 \frac{EG_C}{6{\sigma_c}^2}. \tag{4.2}$$

This expression allows relating the length scale parameter to the material parameters of the analysis. It has to be remarked that the derivation of this formula is based on the simple assumptions of linear elasticity, quadratic degradation function, and AT2 formulation of the fracture energy density, and it might be expanded for more complex formulations. According to (4.2), the value $\ell = 0.0078$ mm is obtained. By employing adaptive local refinement (Section 3.3) and 5 levels of refinement from the initial mesh, it is possible to have a minimum element size of $h = 0.05$ mm. From this value, in order to respect the rule of thumb according to which $h = \ell/2$ (quadratic shape functions are assumed), a length scale parameter $\ell = 0.100$ mm is adopted for the simulations. This value is larger than the one obtained by the relation (4.2) but still comparable to it.

Figure 4.6 shows the results of three analyses with different notch geometries. It is possible to notice that, for the T90 case, moderate cracking appears at the point where the displacement is imposed. This fact can slightly reduce the reliability of the prediction. The results of the simulations for all the specimens, in terms of fracture load and fracture angle, are summarized in Table 4.1. Three repetitions of the experimental tests for each specimen were performed. Here, the average value from the three experiments is reported. The analysis fracture load is the maximum load from the load-displacement curve of the simulations, that for all the specimens consists of an almost linearly increasing part followed by an abrupt drop corresponding to the step in which the crack fully develops. The fracture angle φ is referred to the notch bisector direction and it is measured in part of the crack close to the notch. The predicted results show good agreement with the experimental data, both in terms of critical load (which is often overestimated in the simulations) and fracture direction. The achievement is relevant, considering that only two parameters related to fracture, i.e. the tensile strength σ_c and the fracture toughness G_c (or the critical stress intensity factor K_{IC}), are needed in order to describe the failure of the specimens with the phase-field method.

Despite the good results obtained with these simulations, the topic regarding the correct choice of ℓ remains a challenging question, especially when the prediction of experimental results, which ultimately is one of the reasons for developing the phase-field approach to fracture, is involved. As already recalled, the length scale parameter can be intended as a regularization parameter for the model but also as related to material properties (Equation (4.2)). Additionally, ℓ scales the fracture toughness G_c in all the expressions of the fracture energy density (see for example Equation (2.44)). Bilgen et al. [83] and Vignollet et al. [125] note that the fracture load of phase-field analyses increases as the length scale parameter is decreased, as this increases the critical stress according to Equation (4.2). This fact seems to be in contradiction with the concept of the Γ convergence. Sargado

Specimen	**Maximum load** P [N]			**Fracture angle** φ [$\circ$]	
	Average from tests	Simulations	Relative difference	Average from tests	Simulations
V30, $b = 1$	837.7	1017.5	+21.5 %	11.8	9
V60, $b = 1$	1016.7	1029.6	+1.3 %	14.0	10
V90, $b = 1$	882.3	1118.2	+26.7 %	5.8	7
V30, $b = 9$	895.7	1044.7	+16.6 %	24.6	23
V60, $b = 9$	1038.7	1084.2	+4.4 %	21.3	22
V90, $b = 9$	959.3	1185.4	+23.6 %	18.4	20
T30	1351.0	1311.8	−2.9 %	57.9	60
T60	1438.7	1511.0	+5.0 %	48.4	56
T90	1589.3	1596.8	+0.5 %	36.7	49

Table 4.1: Summary of the numerical results of the simulations of the fracture of the V-notched specimens and comparison with the experimental results.

et al. [85] present an example including a crack nucleating from a sharp notch for which a convergence of the critical load is observed for very small values of ℓ, but the "converged" critical load overestimates the resistance of the specimen, with respect to analytical solutions. According to Linse et al. [126], the discrepancies between the theoretical proofs of the Γ convergence and the results from numerical simulations are due to the finite size of the specimens (especially when this is comparable with ℓ) and to the introduction, in the phase-field models, of the degradation function and of the history field for enforcing fracture irreversibility. The result of the extensive work in Tanné et al. [55] suggests that ℓ should be considered as an internal length for the material and that choosing it according to (4.2) provides reliable quantitative predictions of the crack nucleation for different notched geometries. Moreover, the higher accuracy of the AT1 formulation for the fracture energy density with respect to the AT2 one (employed in this work) is highlighted.

4.3 Simulation of the buckling of a square tube

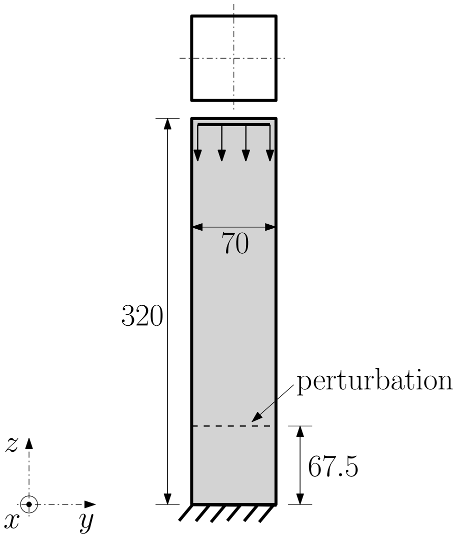

Figure 4.7: Setup of the simulation of the buckling of a square tube (dimensions in mm).

The effectiveness of the penalty contact formulation (see Section 2.5) is tested against a challenging benchmark represented by the buckling of a square tube, subjected to compression in the axial direction. The example is proposed in Benson et al. [12], solved using a Reissner-Mindlin shell formulation implemented in the commercial code LS-DYNA and employing a single surface contact algorithm [127]. The setup of the problem is shown in Figure 4.7 (the shell thickness is $t = 1.2$ mm). The lower end of the tube is clamped, while the top edges are subjected to an imposed displacement in axial direction (z direction), in compression. The analysis is here performed in the quasi-static regime, while in the result published in [12], the displacement is imposed at a constant velocity (5646 mm/s). For triggering the buckling of the tube under compression, a geometrical imperfection is inserted in the geometry at the height of 67.5 mm from the base. The imperfection modifies the initial coordinates of the closest line of control points on the $y - z$ face by 0.05 mm in the x direction and on the $x - y$ face by 0.05 mm in the z direction. The elasto-plastic material model implemented for the isogeometric Kirchhoff-Love shell formulation is adopted (see Section 2.1.1). The elastic parameters are the Young's modulus $E = 199.4 \times 10^3$ MPa and the

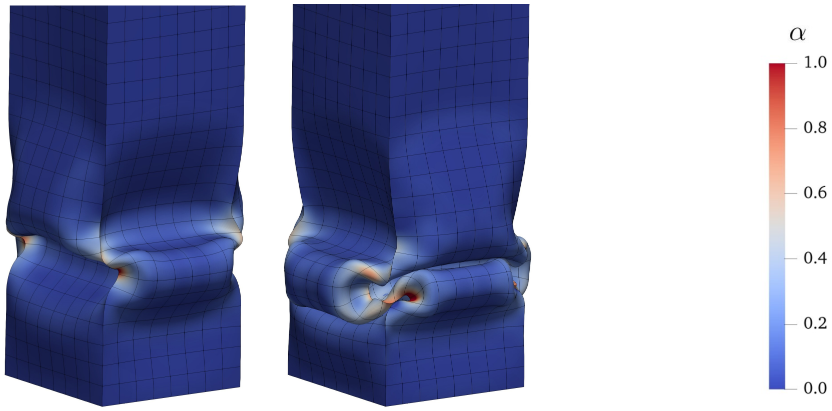

(a) $u_{z,\text{imp}} = 28$ mm (b) $u_{z,\text{imp}} = 85$ mm

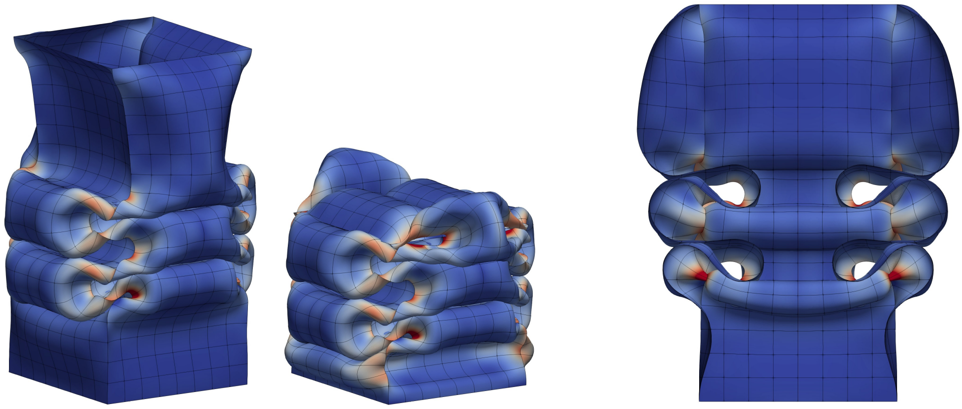

(c) $u_{z,\text{imp}} = 180$ mm (d) $u_{z,\text{imp}} = 250$ mm (e) $u_{z,\text{imp}} = 180$ mm, section view

Figure 4.8: Results of the simulation of the buckling of a square tube at different values of the imposed displacement $u_{z,\text{imp}}$. The colormap indicates the value of the hardening variable α.

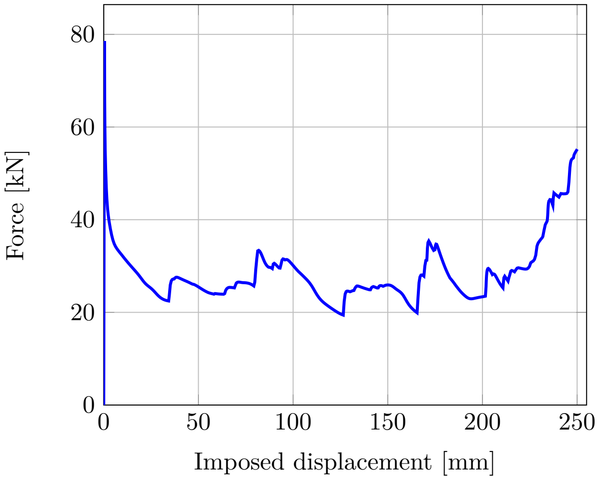

Figure 4.9: Load-displacement curve for the simulation of the buckling of a square tube.

Poisson's ratio $\nu = 0.30$, while a linear hardening law:

$$R(\alpha) = \sigma_y + H_m \alpha, \tag{4.3}$$

with yielding stress $\sigma_y = 336.6$ MPa and hardening modulus $H_m = 1$ MPa is adopted. Due to the symmetry of the geometry and of the boundary conditions, only one quarter of the tube is simulated employing symmetry. Patch coupling, symmetry and clamping are enforcing adopting the penalty formulation presented in Section 2.4. The contact is simulated according to the penalty formulation from Section 2.5, with the penalty parameter taken as $\alpha_N = 10^5$. Self-contact between the patches needs to be taken into account. Element with size $h = 8.75$ mm and quadratic shape functions are considered. No phase-field fracture formulation is included in this analysis, which simulates only the elasto-plastic behavior of the structure.

Figure 4.8 shows the results of the simulation at different stages of the analysis. It is possible to evaluate the complexity of the deformation of the analysis and the multiple contact points present. Figure 4.8e clearly shows how self-contact of the patches is involved and needs to be simulated. For imposed displacement higher than $u_{z,\text{imp}} = 180$ mm (so, after the situation depicted in Figure 4.8c) the deformation of the tube becomes unphysical, as the top edges of the tube have a position lower than the deformed side. Anyway, the simulation was continued until an imposed displacement $u_{z,\text{imp}} = 250$. This final stage is depicted in Figure 4.8d. Figure 4.9 shows the load-displacement curve resulting from the simulation. The initial peak is followed by a sudden drop due to the buckling of the tube triggered by the imperfection in the geometry. In the following part of the analysis, the successive increases and decreases of the load-displacement curve correspond to successive identification of new contact points between the patches. This challenging example demonstrates the effectiveness of the penalty contact formulation and of the pre-search algorithm presented in Section 2.5, which allows for describing such a complex deformation pattern involving also self-contact. Nevertheless, the pre-search contact might be further improved, as this analysis fails to converge if a finer mesh is employed. The reason for the non convergence is indeed the fact that the point search algorithm identifies a wrong contact point in correspondence with the corner patch edges.

5 Conclusions

The work performed during the PhD was focused on the development of the phase-field model for fracture towards its applicability to real-world structures, especially constituted by multiple Kirchhoff-Love shell and plate members, in the IGA discretization framework.

Original contributions include the development of a novel approach for coupling the displacement and rotational behaviors across the interfaces of patches. The simplicity of the model lies in the fact that all the penalty parameters are controlled by a single dimensionless parameter defined regardless of the problem type and configuration. Moreover, the approach shows great flexibility as it can handle patches with arbitrary angles at the connection, matching and non-matching discretizations at the interface (an advantage in case adaptive local refinement technologies are used), and even non-conforming geometries at the connection. The approach can additionally be applied in the context of phase-field fracture simulations and used for guaranteeing C^0 and C^1 continuity of the phase-field, depending on the chosen formulation, between the patch interfaces. The same global dimensionless parameter adopted for the structural coupling controls also the penalty terms of the phase-field coupling. Within this framework, crack growing along patch connections or crossing them can be simulated without problems.

A penalty based formulation for the simulation of frictionless contact conditions is employed and enriched with a pre-search algorithm that allows improving the point search routines for the contact points. The formulation is positively tested against challenging numerical and experimental benchmarks. In the context of phase-field simulations, both the patch coupling and contact penalty formulation need to have their terms scaled by the phase-field degradation function in order to maintain the numerical proportion between structural and penalty stiffness and in order the relax the penalty constraints in the cracked zones. For contact simulations, this means enabling the penetration in fractured areas. The adequate choice of the penalty terms is suggested by the stability and convergence of the numerical analyses performed in this work.

A phase-field formulation for brittle and ductile fracture is combined with an isogeometric rotation-free Kirchhoff-Love shell formulation. According to this approach, the phase-field is defined only at the shell midsurface, while a nonlinear distribution of the stress tensor varying through the thickness can be described.

In order to improve the efficiency of the time-consuming phase-field simulations, a predictor-corrector adaptive local refinement algorithm based on LR NURBS is presented and adopted. The algorithm allows the refinement of the mesh only where required by the phase-field model, i.e. around the fractured regions, without *a priori* knowledge of the crack path. The approach is capable of handling different challenges related to brittle and ductile fracture formulations, respectively. In the first case, the fact that brittle cracks often fully develop in the geometry in a single load-step. For the ductile case, the mesh sensitivity of the local plasticity model, that is alleviated thanks to the fact that the plastic strains stop accumulating when the fracture develops.

The computational cost of the solution of the phase-field fracture numerical problem is reduced by the adoption of the aforementioned adaptive mesh refinement, of a strongly coupled staggering solution scheme (which is proven to work both for brittle and ductile fracture simulation) for the system of coupled equations and of the fourth-order phase-field formulation (if the geometry of the problem allows this latter choice).

The combination of these numerical formulations and solution techniques allows the application of the phase-field fracture model to complex shell structures with a reasonable computational effort. An example of this is represented by the numerical prediction of the experimental outcome of indentation tests performed on stiffened steel plates, with good matching of the results both in terms of fracture path and load-displacement curves.

5.1 Recommendations for future work

The research work performed for this thesis presents several possible directions for development. Among all, the following points are considered to be of major interest:

- The development of the phase-field method towards its application for the simulation of real-world structures was a clear focus of this thesis work. Nevertheless, still some gaps need to be closed for a possible use of the method at industrial level, at least for special applications. While the necessary material fracture parameters for the model are usually known (e.g. the fracture toughness) or can be determined by the comparison with the results of experimental tests on simple geometries (e.g. the critical hardening value), the length scale parameter remains the most uncertain input value for phase-field fracture simulations. For the brittle fracture case, numerical relations linking the length scale parameter with the toughness, the stiffness and the material strength exist and have been demonstrated to provide reliable results for the prediction of fracture [55]. These relations have not yet been proven working for complex stress states or in the ductile fracture context. It is still an open question whether the length scale parameter can be reliably determined *a priori* using the abovementioned relations (knowing also that it is not always possible to determine the tensile strength of a material, due to its dependence on the presence of defects) or it should be determined on the base of experimental results. A systematic study campaign devoted to demonstrating if the length scale can be considered or not as a constant material parameter independently on the load conditions and of the situation of crack nucleation or growth, and how to determine it, would contribute to the applicability of the phase-field method.

- In the view of simulating real-world structures, but also comparing the results of experiments and simulations (as for example mentioned in the previous point), the present isogeometric formulation and implementation needs to be enhanced with the possibility of handling more complex geometries. The use of multipatch formulations, even if it increases the range of geometries that can be simulated, cannot solve the problems in modeling geometrical features as holes, chamfers or notches in the context of IGA. For this reason, technologies for handling NURBS trimmed patches need to be adopted, especially if the geometry to analyze is generated in CAD software, as usually happens at industrial level. Moreover, the combination of IGA trimming and adaptive local refinement technologies is challenging but it can potentially provide great flexibility for modeling advanced geometries.

- One of the most important structural failure mechanism is fatigue. The extension of the phase-field model for embedding fatigue effects and therefore simulating the fatigue failure of shell structures represents an interesting and promising research field, given the contributions already presented in the literature. Multiple points need to be addressed, ranging from the difference between low- and high-cycle fatigue to the experimental validation of the proposed approaches, including the efficiency of the methodology, which should not require the simulation of all the load cycles.

Other possible developments related to the thesis work, here briefly mentioned, include:

- In view of increasing the applicability and use of the phase-field model, extension of the presented approach to the dynamic framework for the simulation of dynamic fracture and, therefore, of a wider range of failure scenarios.
- Adoption of different plasticity models, for example non-local ones, in order to avoid the mesh sensitivity effect also in elasto-plastic simulations that do not employ the phase-field model.
- Simulation of the fracture of thick shell structures by considering different shell formulations, as for example Reissner-Mindlin shell models.

References

[1] T. J. Hughes, J. A. Cottrell, Y. Bazilevs, Isogeometric analysis: CAD, finite elements, NURBS, exact geometry and mesh refinement, Computer methods in applied mechanics and engineering 194 (39) (2005) 4135–4195.

[2] J. A. Cottrell, T. J. Hughes, Y. Bazilevs, Isogeometric analysis: toward integration of CAD and FEA, John Wiley & Sons, 2009.

[3] R. Bouclier, T. Elguedj, A. Combescure, Efficient isogeometric NURBS-based solid-shell elements: Mixed formulation and B-method, Computer Methods in Applied Mechanics and Engineering 267 (2013) 86–110.

[4] S. Hosseini, J. J. C. Remmers, C. V. Verhoosel, R. de Borst, An isogeometric solid-like shell element for nonlinear analysis, International Journal for Numerical Methods in Engineering 95 (3) (2013) 238–256.

[5] S. Hosseini, J. J. C. Remmers, C. V. Verhoosel, R. de Borst, An isogeometric continuum shell element for non-linear analysis, Computer Methods in Applied Mechanics and Engineering 271 (2014) 1–22.

[6] J. F. Caseiro, R. A. F. Valente, A. Reali, J. Kiendl, F. Auricchio, R. J. Alves de Sousa, On the Assumed Natural Strain method to alleviate locking in solid-shell NURBS-based finite elements, Computational Mechanics 53 (6) (2014) 1341–1353.

[7] J. F. Caseiro, R. A. F. Valente, A. Reali, J. Kiendl, F. Auricchio, R. J. Alves de Sousa, Assumed Natural Strain NURBS-based solid-shell element for the analysis of large deformation elasto-plastic thin-shell structures, Computer Methods in Applied Mechanics and Engineering 284 (2015) 861–880.

[8] J. Kiendl, K.-U. Bletzinger, J. Linhard, R. Wüchner, Isogeometric shell analysis with Kirchhoff–Love elements, Computer Methods in Applied Mechanics and Engineering 198 (49) (2009) 3902–3914.

[9] D. J. Benson, Y. Bazilevs, M.-C. Hsu, T. J. R. Hughes, A large deformation, rotation-free, isogeometric shell, Computer Methods in Applied Mechanics and Engineering 200 (13) (2011) 1367–1378.

[10] N. Nguyen-Thanh, J. Kiendl, H. Nguyen-Xuan, R. Wüchner, K. U. Bletzinger, Y. Bazilevs, T. Rabczuk, Rotation free isogeometric thin shell analysis using PHT-splines, Computer Methods in Applied Mechanics and Engineering 200 (47) (2011) 3410–3424.

[11] T. X. Duong, F. Roohbakhshan, R. A. Sauer, A new rotation-free isogeometric thin shell formulation and a corresponding continuity constraint for patch boundaries, Special Issue on Isogeometric Analysis: Progress and Challenges 316 (2017) 43–83.

[12] D. J. Benson, Y. Bazilevs, M. C. Hsu, T. J. R. Hughes, Isogeometric shell analysis: The Reissnmoder-Mindlin shell, Computer Methods in Applied Mechanics and Engineering 199 (5) (2010) 276–289.

[13] W. Dornisch, S. Klinkel, B. Simeon, Isogeometric Reissnmoder-Mindlin shell analysis with exactly calculated director vectors, Computer Methods in Applied Mechanics and Engineering 253 (2013) 491–504.

[14] B. Oesterle, R. Sachse, E. Ramm, M. Bischoff, Hierarchic isogeometric large rotation shell elements including linearized transverse shear parametrization, Computer Methods in Applied Mechanics and Engineering 321 (2017) 383–405.

[15] J. Kiendl, E. Marino, L. De Lorenzis, Isogeometric collocation for the Reissnmoder-Mindlin shell problem, Computer Methods in Applied Mechanics and Engineering 325 (2017) 645–665.

[16] R. Echter, B. Oesterle, M. Bischoff, A hierarchic family of isogeometric shell finite elements, Computer Methods in Applied Mechanics and Engineering 254 (2013) 170–180.

[17] Z. Lei, F. Gillot, L. Jezequel, A C0/G1 multiple patches connection method in isogeometric analysis, Applied Mathematical Modelling 39 (15) (2015) 4405–4420.

[18] M. Breitenberger, A. Apostolatos, B. Philipp, R. Wüchner, K.-U. Bletzinger, Analysis in computer aided design: Nonlinear isogeometric B-Rep analysis of shell structures, Computer Methods in Applied Mechanics and Engineering 284 (2015) 401–457.

[19] J. Kiendl, Y. Bazilevs, M.-C. Hsu, R. Wüchner, K.-U. Bletzinger, The bending strip method for isogeometric analysis of Kirchhoff-Love shell structures comprised of multiple patches, Computer Methods in Applied Mechanics and Engineering 199 (37-40) (2010) 2403–2416.

[20] A. Goyal, B. Simeon, On penalty-free formulations for multipatch isogeometric Kirchhoff-Love shells, Mathematics and Computers in Simulation 136 (2017) 78–103.

[21] W. Dornisch, G. Vitucci, S. Klinkel, The weak substitution method - an application of the mortar method for patch coupling in NURBS-based isogeometric analysis, Int. J. Numer. Meth. Engng 103 (3) (2015) 205–234.

[22] E. Brivadis, A. Buffa, B. Wohlmuth, L. Wunderlich, Isogeometric mortar methods, Computer Methods in Applied Mechanics and Engineering 284 (2015) 292–319.

[23] Y. Guo, M. Ruess, Nitsche's method for a coupling of isogeometric thin shells and blended shell structures, Computer Methods in Applied Mechanics and Engineering 284 (2015) 881–905.

[24] N. Nguyen-Thanh, K. Zhou, X. Zhuang, P. Areias, H. Nguyen-Xuan, Y. Bazilevs, T. Rabczuk, Isogeometric analysis of large-deformation thin shells using RHT-splines for multiple-patch coupling, Computer Methods in Applied Mechanics and Engineering 316 (2017) 1157–1178.

[25] A. Trädegård, F. Nilsson, S. Östlund, FEM-remeshing technique applied to crack growth problems, Computer Methods in Applied Mechanics and Engineering 160 (1) (1998) 115–131.

[26] N. Moës, J. Dolbow, T. Belytschko, A finite element method for crack growth without remeshing, International Journal for Numerical Methods in Engineering 46 (1) (1999) 131–150.

[27] M. Ortiz, A. Pandolfi, Finite-deformation irreversible cohesive elements for three-dimensional crack-propagation analysis, International Journal for Numerical Methods in Engineering 44 (9) (1999) 1267–1282.

[28] R. de Borst, C. V. Verhoosel, Damage, Material Instabilities, and Failure, American Cancer Society, 2017, pp. 1–50.

[29] Z. P. Bazant, G. Pijaudier-Cabot, Nonlocal Continuum Damage, Localization Instability and Convergence, J. Appl. Mech 55 (2) (12/2) 287–293.

[30] R. Peerlings, R. Borst, W. Brekelmans, J. Vree, I. Spee, Some observations on localization in non-local and gradient damage models, European Journal of Mechanics. A, Solids 15 (6) (1996) 937–953.

[31] A. A. Griffith, The phenomena of rupture and flow in solids, Philosophical Transactions of the Royal Society of London. Series A, Containing Papers of a Mathematical or Physical Character 221 (1921) 163–198.

[32] G. A. Francfort, J.-J. Marigo, Revisiting brittle fracture as an energy minimization problem, Journal of the Mechanics and Physics of Solids 46 (8) (1998) 1319–1342.

[33] B. Bourdin, G. A. Francfort, J.-J. Marigo, Numerical experiments in revisited brittle fracture, Journal of the Mechanics and Physics of Solids 48 (4) (2000) 797–826.

[34] M. Ambati, T. Gerasimov, L. De Lorenzis, A review on phase-field models of brittle fracture and a new fast hybrid formulation, Computational Mechanics 55 (2) (2015) 383–405.

[35] J.-Y. Wu, V. P. Nguyen, C. T. Nguyen, D. Sutula, S. Bordas, S. Sinaie, Phase field modeling of fracture, Advances in Applied Mechancis: Multiscale Theory and Computation 52 (2018).

[36] R. Alessi, M. Ambati, T. Gerasimov, S. Vidoli, L. De Lorenzis, Comparison of phase-field models of fracture coupled with plasticity, in: Advances in Computational Plasticity: A Book in Honour of D. Roger J. Owen, Springer International Publishing, Cham, 2018, pp. 1–21.

[37] J. Cho, K.-S. Lee, Finite element simulation of crack propagation based on phase field theory, Journal of Mechanical Science and Technology 27 (10) (2013) 3073–3085.

[38] J. D. Clayton, J. Knap, A geometrically nonlinear phase field theory of brittle fracture, International Journal of Fracture 189 (2) (2014) 139–148.

[39] B. Li, C. Peco, D. Millán, I. Arias, M. Arroyo, Phase-field modeling and simulation of fracture in brittle materials with strongly anisotropic surface energy, International Journal for Numerical Methods in Engineering 102 (3-4) (2015) 711–727.

[40] S. Teichtmeister, D. Kienle, F. Aldakheel, M.-A. Keip, Phase field modeling of fracture in anisotropic brittle solids, International Journal of Non-Linear Mechanics 97 (Supplement C) (2017) 1–21.

[41] A. C. Hansen-Dörr, R. de Borst, P. Hennig, M. Kästner, Phase-field modelling of interface failure in brittle materials, Computer Methods in Applied Mechanics and Engineering 346 (2019) 25–42.

[42] A. C. Hansen-Dörr, F. Dammaß, R. de Borst, M. Kästner, Phase-field modeling of crack branching and deflection in heterogeneous media, Engineering Fracture Mechanics 232 (2020) 107004.

[43] J. L. Boldrini, E. A. Barros de Moraes, L. R. Chiarelli, F. G. Fumes, M. L. Bittencourt, A non-isothermal thermodynamically consistent phase field framework for structural damage and fatigue, Computer Methods in Applied Mechanics and Engineering 312 (2016) 395–427.

[44] A. Mesgarnejad, A. Imanian, A. Karma, Phase-field models for fatigue crack growth, Theoretical and Applied Fracture Mechanics 103 (2012) 102282.

[45] P. Carrara, M. Ambati, R. Alessi, L. De Lorenzis, A framework to model the fatigue behavior of brittle materials based on a variational phase-field approach, Computer Methods in Applied Mechanics and Engineering 361 (2020) 112731.

[46] M. Seiler, T. Linse, P. Hantschke, M. Kästner, An efficient phase-field model for fatigue fracture in ductile materials, Engineering Fracture Mechanics 224 (2020) 106807.

[47] M. A. Msekh, J. M. Sargado, M. Jamshidian, P. M. Areias, T. Rabczuk, Abaqus implementation of phase-field model for brittle fracture, Computational Materials Science 96 (2015) 472–484.

[48] G. Liu, Q. Li, M. A. Msekh, Z. Zuo, Abaqus implementation of monolithic and staggered schemes for quasi-static and dynamic fracture phase-field model, Computational Materials Science 121 (2016) 35–47.

[49] G. Molnár, A. Gravouil, 2D and 3D Abaqus implementation of a robust staggered phase-field solution for modeling brittle fracture, Finite Elements in Analysis and Design 130 (Supplement C) (2017) 27–38.

[50] K. Seleš, T. Lesičar, Z. Tonković, J. Sorić, A residual control staggered solution scheme for the phase-field modeling of brittle fracture, Engineering Fracture Mechanics (2018).

[51] M. J. Borden, T. J. R. Hughes, C. M. Landis, C. V. Verhoosel, A higher-order phase-field model for brittle fracture: Formulation and analysis within the isogeometric analysis framework, Computer Methods in Applied Mechanics and Engineering 273 (2014) 100–118.

[52] A. Mesgarnejad, B. Bourdin, M. M. Khonsari, Validation simulations for the variational approach to fracture, Computer Methods in Applied Mechanics and Engineering 290 (2015) 420–437.

[53] K. H. Pham, K. Ravi-Chandar, C. M. Landis, Experimental validation of a phase-field model for fracture, International Journal of Fracture 205 (1) (2017) 83–101.

[54] T. Wu, A. Carpiuc-Prisacari, M. Poncelet, L. De Lorenzis, Phase-field simulation of interactive mixed-mode fracture tests on cement mortar with full-field displacement boundary conditions, Engineering Fracture Mechanics 182 (2017) 658–688.

[55] E. Tanné, T. Li, B. Bourdin, J.-J. Marigo, C. Maurini, Crack nucleation in variational phase-field models of brittle fracture, Journal of the Mechanics and Physics of Solids 110 (2018) 80–99.

[56] D. Wick, T. Wick, R. J. Hellmig, H.-J. Christ, Numerical simulations of crack propagation in screws with phase-field modeling, Computational Materials Science 109 (2015) 367–379.

[57] M. J. Borden, T. J. R. Hughes, C. M. Landis, A. Anvari, I. J. Lee, A phase-field formulation for fracture in ductile materials: Finite deformation balance law derivation, plastic degradation, and stress triaxiality effects, Computer Methods in Applied Mechanics and Engineering 312 (2016) 130–166.

[58] M. Ambati, R. Kruse, L. De Lorenzis, A phase-field model for ductile fracture at finite strains and its experimental verification, Computational Mechanics 57 (1) (2016) 149–167.

[59] J. M. Kiendl, Isogeometric analysis and shape optimal design of shell structures, Thesis (2011).

[60] J. Kiendl, M.-C. Hsu, M. C. H. Wu, A. Reali, Isogeometric Kirchhoff-Love shell formulations for general hyperelastic materials, Computer Methods in Applied Mechanics and Engineering 291 (2015) 280–303.

[61] J. C. Simo, A framework for finite strain elastoplasticity based on maximum plastic dissipation and the multiplicative decomposition: Part I. Continuum formulation, Computer Methods in Applied Mechanics and Engineering 66 (2) (1988) 199–219.

[62] M. Ambati, J. Kiendl, L. De Lorenzis, Isogeometric Kirchhoff-Love shell formulation for elasto-plasticity, Computer Methods in Applied Mechanics and Engineering 340 (2018) 320–339.

[63] D. R. Forsey, R. H. Bartels, Hierarchical B-spline refinement, ACM Siggraph Computer Graphics 22 (4) (1988) 205–212.

[64] A.-V. Vuong, C. Giannelli, B. Jüttler, B. Simeon, A hierarchical approach to adaptive local refinement in isogeometric analysis, Computer Methods in Applied Mechanics and Engineering 200 (49) (2011) 3554–3567.

[65] C. Giannelli, B. Jüttler, H. Speleers, THB-splines: The truncated basis for hierarchical splines, Computer Aided Geometric Design 29 (7) (2012) 485–498.

[66] T. W. Sederberg, J. Zheng, A. Bakenov, A. Nasri, T-splines and T-NURCCs, ACM transactions on graphics (TOG) 22 (3) (2003) 477–484.

[67] Y. Bazilevs, V. M. Calo, J. A. Cottrell, J. A. Evans, T. J. R. Hughes, S. Lipton, M. A. Scott, T. W. Sederberg, Isogeometric analysis using T-splines, Computer Methods in Applied Mechanics and Engineering 199 (5) (2010) 229–263.

[68] E. J. Evans, M. A. Scott, X. Li, D. C. Thomas, Hierarchical T-splines: Analysis-suitability, Bézier extraction, and application as an adaptive basis for isogeometric analysis, Computer Methods in Applied Mechanics and Engineering 284 (2015) 1–20.

[69] T. Dokken, T. Lyche, K. F. Pettersen, Polynomial splines over locally refined box-partitions, Computer Aided Geometric Design 30 (3) (2013) 331–356.

[70] K. A. Johannessen, T. Kvamsdal, T. Dokken, Isogeometric analysis using LR B-splines, Computer Methods in Applied Mechanics and Engineering 269 (2014) 471–514.

[71] K. A. Johannessen, F. Remonato, T. Kvamsdal, On the similarities and differences between Classical Hierarchical, Truncated Hierarchical and LR B-splines, Computer Methods in Applied Mechanics and Engineering 291 (2015) 64–101.

[72] C. Zimmermann, R. A. Sauer, Adaptive local surface refinement based on LR NURBS and its application to contact, Computational Mechanics 60 (6) (2017) 1011–1031.

[73] K. Pham, H. Amor, J.-J. Marigo, C. Maurini, Gradient damage models and their use to approximate brittle fracture, International Journal of Damage Mechanics 20 (4) (2011) 618–652.

[74] R. de Borst, C. V. Verhoosel, Gradient damage vs phase-field approaches for fracture: Similarities and differences, Computer Methods in Applied Mechanics and Engineering 312 (2016) 78–94.

[75] B. Bourdin, G. A. Francfort, J.-J. Marigo, The variational approach to fracture, Journal of elasticity 91 (1-3) (2008) 5–148.

[76] A. Braides, A. Garroni, On the non-local approximation of free-discontinuity problems, Communications in Partial Differential Equations 23 (5-6) (1998) 817–829.

[77] L. Ambrosio, V. Tortorelli, On the approximation of free discontinuity problems, Bollettino Unione Matematica Italiana B 6 (1992) 105–123.

[78] C. Miehe, M. Hofacker, F. Welschinger, A phase field model for rate-independent crack propagation: Robust algorithmic implementation based on operator splits, Computer Methods in Applied Mechanics and Engineering 199 (45) (2010) 2765–2778.

[79] H. Amor, J.-J. Marigo, C. Maurini, Regularized formulation of the variational brittle fracture with unilateral contact: Numerical experiments, Journal of the Mechanics and Physics of Solids 57 (8) (2009) 1209–1229.

[80] F. Freddi, G. Royer-Carfagni, Regularized variational theories of fracture: A unified approach, Journal of the Mechanics and Physics of Solids 58 (8) (2010) 1154–1174.

[81] C. Steinke, M. Kaliske, A phase-field crack model based on directional stress decomposition, Computational Mechanics 63 (5) (2019) 1019–1046.

[82] K. Paul, C. Zimmermann, K. K. Mandadapu, T. J. R. Hughes, C. M. Landis, R. A. Sauer, An adaptive space-time phase field formulation for dynamic fracture of brittle shells based on LR NURBS, Computational Mechanics (2020).

[83] C. Bilgen, A. Kopaničáková, R. Krause, K. Weinberg, A detailed investigation of the model influencing parameters of the phase-field fracture approach, GAMM-Mitteilungen 0 (0) (2019) e202000005.

[84] C. Kuhn, A. Schlüter, R. Müller, On degradation functions in phase field fracture models, Computational Materials Science 108 (2015) 374–384.

[85] J. M. Sargado, E. Keilegavlen, I. Berre, J. M. Nordbotten, High-accuracy phase-field models for brittle fracture based on a new family of degradation functions, Journal of the Mechanics and Physics of Solids 111 (2018) 458–489.

[86] M. Artina, M. Fornasier, S. Micheletti, S. Perotto, Anisotropic mesh adaptation for crack detection in brittle materials, SIAM Journal on Scientific Computing 37 (4) (2015) B633–B659.

[87] T. Gerasimov, L. De Lorenzis, A line search assisted monolithic approach for phase-field computing of brittle fracture, Computer Methods in Applied Mechanics and Engineering 312 (2016) 276–303.

[88] F. P. Duda, A. Ciarbonetti, P. J. Sánchez, A. E. Huespe, A phase-field/gradient damage model for brittle fracture in elastic-plastic solids, International Journal of Plasticity 65 (2015) 269–296.

[89] R. Alessi, J.-J. Marigo, S. Vidoli, Gradient damage models coupled with plasticity and nucleation of cohesive cracks, Archive for Rational Mechanics and Analysis 214 (2) (2014) 575–615.

[90] R. Alessi, J.-J. Marigo, S. Vidoli, Gradient damage models coupled with plasticity: Variational formulation and main properties, Mechanics of Materials 80 (2015) 351–367.

[91] C. Kuhn, T. Noll, R. Müller, On phase field modeling of ductile fracture, GAMM-Mitteilungen 39 (1) (2016) 35–54.

[92] C. Huang, X. Gao, Development of a phase field method for modeling brittle and ductile fracture, Computational Materials Science 169 (2019) 109089.

[93] P. Rodriguez, J. Ulloa, C. Samaniego, E. Samaniego, A variational approach to the phase field modeling of brittle and ductile fracture, International Journal of Mechanical Sciences 144 (2018) 502–517.

[94] C. Miehe, S. Teichtmeister, F. Aldakheel, Phase-field modelling of ductile fracture: a variational gradient-extended plasticity-damage theory and its micromorphic regularization, Philosophical Transactions of the Royal Society A: Mathematical, Physical and Engineering Sciences 374 (2066) (2016) 20150170.

[95] M. Dittmann, F. Aldakheel, J. Schulte, P. Wriggers, C. Hesch, Variational phase-field formulation of non-linear ductile fracture, Computer Methods in Applied Mechanics and Engineering 342 (2018) 71–94.

[96] M. Ambati, T. Gerasimov, L. De Lorenzis, Phase-field modeling of ductile fracture, Computational Mechanics 55 (5) (2015) 1017–1040.

[97] P. Areias, T. Rabczuk, M. A. Msekh, Phase-field analysis of finite-strain plates and shells including element subdivision, Computer Methods in Applied Mechanics and Engineering 312 (2016) 322–350.

[98] F. Amiri, D. Millán, Y. Shen, T. Rabczuk, M. Arroyo, Phase-field modeling of fracture in linear thin shells, Theoretical and Applied Fracture Mechanics 69 (2014) 102–109.

[99] H. Ulmer, M. Hofacker, C. Miehe, Phase field modeling of fracture in plates and shells, Proc. Appl. Math. Mech. 12 (1) (2012) 171–172.

[100] J. Kiendl, M. Ambati, L. De Lorenzis, H. Gomez, A. Reali, Phase-field description of brittle fracture in plates and shells, Computer Methods in Applied Mechanics and Engineering 312 (2016) 374–394.

[101] G. Kikis, M. Ambati, L. De Lorenzis, S. Klinkel, Phase-field model of brittle fracture in Reissnmoder-Mindlin plates and shells, Computer Methods in Applied Mechanics and Engineering 373 (2021) 113490.

[102] U. Pillai, S. P. Triantafyllou, I. Ashcroft, Y. Essa, F. M. de la Escalera, Phase-field modelling of brittle fracture in thin shell elements based on the MITC4+ approach, Computational Mechanics 65 (6) (2020) 1413–1432.

[103] J. Reinoso, M. Paggi, C. Linder, Phase field modeling of brittle fracture for enhanced assumed strain shells at large deformations: formulation and finite element implementation, Computational Mechanics 59 (6) (2017) 981–1001.

[104] M. Ambati, L. De Lorenzis, Phase-field modeling of brittle and ductile fracture in shells with isogeometric NURBS-based solid-shell elements, Computer Methods in Applied Mechanics and Engineering 312 (Supplement C) (2016) 351–373.

[105] L. Piegl, W. Tiller, The NURBS book, Springer Science & Business Media, 2012.

[106] D. Vågnes, Isogeometric structural analysis of wind turbine blade, Master's thesis, NTNU (2018).

[107] L. De Lorenzis, P. Wriggers, C. Weißenfels, Computational Contact Mechanics with the Finite Element Method, American Cancer Society, 2017, pp. 1–45.

[108] R. Dimitri, L. De Lorenzis, M. A. Scott, P. Wriggers, R. L. Taylor, G. Zavarise, Isogeometric large deformation frictionless contact using T-splines, Computer Methods in Applied Mechanics and Engineering 269 (2014) 394–414.

[109] E. L. Holten, Isogeometric contact analysis: Implementation of a penalty-based algorithm, Master's thesis, NTNU (2019).

[110] M. E. Matzen, Isogeometrische modellierung und diskretisierung von kontaktproblemen, Ph.D. thesis (2015).

[111] S. Burke, C. Ortner, E. Süli, An adaptive finite element approximation of a variational model of brittle fracture, SIAM Journal on Numerical Analysis 48 (3) (2010) 980–1012.

[112] G. Del Piero, G. Lancioni, R. March, A variational model for fracture mechanics: Numerical experiments, Journal of the Mechanics and Physics of Solids 55 (12) (2007) 2513–2537.

[113] T. Wick, Goal functional evaluations for phase-field fracture using PU-based DWR mesh adaptivity, Computational Mechanics 57 (6) (2016) 1017–1035.

[114] T. Heister, M. F. Wheeler, T. Wick, A primal-dual active set method and predictor-corrector mesh adaptivity for computing fracture propagation using a phase-field approach, Computer Methods in Applied Mechanics and Engineering 290 (2015) 466–495.

[115] M. Klinsmann, D. Rosato, M. Kamlah, R. M. McMeeking, An assessment of the phase field formulation for crack growth, Computer Methods in Applied Mechanics and Engineering 294 (2015) 313–330.

[116] S. Nagaraja, M. Elhaddad, M. Ambati, S. Kollmannsberger, L. De Lorenzis, E. Rank, Phase-field modeling of brittle fracture with multi-level hp-FEM and the finite cell method, Computational Mechanics (2018).

[117] M. J. Borden, C. V. Verhoosel, M. A. Scott, T. J. Hughes, C. M. Landis, A phase-field description of dynamic brittle fracture, Computer Methods in Applied Mechanics and Engineering 217 (2012) 77–95.

[118] M. Kästner, P. Hennig, T. Linse, V. Ulbricht, Phase-field modelling of damage and fracture–convergence and local mesh refinement, in: Advanced Methods of Continuum Mechanics for Materials and Structures, Springer, 2016, pp. 307–324.

[119] P. Hennig, S. Müller, M. Kästner, Bézier extraction and adaptive refinement of truncated hierarchical NURBS, Computer Methods in Applied Mechanics and Engineering 305 (2016) 316–339.

[120] P. Hennig, M. Ambati, L. De Lorenzis, M. Kästner, Projection and transfer operators in adaptive isogeometric analysis with hierarchical B-splines, Computer Methods in Applied Mechanics and Engineering 334 (2018) 313–336.

[121] J. Besson, Continuum models of ductile fracture: A review, International Journal of Damage Mechanics 19 (1) (2010) 3–52.

[122] F. J. Gómez, M. Elices, F. Berto, P. Lazzarin, Fracture of V-notched specimens under mixed mode (I + II) loading in brittle materials, International Journal of Fracture 159 (2) (2009) 121.

[123] T. L. Anderson, Fracture mechanics: fundamentals and applications, CRC press, 2005.

[124] C. Kuhn, R. Müller, A continuum phase field model for fracture, Engineering Fracture Mechanics 77 (18) (2010) 3625–3634.

[125] J. Vignollet, S. May, R. de Borst, C. V. Verhoosel, Phase-field models for brittle and cohesive fracture, Meccanica 49 (11) (2014) 2587–2601.

[126] T. Linse, P. Hennig, M. Kästner, R. de Borst, A convergence study of phase-field models for brittle fracture, Engineering Fracture Mechanics 184 (2017) 307–318.

[127] D. J. Benson, J. O. Hallquist, A single surface contact algorithm for the post-buckling analysis of shell structures, Computer Methods in Applied Mechanics and Engineering 78 (2) (1990) 141–163.

Appendix A: Attached papers

A.1 Paper 1

Austin J. Herrema*, Emily L. Johnson*, Davide Proserpio*, Michael C.H. Wu, Josef Kiendl, Ming-Chen Hsu

Penalty coupling of non-matching isogeometric Kirchhoff-Love shell patches with application to composite wind turbine blades

Computer Methods in Applied Mechanics and Engineering, 2019; 346 (810-840)

*These three authors contributed equally to this work.

Penalty coupling of non-matching isogeometric Kirchhoff–Love shell patches with application to composite wind turbine blades

Austin J. Herrema[a,1], Emily L. Johnson[a,1], Davide Proserpio[b,1], Michael C.H. Wu[a], Josef Kiendl[b], Ming-Chen Hsu[a,*]

[a] *Department of Mechanical Engineering, Iowa State University, 2025 Black Engineering, Ames, IA 50011, USA*
[b] *Department of Marine Technology, Norwegian University of Science and Technology, O. Nielsens veg 10, 7052 Trondheim, Norway*

Abstract

Isogeometric analysis (IGA) has been a particularly impactful development in the realm of Kirchhoff–Love thin-shell analysis because the high-order basis functions employed naturally satisfy the requirement of C^1 continuity. Still, engineering models of appreciable complexity, such as wind turbine blades, are typically modeled using multiple surface patches and, often, neither rotational continuity nor conforming discretization can be practically obtained at patch interfaces. A penalty approach for coupling adjacent patches is therefore presented. The proposed method imposes both displacement and rotational continuity and is applicable to either smooth or non-smooth interfaces and either matching or non-matching discretization. The penalty formulations require only a single, dimensionless penalty coefficient for both displacement and rotation coupling terms, alleviating the problem-dependent nature of the penalty parameters. Using this coupling methodology, numerous benchmark problems encapsulating a variety of analysis types, geometrical and material properties, and matching and non-matching interfaces are addressed. The coupling methodology produces consistently accurate results throughout all tests. Furthermore, the suggested penalty coefficient of $\alpha = 10^3$ is shown to be effective for the wide range of problem configurations addressed. Finally, a realistic wind turbine blade model, consisting of 27 patches and 51 coupling interfaces and having a chordwise- and spanwise-variant composite material definition, is subjected to buckling, vibration, and nonlinear deformation analysis using the proposed approach.

Keywords: isogeometric analysis; Kirchhoff–Love shell; patch coupling; penalty parameter; non-matching interface; wind turbine blade

---

[*] Corresponding author

Email addresses: `josef.kiendl@ntnu.no` (Josef Kiendl), `jmchsu@iastate.edu` (Ming-Chen Hsu)

[1] These three authors contributed equally to this work.

Preprint submitted to Computer Methods in Applied Mechanics and Engineering *September 18, 2018*

Contents

1. Introduction

Modern engineering industries often commit significant resources to performing numerical analyses based on the finite element method. Yet, significant portions of the design-and-analysis workflow are consumed by time-consuming and labor-intensive activities such as model cleanup and finite element mesh generation [1]. Hughes et al. [2] sought to improve this outlook with the introduction of isogeometric analysis (IGA), an analysis approach in which the functions employed by computer-aided design (CAD) software are directly employed as finite element bases during analysis. Isogeometric analysis has been particularly impactful in the realm of thin-shell analysis [3–7]. Kirchhoff–Love theory is typically applied to thin-shell structures—indicated by $R/t \geq 20$, where R is the shell's radius of curvature and t is its thickness [8]—and assumes that transverse shear strains are negligible, a reasonable assumption for many shell structures of interest. Importantly, second-order derivatives appear in the governing variational equations of the Kirchhoff–Love theory; this implies the necessity of C^1-continuous approximation functions. This condition has always been a major obstacle for the development of efficient finite element thin-shell formulations. However, in isogeometric Kirchhoff–Love shell analysis that uses, for example, non-uniform rational B-splines (NURBS), the most widely used spline-based mathematical functions in CAD and IGA, the C^1-smoothness requirement can be naturally satisfied in the interior of NURBS patches.

Models of complex, real-world objects, such as wind turbine blades, tend to be composed of multiple patches due to practical or technical limitations in geometry modeling or to capture design features such as material discontinuities. Despite the many potential advantages offered by isogeometric Kirchhoff–Love shells, they cannot be readily applied to such complex, multi-patch designs; additional action must be taken to enforce continuity at patch interfaces. Firstly, the patches must be connected, i.e., C^0 continuity must be imposed. For conforming meshes, where the control points of the two patches are co-located at their interface, this can be easily done by directly coupling the degrees of freedom of the boundary control points on both patches. This is not possible, however, in the case of non-conforming patches (patches which do share a common boundary in the physical space but have different discretizations along that boundary), or when patches only approximately share a common boundary in the physical space, a possible result of CAD modeling operations. The term *non-matching* is used to refer to both of these situations. In traditional finite element analysis, such geometric mismatches are typically corrected during mesh generation, ensuring that the resultant mesh is analysis-suitable. Because IGA circumvents mesh generation procedures, however, the analysis method itself must be capable of coupling non-matching patches. Additionally, for Kirchhoff–Love shell analysis, C^1 continuity must also be imposed on patch boundaries. Strictly speaking, C^1 continuity applies only to smooth patch interfaces, while complex shell structures typically also include non-smooth patch interfaces, i.e., patches joined with an angle other than 180 degrees. In such cases, it is the angle between the patches that must be maintained during deformation analysis. Therefore, the term *rotational continuity*, rather than C^1 continuity, is used when referring to patch interfaces of arbitrary angle (including smooth interfaces). Accordingly, C^0 continuity is referred to as *displacement continuity*.

A significant amount of research effort has been devoted to imposing rotational continuity within isogeometric Kirchhoff–Love shell analysis of multi-patch structures. In Kiendl et al. [3], it was shown that, for smooth and conforming patches, the constraint can be fulfilled by direct coupling of degrees of freedom of the first two rows of control points along the joint boundary, provided that the control points across this common edge are collinear. As a more general alternative, the bending strip method was introduced by Kiendl et al. [9]. It is a penalty-like approach, which can couple both smooth and non-smooth patch interfaces. Goyal and Simeon [10] extended the bending strip approach by proposing alternate formulations that improve problem conditioning. In all cases, however, the bending strip method is still restricted to conforming discretizations. Lei et al. [11], instead, presented a penalty formulation that can handle non-conforming meshes. However, the method is restricted to smooth patch interfaces. Breitenberger et al. [12] have used penalty formulations for both displacement and rotational continuity and applied them to complex B-rep CAD models with non-matching interfaces. However, their formulation for rotational continuity was restricted to rotational deformation less than 90°, which is a significant limitation in large deformation analysis and for rotating structures. Duong et al. [13] proposed a different penalty formulation for rotational continuity, which has no restrictions on the rotational deformation. However, it was limited to conforming patch interfaces and the penalty parameters must be selected in a problem-dependent fashion.

Mortar methods have also been used for patch coupling in the context of IGA [14, 15]. However, the mortar method requires solving a saddle point problem for the Lagrange multiplier which can sometimes be challenging. Guo et al. [16, 17] and Nguyen-Thanh et al. [18] have developed formulations for Kirchhoff–Love shell patch coupling based on Nitsche's method. The advantage of such formulations is that they are less dependent on stabilization or penalty parameters than penalty methods. However, the formulations depend on the variational formulation employed and, as a result, are relatively difficult to implement for general-purpose analysis codes. Citing the complexity of Nitsche's method, Coox et al. [19] alternatively proposed a Virtual Uncommon-Knot-Inserted Master–Slave (VUKIMS) coupling technique based on master–slave interface constraints derived from the interface knot vectors.

The general advantage of penalty methods lies in their simplicity and flexibility. However, an inherent issue in these methods is the choice of penalty parameters. If the value of the penalty parameter is too low, the constraint is not satisfied accurately enough. If the penalty parameter value is too high, the matrices may become ill-conditioned and the solution of the linear system is prone to large numerical errors. Ideally, penalty formulations should scale with geometric and material properties in a way that makes the choice of the penalty parameters problem-independent. Otherwise, these parameters have to be chosen ad-hoc for each problem. They also should scale with the element size in order to make sure that the penalty error decreases with mesh refinement. When different constraints, like displacement and rotational continuity, are to be imposed simultaneously with penalty formulations, one also has to ensure the correct balance between the different penalty parameters. This can be very challenging when these parameters are chosen ad-hoc.

In this paper, we present novel penalty formulations for imposing both displacement and rotational continuity in multi-patch Kirchhoff–Love shell analysis. The proposed formulations work for smooth and non-smooth, matching and non-matching (or conforming and non-conforming) patch interfaces. Both displacement and rotational continuity are controlled by a single, dimensionless penalty coefficient and proper scaling of the different penalty terms with the geometric and material parameters of the problem allows for a problem-independent choice of the penalty coefficient value. The presented approach shares similarities with those in Breitenberger et al. [12] and Duong et al. [13]. However, it is shown that the choice of the penalty parameter values is heavily problem-dependent in those formulations. The presented formulation is tested on a large series of benchmark problems, from linear to nonlinear analysis and from isotropic to composite materials. The examples demonstrate the accuracy and robustness of the proposed method. As a result of these studies, a universal recommendation for the choice of the penalty coefficient is obtained.

This paper is outlined as follows. In Section 2, the isogeometric Kirchhoff–Love shell formulation and the penalty formulation for patch coupling are presented. An effective selection of penalty parameters is also proposed. In Section 3, the formulations are evaluated using several linear and nonlinear benchmark problems, and the effective range of the relatively problem-agnostic penalty coefficient is demonstrated. In Section 4, the proposed method is applied to the structural analysis of a realistic composite wind turbine blade; the effectiveness of the method is demonstrated using linear buckling, vibration, and nonlinear deflection analyses. In Section 5, conclusions are drawn.

2. Shell formulations

2.1. Composite isogeometric Kirchhoff–Love shells

The proposed penalty formulation is dependent on the Kirchhoff–Love shell formulation itself. Thus, a brief review of the shell formulation is provided. An isogeometric Kirchhoff–Love thin-shell formulation was first proposed by Kiendl et al. [3] and was reformulated for composite shells in Bazilevs et al. [20]. The shell formulation is extended to handle general hyperelastic materials in Kiendl et al. [6]. The details relevant to the penalty formulation for patch coupling are given here. The variational formulation is based on the principle of virtual work:

$$\delta W = \delta W^{\text{int}} - \delta W^{\text{ext}} = 0 \,, \tag{1}$$

where W is the total work, W^{int} is the internal work, W^{ext} is the external work, and δ denotes a variation with respect to the virtual displacement variables $\delta\mathbf{u}$:

$$\delta W = \frac{\partial W}{\partial \mathbf{u}} \delta\mathbf{u} \,. \tag{2}$$

The internal virtual work is given by

$$\delta W^{\mathrm{int}} = \int_{\Omega} (\mathbf{S} : \delta\mathbf{E})\, \mathrm{d}\Omega \,, \tag{3}$$

where Ω is the shell volume in the undeformed configuration, $\mathbf{S}$ is the second Piola–Kirchhoff stress tensor, and $\mathbf{E}$ is the Green–Lagrange strain tensor.

For the Kirchhoff–Love shell theory, both normal and transverse shear strains are neglected; only the in-plane strain components are considered. The Green–Lagrange strain is assumed to vary linearly through the shell thickness and can be expressed as a combination of membrane and bending strains of the midsurface. Let Greek indices $\alpha = 1, 2$ and $\beta = 1, 2$ denote the in-plane components. The covariant components of $\mathbf{E}$ can be obtained as

$$E_{\alpha\beta} = \varepsilon_{\alpha\beta} + \xi_3 \kappa_{\alpha\beta} \,, \tag{4}$$

where $\varepsilon_{\alpha\beta}$ and $\kappa_{\alpha\beta}$ are the covariant components of the membrane strain tensor, $\boldsymbol{\varepsilon}$, and curvature change (due to bending) tensor, $\boldsymbol{\kappa}$, of the midsurface, respectively, $\xi_3 \in [-0.5t, 0.5t]$ is the through-thickness coordinate, and t is the thickness of the shell. Let $\mathbf{x}(\xi_1, \xi_2)$ be the spatial coordinate of the midsurface in the deformed configuration with ξ_1 and ξ_2 being the parametric coordinates used in defining the midsurface, and $\mathbf{a}_\alpha$ be the covariant surface basis vectors in the deformed configurations, obtained as $\mathbf{a}_\alpha = \mathbf{x}_{,\alpha}$, where $(\cdot)_{,\alpha} = \partial(\cdot)/\partial\xi_\alpha$ indicates the partial derivatives with respect to ξ_α. Let geometric variables indicated by $\mathring{(\cdot)}$ refer to the undeformed configuration. Membrane strain and curvature change coefficients are defined as

$$\varepsilon_{\alpha\beta} = \frac{1}{2}\left(\mathbf{a}_\alpha \cdot \mathbf{a}_\beta - \mathring{\mathbf{a}}_\alpha \cdot \mathring{\mathbf{a}}_\beta\right) \,, \tag{5}$$

$$\kappa_{\alpha\beta} = \mathring{\mathbf{a}}_{\alpha,\beta} \cdot \mathring{\mathbf{a}}_3 - \mathbf{a}_{\alpha,\beta} \cdot \mathbf{a}_3 \,, \tag{6}$$

where $\mathbf{a}_3$ is the unit vector normal to the shell midsurface in the deformed configuration, given by

$$\mathbf{a}_3 = \frac{\mathbf{a}_1 \times \mathbf{a}_2}{\|\mathbf{a}_1 \times \mathbf{a}_2\|} \,. \tag{7}$$

In this work, linear elastic material behavior is assumed, corresponding to a St. Venant–Kirchhoff material model. The stress–strain relationship is expressed by

$$\mathbf{S} = \mathbb{C}\mathbf{E} \,, \tag{8}$$

where $\mathbb{C}$ is a constitutive material tensor. Introducing Eq. (8) into Eq. (3), separating out the through-thickness integration, and utilizing the definition of the strain tensor $\mathbf{E}$ given in Eq. (4),

Figure 1: Composite layup with non-uniform and non-symmetric ply distribution.

one obtains

$$\delta W^{\text{int}} = \int_{\mathcal{S}} \delta \boldsymbol{\varepsilon} \cdot \left(\left(\int_{-t/2}^{t/2} \mathbb{C} \, \mathrm{d}\xi_3 \right) \boldsymbol{\varepsilon} + \left(\int_{-t/2}^{t/2} \xi_3 \mathbb{C} \, \mathrm{d}\xi_3 \right) \boldsymbol{\kappa} \right) \mathrm{d}\mathcal{S} + \int_{\mathcal{S}} \delta \boldsymbol{\kappa} \cdot \left(\left(\int_{-t/2}^{t/2} \xi_3 \mathbb{C} \, \mathrm{d}\xi_3 \right) \boldsymbol{\varepsilon} + \left(\int_{-t/2}^{t/2} \xi_3^2 \mathbb{C} \, \mathrm{d}\xi_3 \right) \boldsymbol{\kappa} \right) \mathrm{d}\mathcal{S} \,, \tag{9}$$

where $\mathcal{S}$ is the shell surface domain. In the case of composite materials, the structure is assumed to be composed of a number of orthotropic plies. Let k be the index of each ply and $\mathbb{C}_k$ be the material tensor of each ply obtained by transforming its orthotropic material tensor from the ply material coordinates to the shell coordinates. According to the classical laminate theory [21], the homogenized extensional (membrane) stiffness, $\mathbb{A}$, coupling stiffness, $\mathbb{B}$, and bending stiffness, $\mathbb{D}$, are given by

$$\mathbb{A} = \int_{-t/2}^{t/2} \mathbb{C} \, \mathrm{d}\xi_3 = \sum_{k=1}^{n} \mathbb{C}_k t_k \,, \tag{10}$$

$$\mathbb{B} = \int_{-t/2}^{t/2} \xi_3 \mathbb{C} \, \mathrm{d}\xi_3 = \sum_{k=1}^{n} \mathbb{C}_k t_k z_k \,, \tag{11}$$

$$\mathbb{D} = \int_{-t/2}^{t/2} \xi_3^2 \mathbb{C} \, \mathrm{d}\xi_3 = \sum_{k=1}^{n} \mathbb{C}_k \left(t_k z_k^2 + \frac{t_k^3}{12} \right) . \tag{12}$$

In the above, n is the total number of piles, t_k is the thickness of the kth ply, and z_k is the distance from the centroid of the kth ply to the mid-plane of the laminate, as illustrated in Figure 1. The internal virtual work for a composite shell can therefore be defined:

$$\delta W^{\text{int}} = \int_{\mathcal{S}} \delta \boldsymbol{\varepsilon} \cdot (\mathbb{A} \boldsymbol{\varepsilon} + \mathbb{B} \boldsymbol{\kappa}) \, \mathrm{d}\mathcal{S} + \int_{\mathcal{S}} \delta \boldsymbol{\kappa} \cdot (\mathbb{B} \boldsymbol{\varepsilon} + \mathbb{D} \boldsymbol{\kappa}) \, \mathrm{d}\mathcal{S} \,. \tag{13}$$

More details about this formulation can be found in Kiendl [22].

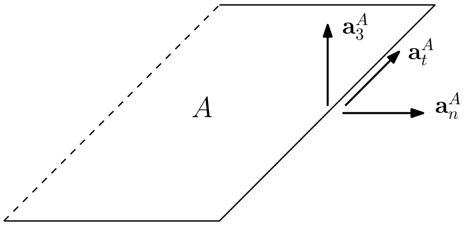

Figure 2: The unit normal vector, $\mathbf{a}_3^{\mathrm{A}}$; unit tangent vector, $\mathbf{a}_t^{\mathrm{A}}$; and in-plane unit normal vector, $\mathbf{a}_n^{\mathrm{A}}$, at an edge of patch $\mathcal{S}^{\mathrm{A}}$.

2.2. *A penalty formulation for non-matching patch coupling*

A penalty approach for coupling adjacent patches having either matching or non-matching discretization and either smooth or non-smooth interfaces is presented here. In the following, it is assumed that there are two patches, $\mathcal{S}^{\mathrm{A}}$ and $\mathcal{S}^{\mathrm{B}}$, which, in the undeformed configuration, are approximately co-located along an interface curve, $\mathcal{L}$. For enforcing displacement continuity between the two patches, the following penalty virtual work is introduced:

$$\delta W^{\mathrm{pd}} = \int_{\mathcal{L}} \alpha_{\mathrm{d}} \left(\mathbf{u}^{\mathrm{A}} - \mathbf{u}^{\mathrm{B}}\right) \cdot \left(\delta\mathbf{u}^{\mathrm{A}} - \delta\mathbf{u}^{\mathrm{B}}\right) \mathrm{d}\mathcal{L}\,, \tag{14}$$

where superscripts A and B indicate quantities evaluated on patches $\mathcal{S}^{\mathrm{A}}$ or $\mathcal{S}^{\mathrm{B}}$, respectively, α_{d} is a penalty parameter of large magnitude, further discussed in the following section, and $\mathbf{u}^{\mathrm{A}}$ and $\mathbf{u}^{\mathrm{B}}$ are the displacements of corresponding locations on $\mathcal{S}^{\mathrm{A}}$ and $\mathcal{S}^{\mathrm{B}}$, respectively, along $\mathcal{L}$. Equation (14) dictates that, if the distance between points on $\mathcal{S}^{\mathrm{A}}$ and $\mathcal{S}^{\mathrm{B}}$ is not the same in the deformed and undeformed configurations, a large penalty energy is introduced into the system.

The coupling methodology must also maintain the angle formed by patches $\mathcal{S}^{\mathrm{A}}$ and $\mathcal{S}^{\mathrm{B}}$. For imposing rotational continuity between two patches, the following penalty virtual work is introduced:

$$\begin{aligned}\delta W^{\mathrm{pr}} = \int_{\mathcal{L}} \alpha_{\mathrm{r}} \Big(&\left(\mathbf{a}_3^{\mathrm{A}} \cdot \mathbf{a}_3^{\mathrm{B}} - \mathring{\mathbf{a}}_3^{\mathrm{A}} \cdot \mathring{\mathbf{a}}_3^{\mathrm{B}}\right)\left(\delta\mathbf{a}_3^{\mathrm{A}} \cdot \delta\mathbf{a}_3^{\mathrm{B}} - \delta\mathring{\mathbf{a}}_3^{\mathrm{A}} \cdot \delta\mathring{\mathbf{a}}_3^{\mathrm{B}}\right) \\ &+ \left(\mathbf{a}_n^{\mathrm{A}} \cdot \mathbf{a}_3^{\mathrm{B}} - \mathring{\mathbf{a}}_n^{\mathrm{A}} \cdot \mathring{\mathbf{a}}_3^{\mathrm{B}}\right)\left(\delta\mathbf{a}_n^{\mathrm{A}} \cdot \delta\mathbf{a}_3^{\mathrm{B}} - \delta\mathring{\mathbf{a}}_n^{\mathrm{A}} \cdot \delta\mathring{\mathbf{a}}_3^{\mathrm{B}}\right)\Big) \mathrm{d}\mathcal{L}\,,\end{aligned} \tag{15}$$

where α_{r} is a penalty parameter that will be discussed in detail in the following section. In Eq. (15), we introduce the in-plane unit normal vector, $\mathbf{a}_n^{\mathrm{A}}$, which lies in the plane of patch $\mathcal{S}^{\mathrm{A}}$ and is orthogonal to the penalty curve, $\mathcal{L}$. Given the natural tangent vector of the penalty curve on patch $\mathcal{S}^{\mathrm{A}}$, $\tilde{\mathbf{a}}_t^{\mathrm{A}}$, its unit vector, $\mathbf{a}_t^{\mathrm{A}}$, can be obtained as $\mathbf{a}_t^{\mathrm{A}} = \tilde{\mathbf{a}}_t^{\mathrm{A}} / \|\tilde{\mathbf{a}}_t^{\mathrm{A}}\|$. $\mathbf{a}_n^{\mathrm{A}}$ can then be computed as $\mathbf{a}_n^{\mathrm{A}} = \mathbf{a}_t^{\mathrm{A}} \times \mathbf{a}_3^{\mathrm{A}}$ (see Figure 2). Note that $\mathbf{a}_t^{\mathrm{A}}$ and $\mathbf{a}_3^{\mathrm{A}}$ are orthogonal unit vectors.

The first term in the right hand side of Eq. (15) penalizes variations in the scalar product of the

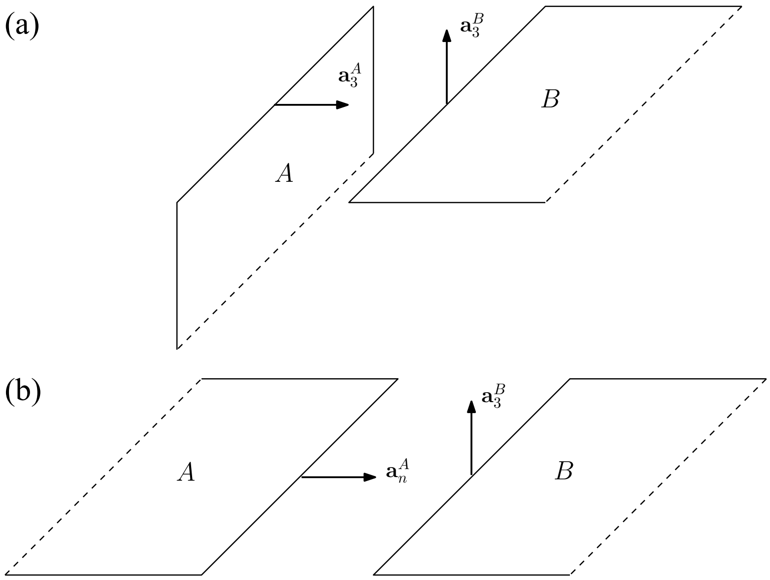

Figure 3: Patch interfaces having an interface angle of (a) 90 degrees and (b) 180 degrees.

normal vectors of the two patches. As will be shown in more detail later, the variation of the scalar product of two parallel unit vectors vanishes; thus, the formulation is enhanced by the second term which penalizes variations in the scalar product of the in-plane normal vector of patch $\mathcal{S}^{\mathrm{A}}$ and the normal vector of patch $\mathcal{S}^{\mathrm{B}}$. Regardless of the patch angle, both terms are calculated and added together. With this combination, the patches are allowed to form arbitrary angles at their interface. For patch interfaces forming an angle of 90°, see Figure 3a, only the first term is active. For patches having an angle of 180° at their interface, see Figure 3b, only the second term is active. For all other interface angles, both terms are active with complementary strengths.

Finally, the virtual work formulation, Eq. (1), is augmented by the contributions of Eqs. (14) and (15), and is restated as

$$\delta W = \delta W^{\mathrm{int}} + \delta W^{\mathrm{pd}} + \delta W^{\mathrm{pr}} - \delta W^{\mathrm{ext}} = 0\,. \tag{16}$$

The above equation states the equilibrium condition of virtual work that must be fulfilled for any arbitrary variation of the displacement variables δu_r. Equation (16) is a nonlinear equation system which can be linearized for the purposes of solving the shell problem using the Newton–Raphson method:

$$\frac{\partial^2 W}{\partial u_r \partial u_s} \Delta u_s = -\frac{\partial W}{\partial u_r}\,. \tag{17}$$

The first derivative of the virtual work terms is the residual force vector, whereas the second derivative yields the stiffness matrix. The contributions from the internal and external virtual work are detailed in Kiendl et al. [6]. Here, the first and second derivatives of the penalty virtual work are presented. The derivatives of the displacement penalty virtual work, Eq. (14), are given as follows:

$$\frac{\partial W^{\mathrm{pd}}}{\partial u_r} = \int_{\mathcal{L}} \alpha_{\mathrm{d}} \left(\mathbf{u}^{\mathrm{A}} - \mathbf{u}^{\mathrm{B}}\right) \cdot \left(\mathbf{u}^{\mathrm{A}}_{,r} - \mathbf{u}^{\mathrm{B}}_{,r}\right) \mathrm{d}\mathcal{L} \,, \tag{18}$$

$$\frac{\partial W^{\mathrm{pd}}}{\partial u_r \partial u_s} = \int_{\mathcal{L}} \alpha_{\mathrm{d}} \left(\mathbf{u}^{\mathrm{A}}_{,s} - \mathbf{u}^{\mathrm{B}}_{,s}\right) \cdot \left(\mathbf{u}^{\mathrm{A}}_{,r} - \mathbf{u}^{\mathrm{B}}_{,r}\right) \mathrm{d}\mathcal{L} \,. \tag{19}$$

Similarly, the first and second derivatives of the rotation penalty virtual work, Eq. (15), are

$$\begin{aligned} \frac{\partial W^{\mathrm{pr}}}{\partial u_r} = \int_{\mathcal{L}} \alpha_{\mathrm{r}} \Big(& \left(\mathbf{a}^{\mathrm{A}}_3 \cdot \mathbf{a}^{\mathrm{B}}_3 - \mathring{\mathbf{a}}^{\mathrm{A}}_3 \cdot \mathring{\mathbf{a}}^{\mathrm{B}}_3\right) \left(\mathbf{a}^{\mathrm{A}}_{3,r} \cdot \mathbf{a}^{\mathrm{B}}_3 + \mathbf{a}^{\mathrm{A}}_3 \cdot \mathbf{a}^{\mathrm{B}}_{3,r}\right) \\ & + \left(\mathbf{a}^{\mathrm{A}}_n \cdot \mathbf{a}^{\mathrm{B}}_3 - \mathring{\mathbf{a}}^{\mathrm{A}}_n \cdot \mathring{\mathbf{a}}^{\mathrm{B}}_3\right) \left(\mathbf{a}^{\mathrm{A}}_{n,r} \cdot \mathbf{a}^{\mathrm{B}}_3 + \mathbf{a}^{\mathrm{A}}_n \cdot \mathbf{a}^{\mathrm{B}}_{3,r}\right) \Big) \mathrm{d}\mathcal{L} \,, \end{aligned} \tag{20}$$

$$\begin{aligned} \frac{\partial W^{\mathrm{pr}}}{\partial u_r \partial u_s} = \int_{\mathcal{L}} \alpha_{\mathrm{r}} \Big(& \left(\mathbf{a}^{\mathrm{A}}_3 \cdot \mathbf{a}^{\mathrm{B}}_3 - \mathring{\mathbf{a}}^{\mathrm{A}}_3 \cdot \mathring{\mathbf{a}}^{\mathrm{B}}_3\right) \left(\mathbf{a}^{\mathrm{A}}_{3,rs} \cdot \mathbf{a}^{\mathrm{B}}_3 + \mathbf{a}^{\mathrm{A}}_{3,r} \cdot \mathbf{a}^{\mathrm{B}}_{3,s} + \mathbf{a}^{\mathrm{A}}_{3,s} \cdot \mathbf{a}^{\mathrm{B}}_{3,r} + \mathbf{a}^{\mathrm{A}}_3 \cdot \mathbf{a}^{\mathrm{B}}_{3,rs}\right) \\ & + \left(\mathbf{a}^{\mathrm{A}}_{3,s} \cdot \mathbf{a}^{\mathrm{B}}_3 + \mathbf{a}^{\mathrm{A}}_3 \cdot \mathbf{a}^{\mathrm{B}}_{3,s}\right) \left(\mathbf{a}^{\mathrm{A}}_{3,r} \cdot \mathbf{a}^{\mathrm{B}}_3 + \mathbf{a}^{\mathrm{A}}_3 \cdot \mathbf{a}^{\mathrm{B}}_{3,r}\right) \\ & + \left(\mathbf{a}^{\mathrm{A}}_n \cdot \mathbf{a}^{\mathrm{B}}_3 - \mathring{\mathbf{a}}^{\mathrm{A}}_n \cdot \mathring{\mathbf{a}}^{\mathrm{B}}_3\right) \left(\mathbf{a}^{\mathrm{A}}_{n,rs} \cdot \mathbf{a}^{\mathrm{B}}_3 + \mathbf{a}^{\mathrm{A}}_{n,r} \cdot \mathbf{a}^{\mathrm{B}}_{3,s} + \mathbf{a}^{\mathrm{A}}_{n,s} \cdot \mathbf{a}^{\mathrm{B}}_{3,r} + \mathbf{a}^{\mathrm{A}}_n \cdot \mathbf{a}^{\mathrm{B}}_{3,rs}\right) \\ & + \left(\mathbf{a}^{\mathrm{A}}_{n,s} \cdot \mathbf{a}^{\mathrm{B}}_3 + \mathbf{a}^{\mathrm{A}}_n \cdot \mathbf{a}^{\mathrm{B}}_{3,s}\right) \left(\mathbf{a}^{\mathrm{A}}_{n,r} \cdot \mathbf{a}^{\mathrm{B}}_3 + \mathbf{a}^{\mathrm{A}}_n \cdot \mathbf{a}^{\mathrm{B}}_{3,r}\right) \Big) \mathrm{d}\mathcal{L} \,. \end{aligned} \tag{21}$$

Equations (20) and (21) require the first and second derivatives of $\mathbf{a}_n$, which are defined below:

$$\mathbf{a}_{t,r} = \frac{1}{\|\tilde{\mathbf{a}}_t\|} \left(\tilde{\mathbf{a}}_{t,r} - \left(\mathbf{a}_t \cdot \tilde{\mathbf{a}}_{t,r}\right) \mathbf{a}_t\right) \,, \tag{22}$$

$$\mathbf{a}_{n,r} = \mathbf{a}_{t,r} \times \mathbf{a}_3 + \mathbf{a}_t \times \mathbf{a}_{3,r} \,, \tag{23}$$

and

$$\mathbf{a}_{t,rs} = \frac{1}{\|\tilde{\mathbf{a}}_t\|} \left(\mathbf{a}_{t,s} \cdot \tilde{\mathbf{a}}_{t,r}\right) \mathbf{a}_t + \frac{1}{\|\tilde{\mathbf{a}}_t\|^2} \left(2 \left(\mathbf{a}_t \cdot \tilde{\mathbf{a}}_{t,r}\right) \left(\mathbf{a}_t \cdot \tilde{\mathbf{a}}_{t,s}\right) \mathbf{a}_t - \left(\mathbf{a}_t \cdot \tilde{\mathbf{a}}_{t,s}\right) \tilde{\mathbf{a}}_{t,r} - \left(\mathbf{a}_t \cdot \tilde{\mathbf{a}}_{t,r}\right) \tilde{\mathbf{a}}_{t,s}\right) \,, \tag{24}$$

$$\mathbf{a}_{n,rs} = \mathbf{a}_{t,rs} \times \mathbf{a}_3 + \mathbf{a}_{t,r} \times \mathbf{a}_{3,s} + \mathbf{a}_{t,s} \times \mathbf{a}_{3,r} + \mathbf{a}_t \times \mathbf{a}_{3,rs} \,. \tag{25}$$

Additional details regarding the discretization of the variables used in these expressions can be found in Kiendl et al. [6]. Note that, for the case of patch coupling at patch edges, $\tilde{\mathbf{a}}_t$ is simply $\mathbf{a}_1$ or $\mathbf{a}_2$, depending on the edge ($\mathbf{a}_1$ and $\mathbf{a}_2$ are generally not unit vectors). Thus, the first and second derivatives of $\tilde{\mathbf{a}}_t$ often correspond to the derivatives of $\mathbf{a}_1$ or $\mathbf{a}_2$. If the penalty formulation is integrated over a trimming curve, it is possible to use the tangent of the trimming curve's projection on the patch as $\tilde{\mathbf{a}}_t$. Trimming is outside the scope of the present work and will be investigated in the future.

Remark 1. Close investigation of Eq. (21) reveals the importance of having complementary terms in Eq. (15). Consider patches forming an angle of 180° wherein the vectors $\mathbf{a}_3^{\mathrm{A}}$ and $\mathbf{a}_3^{\mathrm{B}}$ are parallel. In this situation, the vector derivative $\mathbf{a}_{3,s}^{\mathrm{A}}$ is orthogonal to $\mathbf{a}_3^{\mathrm{B}}$ and, similarly, $\mathbf{a}_{3,s}^{\mathrm{B}}$ is orthogonal to $\mathbf{a}_3^{\mathrm{A}}$; thus, the entire term $\left(\mathbf{a}_{3,s}^{\mathrm{A}} \cdot \mathbf{a}_3^{\mathrm{B}} + \mathbf{a}_3^{\mathrm{A}} \cdot \mathbf{a}_{3,s}^{\mathrm{B}}\right)$ in Eq. (21) would be equal to zero. Furthermore, in geometrically linear analysis and in the first step of geometrically nonlinear analysis, the deformed and undeformed configurations are equivalent and, correspondingly, the term $\left(\mathbf{a}_3^{\mathrm{A}} \cdot \mathbf{a}_3^{\mathrm{B}} - \mathring{\mathbf{a}}_3^{\mathrm{A}} \cdot \mathring{\mathbf{a}}_3^{\mathrm{B}}\right)$ is equal to zero. Thus, in this particular configuration, there is zero penalty stiffness contribution from the first two lines of Eq. (21); however, there would still be penalty stiffness contribution from the last two lines of Eq. (21). Conversely, it can be shown that, for configurations wherein patches form an angle of 90°, the opposite is true: the last two lines of Eq. (21) have zero penalty stiffness contribution while the first two lines of Eq. (21) have non-zero penalty stiffness contribution. The formulations are therefore complementary throughout a range of possible patch angles.

Remark 2. Equations (18)–(21) can also be used to weakly impose boundary and symmetry conditions on a patch. For restraining the displacement on a boundary of patch $\mathcal{S}^{\mathrm{A}}$ in the case of simply supported or clamped boundary conditions, one can use Eqs. (18) and (19) and set $\mathbf{u}^{\mathrm{B}}$ and its derivatives to zero. For restraining the displacement in the case of a symmetry condition, only the component of $\mathbf{u}^{\mathrm{A}}$ normal to the symmetry plane is considered in the equations. For restraining the rotation in the case of a clamped boundary condition, one can use Eqs. (20) and (21), excluding the second line of (20) and the last two lines of (21), and replacing $\mathbf{a}_3^{\mathrm{B}}$ and $\mathring{\mathbf{a}}_3^{\mathrm{B}}$ by $\mathring{\mathbf{a}}_n^{\mathrm{A}}$. (Note that the terms associated with the derivatives of $\mathbf{a}_3^{\mathrm{B}}$ become zero.) For restraining the rotation in the case of a symmetry condition, $\mathbf{a}_3^{\mathrm{B}}$ and $\mathring{\mathbf{a}}_3^{\mathrm{B}}$ are replaced by the normal vector of the symmetry plane. Finally, in the case of restraining the displacement and rotation of a symmetry condition, the resulting terms from Eqs. (18)–(21) are multiplied by two to correctly represent contributions from both sides of the symmetry plane.

2.3. Implementation

For cases in which the discretization of patches $\mathcal{S}^{\mathrm{A}}$ and $\mathcal{S}^{\mathrm{B}}$ is non-matching along $\mathcal{L}$, there are various possibilities regarding the discretization of $\mathcal{L}$. The discretization of $\mathcal{L}$ can theoretically be entirely independent of the discretizations of both $\mathcal{S}^{\mathrm{A}}$ and $\mathcal{S}^{\mathrm{B}}$. However, for cases which employ patch coupling along patch edges, one might naturally employ the discretization of $\mathcal{S}^{\mathrm{A}}$, $\mathcal{S}^{\mathrm{B}}$, or some combination of the two to construct the penalty terms. For the sake of straightforward implementation, this work employs the discretization of the patch edge which, across the penalty domain $\mathcal{L}$, has the largest number of elements. For cases in which the discretization of both edges is relatively uniform, this is a conservative choice in that it ensures that the entirety of both edges is penalized. In contrast, if the coarser discretization is selected, it is possible that some of the smaller elements would go unconstrained. Of course, the choice of discretization for $\mathcal{L}$ could impact the results; this represents a future research opportunity. As the examples in later sections demonstrate, however, the simple approach described here is often sufficient.

In other configurations, the interface of patches $\mathcal{S}^{\mathrm{A}}$ and $\mathcal{S}^{\mathrm{B}}$ may not be a patch edge. Instead, $\mathcal{L}$ may be an intersection of two NURBS surfaces. In general, it may not be feasible to determine the mathematically exact intersection of the two surfaces; CAD systems are typically tasked with finding approximate, NURBS-curve representations of such intersections according to system- or user-defined tolerances. In this case, the integration domain $\mathcal{L}$ may be defined by the approximate intersection curve and the discretizations of $\mathcal{L}$, $\mathcal{S}^{\mathrm{A}}$, and $\mathcal{S}^{\mathrm{B}}$ may not correlate. The proposed methodology is still applicable in such circumstances.

When evaluating Eqs. (18)–(21), one must integrate over $\mathcal{L}$ whilst incorporating variables defined on both $\mathcal{S}^{\mathrm{A}}$ and $\mathcal{S}^{\mathrm{B}}$. In the numerical setting, Gaussian quadrature points are defined along $\mathcal{L}$.[2] At each quadrature point on $\mathcal{L}$, variables with superscripts "A" or "B" in the penalty formulations are evaluated at the points on patches $\mathcal{S}^{\mathrm{A}}$ and $\mathcal{S}^{\mathrm{B}}$ which are physically nearest to the quadrature point on $\mathcal{L}$. Note that these nearest points on $\mathcal{S}^{\mathrm{A}}$ and $\mathcal{S}^{\mathrm{B}}$ may not be a quadrature point of the respective patches. For many simple configurations, the corresponding points on $\mathcal{L}$ and the two patches are exactly co-located. For more complex situations (such as the case of non-watertight geometries), the nearest points can be determined using the approach proposed in Bazilevs et al. [23, Section 3.4].

It is also important to properly assemble the contributions of Eqs. (18)–(21) to the global system matrices. This is especially relevant for cases in which the discretization of $\mathcal{L}$ does not match the discretization of one or both of the shell surfaces. In the traditional approach of element-wise assembly, one would first form the element matrices with respect to the elements of $\mathcal{L}$. However, a single element of $\mathcal{L}$ may not correlate with an element in the shells $\mathcal{S}^{\mathrm{A}}$ or $\mathcal{S}^{\mathrm{B}}$, making the assembly impossible. This problem is resolved by simply assembling the contributions of Eqs. (18)–(21) directly at each quadrature point to the global matrices. As described above, each quadrature point on $\mathcal{L}$ is associated with the nearest points on $\mathcal{S}^{\mathrm{A}}$ and $\mathcal{S}^{\mathrm{B}}$. For each quadrature point on $\mathcal{L}$, the basis function information at each of the nearest points on $\mathcal{S}^{\mathrm{A}}$ and $\mathcal{S}^{\mathrm{B}}$ can be employed to directly apply the penalty contributions to the degrees of freedom of the shell problem.

---

[2] In this work, the full Gauss quadrature rule is used to integrate $\mathcal{L}$. The effect of different quadrature rules and the potential for overconstraining and locking are interesting topics that represent avenues for future research.

2.4. Selection of penalty parameters

A key drawback of penalty methods is that the penalty parameters must be high enough to ensure constraint satisfaction without creating excessive ill-conditioning. The selection of penalty parameters, usually performed empirically by the analyst, has a strong influence on the solution quality. A straightforward strategy is to directly employ a single value for both displacement and rotation penalties:

$$\alpha_{\mathrm{d}} = \alpha_{\mathrm{r}} = \alpha \; , \tag{26}$$

where α is an adjustable penalty parameter. As will be shown, this strategy does not ensure that a given value of α is appropriate for a variety of problem configurations and, in practice, requires user selection of α based on trial and error.

In this work, it is shown that, rather than requiring user selection of the penalty parameters, the parameters can be formulated according to the problem configuration, that is, according to geometry and material properties. A single value of α, scaled by problem-specific parameters, can then be reliably used for various problems. In this work, the displacement and rotation penalty parameters are formulated with respect to the shell membrane and bending stiffnesses, respectively, in order to make the penalty terms dimensionally consistent with the rest of the problem and in order to scale the terms according to kinematically-relevant stiffness properties:

$$\alpha_{\mathrm{d}} = \alpha \frac{\max_{i,j}\left(\mathbb{A}_{ij}\right)}{h} \; , \tag{27}$$

$$\alpha_{\mathrm{r}} = \alpha \frac{\max_{i,j}\left(\mathbb{D}_{ij}\right)}{h} \; , \tag{28}$$

where α is a penalty coefficient, $\mathbb{A}_{ij}$ and $\mathbb{D}_{ij}$ are the membrane and bending stiffnesses given in Eqs. (10) and (12), respectively, $h = \left(h^{\mathrm{A}} + h^{\mathrm{B}}\right)/2$, h^{A} and h^{B} are the lengths of the local elements in the direction most parallel to the penalty curve, $i = 1, 2$, and $j = 1, 2$. For uniform isotropic configurations, the expressions reduce to

$$\alpha_{\mathrm{d}} = \alpha \frac{E\,t}{h\,(1-\nu^2)} \; , \tag{29}$$

$$\alpha_{\mathrm{r}} = \alpha \frac{E\,t^3}{12\,h\,(1-\nu^2)} \; , \tag{30}$$

where E is Young's modulus, t is the shell thickness, and ν is Poisson's ratio.

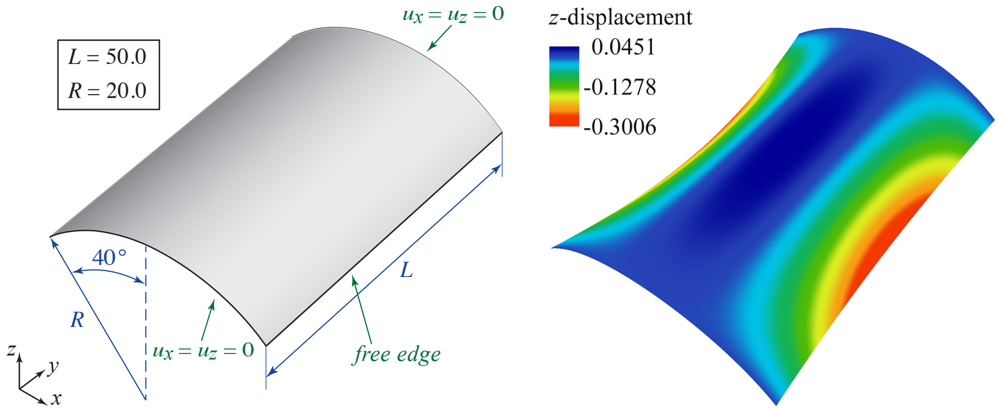

Figure 4: Scordelis-Lo roof problem description and deformation (scaled by a factor of 10 for visualization).

3. Benchmark examples

A variety of geometrically linear and nonlinear benchmark examples are employed to explore the behavior of the coupling methodology and the formulations for the penalty parameters proposed in Eqs. (27) and (28). Examples featuring different geometries, material properties, and analysis types are selected, and a combination of matching and non-matching discretization strategies are used throughout, all to demonstrate the effectiveness and flexibility of the method. The appropriate range for the dimensionless penalty coefficient, α, is also explored. The geometrically linear analyses are done by performing only one iteration step of the nonlinear analysis. Linear systems are solved using direct solvers, eigenvalue problems are solved using a SLEPc-based Krylov–Schur solver [24, 25], and the highly nonlinear examples in Sections 3.6 and 3.7 employ the modified Riks (arc length) method [26].

3.1. Scordelis-Lo roof

The Scordelis-Lo roof is a geometrically linear problem from the well-known shell obstacle course proposed by Belytschko et al. [27] to test accuracy and robustness in complex strain states. The problem configuration and dimensions of the geometry are shown in Figure 4. The ends of the geometry are supported by rigid diaphragms while the remaining edges are left unconstrained. A uniform gravitational load of 90.0 per unit area is applied to the roof, and the resulting linear deformation is quantified by evaluating the vertical displacement of the midpoint of the free edge. For the benchmark problem, the thickness and Young's modulus of the roof are $t = 0.25$ and $E = 4.32 \times 10^8$, respectively. Figure 4 also shows the deformation of the roof.

The geometry of the Scordelis-Lo roof is modeled using multiple NURBS patches of degree 3 with both matching and non-matching discretizations as shown in Figures 5a and 5b, respectively.

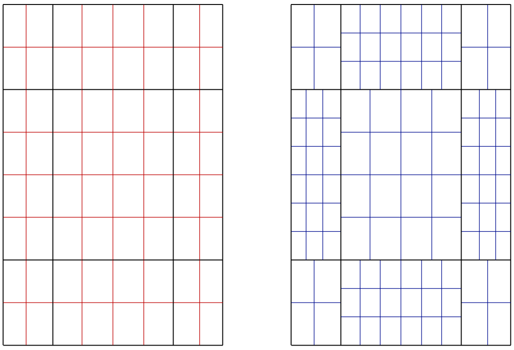

(a) Matching (b) Non-matching

Figure 5: Meshes for the matching and non-matching configurations of the Scordelis-Lo roof. Thick black lines indicate patch boundaries.

For the purpose of exploring the effective range of α, the deformation of both the matching and non-matching cases is calculated using the proposed penalty parameter formulations, Eqs. (27) and (28), and the α-only formulation, Eq. (26), over a range of values of α. This same study is repeated for cases wherein the shell thickness, t, and Young's modulus, E, have been modified. Throughout these studies, analyses are performed using the meshes shown in Figures 5a and 5b with two levels of h-refinement; the meshes in Figure 5 will be used for the convergence study presented later.

The results of the analyses performed using the benchmark material parameters are shown for the proposed penalty formulations in Figure 6a and for the α-only penalty formulations in Figure 6b. The displacements are normalized by a converged reference value, $u_z = -3.005925 \times 10^{-1}$, obtained using a single-patch model discretized with 128×128 bicubic elements. As expected, the results in both cases indicate a range of values of α for which the penalty coupling methodology is effective and produces the correct result. Also note that accurate results are obtained for both the matching and non-matching cases. These results clearly show that, if the value of the penalty parameter is too low, the patch coupling constraint is not enforced. If the penalty parameter value is too high, the matrices may become ill-conditioned and the solution of the linear system is prone to large numerical errors. Both scenarios lead to solutions deviating from the reference results. For this reason, we recommend using a penalty value that is sufficiently high to produce an accurate result but no higher than necessary.

The results in Figures 6a and 6b alone do not indicate the importance of the proposed penalty formulations. The value can be understood, however, upon performing the same analysis with different sets of material parameters. The results obtained using a thickness of $t = 0.025$ instead of $t = 0.25$ are shown for the proposed and α-only formulations in Figures 6c and 6d, respectively. The displacements are normalized by a converged reference value of $u_z = -32.01045$, obtained us-

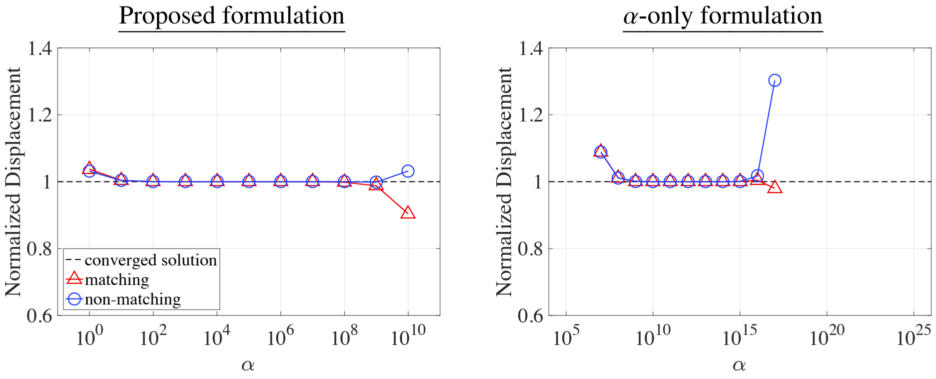

(a) $E = 4.32 \times 10^8$, $t = 0.25$ (b) $E = 4.32 \times 10^8$, $t = 0.25$

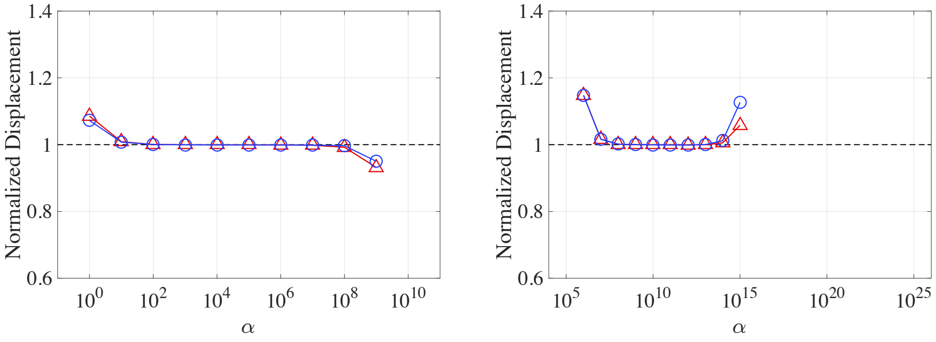

(c) $E = 4.32 \times 10^8$, $\boldsymbol{t} \mathbf{= 0.025}$ (d) $E = 4.32 \times 10^8$, $\boldsymbol{t} \mathbf{= 0.025}$

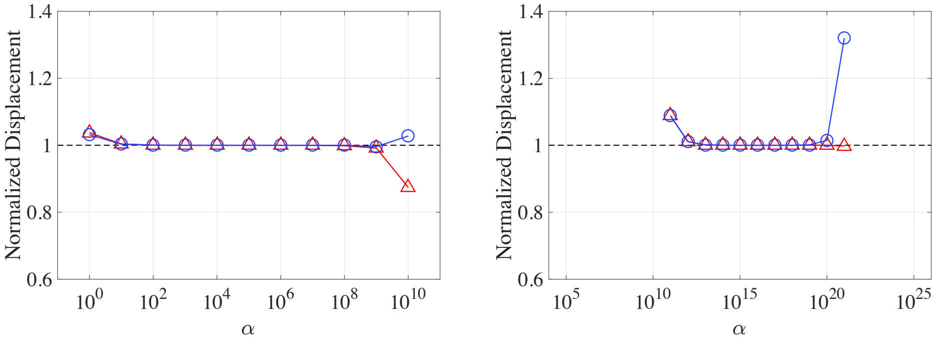

(e) $\boldsymbol{E} \mathbf{= 4.32 \times 10^{12}}$, $t = 0.25$ (f) $\boldsymbol{E} \mathbf{= 4.32 \times 10^{12}}$, $t = 0.25$

Figure 6: Vertical displacement at midpoint of the free edge of the Scordelis-Lo roof, normalized with respect to the converged reference value, with varying penalty value α using the proposed penalty approach and the α-only approach for both matching and non-matching discretizations and different combinations of setup variables.

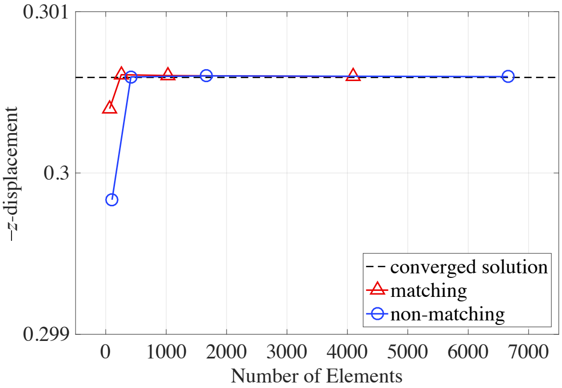

Figure 7: Vertical displacement at midpoint of the free edge of the Scordelis-Lo roof under h-refinement for the proposed penalty approach with $\alpha = 10^3$.

ing the same single-patch mesh as before. Similarly, the results obtained using a Young's modulus of $E = 4.32\times10^{12}$ instead of $E = 4.32\times10^8$ are shown for the proposed and α-only formulations in Figures 6e and 6f, respectively. The displacements are normalized by a converged reference value of $u_z = -3.005925 \times 10^{-5}$, obtained from a single-patch simulation.

For the cases employing the α-only penalty formulation, shown in Figures 6b, 6d, and 6f, the range of values of α that produce accurate results shifts significantly, by as much as five orders of magnitude, when the problem parameters are changed. This illustrates one of the key drawbacks of penalty methods: because the effective range of α is problem-dependent, an analyst would be forced to select the penalty parameter based on experience. In contrast, for the cases employing the proposed penalty formulations, shown in Figures 6a, 6c, and 6e, the effective range of α remains consistent for all problem configurations. Specifically, an accurate range of approximately $\alpha = 10^2$ to $\alpha = 10^8$ is observed. Thus, a value of $\alpha = 10^3$ is recommended; this value is high enough to reliably produce correct results, but is no higher than necessary.

Solution convergence under mesh refinement can also be demonstrated using the proposed penalty approach. Results are compared to the converged displacement from the single-patch simulations. The coarsest geometries for the matching and non-matching multi-patch configurations are shown in Figures 5a and 5b, and refinement is performed via global h-refinement. All analyses use $\alpha = 10^3$. The results in Figure 7 indicate satisfactory convergence for both the matching and non-matching cases.

3.2. Simply supported plate under sinusoidal load

A simply supported plate problem is employed to study the convergence and conditioning behavior of the proposed penalty approach. The setup for this problem is shown in Figure 8. The

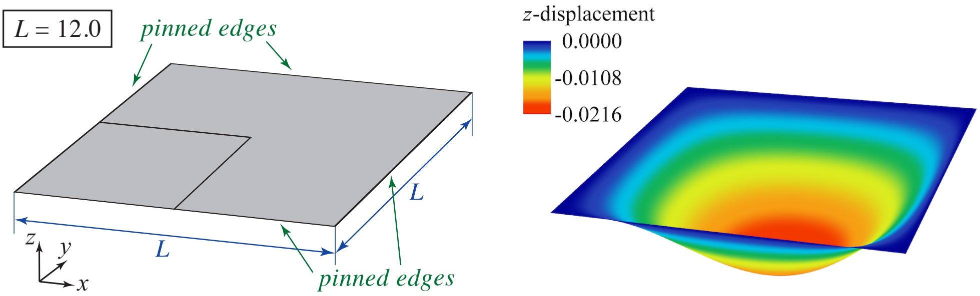

Figure 8: Simply supported plate problem description and deformation (scaled by a factor of 200 for visualization).

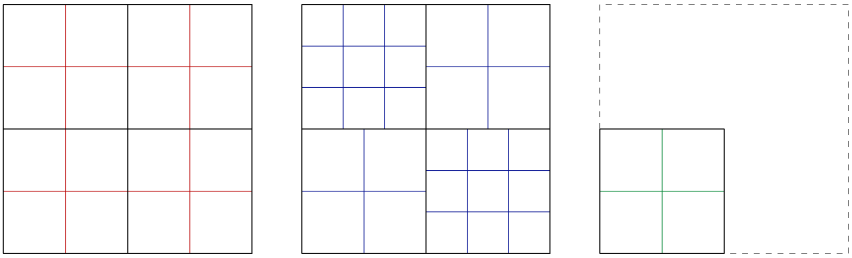

(a) Matching (b) Non-matching (c) Quarter

Figure 9: Meshes for the matching and non-matching full geometry configurations and the quarter geometry configuration of the simply supported plate.

square plate is subjected to a sinusoidal pressure load of $p(x, y) = p_0 \sin(\pi x/L) \sin(\pi y/L)$. The example and results included here utilize a plate with $L = 12.0$, thickness $t = 0.375$, Young's modulus $E = 4.8 \times 10^5$, Poisson's ratio $\nu = 0.38$, and load amplitude $p_0 = 1.0$. The plate deformation is evaluated at the center of the plate, the location of maximum displacement, and is compared to the analytical solution [28],

$$u_{\max} = \frac{p_0 L^4}{4\pi^4 D}\,, \text{ where } D = \frac{Et^3}{12(1-\nu^2)}. \tag{31}$$

The deformation of the plate is also shown in Figure 8.

To evaluate the performance of the penalty approach for patch coupling and for imposing symmetry conditions, a variety of configurations of this problem are considered. A full plate geometry with four NURBS patches of degree 3 is used to assess patch coupling, while a quarter plate geometry with a single patch of degree 3 is used to assess the enforcement of symmetry conditions. In the full plate geometry, both matching and non-matching mesh configurations are investigated, as shown in Figures 9a and 9b, respectively. Figure 9c shows the mesh configuration of the quarter

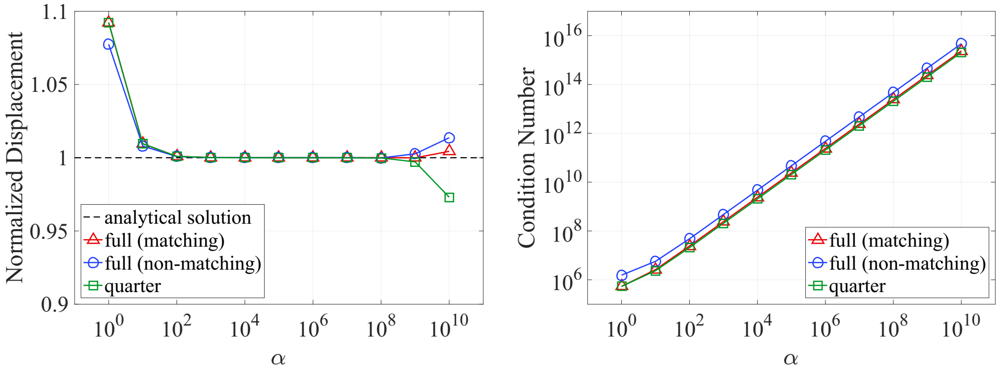

Figure 10: Normalized displacement at the plate center and condition number of the stiffness matrix with varying α.

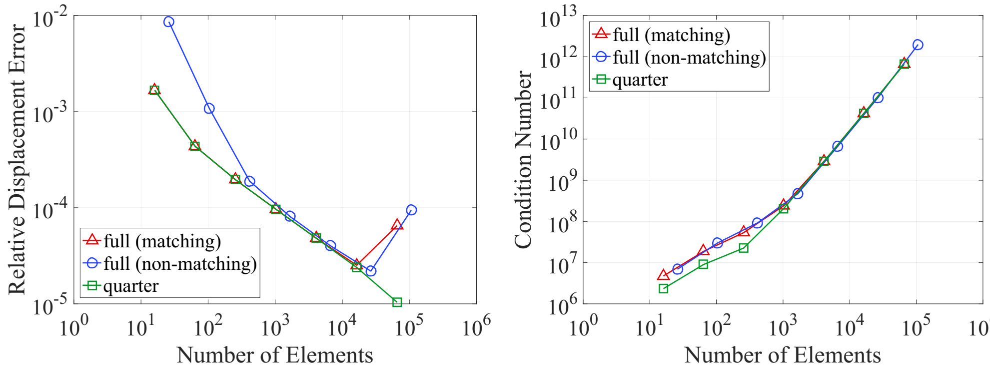

Figure 11: Relative error of the displacement at the plate center and condition number of the plate stiffness matrix under h-refinement with $\alpha = 10^3$. The number of elements for the quarter patch results is scaled by four for comparison.

plate geometry.

For each analysis, the displacement at the center of the plate and the condition number of the stiffness matrix are calculated. Results for both displacement and condition number with varying α are shown in Figure 10. These results use the meshes shown in Figure 9 with three levels of h-refinement. The displacement values indicate the same effective range of α demonstrated in Section 3.1 for each configuration, while the condition number increases with α as expected. The convergence of the displacement and condition number are also studied for the plate under h-refinement, as shown in Figure 11. All convergence results are computed with $\alpha = 10^3$, and the number of elements in the quarter plate configurations is scaled by four for comparison with the full plate geometry. The refinement study highlights the fact that the condition number increases

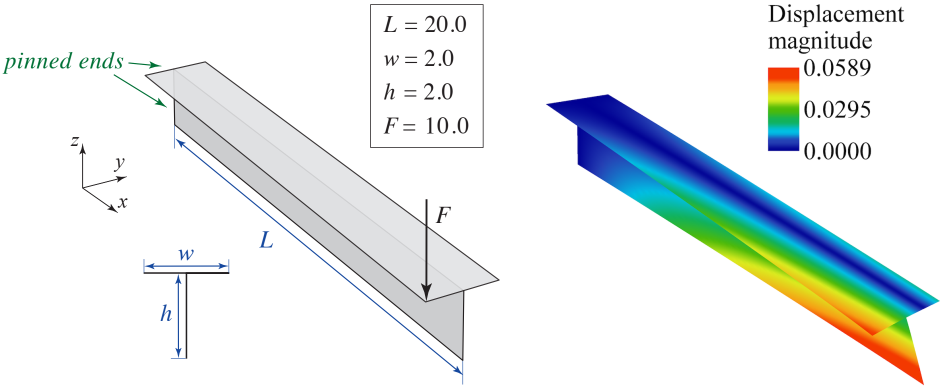

Figure 12: T-beam problem description and deformation (scaled by a factor of 10 for visualization).

with refinement. While this feature helps with overall solution convergence under refinement, it also dictates that, for some cases with excessive refinement, the results may deteriorate.

3.3. T-beam

Complex shell structures typically also include non-smooth patch interfaces, i.e., patches joined with a certain angle; the angle between the patches must be maintained during deformation analysis. An example of this is a T-beam, as depicted in Figure 12. The T-beam is modeled using two planar geometries which are orthogonal at their interface. As shown in Figure 12, one end of the beam is pinned and a force of $F = 10.0$ is applied to one corner of the opposite end in the $-z$ direction. Figure 12 also indicates the dimensions of the geometry. The patches have a Young's modulus of $E = 1.0 \times 10^7$, a thickness of $t = 0.1$, and a Poisson's ratio of $\nu = 0.0$. The deformed geometry is shown in Figure 12.

The T-beam is modeled using two NURBS patches of degree 3. Again, both matching and non-matching mesh configurations are constructed as shown in Figures 13 and 14. For the analyses considered here, two h-refinements are performed on each of the meshes shown in Figures 13 and 14. The geometrically linear analysis is performed, and the angle between the patches at the end of the beam is calculated. If the patches have been properly coupled, an angle of 90° should be maintained. The left side of Figure 15 shows the resultant angle between the two patches for both the matching and non-matching cases for a range of α values. Note that, for relatively low values of α, the structure is effectively unconstrained at its interface, resulting in an angle of approximately 93.5° between the patches. However, in the range of approximately $\alpha = 10^{-2}$ to $\alpha = 10^2$ the constraint begins to take effect, resulting in the desired angle of 90° between the patches for $\alpha > 10^2$. Again, a wide range of acceptable values of α is observed; the range is similar to those observed in the previous examples. Thus, the suggested value of $\alpha = 10^3$ remains

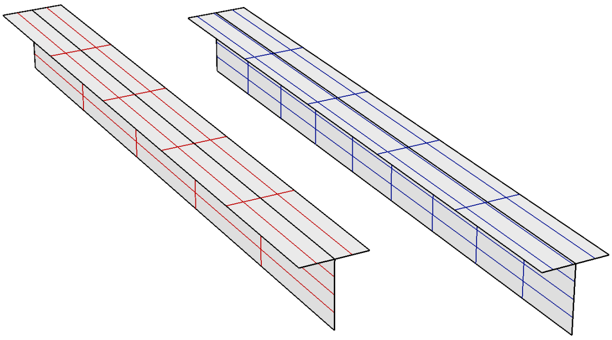

Figure 13: Meshes for the matching (left) and non-matching (right) configurations of the T-beam problem.

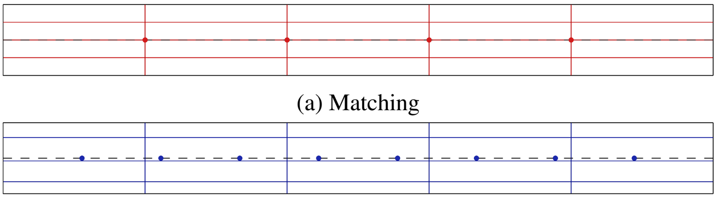

(a) Matching

(b) Non-matching

Figure 14: Top view of meshes for the matching and non-matching configurations of the T-beam problem. Circular markers indicate discretization of perpendicular patch.

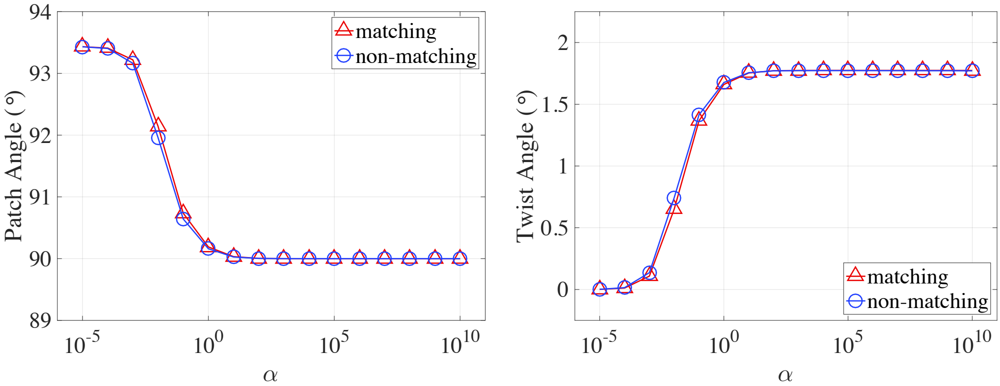

Figure 15: Angle between patches of the T-beam (left) and total twist at the end of the vertical patch (right) with varying penalty value α for both matching and non-matching configurations.

appropriate in this case.

The right side of Figure 15 shows the total twist at the free end of the T-beam measured using the vertical patch. When the penalty value is too low, the patches are effectively uncoupled and the

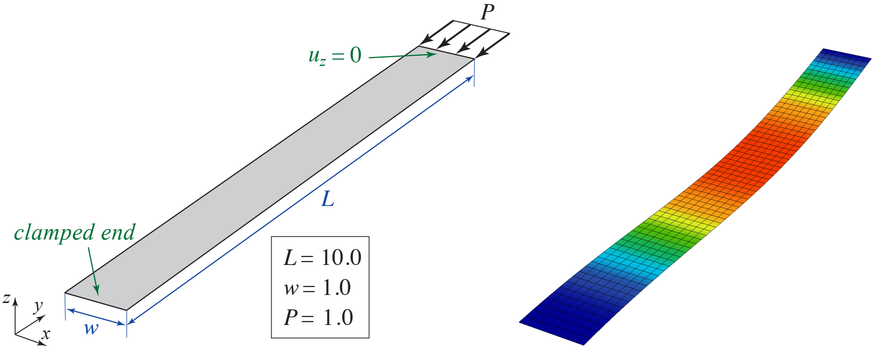

Figure 16: Plate buckling problem description and the deformation for the first buckling mode (color contour indicates relative displacement magnitude).

strain energy is not transferred to the vertical patch, resulting in a twist angle of zero degrees. As the penalty value increases, a consistently reasonable twist angle is observed. Similar results are obtained for both the matching and non-matching configurations.

3.4. Plate buckling

Another important type of analysis that is commonly performed in the design of shell structures, such as wind turbine blades, is linear buckling analysis. Thus, the performance of the proposed penalty formulation is also explored in the context of linear buckling. Linear buckling analysis, or eigenvalue buckling analysis, entails solving the equation

$$\left(\mathbf{K}^{\text{lin}} + \lambda_i \mathbf{K}_{\text{g}}\right) \mathbf{v}_i = 0 \,, \tag{32}$$

where $\mathbf{K}^{\text{lin}}$ is the linear stiffness matrix of the structure, $\mathbf{K}_{\text{g}}$ is the geometric stiffness matrix based on the applied load, and λ_i is the i^{th} eigenvalue associated with mode vector $\mathbf{v}_i$. In this context, an eigenvalue λ_i is a scalar multiplier of the applied loads that will, in theory, cause buckling of the structure; $\mathbf{v}_i$ is the corresponding buckling mode shape.

A plate is employed in a simple buckling configuration, as shown in Figure 16, with one end clamped and the other supported in the vertical direction. The problem is modeled using both matching and non-matching multi-patch configurations. All of the patches are bicubic NURBS surfaces. The discretization of the patches is shown in Figure 17. The patch sizes are intentionally selected such that the patch boundaries do not occur on axes of symmetry. This makes the problem more difficult because, if the penalty does not function properly, it may produce a non-symmetric result. For this problem, Young's modulus is $E = 1.0 \times 10^3$, Poisson's ratio is $\nu = 0.0$, thickness is $t = 0.1$, and the applied distributed force is $P = 1.0$ in terms of force per unit length.

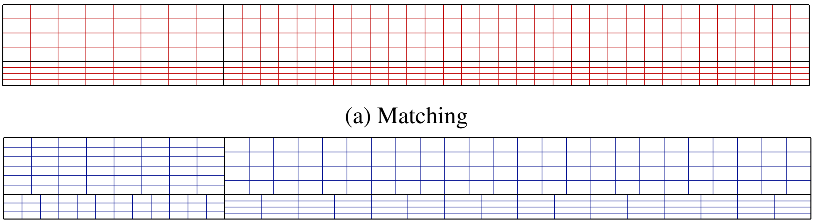
(a) Matching

(b) Non-matching

Figure 17: Meshes for the matching and non-matching configurations of the plate buckling problem.

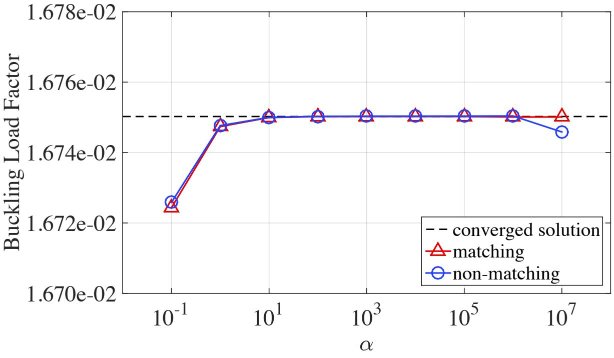

Figure 18: Buckling load factor with varying α for both matching and non-matching configurations of the plate buckling problem.

The plot in Figure 18 indicates that, for a similar range of α parameters observed in the previous problems, the multi-patch configurations produce buckling load factors of sufficient accuracy when compared to a converged result obtained using a single-patch configuration. This illustrates the accuracy of the proposed formulation in the context of linear buckling analysis. Also note that the suggested value of $\alpha = 10^3$ is appropriate here.

3.5. Nonlinear slit annular plate

All of the examples considered thus far have employed linear analysis. However, the presented methodology is also applicable in the geometrically nonlinear setting. Sze et al. [29] identified and reproduced a number of common benchmark problems for nonlinear analysis, one of which is a slit annular plate subjected to a lifting line force. The slit annular plate problem is reproduced using multi-patch models to verify the proposed coupling methodology in the nonlinear setting.

The slit annular plate setup and deformation are illustrated in Figure 19. One side of the slit is clamped, while the other is allowed to freely deform under the applied distributed force, P. The deformation is quantified by tracking the vertical displacement of points A and B, identified in

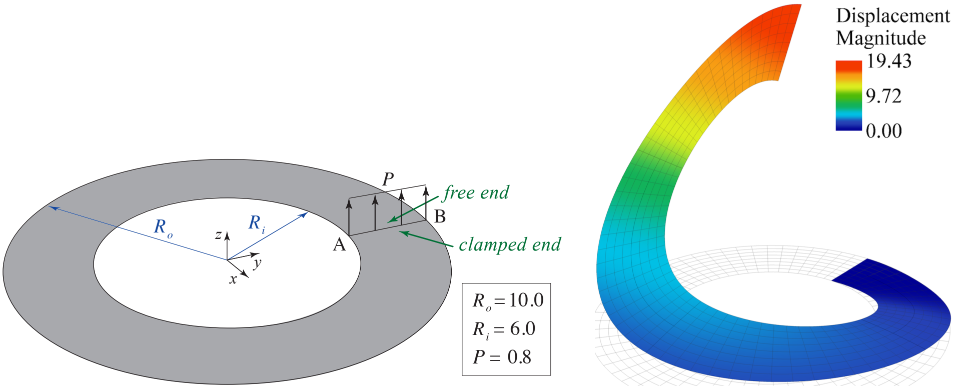

Figure 19: Nonlinear slit annular plate problem description and deformation.

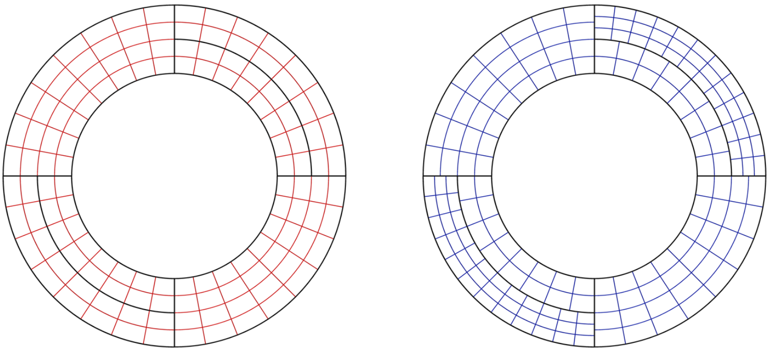

(a) Matching

(b) Non-matching

Figure 20: Meshes for the matching and non-matching cases of the nonlinear slit annular plate. Thick black lines indicate patch boundaries.

Figure 19, at incremental loads up to $P = 0.8$. Young's modulus is $E = 21.0 \times 10^6$, thickness is $t = 0.03$, and Poisson's ratio is $\nu = 0.0$.

Refinement studies are not typically performed for the slit annular plate problem in the literature. However, because cases with different discretizations are considered in this work, a refinement study is performed for both matching and non-matching configurations to ensure that the results are comparable. For all of the cases, cubic NURBS patches are employed. The coarsest meshes used in the refinement study are shown in Figure 20, and the displacement of point B due to the the maximum load of $P = 0.8$ under h-refinement is shown in Figure 21. For this analysis, the recommended value of $\alpha = 10^3$ is employed. Convergence is achieved with approximately two h-refinements for both the matching and non-matching cases. Thus, these levels of refinement are used for the following verification of α.

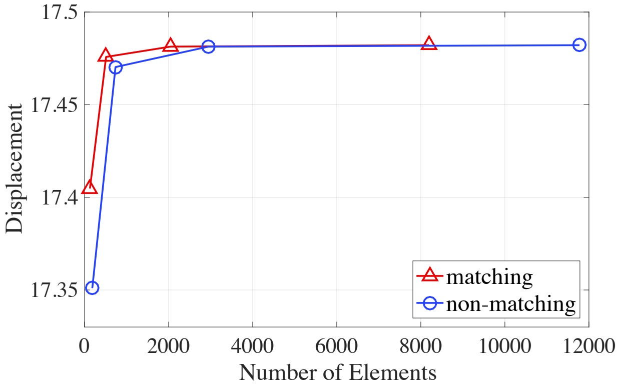

Figure 21: Vertical displacement at point B of the slit annular plate under h-refinement for both matching and non-matching configurations.

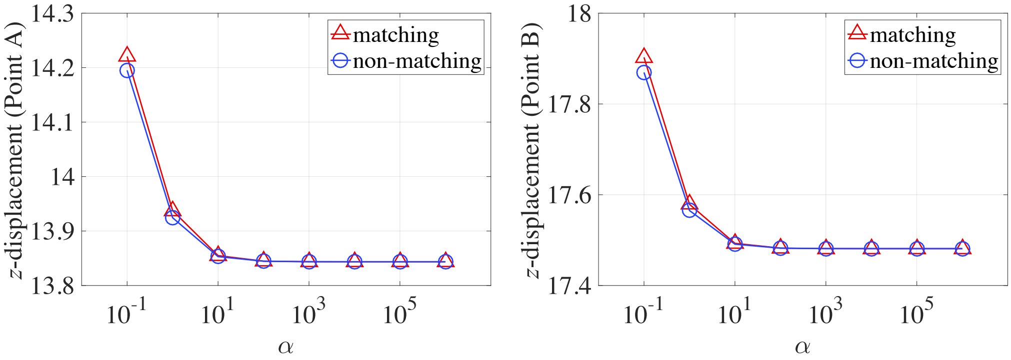

Figure 22: Vertical displacement at points A and B of the slit annular plate due to the maximum applied P for varying values of α.

Figure 22 shows the displacements at A and B for the maximum load of $P = 0.8$ and a range of α values. The accuracy of the method is clearly demonstrated for $\alpha = 10^2$ through $\alpha = 10^6$, with identical results obtained in both the matching and non-matching cases. In nonlinear analysis, a badly conditioned problem is more likely to exhibit divergent behavior, as is the case for $\alpha \geq 10^7$ for this problem. Still, the problem is tractable for a wide range of values of α, and the acceptable range is similar to the range observed in the previous examples. The suggestion of $\alpha = 10^3$ remains appropriate.

Figure 23 shows the displacements of point A and point B under varying applied forces both for the presented methodology and as reported by Sze et al. [29] using a 6×30 mesh of four-node S4R elements in ABAQUS [30]. A penalty coefficient of $\alpha = 10^3$ is used for this comparison, and good agreement with the reference results is observed over the entirety of the load spectrum.

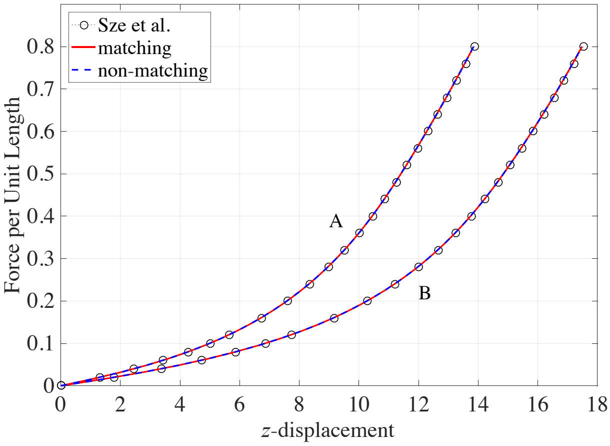

Figure 23: Vertical displacement of points A and B versus applied distributed load for the nonlinear slit annular plate with $\alpha = 10^3$.

3.6. Nonlinear pinched semi-cylindrical shell

The proposed methodology, and in particular the penalty parameter formulations (27) and (28), were also designed to accommodate composite materials. Here, the performance of the proposed method is investigated using a nonlinear pinched semi-cylinder example, shown in Sze et al. [29], featuring isotropic and laminated materials. Figure 24 illustrates the setup and the deformation of the problem. The semi-cylindrical shell is subject to a point load at the middle of the free end of the cylinder. The other end is fully clamped. Along its longitudinal edges, the vertical displacement and the rotation about the y-axis are constrained. For the isotropic configuration, material parameters are $E = 2.0685 \times 10^7$ and $\nu = 0.3$, while for the laminated configuration $E_L = 2.0685 \times 10^7$, $E_T = 0.517125 \times 10^7$, $G_{LT} = 0.7956 \times 10^7$, and $\nu_{LT} = \nu_{TT} = 0.3$. Ply configurations of [0/90/0] and [90/0/90] are used, with each ply having a thickness of $t = 0.01$. The total shell thickness is $t = 0.03$ for all cases. The applied load of $F = 2000$ is scaled by the load factor λ, where $0 < \lambda \leq 1$.

Due to symmetry, the problem is solved by modeling only one half of the structure. The boundary and symmetry conditions are imposed using the proposed penalty approach. A single-patch configuration as well as a non-matching multi-patch configuration are considered to highlight the formulations' performance in the context of nonlinear analysis of composite shells. In both cases, quadratic NURBS patches are used. The two configurations are shown in Figure 25. Note that the multi-patch model includes penalties for clamping, symmetry, and non-matching patch coupling.

Displacements at the location of the applied load under the full load of $F = 2000$ are shown

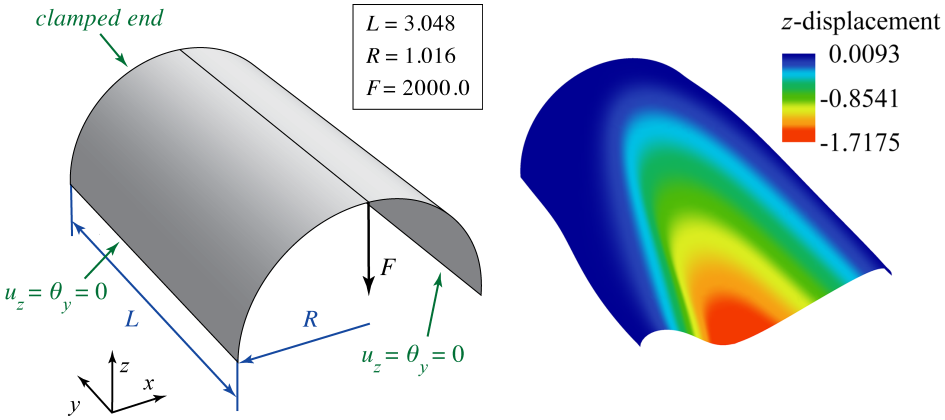

Figure 24: Nonlinear semi-cylinder problem description and deformation at the maximum applied load for the isotropic material case.

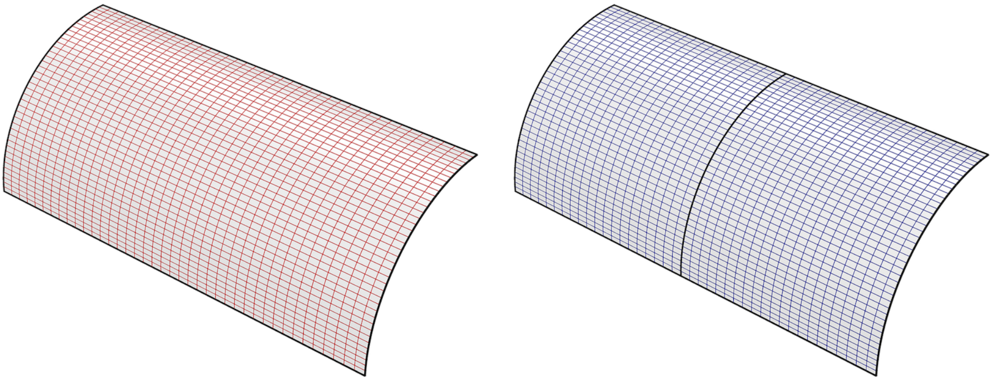
(a) Single patch

(b) Non-matching multi-patch

Figure 25: Meshes for the single-patch and non-matching multi-patch cases of the half geometry of the semi-cylinder. Thick black lines indicate patch boundaries.

for the multi-patch model over a range of penalty parameter values in Figure 26. The results are consistent between $\alpha = 10^2$ and $\alpha = 10^5$, demonstrating the stability of the proposed methodology and confirming the choice of the penalty coefficient of $\alpha = 10^3$. The displacements at the location of the applied load for varying load levels and using $\alpha = 10^3$ are shown in Figure 27. Good agreement with the reference results [29] is observed for all discretizations and material configurations considered, indicating the effectiveness of the proposed method even for nonlinear composite applications.

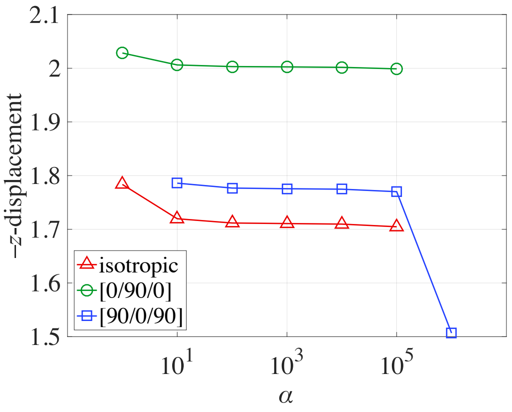

Figure 26: Vertical displacements at the point where the load is applied for the nonlinear semi-cylinder at the maximum load for varying α. The study is performed for the non-matching multi-patch model. The simulations did not converge at $\alpha = 10^6$ for the isotropic and [0/90/0] cases, and at $\alpha = 10^0$ for the [90/0/90] case.

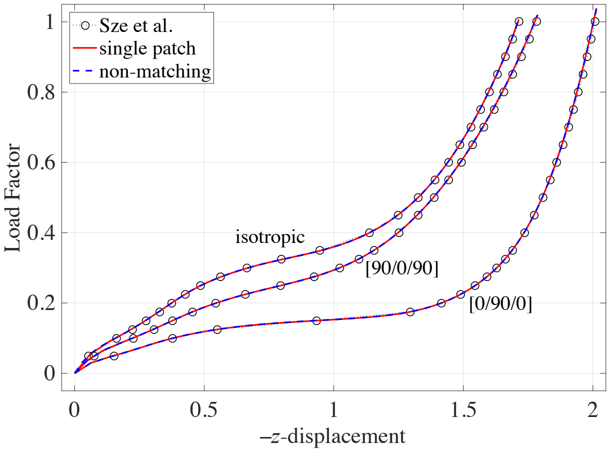

Figure 27: Load factor versus vertical displacement for the nonlinear semi-cylinder problem with $\alpha = 10^3$.

3.7. Hinged cylindrical shallow roof

To further demonstrate the effectiveness of the proposed penalty formulation for challenging, nonlinear problems, the approach is applied to the hinged cylindrical shallow roof [29], a structure involving challenging snap-through and snap-back behaviors in both isotropic and laminated configurations. The problem description and the dimensions of the shallow roof are shown in Figure 28. The shell structure has hinged supports along two edges and is subjected to a concentrated

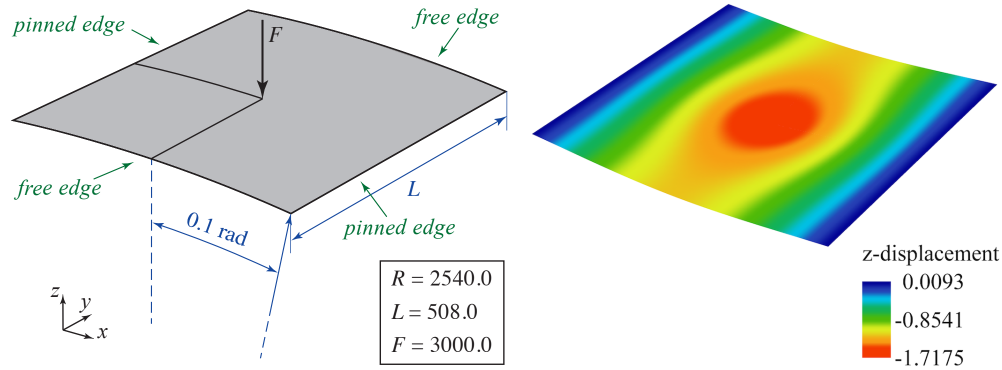

Figure 28: Shallow roof problem description and deformation at the maximum applied load for the isotropic material case.

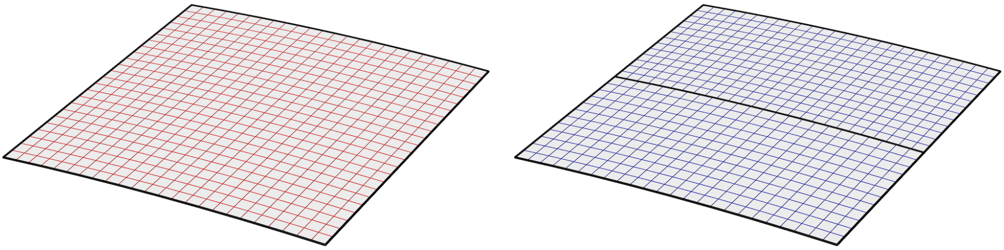

(a) Single patch

(b) Non-matching multi-patch

Figure 29: Meshes for the single patch and non-matching multi-patch cases of the quarter geometry of the shallow roof. Thick black lines indicate patch boundaries.

load up to $F = 3000$. Both isotropic material ($E = 3102.75$, $\nu = 0.3$) and laminated material ($E_L = 3300$, $E_T = 1100$, $G_{LT} = 660$, $\nu_{LT} = \nu_{TT} = 0.25$) are considered; in the case of laminated material, two different ply configurations, [0/90/0] and [90/0/90], are considered. All plies are equal in thickness, having a total shell thickness of $t = 6.35$.

Due to symmetry, only a quarter of the structure is modeled and symmetry conditions are applied with the proposed penalty formulation. As in the previous example, both single-patch and non-matching multi-patch configurations are considered for the quarter geometry (Figure 29), employing bivariate NURBS of degree 2. The load F is scaled by the load factor λ ($0 < \lambda \leq 1$) and applied incrementally up to the maximum value of 3000.

Figure 30 shows the displacement of the central point under the maximum load for different α values. This study is performed for the non-matching multi-patch model featuring one quarter of the structure with patch coupling and symmetry conditions applied using the penalty method. The trend of the results is similar to those of the previous analyses; non-convergence is observed for

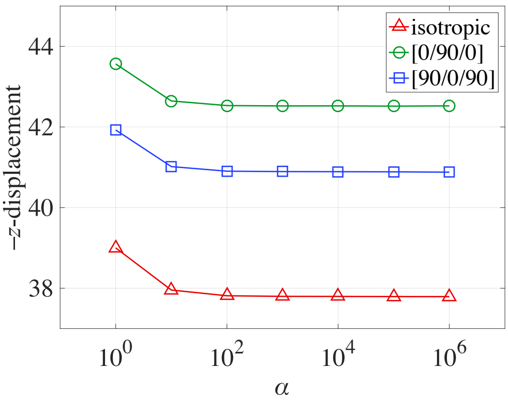

Figure 30: Vertical displacement of the central point of the shallow roof under the maximum load for various values of the penalty parameter α. The study is performed for the non-matching multipatch model featuring one quarter of the structure.

high values of the penalty parameter, due to poor conditioning, while stable results are obtained for $10^2 \leq \alpha \leq 10^6$.

The results of the nonlinear simulations for the isotropic and laminated cases throughout the load range and for both discretization strategies are shown in Figure 31. The results show good agreement with the reference solutions [29]. Furthermore, the results confirm the validity of the proposed formulation and $\alpha = 10^3$ for highly nonlinear problems, including complex snap-through and snap-back situations, for both isotropic and laminated materials.

4. Application to wind turbine blade analysis

Wind turbine blade design and analysis is an example of a field in which the use of isogeometric Kirchhoff–Love shell analysis could be especially advantageous. Due to the complexity of wind turbine blade structures and the wide range of conditions they must withstand, thorough blade design is a highly iterative process that is governed, in part, by workflow automation and analysis efficiency, both of which may be improved through the application of IGA. The isogeometric Kirchhoff–Love shell formulation has been shown to accurately capture the dynamic kinematic behavior of wind turbine blades [31, 32]. This formulation has also been employed for numerous fluid–structure interaction (FSI)-based analyses of full-scale wind turbines [20, 23, 33–35] and for IGA-based parametric design and optimization of a simplified blade design [36, 37]. The blades in the aforementioned work were modeled using a single-patch NURBS or T-spline surface, or multiple matching NURBS patches coupled using the bending strip method. In this work, a complex 5 MW blade design with shear webs and discontinuous composite definitions is modeled using

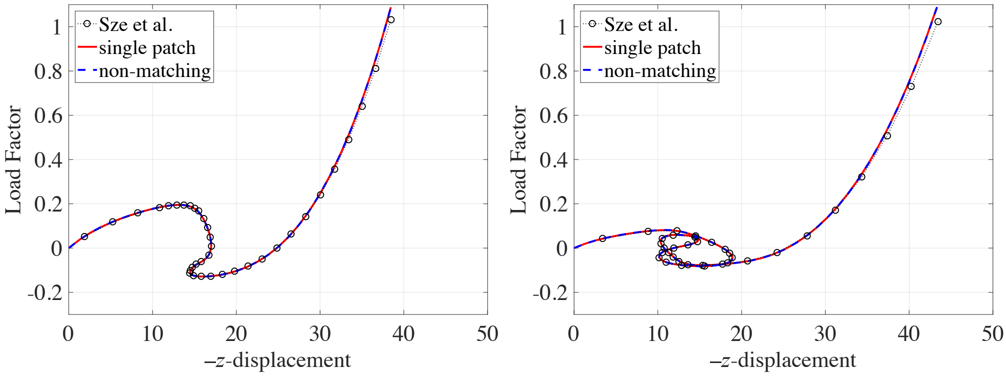

(a) Isotropic

(b) Laminated [0/90/0]

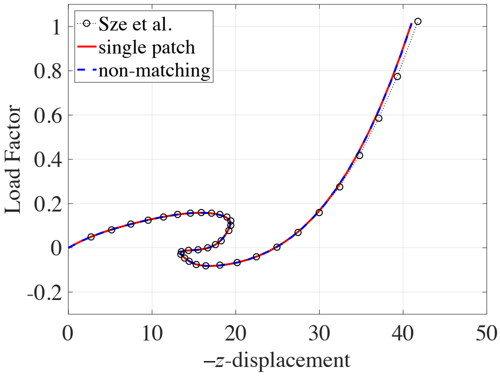

(c) Laminated [90/0/90]

Figure 31: Vertical displacement of the central point versus applied distributed load for the nonlinear shallow roof with $\alpha = 10^3$.

multiple non-matching NURBS patches that are coupled using the proposed penalty approach.

4.1. Blade definition

Resor [38] developed a detailed, composite wind turbine blade design based on the basic 5 MW blade design proposed by Jonkman et al. [39]. Resor [38] discusses geometry and material design details as well as comprehensive design analysis procedures. Due to its realistic material distribution, this NREL/SNL 5 MW blade design is a good candidate for demonstrating the effectiveness of the presented coupling methodology for complex composite structures.

Figure 32 shows the NREL/SNL 5 MW wind turbine blade geometry modeled using NURBS surfaces of degree 3. Note that the thick black lines indicate the edges of the 27 NURBS patches. The blade shell is modeled with multiple patches to accurately capture sharp discontinuities in material definition at the patch edges. The shear webs must also be modeled as independent NURBS

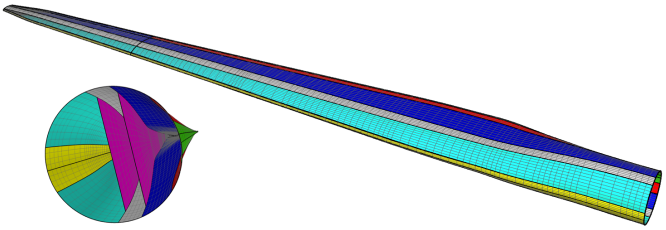

	Material Zone	Stack Usage
🟨	Leading Edge (LE)	1,2,3,2
🟦	LE Panel	1,2,3,7,2
⬜	Spar Cap	1,2,3,4,2
🟩	Trailing Edge (TE)	1,2,3,2
🟥	TE Reinforcement	1,2,3,5,6,2
🟦	TE Panel	1,2,3,6,2
🟪	Shear Web	8,9,8

Figure 32: NREL/SNL 5 MW wind turbine blade geometry, discretization, and stack usage for each material zone. Element edges indicated by grey lines, patch edges indicated by thick black lines.

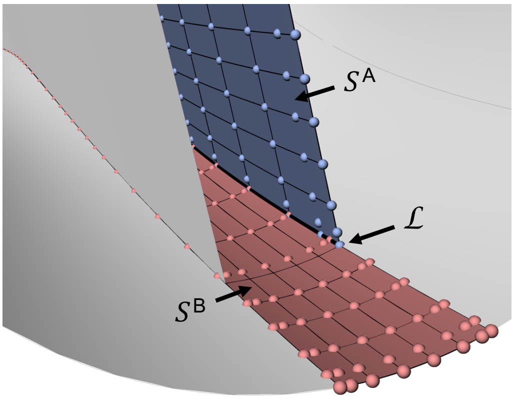

Figure 33: Non-matching discretization between the patches used to model the spar cap (red) and shear web (blue) of a wind turbine blade. Control point locations indicated by spheres.

surfaces. Even in this relatively straightforward geometrical configuration, it is somewhat difficult to ensure matching spanwise discretization for all patches, as shown in Figure 33, highlighting the value of a methodology for coupling non-matching patches.

Each of the colored regions in Figure 32 indicates a unique composite material stacking sequence. Furthermore, each material stack in each of these zones has a unique thickness profile along the blade's span. The stacking sequence in each material zone, in terms of stack ID, is shown in Figure 32. The name, material, and spanwise thickness distribution of each stack is given in Figure 34. Material properties and other details can be seen in Resor [38]. Note that Resor [38] assumes that material thicknesses are constant in between a predefined set of spanwise stations. In the present work, material thicknesses are defined as piecewise linear functions of blade span which are evaluated at every quadrature point when determining homogenized material properties. This smoother material distribution is expected to influence results only slightly.

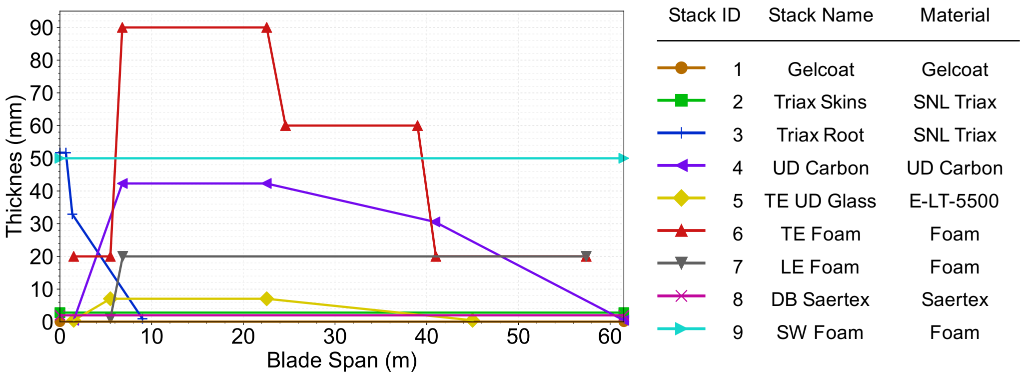

	Stack ID	Stack Name	Material
●	1	Gelcoat	Gelcoat
■	2	Triax Skins	SNL Triax
+	3	Triax Root	SNL Triax
◀	4	UD Carbon	UD Carbon
◆	5	TE UD Glass	E-LT-5500
▲	6	TE Foam	Foam
▼	7	LE Foam	Foam
×	8	DB Saertex	Saertex
▶	9	SW Foam	Foam

Figure 34: Thickness distribution as a function of blade span for all material stacks as well as stack IDs, names, and materials.

4.2. Linear buckling analysis

All examples considered thus far have been either isotropic configurations, for which the penalty formulations are given by Eqs. (29) and (30), or composite configurations featuring a uniform composite definition, for which the penalty formulations are given by Eqs. (27) and (28). Some composite structures, however, especially wind turbine blades, may have composite definitions that are not uniform. Specifically, sharp material discontinuities can even occur in between, for example, a blade's spar cap—which has a thick, stiff material definition—and the leading and trailing edge panels, which are comparatively weak. Because the penalty parameter formulations should be based on local material properties, it is necessary to identify formulations capable of addressing such discontinuities.

A number of possible formulations which resolve discontinuities in material description are explored here. Linear buckling analysis, as described in Eq. (32), is employed for this study because it is among the most important types of analyses performed for wind turbine blade structural design and is one of the primary uses for three-dimensional shell models. Aerodynamic loads are generated using NREL's FAST [40], an aeroelastic wind turbine modeling software that uses engineering models such as blade element momentum theory to simulate the dynamic structural and aerodynamic performance of wind turbines. The NREL/SNL 5 MW wind turbine is simulated under a 50-year extreme wind condition having 70 m/s winds, a fixed rotor, blades feathered to 90°, and 15° of yaw misalignment as specified by design load case (DLC) 6.1 in the IEC 61400 design standard [41]. This is commonly a design-governing load case in wind turbine blade design. The aerodynamic loads at the time instance featuring the largest blade root bending moment in the flapwise direction are collected and applied to the IGA-based buckling analysis through chordwise-constant but spanwise-variable distributed loads.

The various approaches considered for the penalty parameter formulations are described below. In the following, i and j are restricted to $i = 1, 2$ and $j = 1, 2$.

- **Minimum**: The minimum local stiffness between patches A and B is selected. The intent of this method is to yield a penalty value that is sufficiently high locally without producing penalty values that are excessively high with respect to less stiff portions of the model.

$$\alpha_{\mathrm{d}} = \alpha \frac{\min\left(\max_{i,j}\left(\mathbb{A}_{ij}^{\mathrm{A}}\right), \max_{i,j}\left(\mathbb{A}_{ij}^{\mathrm{B}}\right)\right)}{h}, \tag{33}$$

$$\alpha_{\mathrm{r}} = \alpha \frac{\min\left(\max_{i,j}\left(\mathbb{D}_{ij}^{\mathrm{A}}\right), \max_{i,j}\left(\mathbb{D}_{ij}^{\mathrm{B}}\right)\right)}{h}. \tag{34}$$

- **Maximum**: In this method, the maximum local stiffness between patches A and B is selected. This method prioritizes maximizing the influence of the penalty locally.

$$\alpha_{\mathrm{d}} = \alpha \frac{\max\left(\max_{i,j}\left(\mathbb{A}_{ij}^{\mathrm{A}}\right), \max_{i,j}\left(\mathbb{A}_{ij}^{\mathrm{B}}\right)\right)}{h}, \tag{35}$$

$$\alpha_{\mathrm{r}} = \alpha \frac{\max\left(\max_{i,j}\left(\mathbb{D}_{ij}^{\mathrm{A}}\right), \max_{i,j}\left(\mathbb{D}_{ij}^{\mathrm{B}}\right)\right)}{h}. \tag{36}$$

- **Average**: This method dictates that, between patches A and B, the average local stiffness should be used in the penalty formulation. This approach seeks to allow the material properties of both patches to influence the penalty parameter.

$$\alpha_{\mathrm{d}} = \alpha \frac{\max_{i,j}\left(\mathbb{A}_{ij}^{\mathrm{A}}\right) + \max_{i,j}\left(\mathbb{A}_{ij}^{\mathrm{B}}\right)}{2h}, \tag{37}$$

$$\alpha_{\mathrm{r}} = \alpha \frac{\max_{i,j}\left(\mathbb{D}_{ij}^{\mathrm{A}}\right) + \max_{i,j}\left(\mathbb{D}_{ij}^{\mathrm{B}}\right)}{2h}. \tag{38}$$

- **Minimum Transverse**: In this approach, the material matrices are rotated such that the $\mathring{\mathbf{e}}_1$ direction of the rotated matrices, $\tilde{\mathbb{A}}$ and $\tilde{\mathbb{D}}$, is consistent with the local tangential direction of the penalty curve. Then, the stiffness transverse to the penalty curve, or $\tilde{\mathbb{A}}_{22}$ and $\tilde{\mathbb{D}}_{22}$, can be directly used in the formulation. Between the two patches, the minimum $\tilde{\mathbb{A}}_{22}$ or $\tilde{\mathbb{D}}_{22}$ is selected, citing the same logic employed in the “Minimum” approach.

$$\alpha_{\mathrm{d}} = \alpha \frac{\min\left(\tilde{\mathbb{A}}_{22}^{\mathrm{A}}, \tilde{\mathbb{A}}_{22}^{\mathrm{B}}\right)}{h}, \tag{39}$$

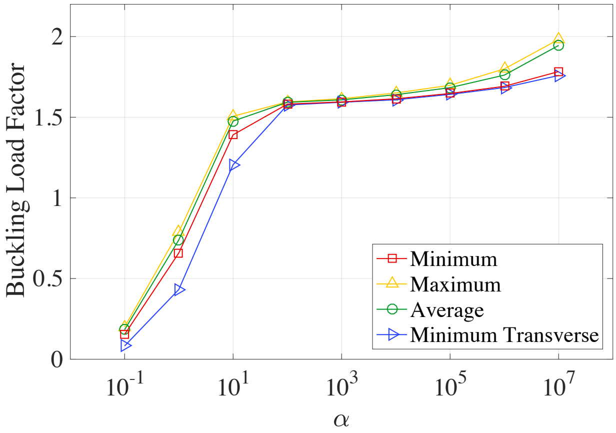

Figure 35: Lowest buckling load factor as a function of α for the various possible methods of formulating the penalty parameter for composite configurations featuring material discontinuities.

$$\alpha_{\mathrm{r}} = \alpha \frac{\min\left(\tilde{\mathbb{D}}^{\mathrm{A}}_{22}, \tilde{\mathbb{D}}^{\mathrm{B}}_{22}\right)}{h} \,. \tag{40}$$

Each of these methods is used with a range of α values in buckling analysis of the NREL/SNL 5 MW blade, as shown in Figure 35. Due to the technical challenges presented in this problem, such as the large number of penalty coupling curves (51) and highly non-uniform material definition across the blade structure, one should not expect a level of α parameter flexibility comparable to that seen in previous benchmark examples. Still, all methods feature a plateau at around $\alpha = 10^2$ to $\alpha = 10^4$, reinforcing the validity of using $\alpha = 10^3$ in general.

Both the “Maximum” and “Average” methods are shown to decrease in accuracy more quickly than the “Minimum” and “Minimum Transverse” methods with increasing α. Because the “Minimum” and “Minimum Transverse” methods utilize similar logic and exhibit comparable performance, we recommend using the “Minimum” method for the sake of implementation simplicity. The first three buckling modes obtained using this approach and $\alpha = 10^3$ are shown in Figure 36, and the “Minimum” method is used for the remainder of the analyses.

4.3. Vibration analysis

A blade’s vibration characteristics are another potential design-driver. It is critical that a blade’s natural frequencies of vibration do not align with certain turbine operational frequencies, such as the rotor’s rotational speed or the fundamental tower frequency, in order to avoid resonance. Linear vibration analysis is performed by considering the eigenvalue problem

$$\left(\mathbf{K}^{\mathrm{lin}} - \lambda_i \mathbf{M}\right) \mathbf{v}_i = 0 \,, \tag{41}$$

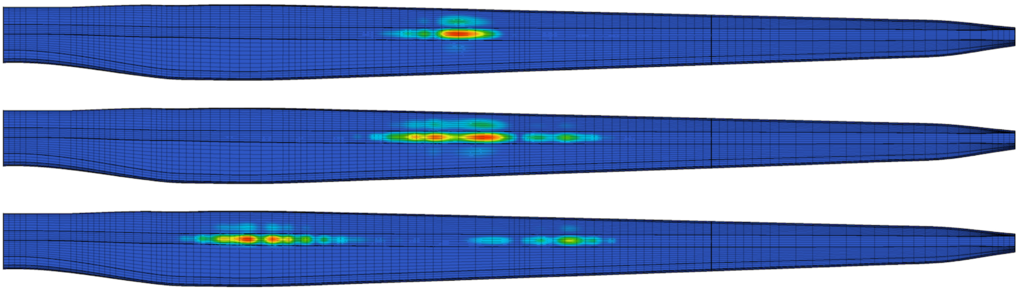

Figure 36: First (top), second (middle), and third (bottom) buckling modes of the NREL/SNL 5 MW blade using $\alpha = 10^3$. Color contour indicates relative magnitude of deflection in buckling.

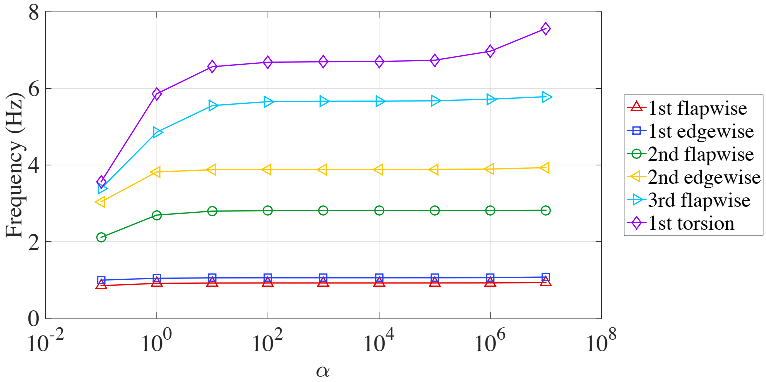

Figure 37: NREL/SNL 5 MW blade frequencies of vibration using the proposed methodology and a range of values of α.

where $\mathbf{K}^{\text{lin}}$ is the linear stiffness matrix of the structure, $\mathbf{M}$ is the mass matrix, and λ_i is the i^{th} eigenvalue associated with mode vector $\mathbf{v}_i$. The relation of the i^{th} frequency of vibration, ω_i, to the eigenvalue is given by the equation $\omega_i^2 = \lambda_i$.

Vibration analysis results using a range of α values are shown in Figure 37. Again, consistent behavior is seen over a range of values of α with $\alpha = 10^3$ remaining appropriate. Because vibration analysis is not load-dependent, the results can also be reasonably compared to the results found in Resor [38]. Although the model developed by Resor [38] does not evaluate the material thickness distributions the same way as the IGA-based framework—that is, material thicknesses aren't evaluated at every quadrature point, leading to a less smooth distribution overall—the comparison in Table 1 demonstrates good agreement overall.

Mode	Ref. Frequency (Hz)	IGA Frequency (Hz)	Difference (%)
1st flapwise	0.87	0.919	5.63
1st edgewise	1.06	1.054	0.57
2nd flapwise	2.68	2.809	4.81
2nd edgewise	3.91	3.886	0.61
3rd flapwise	5.57	5.666	1.72
1st torsion	6.45	6.698	3.84

Table 1: Comparison of vibration analysis results between the reference [38] and the proposed IGA-based method with $\alpha = 10^3$.

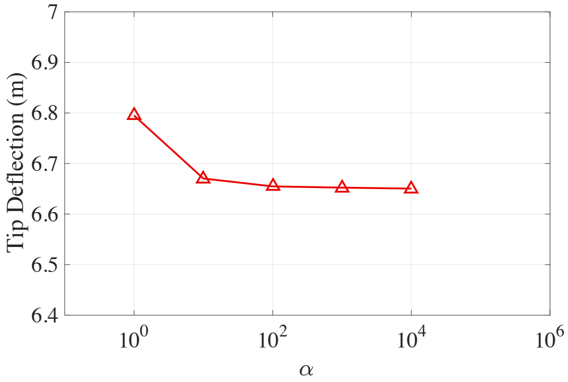

Figure 38: Maximum flapwise tip deflection due to nonlinear analysis for a range of values for α.

4.4. Nonlinear deflection analysis

Maximum blade tip deflection is yet another important consideration in wind turbine blade design, especially as longer and more flexible blades are developed. Care must be taken to ensure that there is appropriate clearance between the rotor and the tower. The same loads that are used in Section 4.2 are applied and nonlinear deformation analysis is performed for a range of α values, as shown in Figure 38.

Because a large number of penalty curves and a variable composite material definition are used, nonlinear convergence is more difficult to achieve for excessively large values of α. Still, a consistent value for tip deflection can be seen from approximately $\alpha = 10^2$ to $\alpha = 10^4$. From $\alpha = 10^2$ to $\alpha = 10^3$, a change in tip deflection of only 0.037% is observed. Similarly, from $\alpha = 10^3$ to $\alpha = 10^4$, a change in tip deflection of 0.029% is observed. This reinforces the validity of using $\alpha = 10^3$ in general and indicates that the proposed method is appropriate for nonlinear analysis of structures featuring material stiffness discontinuities at patch-coupling interfaces. Finally, the nonlinear deformation of the NREL/SNL 5 MW blade using $\alpha = 10^3$ is shown in Figure 39.

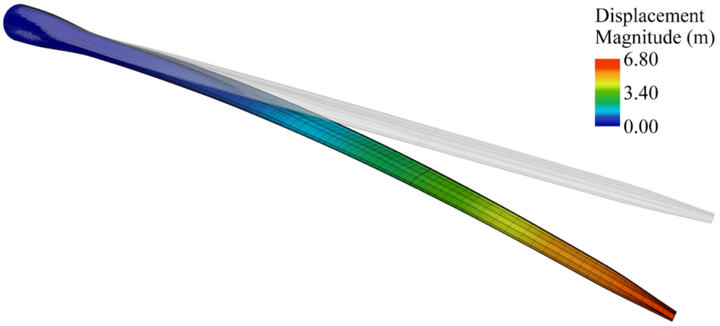

Figure 39: Deformation of the NREL/SNL 5 MW blade due to nonlinear analysis using $\alpha = 10^3$.

5. Conclusion

A new approach for penalty coupling of NURBS patches with non-matching interfaces is proposed. The proposed penalty parameters are dimensionally consistent and the choice of the penalty coefficient is problem-independent. The formulations are based on local stiffness properties and are stated for isotropic and composite configurations, as well as for the unique case of composite configurations with stiffness discontinuities at the coupling interface.

The proposed patch coupling approach is demonstrated on a number of benchmark problems from the literature. For all problems, accurate kinematic performance is observed for a relatively consistent range of penalty coefficient values. As a result, it is suggested that a dimensionless value of $\alpha = 10^3$ be used regardless of problem type or configuration. Through the benchmark problems, the method is shown to be useful for linear, nonlinear, and buckling analyses, for both matching and non-matching discretizations, and for problems involving both isotropic and composite materials.

In order to demonstrate the utility of the proposed approach for complex, large-scale industrial problems, the penalty coupling methodology is applied to the NREL/SNL 5 MW wind turbine blade, a realistic blade model with spanwise- and chordwise-variant composite material definitions. Patch boundaries are used to capture sharp material discontinuities; the blade is therefore modeled using 27 NURBS patches and 51 penalty coupling curves. Because it has a composite definition with a number of material stiffness discontinuities, this example is used to confirm the good performance of the proposed penalty parameter formulations relative to some alternative formulations. Buckling, vibration, and deformation analyses are performed. Using $\alpha = 10^3$, analysis results that are reasonably consistent with the reference results are obtained. Thus, the proposed patch coupling approach has great potential for addressing a wide variety of multi-patch shell analysis problems.

As previously mentioned, one potentially fruitful future use of this methodology would be to use the it in the context of trimmed NURBS geometries. For complex geometries, patch intersections are commonly used to trim NURBS patches. In the analysis setting, these interfaces are often considered to be rigidly coupled. Hence, the proposed penalty methodology could be applied to such trimming curves, which are defined in the parametric space of the NURBS surfaces. Of course, some other approach, such as adaptive refinement, would have to be employed to accommodate proper treatment of the trimmed portions of the NURBS surfaces.

Finally, although only linear elastic material behavior is considered in this work, we believe the proposed penalty formulations can be readily extended to nonlinear materials. This will also be investigated in the future.

Acknowledgments

A.J. Herrema and E.L. Johnson were supported by the U.S. National Science Foundation (NSF) Grant No. DGE-1069283 which funds the activities of the Integrative Graduate Education and Research Traineeship (IGERT) in Wind Energy Science, Engineering, and Policy (WESEP) at Iowa State University. J. Kiendl was partially supported by the Onsager fellowship program of the Norwegian University of Science and Technology. This support is gratefully acknowledged.

References

[1] Y. Bazilevs, V.M. Calo, J.A. Cottrell, J.A. Evans, T.J.R. Hughes, S. Lipton, M.A. Scott, and T.W. Sederberg. Isogeometric analysis using T-splines. *Computer Methods in Applied Mechanics and Engineering*, 199:229–263, 2010.

[2] T.J.R. Hughes, J.A. Cottrell, and Y. Bazilevs. Isogeometric analysis: CAD, finite elements, NURBS, exact geometry and mesh refinement. *Computer Methods in Applied Mechanics and Engineering*, 194:4135–4195, 2005.

[3] J. Kiendl, K.-U. Bletzinger, J. Linhard, and R. Wüchner. Isogeometric shell analysis with Kirchhoff–Love elements. *Computer Methods in Applied Mechanics and Engineering*, 198: 3902–3914, 2009.

[4] D.J. Benson, Y. Bazilevs, M.-C. Hsu, and T.J.R. Hughes. A large deformation, rotation-free, isogeometric shell. *Computer Methods in Applied Mechanics and Engineering*, 200: 1367–1378, 2011.

[5] N. Nguyen-Thanh, J. Kiendl, H. Nguyen-Xuan, R. Wüchner, K.-U. Bletzinger, Y. Bazilevs, and T. Rabczuk. Rotation free isogeometric thin shell analysis using PHT-splines. *Computer Methods in Applied Mechanics and Engineering*, 200(47-48):3410–3424, 2011.

[6] J. Kiendl, M.-C. Hsu, M.C.H. Wu, and A. Reali. Isogeometric Kirchhoff–Love shell formulations for general hyperelastic materials. *Computer Methods in Applied Mechanics and Engineering*, 291:280–303, 2015.

[7] A. Buganza Tepole, H. Kabaria, K.-U. Bletzinger, and E. Kuhl. Isogeometric Kirchhoff–Love shell formulations for biological membranes. *Computer Methods in Applied Mechanics and Engineering*, 293:328–347, 2015.

[8] M. Bischoff, W.A. Wall, K.-U. Bletzinger, and E. Ramm. Models and finite elements for thin-walled structures. In E. Stein, R. de Borst, and T.J.R. Hughes, editors, *Encyclopedia of Computational Mechanics*, Volume 3: Solids and Structures, chapter 3. John Wiley & Sons, 2004.

[9] J. Kiendl, Y. Bazilevs, M.-C. Hsu, R. Wüchner, and K.-U. Bletzinger. The bending strip method for isogeometric analysis of Kirchhoff–Love shell structures comprised of multiple patches. *Computer Methods in Applied Mechanics and Engineering*, 199:2403–2416, 2010.

[10] A. Goyal and B. Simeon. On penalty-free formulations for multipatch isogeometric kirchhoff–love shells. *Mathematics and Computers in Simulation*, 136:78–103, 2017.

[11] Z. Lei, F. Gillot, and L. Jezequel. A C^0/G^1 multiple patches connection method in isogeometric analysis. *Applied Mathematical Modelling*, 39(15):4405–4420, 2015.

[12] M. Breitenberger, A. Apostolatos, B. Philipp, R. Wüchner, and K.-U. Bletzinger. Analysis in computer aided design: Nonlinear isogeometric B-Rep analysis of shell structures. *Computer Methods in Applied Mechanics and Engineering*, 284:401–457, 2015.

[13] T.X. Duong, F. Roohbakhshan, and R.A. Sauer. A new rotation-free isogeometric thin shell formulation and a corresponding continuity constraint for patch boundaries. *Computer Methods in Applied Mechanics and Engineering*, 316:43–83, 2017.

[14] W. Dornisch, G. Vitucci, and S. Klinkel. The weak substitution method - an application of the mortar method for patch coupling in NURBS-based isogeometric analysis. *International Journal for Numerical Methods in Engineering*, 103(3):205–234, 2015.

[15] E. Brivadis, A. Buffa, B. Wohlmuth, and L. Wunderlich. Isogeometric mortar methods. *Computer Methods in Applied Mechanics and Engineering*, 284:292–319, 2015.

[16] Y. Guo and M. Ruess. Nitsche's method for a coupling of isogeometric thin shells and blended shell structures. *Computer Methods in Applied Mechanics and Engineering*, 284:881–905, 2015.

[17] Y. Guo, J. Heller, T.J.R. Hughes, M. Ruess, and D. Schillinger. Variationally consistent iso-

geometric analysis of trimmed thin shells at finite deformations, based on the STEP exchange format. *Computer Methods in Applied Mechanics and Engineering*, 336:39–79, 2018.

[18] N. Nguyen-Thanh, K. Zhou, X. Zhuang, P. Areias, H. Nguyen-Xuan, Y. Bazilevs, and T. Rabczuk. Isogeometric analysis of large-deformation thin shells using RHT-splines for multiple-patch coupling. *Computer Methods in Applied Mechanics and Engineering*, 316: 1157–1178, 2017.

[19] L. Coox, F. Greco, O. Atak, D. Vandepitte, and W. Desmet. A robust patch coupling method for NURBS-based isogeometric analysis of non-conforming multipatch surfaces. *Computer Methods in Applied Mechanics and Engineering*, 316:235–260, 2017.

[20] Y. Bazilevs, M.-C. Hsu, J. Kiendl, R. Wüchner, and K.-U. Bletzinger. 3D simulation of wind turbine rotors at full scale. Part II: Fluid–structure interaction modeling with composite blades. *International Journal for Numerical Methods in Fluids*, 65:236–253, 2011.

[21] J.N. Reddy. *Mechanics of Laminated Composite Plates and Shells: Theory and Analysis, 2nd ed.* CRC Press, Boca Raton, FL, 2004.

[22] J. Kiendl. *Isogeometric Analysis and Shape Optimal Design of Shell Structures*. PhD thesis, Lehrstuhl für Statik, Technische Universität München, 2011.

[23] Y. Bazilevs, M.-C. Hsu, and M.A. Scott. Isogeometric fluid–structure interaction analysis with emphasis on non-matching discretizations, and with application to wind turbines. *Computer Methods in Applied Mechanics and Engineering*, 249–252:28–41, 2012.

[24] V. Hernandez, J.E. Roman, and V. Vidal. SLEPc: A scalable and flexible toolkit for the solution of eigenvalue problems. *ACM Trans. Math. Software*, 31(3):351–362, 2005.

[25] J.E. Roman, C. Campos, E. Romero, and A. Tomas. SLEPc users manual. Technical Report DSIC-II/24/02 - Revision 3.7, D. Sistemes Informàtics i Computació, Universitat Politècnica de València, Valencia, Spain, 2016.

[26] M.A. Crisfield. A fast incremental/iterative solution procedure that handles “snap-through”. *Computers & Structures*, 13(1–3):55–62, 1981.

[27] T. Belytschko, H. Stolarski, W.K. Liu, N. Carpenter, and J.S.-J. Ong. Stress projection for membrane and shear locking in shell finite elements. *Computer Methods in Applied Mechanics and Engineering*, 51:221–258, 1985.

[28] S. Timoshenko and S. Woinowsky-Krieger. *Theory of Plates and Shells (Engineering Societies Monograph), 2nd ed.* McGraw-Hill, 1959.

[29] K.Y. Sze, X.H. Liu, and S.H. Lo. Popular benchmark problems for geometric nonlinear

analysis of shells. *Finite Elements in Analysis and Design*, 40:1551–1569, 2004.

[30] M. Smith. *ABAQUS/Standard User's Manual, Version 6.9*. Simulia, 2009.

[31] A. Korobenko, M.-C. Hsu, I. Akkerman, J. Tippmann, and Y. Bazilevs. Structural mechanics modeling and FSI simulation of wind turbines. *Mathematical Models and Methods in Applied Sciences*, 23(2):249–272, 2013.

[32] Y. Bazilevs, A. Korobenko, X. Deng, and J. Yan. Novel structural modeling and mesh moving techniques for advanced fluid-structure interaction simulation of wind turbines. *International Journal for Numerical Methods in Engineering*, 102(3-4):766–783, 2014.

[33] M.-C. Hsu and Y. Bazilevs. Fluid–structure interaction modeling of wind turbines: simulating the full machine. *Computational Mechanics*, 50:821–833, 2012.

[34] J. Yan, A. Korobenko, X. Deng, and Y. Bazilevs. Computational free-surface fluid–structure interaction with application to floating offshore wind turbines. *Computers & Fluids*, 141: 155–174, 2016.

[35] Y. Bazilevs, A. Korobenko, X. Deng, and J. Yan. Fluid–structure interaction modeling for fatigue-damage prediction in full-scale wind turbine blades. *Journal of Applied Mechanics*, 83:061010–061010–9, 2016.

[36] M.-C. Hsu, C. Wang, A.J. Herrema, D. Schillinger, A. Ghoshal, and Y. Bazilevs. An interactive geometry modeling and parametric design platform for isogeometric analysis. *Computers and Mathematics with Applications*, 70:1481–1500, 2015.

[37] A.J. Herrema, N.M. Wiese, C.N. Darling, B. Ganapathysubramanian, A. Krishnamurthy, and M.-C. Hsu. A framework for parametric design optimization using isogeometric analysis. *Computer Methods in Applied Mechanics and Engineering*, 316:944–965, 2016.

[38] B.R. Resor. Definition of a 5MW/61.5m wind turbine blade reference model. Technical Report SAND2013-2569, Sandia National Laboratories, Albuquerque, NM, 2013.

[39] J. Jonkman, S. Butterfield, W. Musial, and G. Scott. Definition of a 5-MW reference wind turbine for offshore system development. Technical Report NREL/TP-500-38060, National Renewable Energy Laboratory, Golden, CO, 2009.

[40] J.M. Jonkman and M.L. Buhl Jr. FAST user's guide. Technical Report NREL/EL-500-38230, National Renewable Energy Laboratory, Golden, CO, 2005.

[41] Wind turbines–Part 1: Design requirements. Technical Report IEC 61400-1, International Electrotechnical Commission, Geneva, Switzerland, 2005.

A.2 Paper 2

Davide Proserpio, Josef Kiendl, Marreddy Ambati, Laura De Lorenzis, Kjetil André Johannessen, Trond Kvamsdal

Simulation of brittle fracture in shells using a phase-field approach and LR B-splines

7th GACM Colloquium on Computational Mechanics for Young Scientists from Academia and Industry, Stuttgart, 2017

Proceedings of the 7th GACM Colloquium on Computational Mechanics
for Young Scientists from Academia and Industry
October 11-13, 2017 in Stuttgart, Germany

Simulation of brittle fracture in shells using a phase-field approach and LR B-splines

Davide Proserpio[1]*, Josef Kiendl[1], Marreddy Ambati[2], Laura De Lorenzis[2], Kjetil André Johannessen[3] and Trond Kvamsdal[3]

Micro Abstract
We present a phase-field approach to model brittle fracture in plates and shells. For structural analysis, the discretization of the geometry is performed using an isogeometric Kirchhoff-Love shell formulation, extended to local refinement with LR B-splines in order to properly resolve the mesh in the cracked regions, improving the accuracy and efficiency of the analysis.

[1]Department of Marine Technology, Norwegian University of Science and Technology, Trondheim, Norway
[2]Institute of Applied Mechanics, Technical University of Braunschweig, Braunschweig, Germany
[3]Department of Mathematical Sciences, Norwegian University of Science and Technology, Trondheim, Norway
***Corresponding author**: davide.proserpio@ntnu.no

Introduction

The simulation of fracture of structural members plays an important role in many engineering applications, both at the design step and during inspections of in-service structures. In this contribution we focus on thin parts like plates and shells.

The structural model employs Isogeometric Analysis (IGA), a very promising technique introduced by Huges et al. [3]. This method uses Non Rational B-Splines (NURBS) for the description of the geometry, as CAD commercial programs do, making the approach very favourable because meshing of the model for the structural analysis is not required. The smoothness of the basis functions and the continuity across the element boundaries make the implementation of a rotation-free isogeometric Kirchhoff-Love formulation for shell elements highly favourable [7].

In the last years, the phase-field approach for the description of brittle fracture has been developed. With this method, it is possible to approximate sharp cracks with a continuous field in which the discontinuity is represented by a smeared transition of the parameter between the values referred to broken and unbroken material.

The phase field approach to brittle fracture was recently coupled with the isogeometric rotation-free formulation for plates and shells by Kiendl et al. [6]. In order to properly resolve the phase field in the cracked regions, fine meshes are required. Due to the tensor product properties of NURBS, local refinement of the mesh is not possible in traditional Isogeometric Analysis. In order to improve the efficiency of the analyses in terms of computational costs, we employed local refinement (LR) of the mesh using B-splines as basis functions, as described by Johannessen et al. [5].

1 Modelling and implementation aspects

The model used for the analyses employs a discretization of the geometry using an isogeometric Kirchhoff-Love shell formulation [7] with LR B-splines [5]. For the characterization of brittle fracture, we follow a variational formulation with the phase field discretized by the same basis functions as the geometry, assuming geometrical linearity (small strains and small deformations).

1.1 Phase field formulation of fracture for shells

The evolution of the crack is controlled by the minimization of the functional of the free energy over the body, as defined by Francfort and Marigo [4]:

$$E(\boldsymbol{\varepsilon},\Gamma)=\int_\Omega \psi_e(\boldsymbol{\varepsilon})d\Omega+\int_\Omega \psi_s(s,\nabla s)d\Omega \tag{1}$$

where the first integral expresses the elastic strain energy. The second one computes the fracture energy by approximating and replacing the traditional integration computed over the set of crack surfaces [2]. In the adopted formulation, the fracture energy density $\psi_s(s,\nabla s)$ depends on the phase field parameter s:

$$\psi_s(s,\nabla s)=G_c\left(\frac{1}{4\ell_0}(1-s)^2+\ell_0|\nabla s|^2\right) \tag{2}$$

in which G_c is the fracture toughness of the material. The approximation of the crack topology by the continuous field s is governed by the length scale parameter ℓ_0 that defines the amount of smearing of the phase field around the fracture surface. For $\ell_0 \to 0$, the solution converges to sharp crack topology and Griffith's linear elastic fracture mechanics solution [8]. Other than being a regularization parameter for the model, ℓ_0 depends also on the properties of the considered material, in particular the fracture stress/strain and the fracture toughness [1]. Thus, the choice of the length scale parameter is crucial for the simulation. The mesh of the model has to be sufficiently fine in the crack region in order to resolve ℓ_0, so a reduced size of the elements is often required in this area.

The strain tensor $\boldsymbol{\varepsilon}$ can be split into its tensile and compressive contribution. This is required for a correct characterization of the fracture process, preventing cracking to occur in compression.

$$\boldsymbol{\varepsilon}=\boldsymbol{\varepsilon}^+ +\boldsymbol{\varepsilon}^-. \tag{3}$$

Consequently, also the strain energy density and the stress tensor can be split in the same components. Characterization of the fracture occurs by degradating the tensile terms according to a degradation function:

$$g(s)=(1-\eta)\,s^2+\eta, \tag{4}$$

where $0<\eta\ll 1$ for numerical stability of the model in fully cracked situation.

The strong form of the problem is so obtained as momentum and phase field equations:

$$\operatorname{div}\boldsymbol{\sigma}=\mathbf{0}, \tag{5}$$

$$\left(\frac{4\,\ell_0(1-\eta)\psi_e^+}{G_c}+1\right)\,s-4\,\ell_0^2\Delta s=1. \tag{6}$$

Irreversibly of the cracking process is guaranteed by replacing ψ_e^+ whit the so-called history field $\mathcal{H}$, which expresses the maximum of the positive strain energy density over time [8].

In the rotation-free shell formulation a curvilinear coordinate system is used, with θ^1,θ^2 referring to the midsurface, and θ^3 to the thickness direction. At any point of the shell continuum, the two-dimensional strain tensor can be retrieved by:

$$\boldsymbol{\varepsilon}(\theta^3)=\boldsymbol{\varepsilon}^m+\theta^3\boldsymbol{\kappa}. \tag{7}$$

For determining this quantity, membrane strains $\boldsymbol{\varepsilon}^m$ and curvature changes $\boldsymbol{\kappa}$ are required, which depend only on the midsurface displacement field. The stress tensor ($\boldsymbol{\sigma}(\boldsymbol{\varepsilon})$) and strain energy density ($\psi_e(\boldsymbol{\varepsilon})$) can be obtained from the strain tensor applying linear elasticity, under the assumption of plane stress.

In the adopted shell formulation, the split of the strain energy surface density (strain energy per unit area of the midsurface) is performed by integrating along the thickness:

$$\Psi_e^{\pm}=\int_{-h/2}^{h/2}\psi_e^{\pm}(\theta^3)d\theta^3. \tag{8}$$

The integral is computed numerically and, at every thickness integration point, the strain tensor is decomposed into compressive and tensile components, in order to degradate the positive component according to $g(s)$ [6]. The energy functional from Equation 1 is so computed, integrating over the shell midsurface:

$$E_{\ell_0}(\boldsymbol{\varepsilon}^m, \boldsymbol{\kappa}, s) = \int_A \big(g(s)\,\Psi_e^+(\boldsymbol{\varepsilon}^m, \boldsymbol{\kappa}) + \Psi_e^-(\boldsymbol{\varepsilon}^m, \boldsymbol{\kappa}) + \Psi_s(s, \nabla s)\big)\, dA. \tag{9}$$

1.2 Local Refinement of B-splines

By the traditional NURBS (Non Uniform Rational B-Splines) discretization, surfaces can be modelled using two parameters (ξ, η), two sets of knot vectors ($\Xi = \{\xi_1, \xi_2, ..., \xi_{n+p+1}\}$ and $\mathcal{H} = \{\eta_1, \eta_2, ..., \eta_{m+q+1}\}$) and a net of control points $\boldsymbol{P}_{i,j}$, as a tensor product of unidimensional B-splines base functions ($N_{i,p}$ and $M_{j,q}$) of degree $p,\ q$:

$$\boldsymbol{S}(\xi, \eta) = \sum_{i=1}^{n}\sum_{j=1}^{m} N_{i,p} M_{j,q} \boldsymbol{P}_{i,j}. \tag{10}$$

The global knot vector net of lines defines the so-called mesh of the geometry. The tensor product property of traditional B-Splines surfaces allows only a global refinement of the geometry by knot insertion. This means that, if a finer mesh is required only in one part of the patch, the refinement will affect all the geometry and the number of elements will increase considerably, causing an high usage of computational resources (Figure 1b).

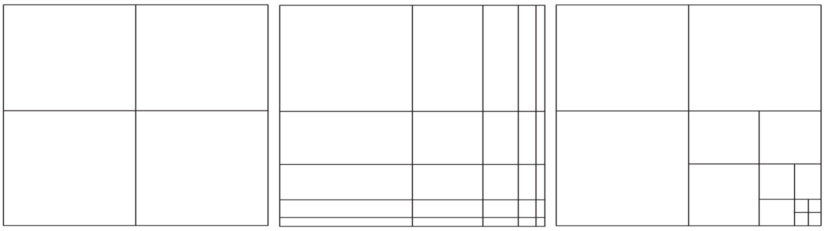

(a) Initial mesh **(b)** Tensor product refinement **(c)** Truly local refinement

Figure 1. Lack of local refinement of tensor B-splines [5]

Employing the approach of Johannessen et al. [5], we switch to a formulation in which "weighted" B-splines are taken as base functions. The ith weighted B-Spline for surface geometries is defined as the product of two univariate B-splines $B_{p,\Xi_i}(\xi), B_{q,\mathcal{H}_i}(\eta)$ of degree p, q :

$$\boldsymbol{B}^{\gamma}_{\boldsymbol{\Xi}i} = \gamma_i B_{p,\Xi_i}(\xi) B_{q,\mathcal{H}_i}(\eta). \tag{11}$$

The univariate local knot vectors $\Xi_i, \mathcal{H}_i$ define the local knot vector $\boldsymbol{\Xi}_i$ on which the B-spline has support. The scalar weight γ simply multiplies the B-splines and it is used for maintaining the partition of unity property during the splitting procedure.

After defining the weighted B-splines, that can be considered as the base functions of the geometry, a LR surface object (referring to the midsurface of the analysed shell) can be expressed as the linear combination of weighted B-Splines and control points:

$$\boldsymbol{S}(\xi, \eta) = \sum_{i=1}^{n} \boldsymbol{B}^{\gamma}_{\boldsymbol{\Xi}i} \boldsymbol{P}_i, \tag{12}$$

in which n is the number of control points, corresponding with the number of B-Splines. It is important to note that, with this definition, there is only one global index i running over the base functions, excluding the global product properties (that are instead maintained only at level of the single B-spline). This is extremely useful for allowing the local refinement of the mesh.

Without entering into the details of the algorithm, a weighted B-spline can be split into two new base functions, generating each a new couple of control points and weights (in order to maintain partition of unity) that will replace the precedent structure. The splitting procedure is performed inserting a line that completely traverses the local knot vector of the original B-spline, dividing in two halves the crossed elements, in order to generate new local knot vectors. The application of this procedure allows the local refinement of the mesh (as for example in Figure 1c).

2 Numerical example: simply supported plate

Some potentialities of the LR B-splines and the phase field approach for shells are shown in the numerical example below. A square plate (size=2×2 mm, thickness=0.02 mm), simply supported at all the four sides, is subjected to an uniform transversal pressure. Material parameters are: $E = 190 \times 10^3$ N/mm^2, $\nu = 0.29$, $G_c = 0.295$ N/mm and $\ell_0 = 0.02$mm. The crack is expected to initiate in the plate centre and than to branch and propagate towards the corners, so the local refinement of the mesh was performed in these regions. Full span strategy for local refinement was used (meaning that, once an element is selected for being split, all the base functions supported by the element are split), in order to obtain a larger footprint of the refinement and a more regular grid.

The simulation was run with arc-length control method until failure. For solving the coupled problem, we employ a staggered approach in which, for every time step, the weak forms of the phase field and the momentum equation are solved.

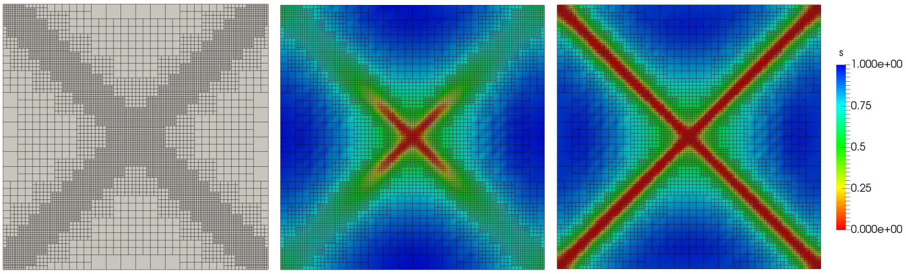

(a) **(b)** **(c)**

Figure 2. Plate model: locally refined mesh and phase field evolution

Figure 2 shows the LR B-splines mesh and the crack evolution by the phase field, where $s = 1$ indicates undamaged and null value refers to fully cracked material. For the complete model, 8640 elements are used and the minimum size in the refined region is 0.0139 mm. The same numerical test was previously run with a uniformly refined NURBS grid that consisted of 7225 elements, for modelling one quarter of the plate, and a constant element size of 0.0117 mm [6]. The load-displacement curve obtained using the LR B-splines mesh is shown in Figure 3. The pressure required for the failure of the plate is in agreement with the results reported in [6].

Conclusions

A phase-field approach for modelling brittle fracture in plates and shells, discretized by using an isogeometric Kirchhoff-Love element formulation, was presented. The implementation of LR B-splines is a tool that allows the refinement of the mesh in the cracked regions, improving the accuracy and efficiency of the analysis by reducing the total number of elements needed. Good agreement was found with results already obtained using NURBS on equivalent experiment.

Further work will include an extension of the model towards adaptive local refinement of the mesh, in order to be able to describe crack patterns not known in advance.

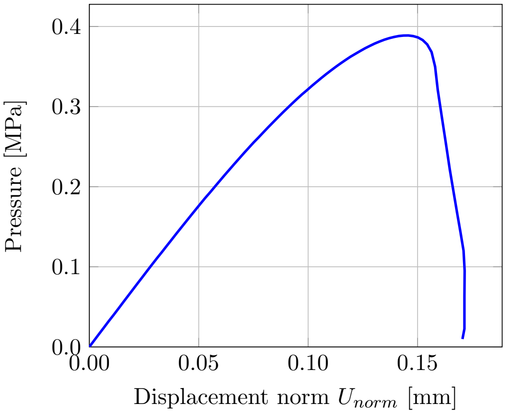

Figure 3. Plate model: load-displacement curve

References

[1] M. J. Borden, C. V. Verhoosel, M. A. Scott, T. J. Hughes, and C. M. Landis. A phase-field description of dynamic brittle fracture. *Computer Methods in Applied Mechanics and Engineering*, 217:77–95, 2012.

[2] B. Bourdin, G. A. Francfort, and J.-J. Marigo. Numerical experiments in revisited brittle fracture. *Journal of the Mechanics and Physics of Solids*, 48(4):797–826, 2000.

[3] J. A. Cottrell, T. J. Hughes, and Y. Bazilevs. *Isogeometric analysis: toward integration of CAD and FEA*. John Wiley & Sons, 2009.

[4] G. A. Francfort and J.-J. Marigo. Revisiting brittle fracture as an energy minimization problem. *Journal of the Mechanics and Physics of Solids*, 46(8):1319–1342, 1998.

[5] K. A. Johannessen, T. Kvamsdal, and T. Dokken. Isogeometric analysis using lr b-splines. *Computer Methods in Applied Mechanics and Engineering*, 269:471–514, 2014.

[6] J. Kiendl, M. Ambati, L. De Lorenzis, H. Gomez, and A. Reali. Phase-field description of brittle fracture in plates and shells. *Computer Methods in Applied Mechanics and Engineering*, 312:374–394, 2016.

[7] J. Kiendl, K.-U. Bletzinger, J. Linhard, and R. Wüchner. Isogeometric shell analysis with kirchhoff–love elements. *Computer Methods in Applied Mechanics and Engineering*, 198(49):3902–3914, 2009.

[8] C. Miehe, M. Hofacker, and F. Welschinger. A phase field model for rate-independent crack propagation: Robust algorithmic implementation based on operator splits. *Computer Methods in Applied Mechanics and Engineering*, 199(45):2765–2778, 2010.

Figure 1 reproduced from Computer Methods in Applied Mechanics and Engineering, Vol. 269, Johannessen, K. A. and Kvamsdal, T. and Dokken, T., Isogeometric analysis using LR B-splines, Pages 471-514, Copyright (2014), with permission from Elsevier.

A.3 Paper 3

Davide Proserpio, Marreddy Ambati, Laura De Lorenzis, Josef Kiendl

A framework for efficient isogeometric computations of phase-field brittle fracture in multipatch shell structures

Computer Methods in Applied Mechanics and Engineering, 2020; 372, (113363)

ELSEVIER

Available online at www.sciencedirect.com
ScienceDirect

Comput. Methods Appl. Mech. Engrg. 372 (2020) 113363

Computer methods in applied mechanics and engineering

www.elsevier.com/locate/cma

A framework for efficient isogeometric computations of phase-field brittle fracture in multipatch shell structures

Davide Proserpio[a,*], Marreddy Ambati[b], Laura De Lorenzis[c], Josef Kiendl[d,a]

[a] *Department of Marine Technology – Norwegian University of Science and Technology, Otto Nielsens veg 10, 7052 Trondheim, Norway*
[b] *Institute of Solid Mechanics – TU Dresden, George-Bähr-Straße 3c, 01069 Dresden, Germany*
[c] *Department of Mechanical and Process Engineering – ETH Zürich, Tannenstraße 3, 8092 Zürich, Switzerland*
[d] *Institute of Engineering Mechanics and Structural Analysis – Bundeswehr University Munich, Werner-Heisenberg-Weg 39, 85577 Neubiberg, Germany*

Received 4 March 2020; accepted 3 August 2020
Available online 24 August 2020

Abstract

We present a computational framework for applying the phase-field approach to brittle fracture efficiently to complex shell structures. The momentum and phase-field equations are solved in a staggered scheme using isogeometric Kirchhoff–Love shell analysis for the structural part and isogeometric second- and fourth-order phase-field formulations for the brittle fracture part. For the application to complex multipatch structures, we propose penalty formulations for imposing all the required interface constraints, i.e., displacement (C^0) and rotational (C^1) continuity for the structure as well as C^0 and C^1 continuity for the phase field, where the latter is required only in the case of the fourth-order phase-field model. All involved penalty terms are scaled with the corresponding problem parameters to ensure a consistent scaling of the penalty contributions to the global system of equations. As a consequence, all coupling terms are controlled by one global penalty parameter, which can be set to 10^3 independent of the problem parameters. Furthermore, we present a multistep predictor–corrector algorithm for adaptive local refinement with LR NURBS, which can accurately predict and refine the region around the crack even in cases where fracture fully develops in a single load step, such that rather coarse initial meshes can be used, which is essential especially for the application to large structures. Finally, we investigate and compare the numerical efficiency of loosely vs. strongly staggered solution schemes and of the second- vs. fourth-order phase-field models.

Keywords: Phase-field model; Brittle fracture; Adaptive refinement; Isogeometric; Shell; Multipatch

---

1. Introduction

The modeling and simulation of crack initiation and propagation for structural members is a challenging research topic of high industrial relevance, as it has applications both during the design process and for the inspection and maintenance of in-service structures. The phase-field approach has emerged, in the last two decades, as a promising approach for the modeling and computation of fracture. The approach consists in the approximation of sharp cracks by a continuous field called phase-field, which allows for the description of arbitrarily complex crack

---

[*] Corresponding author.
E-mail address: davide.proserpio@ntnu.no (D. Proserpio).

https://doi.org/10.1016/j.cma.2020.113363

patterns. Initially proposed for brittle fracture, the method is based on the variational formulation by Francfort and Marigo [1] of Griffith's theory [2], later regularized by Bourdin et al. [3]. Phase-field fracture models may also be categorized as gradient damage models [4,5], which can recover Griffith's solution through Γ-convergence [6]. A variety of contributions to the original phase-field fracture formulation have been proposed. A fundamental aspect is here the split of the elastic strain energy into "active" and "inactive" (often called "positive" and "negative" or "tension" and "compression") parts to avoid fracture developing under compression, for which different approaches have been proposed. Miehe et al. [7] proposed a split based on the spectral decomposition of the strain tensor, Amor et al. [8] a split based on volumetric and deviatoric parts of the strain tensor. An alternative split based on the symmetric and antisymmetric parts of the strain tensor was proposed by Freddi et al. [9], while Steinke and Kaliske [10] introduced a decomposition of the stress tensor with respect to the crack orientation. Besides the mostly used quadratic degradation function, Borden [11] and Kuhn et al. [12] studied the effects of cubic and higher-order degradation functions. Another fundamental aspect is fracture irreversibility, which was introduced by Miehe et al. [7] through a history field, which corresponds to the maximum of the positive part of the strain energy density, while Gerasimov and De Lorenzis [13] ensure irreversibility through a penalty method. The phase-field approach has been successfully applied to the description of brittle fracture [7,8,14,15], ductile fracture [16–19], dynamic fracture [20–22], fracture in anisotropic media [23,24], and to the description of fatigue failure [25–28] among many others. Various works have been devoted to the validation of the numerical simulations through experiments [29–33]. Phase-field formulations for fracture have been discretized with standard finite elements as well as isogeometric analysis (IGA). Borden et al. [34] were the first to exploit the continuity properties of isogeometric discretizations in this context and proposed a higher-order phase-field formulation for fracture. Furthermore, phase-field formulations have also been successfully implemented in the commercial finite element software Abaqus [35–38].

For modeling fracture in thin-walled structures, various approaches have been presented for coupling phase-field models with plate and shell formulations. Solid-shell elements were adopted by Ambati et al. [39], who used through-thickness isogeometric discretization of phase-field and displacement field, and Reinoso et al. [40], who used, for the phase-field variable, a linear interpolation between the top and bottom surfaces. When adopting reduced-order models in which the kinematics is based on midsurface variables, special attention is required for the varying stress distribution through the shell thickness related to bending. Areias et al. [41] used two different phase-fields for describing fracture at the top and bottom of shell surfaces. Amiri et al. [42] and Ulmer et al. [43] used a single phase-field variable defined over the shell midsurface for describing the fracture behavior. However, in the first contribution, the tension–compression split of the elastic strain energy was not considered, while in the second one the split was applied only to the membrane part of the strain tensor. In the work of Kiendl at al. [44] the tension–compression split, based on the spectral decomposition of the strain tensor, was performed at various points through the thickness and numerical integration of the positive and negative strain energy contributions was performed. Paul et al. [45] used a volumetric/deviatoric strain decomposition and employed thickness integration only for the bending part of the strain energy.

In order to correctly resolve the high gradient transition of the phase field around the cracked area, phase-field models require fine meshes at least in the fracture zone. The use of adaptive mesh refinement has been explored with different approaches. Burke et al. [46], Artina et al. [47] and Del Piero et al. [48] showed that local mesh refinement does not influence the propagation of the crack and has little influence both on the energy curves and on the fracture field, justifying the use of adaptive mesh refinement algorithms for saving computational resources when the fracture path is not known in advance. In the first two works, the refinement was defined by an *a posteriori* error estimate, while the third one used the phase-field value as an indicator for the refinement. The same choice was made by Wick [49] and Heister et al. [50], who focused their attention on a predictor–corrector scheme for the adaptive mesh refinement algorithm, allowing for recomputation of load steps after the refinement. Klinsmann et al. [51] employed an approach for refinement or coarsening of the mesh whose indicator depends on the value of the tension part of the elastic energy, the norm of the phase-field gradient and the element size. Nagaraja et al. [52] used an adaptive multi-level hp-refinement approach.

In the context of IGA, due to the tensor-product structure of NURBS (Non-Uniform Rational B-splines), local refinement is not possible for standard NURBS-based discretizations. Different techniques have been introduced for solving the problem of local refinement, including Hierarchical B-splines [53,54] later developed into Truncated Hierarchical B-splines [55], T-Splines [56,57] and Hierarchical T-splines [58]. Dokken et al. [59] introduced Locally

Refined (LR) B-splines, which have been used in the IGA context by Johannessen et al. [60]. LR B-splines have also been shown to produce better matrices, in terms of sparsity and condition number, with respect to other technologies developed for the local refinement of splines [61]. LR B-splines have been extended to LR NURBS by Zimmerman et al. [62]. Adaptive local refinement with T-splines for phase-field fracture analysis was presented by Borden et al. [21] in a simplified version that involved successive runs of the same analysis with meshes refined according to the result of the previous run, thus avoiding the issue of solution transfer between the meshes. Recently, Paul et al. [45] used LR NURBS adaptive mesh refinement for simulating dynamic phase-field fracture in thin shells. Adaptive refinement using Truncated Hierarchical B-splines and Bézier extraction was presented by Kästner and Hennig et al. [63–65], in addition to the possibility of mesh coarsening. These works include detailed discussions about the transfer of the solution between the meshes, distinguishing between quantities related to control and integration points. If only refinement is employed, IGA leads to an error-free projection regarding control point variables, while for the quantities related to the Gauss points, different strategies can be used.

The aforementioned contributions focused their attention on rather simple geometries that can be simulated using single patch isogeometric models. However, most of real-world industrial structures present such a complexity that multipatch models with non-matching discretizations at patch interfaces are needed. If higher-order formulations are employed, like Kirchhoff–Love shells [44] for the structural part or the fourth-order phase-field formulation [34] for the fracture part, continuity over patch boundaries needs to be ensured for the primal unknowns and their first derivatives, which poses additional challenges.

In this paper, we present an isogeometric approach for the efficient simulation of brittle fracture in complex multipatch shell structures, using Kirchhoff–Love shells coupled with second- and fourth-order phase-field formulations. In particular, we present an algorithm for adaptive local refinement, which is crucial for efficient phase-field fracture simulations, especially when applied to large structures. We propose a multistep predictor–corrector algorithm for adaptive refinement with LR NURBS, which can accurately predict and refine the region around the crack even in cases where fracture fully develops in a single load step. Furthermore, we present patch coupling formulations for multipatch structures with non-matching meshes. We propose a penalty approach for both structural and phase-field coupling, considering both C^0 and C^1 continuity. The different penalty contributions involved are scaled with the corresponding problem parameters, such that all coupling terms can be controlled by one global penalty parameter, which can be chosen in a problem-independent fashion. This leads to a robust and accurate framework for fracture simulations on complex multipatch structures. Finally, for optimizing the efficiency of the simulations, we investigate and compare the computational cost of loosely vs. strongly coupled staggering strategies and of second- vs. fourth-order phase-field formulations.

The paper is structured as follows. Section 2 reviews the phase-field formulation for brittle fracture and how it is coupled with an isogeometric rotation-free Kirchhoff–Love shell formulation, including the discretization with LR NURBS and the penalty coupling for the extension to multipatch structures. Section 3 contains the details regarding the solution algorithm, with a focus on the adaptive mesh refinement procedure and on the used staggering scheme. The applicability and efficiency of the proposed approach are tested through several numerical experiments in Section 4, ranging from standard fracture benchmarks to complex multipatch problems. Finally, conclusions are drawn in Section 5.

2. Formulation

2.1. Phase-field model of brittle fracture for shell structures

This section briefly presents the main features of the phase-field approach for modeling brittle fracture and how this formulation can be coupled with plate and shell models, with a focus on Kirchhoff–Love shells which are considered in this contribution.

According to Griffith's theory [2], the equilibrium of a crack is controlled by a potential energy term and a term related to the work required for creating new surfaces. The same two terms are present in the variational formulation of brittle fracture by Franfort and Marigo [1], in which the entire cracking process is described by the minimization of the energy functional

$$E(\boldsymbol{\varepsilon}, \Gamma) = \int_{\Omega \setminus \Gamma} \psi_e(\boldsymbol{\varepsilon}) d\Omega + G_c \int_{\Gamma} d\Gamma. \tag{1}$$

The elastic strain energy is computed by integrating its density ψ_e, which directly depends on the strain tensor $\boldsymbol{\varepsilon}$, over the domain $\Omega \setminus \Gamma$, while the crack energy surface term includes the material fracture toughness G_c. The drawbacks of this formulation, specifically the fact that the discrete crack domain $\Gamma \subset \Omega$ is unknown and evolves during the analysis, are overcome by the regularized formulation by Bourdin et al. [3]. In this approach, the crack surface energy term is approximated as

$$G_c \int_\Gamma d\Gamma \approx \int_\Omega \psi_s(s, \nabla s) d\Omega \tag{2}$$

by introducing a fracture energy density ψ_s, defined over the whole domain Ω, which depends on the phase-field variable s. The continuous variation of s, ranging from 1, corresponding to intact material, to 0, corresponding to fully cracked material, approximates the crack topology in the domain. The expression of the fracture energy density originally proposed in [3]

$$\psi_{s,2^{nd}}(s, \nabla s) = G_c \left[\frac{(1-s)^2}{4\ell} + \ell |\nabla s|^2 \right] \tag{3}$$

leads to a strong form of the phase-field evolution equation in which second-order derivatives of s are present, so that the formulation with this choice is termed "second-order phase-field theory". Alternatively, Borden et al. [34] developed a different expression of the fracture energy density

$$\psi_{s,4^{th}}(s, \nabla s, \Delta s) = G_c \left[\frac{(1-s)^2}{4\ell} + \frac{\ell}{2} |\nabla s|^2 + \frac{\ell^3}{4} (\Delta s)^2 \right], \tag{4}$$

which leads to a "higher-order phase-field model" (also known as "fourth-order" formulation, again referring to the order of the derivatives present in the strong form of the phase-field evolution equation). The higher derivatives present in the latter formulation require at least C^1 continuity between elements. The scalar term ℓ in Eqs. (3) and (4) is a length scale parameter which controls the width of the smeared crack in the phase-field approximated model. For $\ell \to 0$, the approximation converges to the sharp crack solution by Franfort and Marigo (in turn related to Griffith's solution) in the sense of Γ convergence [6].

In order to reproduce the physical asymmetry of the material behavior in tension and compression, the strain tensor $\boldsymbol{\varepsilon}$ is additively decomposed into its positive (tensile) and negative (compressive) components:

$$\boldsymbol{\varepsilon} = \boldsymbol{\varepsilon}^+ + \boldsymbol{\varepsilon}^-. \tag{5}$$

Among the possible approaches proposed in the literature, we adopt a tension–compression split based on the spectral decomposition of the strain tensor as proposed by Miehe et al. [7]

$$\boldsymbol{\varepsilon} = \sum_{i=1}^{3} \varepsilon_i \, \boldsymbol{n}_i \otimes \boldsymbol{n}_i, \tag{6}$$

in which ε_i and $\boldsymbol{n}_i$ represent the eigenvalues and eigenvectors of the strain tensor, respectively. $\boldsymbol{\varepsilon}^+$ and $\boldsymbol{\varepsilon}^-$ are then obtained from the positive and negative principal strains as

$$\boldsymbol{\varepsilon}^\pm = \sum_{i=1}^{3} \langle \varepsilon_i \rangle^\pm \boldsymbol{n}_i \otimes \boldsymbol{n}_i, \tag{7}$$

having $\langle x \rangle^\pm = (x \pm |x|)/2$. According to the split of the strain tensor, the strain energy density and the stress tensor are decomposed into tensile and compressive parts as follows,

$$\psi_e^\pm = \frac{1}{2} \lambda \left(\langle \mathrm{tr}(\boldsymbol{\varepsilon}) \rangle^\pm \right)^2 + \mu \, \mathrm{tr} \left(\left(\boldsymbol{\varepsilon}^\pm \right)^2 \right), \tag{8}$$

$$\boldsymbol{\sigma}^\pm = \lambda \langle \mathrm{tr}(\boldsymbol{\varepsilon}) \rangle^\pm \boldsymbol{I} + 2\mu \, \boldsymbol{\varepsilon}^\pm, \tag{9}$$

with λ and μ as the Lamé constants and $\boldsymbol{I}$ as the identity tensor. The positive terms ψ_e^+ and $\boldsymbol{\sigma}^+$ are then degraded by a degradation function $g(s)$:

$$\psi_e(\boldsymbol{\varepsilon}, s) = g(s) \psi_e^+(\boldsymbol{\varepsilon}) + \psi_e^-(\boldsymbol{\varepsilon}), \tag{10}$$

$$\boldsymbol{\sigma}(\boldsymbol{\varepsilon}, s) = g(s) \boldsymbol{\sigma}^+(\boldsymbol{\varepsilon}) + \boldsymbol{\sigma}^-(\boldsymbol{\varepsilon}). \tag{11}$$

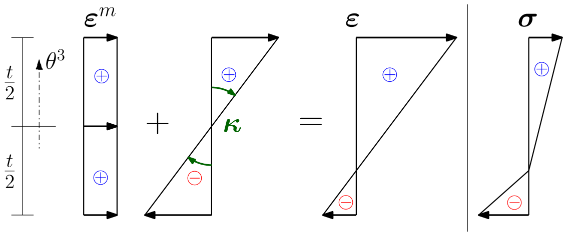

Fig. 1. Combination of the contributions of membrane and bending strain and total strain over the thickness t. Through-thickness stress distribution after degradation of the positive (tensile) component.

The standard quadratic degradation function, including a positive small factor $\eta \approx 0$ to avoid zero stiffness of the material in a fully cracked state, is adopted:

$$g(s) = (1-\eta)s^2 + \eta. \tag{12}$$

According to the approach exposed above, the energy functional from Eq. (1) can be rewritten in its regularized version as:

$$E_\ell(\boldsymbol{\varepsilon}, s) = \int_\Omega \left[g(s)\, \psi_e^+(\boldsymbol{\varepsilon}) + \psi_e^-(\boldsymbol{\varepsilon}) + \psi_s(s, \nabla s) \right] d\Omega. \tag{13}$$

Fracture irreversibility, meaning that the crack does not heal if external loads are removed, is enforced according to Miehe at al. [7] by replacing ψ_e^+ with the so-called history variable $\mathcal{H}$, defined as the maximum of the positive part of the strain energy density over the pseudo-time of the analysis:

$$\mathcal{H}(t) := \max_{\tau \in [0,T]} \psi_e^+(\tau). \tag{14}$$

A critical feature of the phase-field model in combination with plate and shell formulations is the tension–compression split introduced in Eq. (5). At each point of the continuum, the strain tensor is defined as the sum of the membrane and bending parts as follows,

$$\boldsymbol{\varepsilon}(\theta^3) = \boldsymbol{\varepsilon}^m + \theta^3 \boldsymbol{\kappa}, \tag{15}$$

the latter term depending on the curvature $\boldsymbol{\kappa}$ and linearly varying along with the thickness coordinate θ^3. The spectral split requires additional attention because, due to bending, the strains can vary between tension and compression through the shell thickness t, as depicted in Fig. 1. We adopt the approach from Kiendl et al. [44] where, as usually done for Kirchhoff–Love shells, the model is reduced to the behavior of the midsurface variables. So, we define the strain energy surface density Ψ_e, which expresses the strain energy per unit area of the midsurface. Including the tension–compression split of the strain energy density, the positive and negative parts of Ψ_e are computed as:

$$\Psi_e^\pm = \int_{-t/2}^{t/2} \psi_e^\pm(\theta^3) d\theta^3. \tag{16}$$

The dependency of the strain tensor on the thickness coordinate θ^3, as shown in Eq. (15), leads to a nonlinear distribution of the in-plane stress $\boldsymbol{\sigma}$, whose tensile component is degraded according to Eq. (11). For this reason, the integral in Eq. (16) needs to be computed by adopting numerical integration. In each thickness integration point, the total strain is computed as the sum of membrane and bending parts, as in Eq. (15), and the spectral split is then performed. According to this approach, which can be adopted independently of the specific shell formulation, it is possible to describe a nonlinear degradation of stresses and strain energy through the shell thickness (see Fig. 1), assuming only one value of the phase-field variable s and of the degradation function $g(s)$ at the midsurface.

The final expression of the energy functional for brittle fracture problems in thin shells, including degradation only of the positive part of the strain energy surface density, becomes

$$E_\ell(\boldsymbol{\varepsilon}^m, \boldsymbol{\kappa}, s) = \int_A \left[g(s)\, \Psi_e^+(\boldsymbol{\varepsilon}^m, \boldsymbol{\kappa}) + \Psi_e^-(\boldsymbol{\varepsilon}^m, \boldsymbol{\kappa}) + \Psi_s(s, \nabla s) \right] dA, \tag{17}$$

where Ψ_s is defined similarly to $\Psi_e^{\pm}$ by through-thickness integration of the fracture energy density ψ_s. The stationarity condition of (17) with respect to s leads to the phase-field evolution equation for shells. The weak form of the equation, which will be used for the solution of the system, read, for the second- and fourth-order phase-field formulation respectively,

$$\int_A \left[\frac{4\,\ell(1-\eta)\mathcal{H}}{tG_c}+1\right] s\,\delta s\,dA + 4\,\ell^2 \int_A \nabla s\cdot\nabla\delta s dA = \int_A \delta s\,dA, \tag{18}$$

$$\int_A \left[\frac{4\,\ell(1-\eta)\mathcal{H}}{tG_c}+1\right] s\,\delta s\,dA + 2\,\ell^2 \int_A \nabla s\cdot\nabla\delta s dA + \ell^4 \int_A \Delta s\cdot\Delta\delta s dA = \int_A \delta s\,dA, \tag{19}$$

with δs representing a test function for s.

2.2. *Isogeometric formulation for Kirchhoff–Love shell*

The focus of this paper is on thin shell structures and an isogeometric rotation-free Kirchhoff–Love shell formulation, as described by Kiendl et al. [66], is adopted and extended to local refinement through LR NURBS.

2.2.1. *Shell kinematics*

In Kirchhoff–Love shell theory, which includes thin plates as a special case, segments initially perpendicular to the shell midsurface remain straight and perpendicular after deformation. Therefore, transverse shear strains can be neglected and the kinematics of the shell can be fully described by the displacement field of the midsurface.

For describing the shell kinematics, a curvilinear coordinate system is considered, with θ_1 and θ_2 as the parametric coordinates used for defining the midsurface, and $\theta_3 \in [-t/2, +t/2]$ as the through-thickness coordinate. Greek indices $\alpha = 1, 2$ and $\beta = 1, 2$ are adopted for denoting the in-plane components and $(\cdot)_{,\alpha} = \partial(\cdot)/\partial\theta_\alpha$ indicates the partial derivatives with respect to θ_α. Considering a point $\mathbf{r}(\theta_1, \theta_2)$ on the shell midsurface, a covariant coordinate system can be defined by the tangent base vectors $\mathbf{a}_\alpha = \mathbf{r}_{,\alpha}$. The dual contravariant vectors are defined by $\mathbf{a}^\alpha \cdot \mathbf{a}_\beta = \delta^\alpha_\beta$, being δ^α_β the Kronecker delta. The total strain at each point of the shell, see Eq. (15), depends on the membrane strain $\boldsymbol{\varepsilon}^m = \varepsilon^m_{\alpha\beta}\,\mathbf{a}^\alpha \otimes \mathbf{a}^\beta$ and curvature $\boldsymbol{\kappa} = \kappa_{\alpha\beta}\,\mathbf{a}^\alpha \otimes \mathbf{a}^\beta$, whose covariant components can be expressed as follows,

$$\varepsilon^m_{\alpha\beta} = \frac{1}{2}(\mathbf{a}_\beta \cdot \mathbf{u}_{,\alpha} + \mathbf{a}_\alpha \cdot \mathbf{u}_{,\beta}), \tag{20}$$

$$\begin{aligned}\kappa_{\alpha\beta} = &- \mathbf{a}_3 \cdot \mathbf{u}_{,\alpha\beta} + \frac{1}{\|\mathbf{a}_1 \times \mathbf{a}_2\|}\cdot \\ &\cdot \left[(\mathbf{r}_{,\alpha\beta} \times \mathbf{a}_2)\cdot\mathbf{u}_{,1} + (\mathbf{a}_1 \times \mathbf{r}_{,\alpha\beta})\cdot\mathbf{u}_{,2} + \mathbf{r}_{,\alpha\beta}\cdot\mathbf{a}_3\,((\mathbf{a}_2 \times \mathbf{a}_3)\cdot\mathbf{u}_{,1} + (\mathbf{a}_3 \times \mathbf{a}_1)\cdot\mathbf{u}_{,2})\right],\end{aligned} \tag{21}$$

where $\mathbf{a}_3$ represents the unit vector normal to the surface:

$$\mathbf{a}_3 = \frac{\mathbf{a}_1 \times \mathbf{a}_2}{\|\mathbf{a}_1 \times \mathbf{a}_2\|}. \tag{22}$$

The expressions $\boldsymbol{\varepsilon}^m$ and $\boldsymbol{\kappa}$ are the linearized version of the more general and nonlinear strain measures defined for the considered shell formulation, about which details can be found in [66]. This is appropriate in the context of brittle fracture, where usually failure occurs without the development of large displacements. Isogeometric analysis is a favorable choice for the discretization of such a model because it provides the continuity required by the presence of second-order derivatives in the curvature expression (C^1 continuity).

For implementation and solution of the system of coupled equations, the variational formulation based on the virtual work principle, corresponding to the weak form of the momentum equation, is chosen

$$\delta W = \delta W^{\text{int}} - \delta W^{\text{ext}} = 0, \tag{23}$$

in which the internal virtual work is defined as follows,

$$\delta W^{\text{int}} = \int_A (\delta\boldsymbol{\varepsilon} : \boldsymbol{n} + \delta\boldsymbol{\kappa} : \boldsymbol{m})\,dA, \tag{24}$$

with $\delta\boldsymbol{\varepsilon}$ and $\delta\boldsymbol{\kappa}$ computed according to Eqs. (20) and (21) from $\delta\mathbf{u}$, which can be interpreted as virtual displacement field. $\boldsymbol{n}$ and $\boldsymbol{m}$ represent the effective stress resultants, for tension and bending respectively, computed by numerical integration of the stresses through the thickness.

2.2.2. Discretization of the geometry using LR NURBS

In traditional NURBS-based isogeometric analysis, surfaces can be parametrized using two parametric coordinates (ξ, η), two sets of knot vectors ($\Xi = \left\{\xi_1, \xi_2, \ldots, \xi_{n+p+1}\right\}$ and $\mathcal{Z} = \left\{\eta_1, \eta_2, \ldots, \eta_{m+q+1}\right\}$), a net of $n \times m$ control points $\boldsymbol{P}_{i,j}$, and a tensor product of univariate B-spline basis functions ($N_{i,p}$ and $M_{j,q}$) of degree p, q as follows,

$$\boldsymbol{S}(\xi, \eta) = \frac{\sum_{i=1}^{n} \sum_{j=1}^{m} N_{i,p}(\xi) M_{j,q}(\eta) w_{i,j}}{\sum_{k=1}^{n} \sum_{l=1}^{m} N_{k,p}(\xi) M_{l,q}(\eta) w_{k,l}} \boldsymbol{P}_{i,j} = \sum_{i=1}^{n} \sum_{j=1}^{m} R_{i,j}(\xi, \eta) \boldsymbol{P}_{i,j}, \tag{25}$$

where $w_{i,j}$ represent the weights associated with each control point. The univariate B-spline basis functions are defined recursively, with respect to the degree p, by the Cox–de Boor formula, starting from piecewise constants ($p = 0$):

$$p = 0 \qquad N_{i,0}(\xi) = \begin{cases} 1 & \xi_i \le \xi < \xi_{i+1} \\ 0 & \text{elsewhere,} \end{cases} \tag{26}$$

$$p \ge 1 \qquad N_{i,p}(\xi) = \frac{\xi - \xi_i}{\xi_{i+p} - \xi_i} N_{i,p-1}(\xi) + \frac{\xi_{i+p+1} - \xi}{\xi_{i+p+1} - \xi_{i+1}} N_{i+1,p-1}(\xi). \tag{27}$$

The global knot vector net of lines defines the so-called Bézier mesh of the geometry.

In phase-field fracture analyses, a discretization employing a fine mesh around the crack region is needed to correctly resolve the smeared crack profile, which is often very steep and whose width is controlled by the length scale parameter ℓ (see Fig. 19). The tensor product property of standard NURBS surfaces allows only a global refinement of the geometry, thus resulting in a high number of elements needed and therefore in computationally expensive analyses. For this reason, a local refinement technology needs to be adopted to be able to use small elements only in the crack area. We choose to use LR NURBS [62], an extension of LR B-splines [60]. The idea behind LR splines is the fact that each univariate B-Spline basis function has support in the parametric space only over a limited number of knot spans, i.e. $[\xi_i, \xi_{i+p+1}]$, whose knots constitute a "local knot vector" Ξ_i. Bivariate LR B-splines are defined as the product of univariate B-splines over local knot spans as follows,

$$B_{\boldsymbol{\Xi}^k}(\xi, \eta) = N_{\Xi^i,p}(\xi) M_{\mathcal{Z}^j,q}(\eta), \tag{28}$$

and have support over a portion of the domain corresponding to a bivariate local knot vector $\boldsymbol{\Xi}^k$ in parametric space. The LR NURBS shape functions are defined as

$$R^{\gamma}_{\boldsymbol{\Xi}^k}(\xi, \eta) = \gamma_k \frac{B_{\boldsymbol{\Xi}^k}(\xi, \eta) w_k}{\sum_{l=1}^{n_{CP}} B_{\boldsymbol{\Xi}^l}(\xi, \eta) w_l}, \tag{29}$$

and a surface is parametrized as

$$\boldsymbol{S}(\xi, \eta) = \sum_{k=1}^{n_{CP}} R^{\gamma}_{\boldsymbol{\Xi}^k}(\xi, \eta) \boldsymbol{P}_k, \tag{30}$$

in which n_{CP} is the number of control points. The tensor product properties are maintained only at the level of the single function, allowing for an unstructured configuration of the control points. The term γ_k in Eq. (29) is introduced in order to maintain the partition of unity property after splitting of the shape functions. Without entering into the details of the algorithm for the local refinement of the mesh (which can be found in [60]), a LR B-spline or LR NURBS can be split into two new basis functions by inserting a mesh line over a local knot vector, which generates a new couple of control points and weights (in order to maintain the partition of unity) that will replace the preceding structure. The application and the repetition of this procedure in the two parametric directions of the surface allow the local refinement of the mesh. Different refinement strategies have been proposed in [60]. "Full span" (Fig. 2a) and "minimum span" (Fig. 2b) approaches are based on the choice of an element to be refined. In the first case, all the basis functions having support on the element are split by inserting a couple of mesh lines, one for each parametric direction, that span from the minimum to the maximum knot of the support of all the functions supported by the element to be split. A smaller footprint of the refinement is obtained by adopting the second strategy, in which a couple of as short as possible mesh lines, just long enough to split at least one basis function, are inserted through the marked element center. The "structured mesh" strategy (Fig. 2c) consists in the

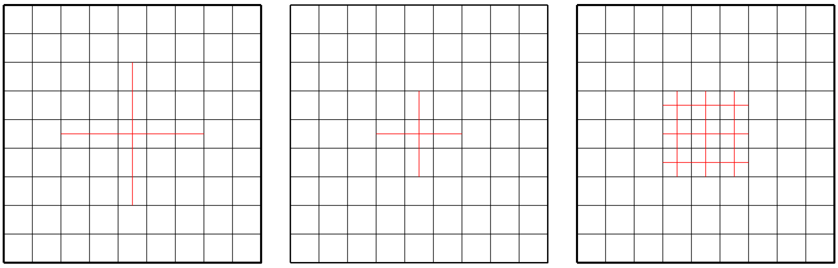

(a) Full span. The selected element to be split was the one in the middle of the mesh.

(b) Minimum span. Since biquadratic NURBS are used, a basis function has support on three knot spans for each parametric direction, and so the inserted mesh lines span over three elements.

(c) Structured mesh. The refined basis function had support over the elements which were split.

Fig. 2. Comparison between the considered refinement strategies for biquadratic NURBS mesh. Red lines indicate inserted mesh lines. (For interpretation of the references to color in this figure legend, the reader is referred to the web version of this article.)

split of all the knot spans of the support of a chosen basis function. Among the three methods, the last one is the one used in this work since it provides a more regular mesh when multiple refinement steps are performed and, moreover, keeps the aspect ratio of the elements in the parametric space constant.

2.3. Penalty formulations for patch coupling

In order to model the fracture of complex multipatch shell structures, a penalty-based methodology for coupling NURBS patches is hereby presented. The approach couples both the structural and the phase-field behavior across the patch interfaces and uses a single dimensionless penalty parameter $\alpha = 10^3$ which is scaled with the structural and phase-field problem parameters.

2.3.1. Structural coupling

According to the approach proposed by Herrema et al. [67], we impose displacement and rotational continuity by augmenting the virtual work formulation, see Eq. (23), with new contributions:

$$\delta W = \delta W^{\text{int}} + \delta W^{\text{pd}} + \delta W^{\text{pr}} - \delta W^{\text{ext}} = 0. \tag{31}$$

The term δW^{pd} corresponds to the virtual work from the penalization of the relative displacement between the two patches A and B $\left(\mathbf{u}^{\text{A}} - \mathbf{u}^{\text{B}}\right)$ along the interface curve $\mathcal{L}$:

$$\delta W^{\text{pd}} = \int_{\mathcal{L}} \alpha_{\text{d}} \left(\mathbf{u}^{\text{A}} - \mathbf{u}^{\text{B}}\right) \cdot \left(\delta\mathbf{u}^{\text{A}} - \delta\mathbf{u}^{\text{B}}\right) \mathrm{d}\mathcal{L}. \tag{32}$$

The second added term δW^{pr}, instead, is devoted to preserving rotational continuity by penalizing the relative rotations between the coupled edges of the patches

$$\begin{aligned}\delta W^{\text{pr}} = \int_{\mathcal{L}} \alpha_{\text{r}} \Big(& \left(\mathbf{a}_3^{\text{A}} \cdot \mathbf{a}_3^{\text{B}} - \mathring{\mathbf{a}}_3^{\text{A}} \cdot \mathring{\mathbf{a}}_3^{\text{B}}\right) \left(\delta\mathbf{a}_3^{\text{A}} \cdot \delta\mathbf{a}_3^{\text{B}} - \delta\mathring{\mathbf{a}}_3^{\text{A}} \cdot \delta\mathring{\mathbf{a}}_3^{\text{B}}\right) + \\ & + \left(\mathbf{a}_n^{\text{A}} \cdot \mathbf{a}_3^{\text{B}} - \mathring{\mathbf{a}}_n^{\text{A}} \cdot \mathring{\mathbf{a}}_3^{\text{B}}\right) \left(\delta\mathbf{a}_n^{\text{A}} \cdot \delta\mathbf{a}_3^{\text{B}} - \delta\mathring{\mathbf{a}}_n^{\text{A}} \cdot \delta\mathring{\mathbf{a}}_3^{\text{B}}\right)\Big) \mathrm{d}\mathcal{L},\end{aligned} \tag{33}$$

where $\mathbf{a}_n$ is the unit vector lying in the plane of the patch and orthogonal to $\mathcal{L}$ and $\mathbf{a}_3$ is the unit vector perpendicular to the surface. The notation $\mathring{(\cdot)}$ indicates the undeformed configuration of these geometric variables. For more details regarding the methodology, see Herrema et al. [67]. The formulation works for smooth and non-smooth patch connections as well as for matching and non-matching meshes at the interface. This is an important feature when we employ adaptive local refinement, which might cause different mesh densities at the two sides of a coupling interface even if the meshes were initially matching. Moreover, the penalty formulations can be used for weakly imposing clamping or symmetry boundary conditions at patch edges by considering only the components relative to the first patch in the penalty virtual work contributions.

According to [67], the penalty parameters α_d and α_r are computed from a global penalty parameter $\alpha = 10^3$ by scaling it with the membrane and bending shell stiffness values, respectively. For the extension to phase-field fracture analysis, we further multiply the penalty parameters α_d and α_r with the degradation function $g(s)$ to ensure a consistent scaling of structural stiffness and penalty stiffness in the fractured zones. For uniform isotropic material configurations, the proposed scaling is as follows

$$\alpha_\mathrm{d} = g(s)\,\alpha\,\frac{E\,t}{h\,(1-\nu^2)}, \tag{34}$$

$$\alpha_\mathrm{r} = g(s)\,\alpha\,\frac{E\,t^3}{12\,h\,(1-\nu^2)}, \tag{35}$$

where E is Young's modulus, ν is Poisson's ratio and t is the shell thickness, while h is the average element length along the coupled edge having the finer discretization.

2.3.2. Phase-field coupling between patches

In order to enforce C^0 continuity of the phase-field between the patch interfaces, we add the following term to the left-hand side of the weak form of the phase-field equation (18) and (19). In analogy with the approach adopted for the structural coupling, the term penalizes the difference of s at the two sides of $\mathcal{L}$:

$$\int_{\mathcal{L}} \alpha_{PF}^{C^0}(s^A - s^B)(\delta s^A - \delta s^B)\mathrm{d}\mathcal{L}. \tag{36}$$

If the higher-order phase-field formulation is employed, we propose an approach for imposing the required C^1 continuity of the phase-field across smooth patch interfaces, in addition to the aforementioned C^0 continuity, by penalizing the relative changes in the directional derivative of the phase-field along $\mathbf{a}_n$ between the two patches:

$$\int_{\mathcal{L}} \alpha_{PF}^{C^1}(\nabla s^A \cdot \mathbf{a}_n^\mathrm{A} - \nabla s^B \cdot \mathbf{a}_n^\mathrm{B})(\nabla \delta s^A \cdot \mathbf{a}_n^\mathrm{A} - \nabla \delta s^B \cdot \mathbf{a}_n^\mathrm{B})\mathrm{d}\mathcal{L}. \tag{37}$$

This term needs to be added to the left-hand side of Eq. (19). In (37), we assume that the normal vectors $\mathbf{a}_n^\mathrm{A}$ and $\mathbf{a}_n^\mathrm{B}$ point in the same direction. The approach is applicable to smooth patch interfaces, while it cannot be extended straightforwardly to patch connections forming a kink. In the latter case, the fact that the vectors $\mathbf{a}_n^\mathrm{A}$ and $\mathbf{a}_n^\mathrm{B}$ belong to two different planes makes the choice of the directional derivative of s to be penalized ambiguous. In such situations, where the C^1 continuity of the phase-field cannot be imposed, we adopt the second-order phase-field formulation, which requires only C^0 continuity of s, see the example in Section 4.6. The term in (37), considering only the components relative to s^A, can be used also for weakly imposing symmetry conditions along one edge.

The penalty parameters are chosen in the same fashion as done for the structural coupling (Section 2.3.1). The global penalty coefficient $\alpha = 10^3$ is scaled by terms that maintain dimensional consistency with the phase-field equation and ensure that $\alpha_{PF}^{C^0}$ and $\alpha_{PF}^{C^1}$ are large enough to guarantee the satisfaction of the imposed continuity constraint without creating ill-conditioning in the phase-field stiffness matrix. The weak forms of the phase-field equations (18) and (19) suggest also the importance of including the term related to the history field $\mathcal{H}$, which is the driving force of the phase-field equation and which becomes numerically predominant when fracture develops. So, for the imposition of phase-field C^0 continuity, the penalty scaling term is defined as follows,

$$\alpha_{PF}^{C^0} = \alpha\left[\frac{4\ell(1-\eta)\mathcal{H}_{max}}{tG_c} + 1\right]h, \tag{38}$$

while for C^1 continuity we define

$$\alpha_{PF}^{C^1} = \alpha\left[\frac{4\ell(1-\eta)\mathcal{H}_{max}}{tG_c} + 1\right]\ell^2 h, \tag{39}$$

where $\mathcal{H}_{max}$ corresponds to the current maximum value of the history field over all the integration points of the structure.

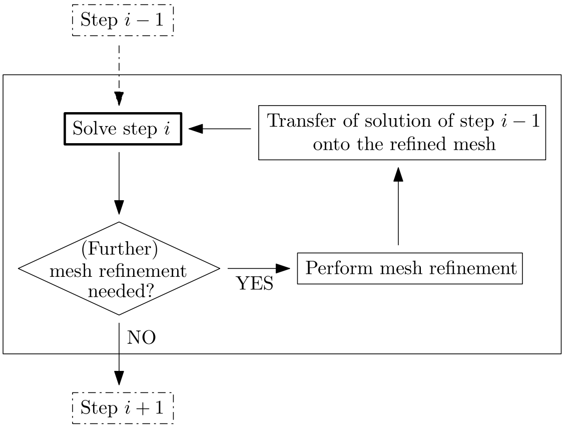

Fig. 3. Adaptive local refinement algorithm for $n = 1$, meaning that only the current step i is recomputed, if needed.

3. Adaptive local refinement and staggering schemes

For performing phase-field fracture simulations on complex structures with a reasonable numerical effort, the use of an adaptive local refinement scheme is crucial. In the following, we present a strategy featuring a multistep predictor–corrector algorithm in order to refine the mesh only where needed, i.e. around the crack area, without *a priori* knowledge of the evolution of the crack. Brittle fracture simulations often involve fast-growing cracks that (fully) develop in a single load step. In this situation, the crack may grow even outside of the mesh region just refined. If this happens, the current load steps or n load steps, including the current one, need to be recomputed with a new further refined mesh, until “convergence of the refinement” is achieved (a typical example of unstable crack growth can be found in Section 4.1).

3.1. Adaptive mesh refinement algorithm employing LR NURBS

As indicator for the refinement, we use the value of the phase field s, similarly to Borden et al. [21]. In this work, it was shown that using the quadratic degradation function (12), crack nucleation starts at $s = 0.75$, and, therefore, $s_t = 0.75$ was also used as threshold value for refinement. In this paper, we use a slightly higher threshold value, namely $s_t = 0.80$. In order to check whether each element needs to be refined, the value of the phase-field s measured at the center of the element is compared with s_t. In general, one can state that the higher s_t leads to a slightly larger area of refinement, but, on the other hand, it leads to fewer recomputation steps due to crack growth out of the refined zone.

Regarding the refinement typology, we choose to employ the “structured mesh” refinement strategy (Section 2.2.2), for which all the knot spans of the support of certain NURBS basis functions are split. These basis functions are selected among all the NURBS having support on each element marked for refinement as the ones which do not include, in their support, any element having already the minimum mesh dimension (see Section 3.2) for the refinement round. This approach guarantees a regular mesh and a smooth transition between zones with different refinement levels.

The optimal number of steps to be recomputed each time the mesh is refined (n) depends on the type of the problem and the type of solver. When convergence of the staggered iterations is achieved in each step (see Section 3.3), relatively large load steps can be used since their size does not affect the accuracy of the results, but only the frequency in capturing the response of the system. Moreover, the smaller the steps, the higher becomes the computational cost of the analyses, as observed also by Gerasimov et al. [13]. For this reason, we choose to use “large” load increments and to set $n = 1$. If smaller steps are used, we suggest values of n between 3 and 5 as good alternatives. In case n is chosen larger than 1, the check on the need for mesh refinement is performed every n steps.

The adaptive mesh refinement algorithm is summarized in Fig. 3 in the form used in this work, i.e. with $n = 1$.

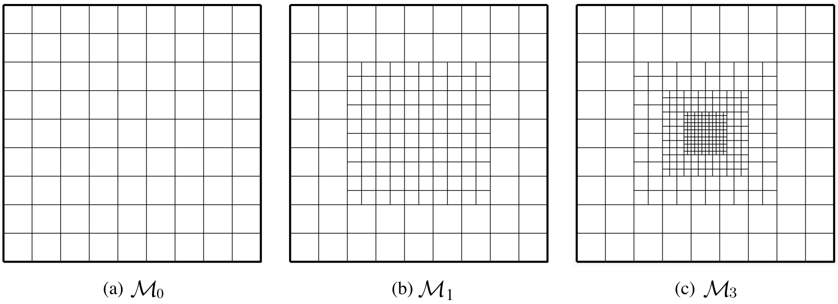

(a) $\mathcal{M}_0$ (b) $\mathcal{M}_1$ (c) $\mathcal{M}_3$

Fig. 4. Examples of different levels of mesh refinement, using the structured mesh strategy.

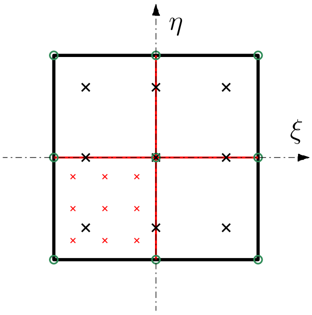

Fig. 5. Transfer operator for the history quantities saved at the integration points for a biquadratic mesh with 3 × 3 Gauss points per element. Black lines indicate the element to be split and black crosses the location of its integration points $(\bar{\xi}_m, \bar{\eta}_m)$, referred to its parametric space. Green circles correspond to the control points of the Bézier element. After the refinement, four elements are generated from the inserted red lines. For one of the newly generated fine elements, the location of the Gauss points $(\bar{\xi}_{m+1}, \bar{\eta}_{m+1})$ is shown. (For interpretation of the references to color in this figure legend, the reader is referred to the web version of this article.)

3.2. Transfer of field and history variables from coarse to refined mesh

Considering an initial non-refined mesh $\mathcal{M}_0$ and m levels of refinement required, there will be m intermediate refinement rounds producing meshes $\mathcal{M}_1$, $\mathcal{M}_2$, …, $\mathcal{M}_{m-1}$, $\mathcal{M}_m$, which can be discarded, except for the last one, at the end of the refinement process (see for example Fig. 4). During each refinement round, some basis functions will be refined, i.e. some elements will be split. In order to avoid excessive mesh refinement by splitting elements that have already been refined during the previous steps of the analysis, we set a minimum element dimension for the m^{th} refinement round equal to $h_0/2^m$, where h_0 is the characteristic element dimension in the initial non-refined mesh $\mathcal{M}_0$. The evaluation of the element size is done in the parametric space so that the mesh distortion does not influence the refinement strategy.

For each refinement round, all the state variables defined over the coarse mesh $\mathcal{M}_m$ need to be transferred to the refined mesh $\mathcal{M}_{m+1}$. For field quantities defined at the control points (displacement $\mathbf{u}$ and phase-field s), the projection occurs according to the same algorithm used for determining the coordinates of the control points in the refined mesh, as outlined in [60]. Regarding the variables stored at the integration points, nominally the history field $\mathcal{H}$, the transfer is based on interpolation of the variable between coarse and refined meshes in a fashion similar to the approached used by Caseiro et al. [68] for transferring strain quantities from integration points to an alternative set of points, see Fig. 5. For each element to be refined, we define locally a set of bivariate Bernstein polynomials $\boldsymbol{B}_m$ constituting the basis functions for a Bézier element with the same polynomial order of the adopted NURBS parametrization. So, the value of the history field in a (ξ, η) point of the coarse mesh element can be computed as

$$\mathcal{H}(\xi, \eta) = \boldsymbol{B}_m(\xi, \eta)\hat{\mathcal{H}}_m, \tag{40}$$

where $\hat{\mathcal{H}}_m$ indicates the (unknown) values of the history field at the control points of the Bézier element. If $(\bar{\xi}_m, \bar{\eta}_m)$ indicates the set of the local coordinates of all the integration points within the Bézier element, the previous expression can be rewritten as:

$$\mathcal{H}(\bar{\xi}_m, \bar{\eta}_m) = \mathbf{B}_m(\bar{\xi}_m, \bar{\eta}_m)\hat{\mathcal{H}}_m. \tag{41}$$

In the latter equation, $\mathbf{B}_m$ collects the value of the Bernstein polynomials in all the integration points. For each of the sub-elements in which the elements is split, the coordinates of the integration points in the parametric space of the fine element are denoted by $(\bar{\xi}_{m+1}, \bar{\eta}_{m+1})$. Analogously to Eq. (41), the projected value of the history field onto the integration points of the refined mesh elements can be found as:

$$\mathcal{H}(\bar{\xi}_{m+1}, \bar{\eta}_{m+1}) = \mathbf{B}_m(\bar{\xi}_{m+1}, \bar{\eta}_{m+1})\hat{\mathcal{H}}_m = \mathbf{B}_m(\bar{\xi}_{m+1}, \bar{\eta}_{m+1})\mathbf{B}_m^{-1}(\bar{\xi}_m, \bar{\eta}_m)\mathcal{H}(\bar{\xi}_m, \bar{\eta}_m). \tag{42}$$

Since the refinement occurs by splitting in half each element along both the parametric directions, the coordinates of the integration points are the same in the Bézier parametric space of each element to be split, and so the term $\mathbf{B}_m(\bar{\xi}_{m+1}, \bar{\eta}_{m+1})\mathbf{B}_m^{-1}(\bar{\xi}_m, \bar{\eta}_m)$ of Eq. (42) is the same for all elements (at each refinement level) and can be precomputed at the beginning of the analysis.

3.3. Staggered solution of the coupled problem

Box 1: Loosely and strongly coupled staggering schemes. In case convergence conditions are not satisfied, iterations are repeated.

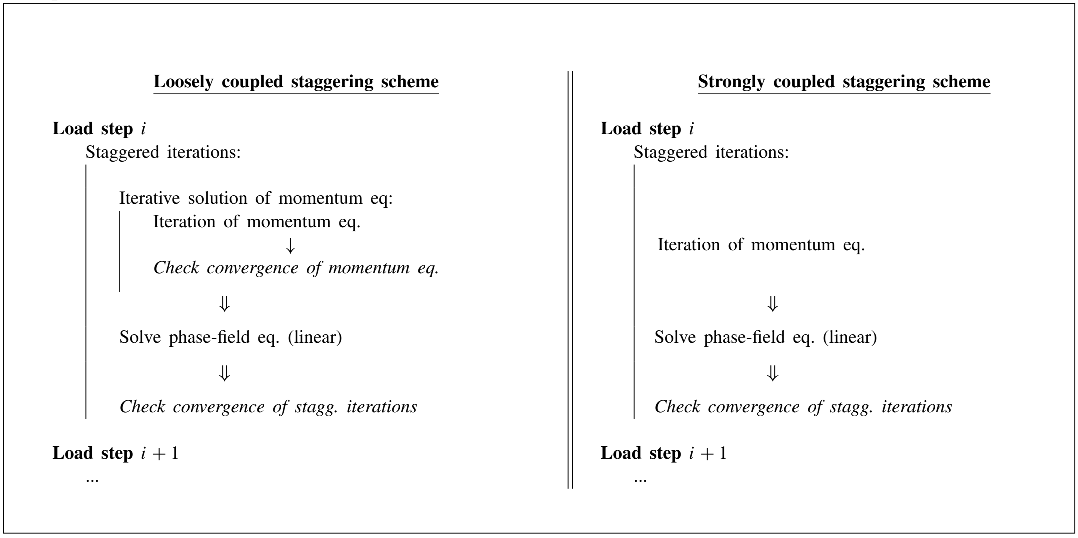

Loosely coupled staggering scheme

Load step i
Staggered iterations:
Iterative solution of momentum eq:
Iteration of momentum eq.
↓
Check convergence of momentum eq.
⇓
Solve phase-field eq. (linear)
⇓
Check convergence of stagg. iterations
Load step $i+1$
...

Strongly coupled staggering scheme

Load step i
Staggered iterations:
Iteration of momentum eq.
⇓
Solve phase-field eq. (linear)
⇓
Check convergence of stagg. iterations
Load step $i+1$
...

For the solution of the non-linear system of coupled equations, the staggered solution idea presented by Bourdin et al. [3] and Miehe et al. [7] consists in solving, for every pseudo-time step of the analysis, first the weak form of the momentum equation (23) for the displacement field $\mathbf{u}$, and then the weak form of the phase-field equation ((18) or (19)) for s. During each solution, the field which is not solved for is kept frozen. We follow the same idea and, after each staggered iteration, we check the convergence of the solution so that the two equations are recomputed, if necessary, until convergence of the staggered iterations is reached. This guarantees that the structure is in equilibrium at the end of each load step. As the momentum equation is nonlinear due to the strain energy split, an iterative solver which finds the equilibrium solution through successive inversion of the structural system is required. In the previously described staggering, which will be called "loosely coupled" scheme, each staggered iteration involves multiple iterations of the momentum equation, followed by a solution of the linear phase-field equation. We adopt instead a "strongly coupled" staggering scheme, in which, during each staggered iteration,

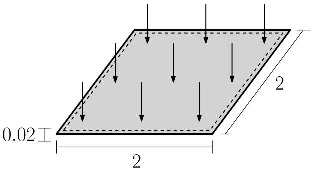

Fig. 6. Setup for the square plate example (dimensions in mm). Black dashed lines indicate pinned edges.

only a single iteration of the equilibrium equation is performed. Then, the solution of the phase-field equation is computed, before checking the convergence of the staggered iteration process with an adequately low tolerance for the residual (see Box 1). By reducing the number of iterations of the momentum equation, which are computationally more expensive than the linear solution of the phase-field equation, the strongly coupled staggered approach is able to decrease the computational effort of the simulations, while obviously providing the same result of the loosely coupled staggering scheme, as shown in Section 4.2.

4. Numerical examples and benchmark tests

The features of the formulation presented in the previous sections will be tested on selected numerical examples. Subsections will be dedicated to the adaptive local refinement algorithm using LR NURBS (Section 4.1), to the loose and strong coupling staggering schemes (Section 4.2), to the standard and higher-order phase-field formulations (Section 4.3) and to the penalty approach for patch coupling (Section 4.4). In these studies, a focus is set on comparing the computational cost of the different approaches. Classical in-plane and plate bending benchmarks will be investigated. The final Sections 4.5 and 4.6 are dedicated to two examples regarding complex shell structures.

For all the simulations, we use quadratic LR NURBS with 3 through-thickness Gauss points for each of the 3×3 Gauss points per element. The minimum element size adopted is always equal to $h = \ell/2$.

4.1. Adaptive local refinement examples

In this section, it will be shown how the adoption of the adaptive local refinement algorithm (Section 3.1) dramatically reduces the computational cost of the analyses and guarantees flexibility in the description of the crack path. Two different examples will be investigated: a plate bending case, in which the phase-field crack nucleates in an unnotched geometry and then fully develops in a single load step, and a 2D plane stress case where the crack evolves and grows gradually during the analysis.

We consider a square plate with geometry outlined in Fig. 6 and material parameters $E = 190 \times 10^3$ N/mm^2, $\nu = 0.29$, $G_c = 0.295$ N/mm and $\ell = 0.02$ mm as in [44]. The plate is simply supported at all the four sides and it is subjected to constant pressure in the out-of-plane direction, resulting in a state of biaxial bending. We compare the results obtained using a uniformly pre-refined NURBS mesh (Fig. 7c) with the ones achieved by employing adaptive local refinement starting from a coarser mesh and prescribing two levels of refinement, in order to obtain the same minimum element size as in the first case. The simulations provide the same result in terms of crack path, as it can be noted by comparing Figs. 7a and 7b, and in terms of load–displacement curve, see Fig. 8. Due to the prescribed convergence of the staggered iterations during the solver, the crack develops in a single load step after the nucleation, as typically happens in the context of brittle fracture. This behavior can be noted from the shape of the load–displacement curves, where a deviation from the linear elastic behavior, corresponding to nucleation, is followed by an abrupt pressure drop, corresponding to instantaneous crack growth. The obtained results are in agreement with previous investigations (see for example [44,69,70]), which show the nucleation of the crack at the center of the plate and its growth towards the corners of the plate. In Fig. 7d the final mesh resulting from the adaptive local refinement algorithm is depicted, with the mesh refined only where needed, i.e. in the crack area. The considerably lower number of elements (Fig. 9a) leads to a significant reduction of computational cost, even if the algorithm requires the step in which the crack develops to be recomputed multiple times (Fig. 9b).

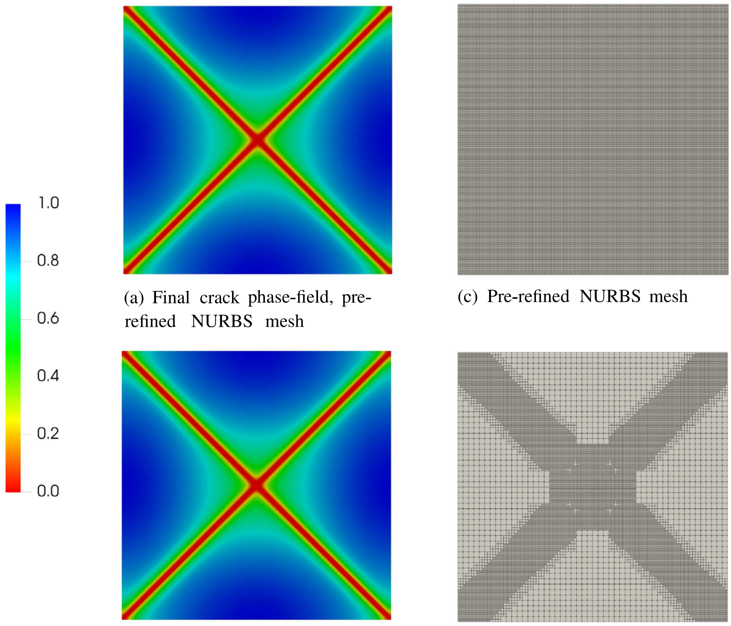

(a) Final crack phase-field, pre-refined NURBS mesh

(c) Pre-refined NURBS mesh

(b) Final crack phase-field, adaptive LR NURBS mesh

(d) Adaptive LR NURBS mesh, final stage

Fig. 7. Square plate example, comparison of results with and without adaptive local mesh refinement. The colormap indicates the value of the phase field.

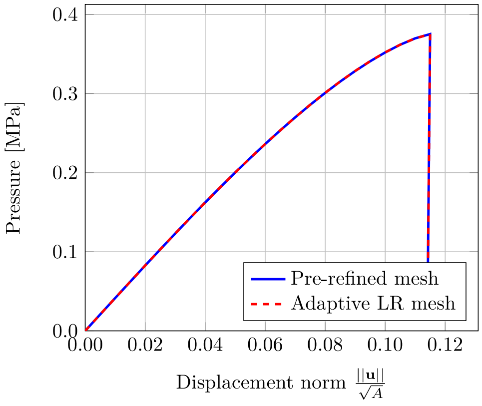

Fig. 8. Load–displacement curves for the square plate example with and without adaptive mesh refinement.

The second example is represented by a square plate containing a notch at one of its sides, where an imposed displacement at the upper edge induces a global tensile or shear state in the specimen. This case, which is a classical benchmark for fracture, has already been investigated in multiple publications (see for example [3,7,13,15,21,36–39,64]). We start by considering the shear situation, since in this case the crack grows gradually, while the tensile case will be investigated in the following parts of the paper. Geometry and boundary conditions are shown in

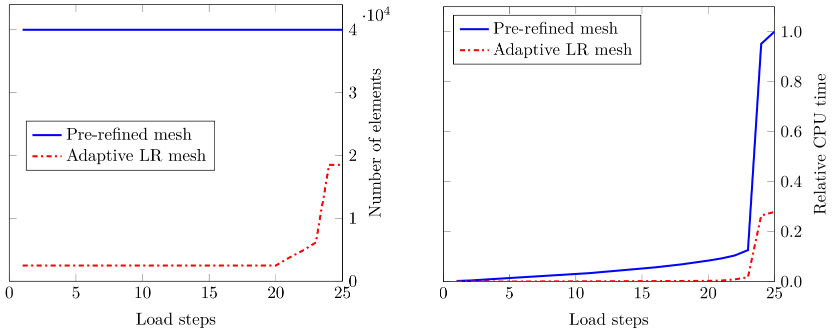

(a) Evolution of the number of elements in the mesh

(b) Relative cumulative time of the analyses. The CPU times in this and similar plots are always scaled by the total time of the slower analysis, in this case the one with pre refined-mesh

Fig. 9. Square plate example, comparison of the efficiency of the analyses with and without adaptive local mesh refinement.

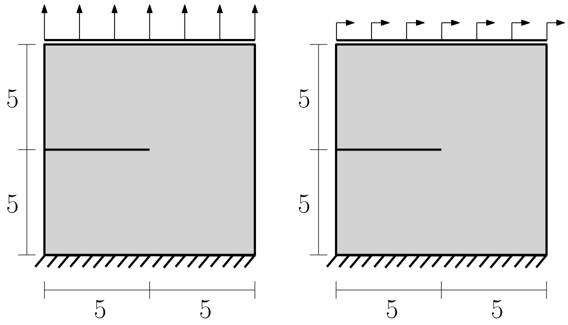

(a) Tensile case

(b) Shear case

Fig. 10. Setup of the single-edge notched test (dimensions in mm).

Fig. 10b (the thickness is $t = 0.1$ mm), while material parameters are $E = 1 \times 10^9$ N/mm^2, $\nu = 0.3$, $G_c = 2$ N/mm and $\ell = 0.05$ mm (as in [44]). Because of the NURBS discretization, which does not allow for discontinuities in the patches, the initial notch needs to modeled through the phase field, as in [21]. For this reason, it is necessary to pre-refine the zone around the initial crack. Three levels of refinements are applied to reach an adequate minimum element size. We want to compare the results of a simulation performed using adaptive local refinement with the ones from a pre-refined mesh. In order to limit the computational time of the analysis with a pre-refined mesh, we use fine elements only in the region where the crack is expected to grow, i.e. the lower-right part of the specimen, making sure to do it in an area large enough not to influence the fracture path (Fig. 11b). The simulations provide the same results in terms of crack path, which is depicted in Fig. 11a. Fig. 11c shows the adaptively refined mesh, having elements of small dimension only around the crack and a smooth transition between fine and coarse mesh. The results of the simulations are the same also in terms of load–displacement curve, see Fig. 12. Regarding the efficiency of the analyses, Fig. 13b and 13c show how the use of the adaptive mesh refinement dramatically reduces the computational time. The relative gain in CPU time for the analysis with adaptive mesh refinement is higher during the first load steps, which do not show any crack development and so do not need to be recalculated, but remains remarkable also in the final steps. The computational cost reduction is obviously related to the lower number of elements required (Fig. 13a) and would be even more evident if all the geometry was to be uniformly pre-refined.

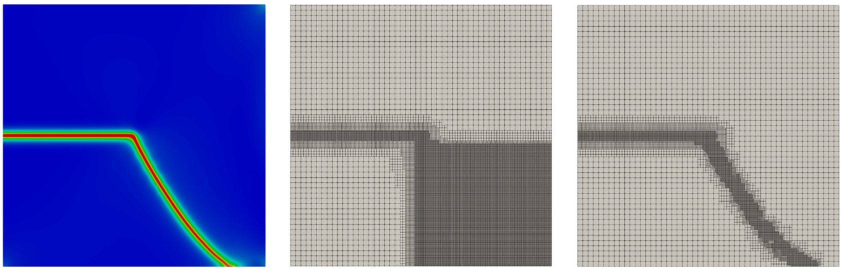

(a) Final crack phase-field

(b) Pre-refined NURBS mesh

(c) Adaptive LR NURBS mesh, final stage

Fig. 11. Single-edge notched specimen shear test, results of the simulations.

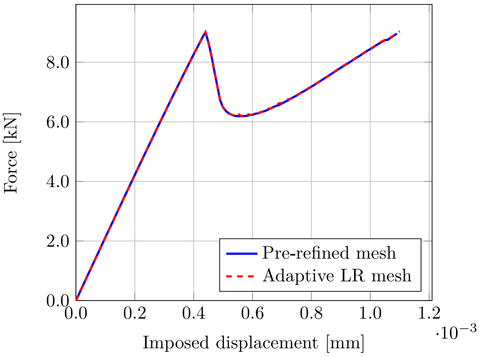

Fig. 12. Load–displacement curves for the single-edge notched specimen in shear with and without adaptive mesh refinement.

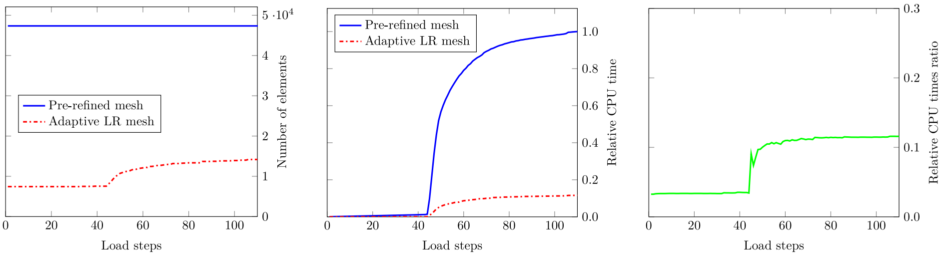

(a) Evolution of the number of elements in the mesh

(b) Relative cumulative time of the analyses (scaled by the total time of the analysis with pre-refined mesh)

(c) Ratio of the cumulative analyses times (adaptively refined over pre-refined mesh simulation time)

Fig. 13. Single-edge notched specimen in shear, comparison of the efficiency of the analyses with pre-refined and adaptively refined mesh.

4.2. Comparison of loosely and strongly coupled staggering schemes

In the following section, the results and efficiency of the “loose” and “strong” coupling staggering schemes outlined in Section 3.3 are compared. For the sake of brevity, we consider only the square plate example (having

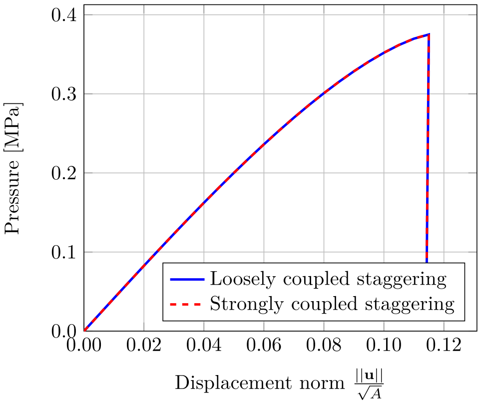

Fig. 14. Load–displacement curves for the square plate example. Comparison of the results with the staggering strategies.

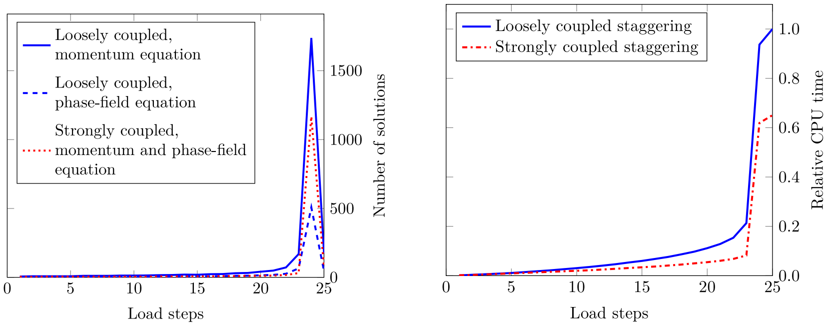

(a) Number of solutions of momentum and phase-field equations per step for the two staggering approaches

(b) Relative cumulative time of the analyses (scaled by the total time of the analysis with loosely coupled staggering)

Fig. 15. Square plate problem, comparison of efficiency of the analyses with loosely and strongly staggered coupling.

the same input parameters as in 4.1), but the same results have been observed in all the cases where the two approaches have been compared. In order to study only the effect of the staggering strategy, we adopt a uniformly pre-refined mesh as in Fig. 7c and, for both the staggering schemes, the final crack path is the same as the one depicted in the same figure. The load–displacement curves in Fig. 14 confirm that both coupling strategies provide identical results, given that at each load step iterations are performed until convergence. Concerning the efficiency of the simulations, the strong coupling strategy requires more solutions of the phase-field equation but fewer solutions of the equilibrium equation (Fig. 15a). Even if this approach needs more staggered iterations, in each of them only one solving of the structural equation is required. Recalling that the solution of the momentum equation is more computationally expensive than the one of the phase-field equation, it becomes clear why the strong staggering approach reduces the computational time of the analysis, as shown in Fig. 15b. The time saving becomes more evident in the final steps of the simulations, where more staggered iterations are required for convergence. For the sake of efficiency, the strongly coupled staggered scheme is adopted in all the following simulations.

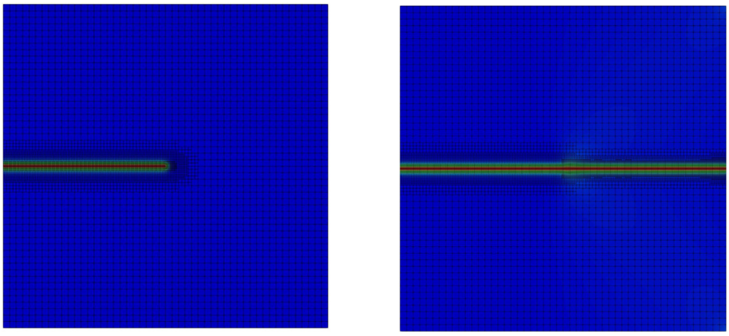

(a) Initial crack state and mesh

(b) Final crack state and mesh

Fig. 16. Single-edge notched specimen in tension with fourth-order phase-field formulation.

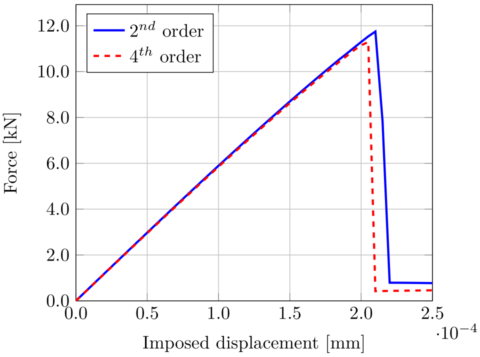

Fig. 17. Load–displacement curves for the single-edge notched specimen in tension. Comparison of the results employing standard and higher-order phase-field formulations.

4.3. Comparison of second- and fourth-order phase-field formulations

We present a comparison between the results of simulations employing second- and fourth-order phase-field formulations, see Eqs. (3) and (4). The choice of a higher-order formulation is natural in the context of isogeometric analysis, but we want to investigate and compare the efficiency of the two models, especially in the context of adaptive local refinement.

We consider the single-edge notched specimen presented in Section 4.1, this time under tension load, and we repeat the simulation for the two phase-field formulations. The geometry of the specimen and the setup of the analysis are shown in Fig. 10a. The example is solved employing adaptive local refinement of the mesh, which was pre-refined only around the initial crack (Fig. 16a). For both the formulations, the final result of the simulations consists in the abrupt fracture of the specimen due to the straight growth of the crack from the initial notch, as shown in Fig. 16b. The difference in the load–displacement curves, showing a higher critical load for the second-order phase-field formulation (Fig. 17), is in agreement with what reported by Borden et al. [34] and by Weinberg et al. [71], the first one highlighting that the residual “cohesive tractions” are more accurately described, i.e. they are smaller, in the fourth-order phase-field model.

In the analysis performed adopting the second-order phase-field model, the crack fully develops in two steps, while, in the case of fourth-order formulation, the crack needs only one step for completely propagating. Fig. 18b

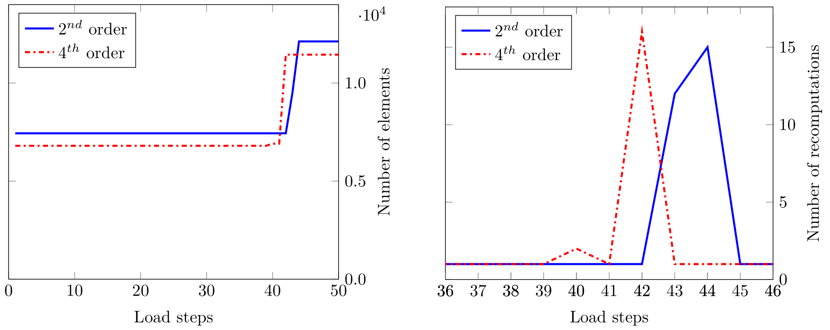

(a) Evolution of the number of elements in the mesh

(b) Number of times each step has to be recomputed

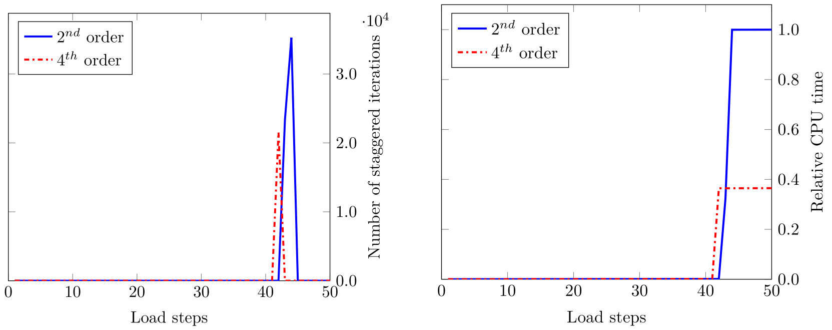

(c) Total number of staggered iteration for the step (including the iterations during the possible step recomputations)

(d) Relative cumulative time of the analyses (scaled by the total time of the second-order phase-field formulation analysis)

Fig. 18. Single-edge notched specimen in tension, comparison of the efficiency of the simulations with second- and fourth-order phase-field formulation.

shows the number of recomputations of the analysis steps corresponding to crack growth (all the steps that are not shown do not need to be recomputed by the algorithm). It is possible to notice that, with the second-order phase-field model, the crack propagation requires a total number of step recomputations, 27, divided into two load steps, much higher than the number of step recomputations required for the higher-order formulation, 16. The reason for this can be found in the higher accuracy in the description of the crack residual stresses of the fourth-order phase-field model, which allows the crack to grow longer for a fixed increase of the imposed displacement. The faster convergence of the higher-order model is confirmed by the lower number of staggered iterations required in each load step, especially in the ones correspondent to the abrupt development of the crack and which therefore need a higher number of iterations (Fig. 18c).

The unidimensional phase-field profiles extracted from the final state of the previous analyses are shown in Fig. 19 and compared with the theoretical ones, which are obtained by analytically solving the unloaded phase-field equations in one dimension after imposing the initial condition $s(x = 0) = 0$. A closed form exponential solution of these profiles exists for both the phase-field formulations [34]. For the second-order model we have:

$$s_{2nd}(x) = 1 - e^{-\frac{|x|}{2\ell}}, \tag{43}$$

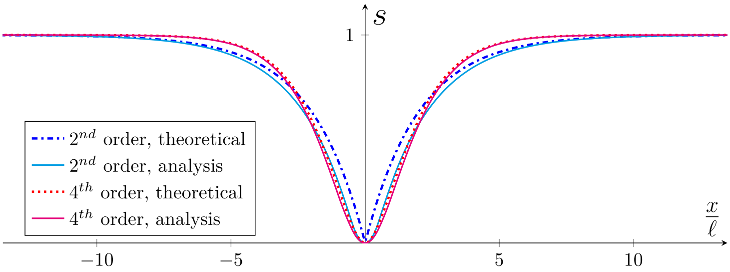

Fig. 19. Comparison of theoretical phase-field profiles with the ones extracted from the single-edge notched specimen in tension simulations, for both second- and fourth-order formulations.

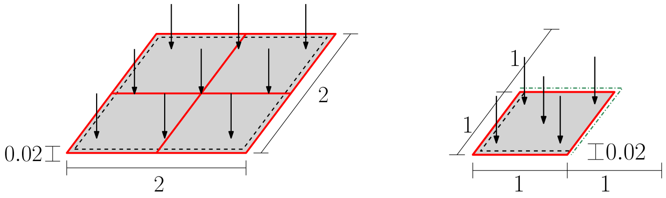

(a) Geometry divided in four patches

(b) Single patch model with double symmetry

Fig. 20. Square plate problem, setup employing penalty patch coupling (dimensions in mm). Black dashed lines indicate pinned edges, red lines correspond to patch boundaries and green dash dotted lines refer to edges subjected to symmetry conditions. (For interpretation of the references to color in this figure legend, the reader is referred to the web version of this article.)

while for fourth-order theory:

$$s_{4^{th}}(x) = 1 - e^{-\frac{|x|}{\ell}}\left(1 + \frac{|x|}{\ell}\right) \tag{44}$$

It can be noted that the higher-order formulation shows a slightly narrower profile, meaning that the area that needs to be refined can be reduced. Therefore, the number of elements used for the solution of the fourth-order analysis is decreased, as can be seen in Fig. 18a. The combination of these factors results in a lower total computational time for the higher-order formulation (Fig. 18d), especially in the context of adaptive refinement.

4.4. Examples involving penalty patch coupling and its use for modeling pre-cracks

We focus our attention on the penalty patch coupling formulation described in 2.3 and we apply it to the examples presented in the previous section. Adaptive local refinement and both second- and fourth-order phase-field models are employed. For the fourth-order phase-field simulations, also, C^1 continuity of the phase-field across patch boundaries is imposed, according to (37).

We start by considering again the square plate example described in 4.1, but this time the geometry is divided into four patches, as shown in Fig. 20a, which are coupled in their structure and the phase-field by the penalty approach presented. We also consider a setup including only 1 patch, corresponding to one-fourth of the plate, involving two symmetric boundary conditions again imposed by penalty (see Fig. 20b).

The results shown in Fig. 21a for the setup with four patches and considering the second-order phase-field model correspond to those of Fig. 7, which were obtained with a single patch arrangement. The results are identical for the three different setups (one patch corresponding to the full model, four patches, one patch with double symmetry corresponding to one quarter of the model), as it can be observed from the load–displacement curves in Fig. 22, which also confirm that the critical load computed using the higher-order phase-field model is slightly lower than the one predicted by the second-order formulation.

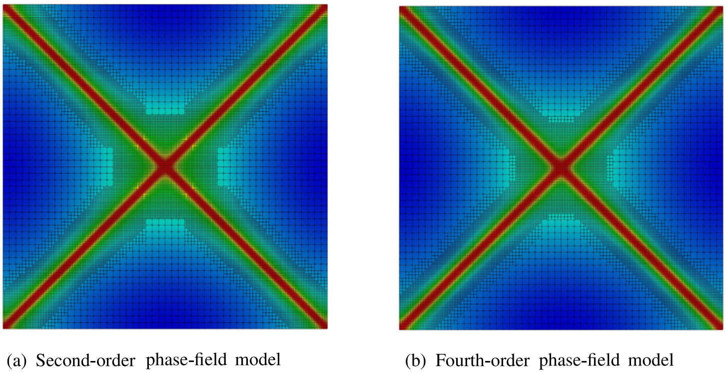
(a) Second-order phase-field model (b) Fourth-order phase-field model

Fig. 21. Square plate problem, final crack state and mesh for the four-patches setup.

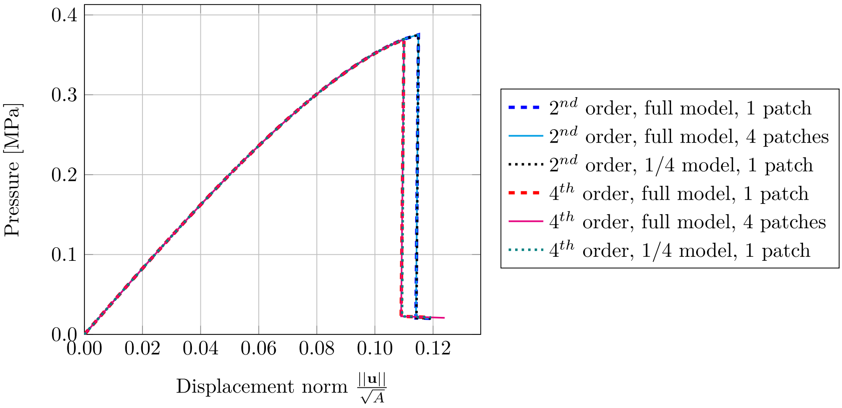

Fig. 22. Load–displacement curves for the square plate example. Comparison of the results using multiple patches and symmetry, employing the penalty coupling approach. Simulations repeated for second- and fourth-order phase-field models.

We show that the patch coupling approach and the adaptive local refinement algorithm are also able to replicate the results obtained in single-patch structures not only when the crack nucleates, as in the square plate example, but also in cases where a crack represented by the phase field develops. For this purpose, the single-edge notched example under tensile load described in Section 4.3 is considered. The geometry is subdivided into three patches as shown in Fig. 23a, so that the crack is expected to grow and propagate across the boundary connecting two patches. The outcome of the simulation is displayed in Fig. 23b, which corresponds to the results of the single-patch model (Fig. 16b). Good agreement of the load–displacement curves for the two cases is also shown in Fig. 24.

The penalty-based patch coupling can be used also for modeling pre-existing cracks as discontinuities in the structures. This idea will be shown by considering the example of the single-edge notched specimen, both in tension and shear, introduced in Section 4.1, whose behavior is determined by the presence of an initial crack. Since we want to compare our results with the ones obtained with classical finite element theory and due to the lower continuity of the Lagrange polynomials, only the second-order phase-field formulation can be considered. The division of the geometry in patches in order to allow the discrete modeling of the pre-crack (along which no patch coupling occurs) is shown in Fig. 25. The mesh is pre-refined at the discrete crack tip, in order to better describe the phase-field crack which is expected to grow from this location. Fig. 26 shows the final stages of the analyses with the pre-crack modeled by using patch discontinuity. The load–displacement curves in Fig. 27 highlight how the different treatment of the pre-crack affects the prediction of the critical fracture load. Regarding the tensile

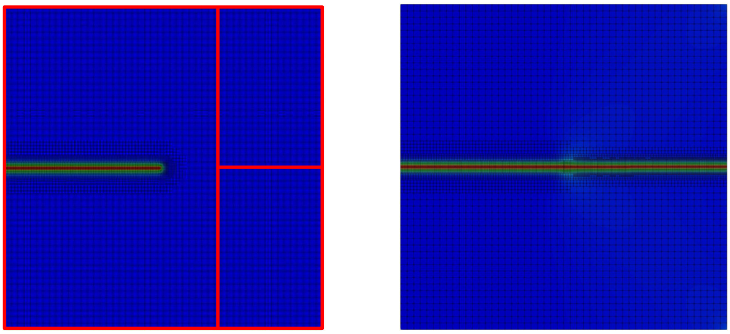

(a) Initial crack state and mesh. Red lines indicate patch boundaries

(b) Final crack state and mesh

Fig. 23. Single-edge notched specimen in tension with a pre-crack and three-patch geometry with the fourth-order phase-field formulation. (For interpretation of the references to color in this figure legend, the reader is referred to the web version of this article.)

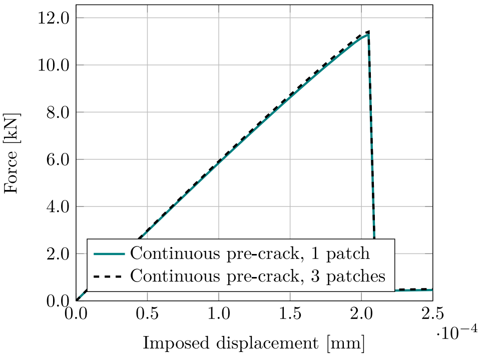

Fig. 24. Load–displacement curve for the single-edge notched specimen in tension with a pre-crack and the fourth-order phase-field formulation. Comparison of the results with different patch arrangements.

case, it appears that a discrete pre-crack is able to better model the brittle behavior of the structure, with the crack developing and growing in only one step. A difference in the critical load is present also for the shear case, possibly due to residual stresses in the phase-field pre-crack. For comparison, we computed both cases also with C^0 finite elements, in whose framework pre-cracks are usually modeled as discontinuities in the mesh that can be easily handled without the use of any patch coupling technology. Linear shape functions were employed with minimum element dimension $h = \ell/4$. The results show that the IGA discrete crack approach featuring penalty coupling of patches can reproduce the load–displacement curves of the classical finite element framework. Another advantage of the discrete crack modeling is the fact that it does not need pre-refinement of the area in which the initial crack is defined (see for example Fig. 16a for comparison with phase-field induced pre-crack), requiring fewer elements and so allowing for faster analyses. However, the modeling of pre-cracks with patch discontinuities needs to be treated carefully since it might involve contact between the uncoupled patches edge, i.e. the crack surfaces. The current approach does not prevent penetration and a contact formulation should be added to the model for avoiding the problem and correctly simulate critical loads. For the examples presented in this work no penetration of crack surfaces happens, but this should be checked when the methodology is applied. In case the pre-crack is modeled using phase-field, the strain energy split and the degradation only of the “tensile” component avoid the penetration problem.

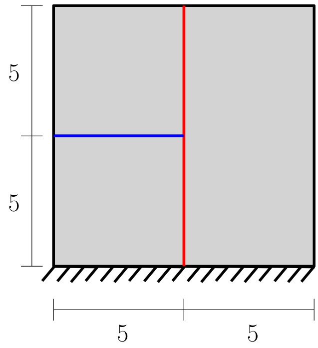

Fig. 25. Setup of the single-edge notched specimens test with discrete pre-crack (dimensions in mm). Lines indicate patch boundaries. Red lines indicate the ones coupled by penalty, blue lines indicate the ones which were not coupled and which constitute the pre-crack. (For interpretation of the references to color in this figure legend, the reader is referred to the web version of this article.)

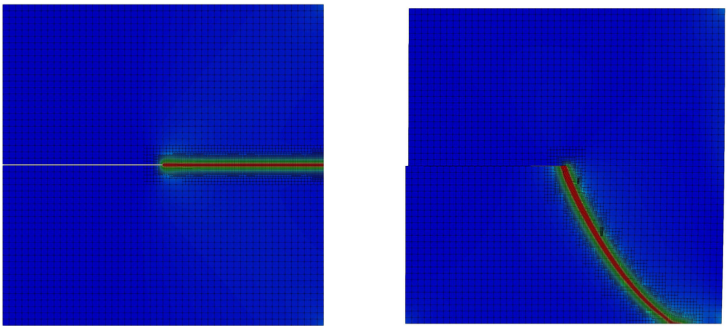

(a) Tensile case

(b) Shear case

Fig. 26. Single-edge notch specimen, final stage of the analyses with discrete pre-crack. Deformed structure scaled by a factor of 100 for visualization.

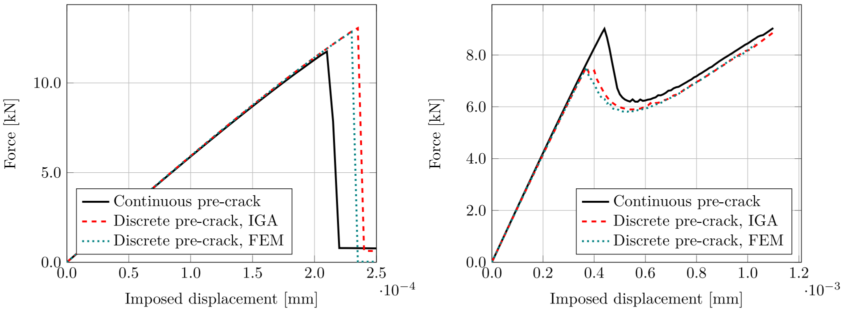

(a) Tensile case

(b) Shear case

Fig. 27. Single-edge notched specimen in tension, comparison of the load–displacements curves with different treatment of the pre-crack.

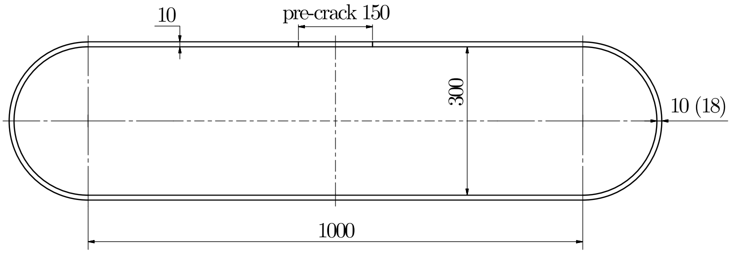

Fig. 28. Fractured pressurized cylinder, setup of the problem (dimensions in mm).

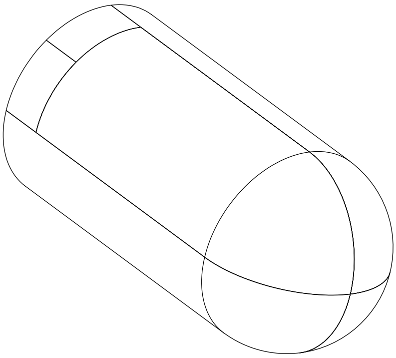

Fig. 29. Fractured pressurized cylinder, half model used for the simulation, thanks to symmetry. Lines indicate the division of the geometry in patches.

4.5. *Multipatch example with smooth patch interfaces: pressurized cylinder with hemispherical caps*

We apply the presented formulation and solution algorithm to a shell example featuring a pressurized cylinder with hemispherical end caps and an initial crack. The example resembles the one considered by Borden et al. [21], who simulated the dynamic brittle fracture of the structure using solid elements. In our case, the shell formulation previously introduced is employed, since it can be favorably used for the discretization of the geometry, as shown in Fig. 28. Two alternative geometries are considered, one with uniform shell thickness equal to 10 mm and one with thicker hemispherical caps having $t = 18$ mm. We take advantage of the symmetry of the problem for modeling only half of the structure (the symmetry condition is imposed by penalty). We use the multipatch approach for modeling the structure and the initial notch with a discrete pre-crack represented by a discontinuity between the patches (see Fig. 29). The material parameters adopted for the analysis are $E = 190 \times 10^3$ N/mm^2, $\nu = 0.3$, $G_c = 22.13$ N/mm and $\ell = 2.5$ mm. Since all the patch interfaces are smooth, the fourth-order phase-field formulation, with C^0 and C^1 continuity of s imposed by penalty between patch boundaries, is adopted. Figs. 30 and 31 show the final crack state for the two situations. In the uniform thickness case, the crack grows straight towards the center of the hemispherical caps, while in the setup with thicker caps the crack branches and grows in circumferential direction along the juncture of cylinder and end-caps. Fig. 32 displays the load–displacement curves for the two cases.

4.6. *Multipatch example with non-smooth patches interfaces: two-field beam with I-profile*

As a final example, we consider a beam having I-shaped cross section, with three supports and subjected to two point loads, each of them acting at the middle of the two beam sections. Geometry and setup of the problem are shown in Fig. 33, while material parameters are $E = 190 \times 10^3$ N/mm^2, $\nu = 0.30$, $G_c = 0.295$ N/mm and $\ell = 7.5$ mm. Each section of the beam is modeled using three patches, one for the web and two for the flanges. In this

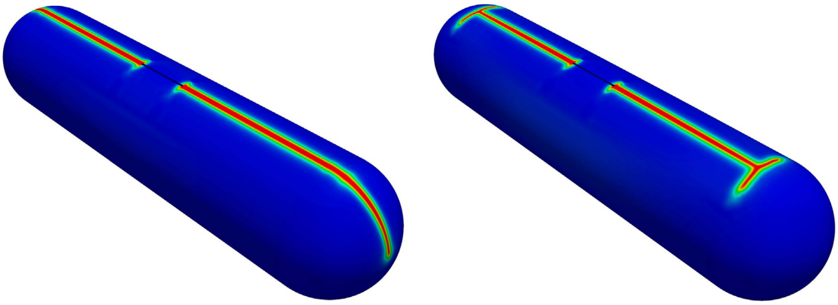

(a) Uniform thickness case (b) Case with thicker end-caps

Fig. 30. Fractured pressurized cylinder problem, final crack state over the deformed structures.

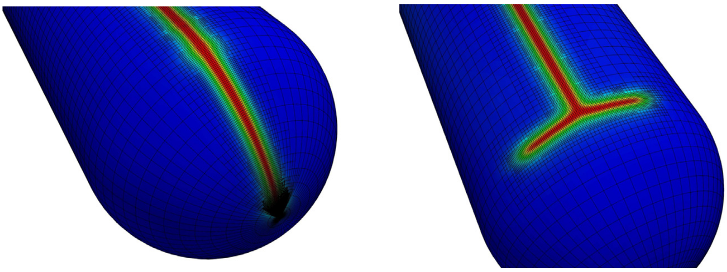

(a) Uniform thickness case (b) Case with thicker end-caps

Fig. 31. Fractured pressurized cylinder problem, details of the crack and the adaptively refined mesh in the region of the hemispherical caps.

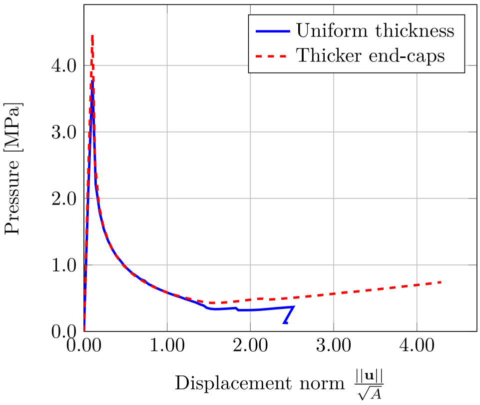

Fig. 32. Load–displacement curves for the fractured pressurized cylinder problem.

situation, the imposition of C^1 continuity for the phase-field at the interface between web and flange patches is not possible using the proposed approach and the term in (37), because the direction of the $\mathbf{a}_n$ vector cannot be chosen univocally for the patches corresponding to the flanges. Accordingly, we adopt for this example the second-order phase-field formulation, which requires only C^0 continuity of s. The simulation is run in arc-length control. Fig. 34

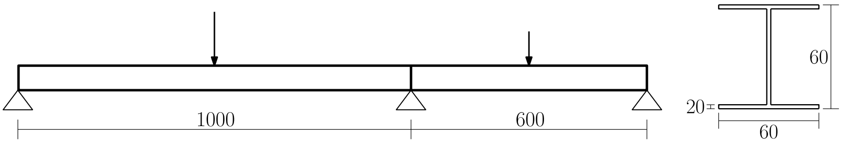

(a) Beam over three supports (b) Beam section

Fig. 33. Setup of the I-beam problem (dimensions in mm).

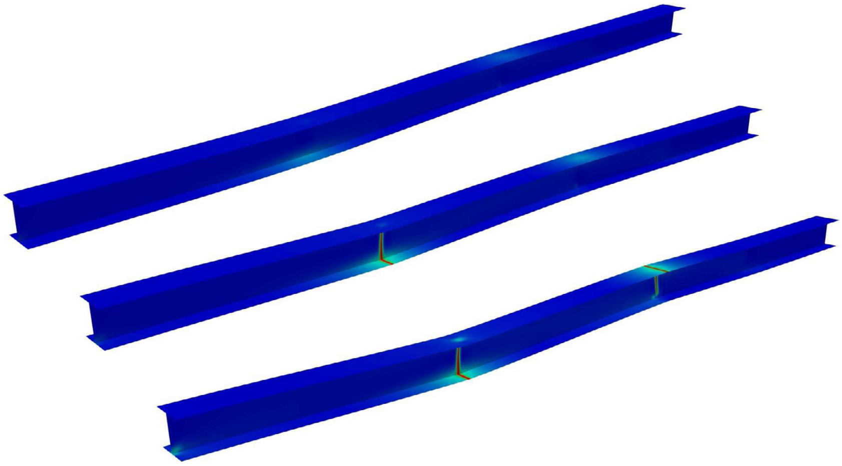

Fig. 34. I-beam problem, crack state over the deformed structure at different stages of the analysis.

shows how the fracture develops at different stages of the analysis. The first crack develops in the longer beam span, from the lower flange in tension towards the web across the patch interface. This failure of the structure corresponds to the first drop in the load–displacement curve presented in Fig. 35. After this point, the beam is still able to carry some load until a second crack develops above the middle support, this time nucleating at the top flange, which is in tension at this location. Fig. 36 shows a close-up view of the adaptively refined mesh around the first crack, which emphasizes the importance of adaptive refinement when applying the phase-field approach to larger structures, where the fractured area may cover only a very small portion of the total domain. In this simulation, the initial mesh includes 5112 elements and the final one after local refinement around the cracks counts 2.92×10^4 elements. For comparison, a uniformly pre-refined mesh with the same minimum element size would instead require 1.31×10^6 elements.

5. Conclusion

We presented an efficient simulation framework to apply the phase-field approach to brittle fracture to complex shell structures. Our framework is based on isogeometric analysis, using a rotation-free Kirchhoff–Love shell formulation for structural analysis and both second- and fourth-order phase-field formulations for fracture.

For the application to multipatch structures, we proposed penalty formulations which can handle arbitrary patch connections with matching or non-matching interfaces. The various penalty terms involved are scaled with the corresponding problem parameters such that they all can be controlled by one global penalty parameter, which is set to $\alpha = 10^3$ independently of the problem parameters. Moreover, the structural penalty terms are degraded with the phase-field degradation function in order to ensure a consistent scaling of structural stiffness and penalty stiffness in the fractured zones.

Furthermore, we presented a multistep predictor–corrector algorithm for adaptive refinement based on LR NURBS, using the phase-field value as refinement indicator. We proposed a local Bézier projection for mapping

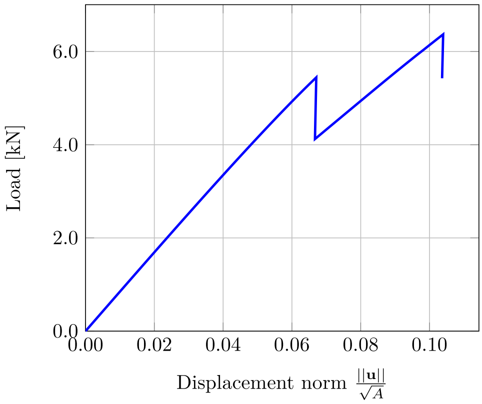

Fig. 35. Load–displacement curve for the I-beam problem.

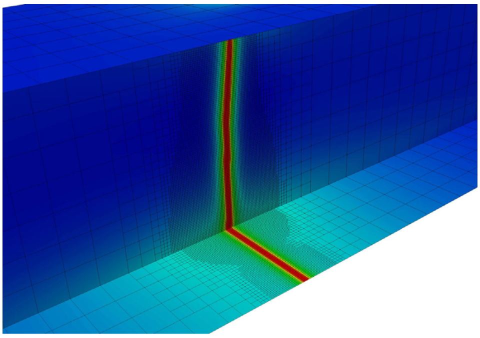

Fig. 36. I-beam problem, detail of the crack and the adaptively refined mesh between the lower flange and the web.

the history field, which is defined at integration points, from coarser to finer meshes. The corresponding projection matrix depends only on the polynomial degree and is identical for all elements of a mesh throughout all load steps, hence it can be precomputed at the beginning of the analysis, making this mapping approach computationally inexpensive. We also demonstrated that the proposed approach can accurately predict and refine the crack path even in cases where fracture fully develops in a single load step, yielding identical results to simulations with static pre-refined meshes. This is crucial for the application to large structures without *a priori* knowledge of the crack path, since uniform refinement with an element size resolving the internal length scale would be prohibitive due to the excessively high number of elements required.

Furthermore, we investigated and compared the computational efficiency of loosely vs. strongly coupled staggering strategies and of second- vs. fourth-order phase-field formulations within our framework. From our simulations, we found that a strongly staggered scheme is generally more efficient since it requires in total fewer solutions of the computationally more expensive momentum equations (the structural problem is intrinsically nonlinear due to the tension–compression split of the strain tensor). Moreover, we found that the fourth-order phase-field model is in general more efficient than the second-order model, although the formulation is more involved, due to different reasons. Firstly, the faster convergence of the method leads to fewer staggered iterations of the coupled problem, i.e., fewer solutions of the momentum equations. Secondly, it has a narrower crack profile which decreases the necessary number of elements to resolve the crack. Finally, the more accurate crack prediction within the proposed predictor–corrector scheme for adaptive refinement leads to fewer recomputation steps compared to the second-order formulation. Therefore, we chose to use the fourth-order model whenever possible, i.e., when the domain is smooth. For non-smooth multipatch structures, however, we resort to the second-order formulation, since the orientation of the directional derivatives at the patch interfaces is not always unique in such cases.

For future research, we plan to extend the presented approach to ductile fracture, envisaging the application to steel structures, as well as the extension to dynamic fracture and fatigue.

Declaration of competing interest

The authors declare that they have no known competing financial interests or personal relationships that could have appeared to influence the work reported in this paper.

Acknowledgments

The authors gratefully acknowledge the support from the Research Council of Norway, NFR, and the German Academic Exchange Service, DAAD, through the project *FATIKA - Isogeometric phase-field modeling of fatigue in slender structures*, project number 281247.

References

[1] G.A. Francfort, J.-J. Marigo, Revisiting brittle fracture as an energy minimization problem, J. Mech. Phys. Solids 46 (8) (1998) 1319–1342.
[2] A.A. Griffith, The phenomena of rupture and flow in solids, Philos. Trans. R. Soc. Lond. Ser. A 221 (1921) 163–198.
[3] B. Bourdin, G.A. Francfort, J.-J. Marigo, Numerical experiments in revisited brittle fracture, J. Mech. Phys. Solids 48 (4) (2000) 797–826.
[4] K. Pham, H. Amor, J.-J. Marigo, C. Maurini, Gradient damage models and their use to approximate brittle fracture, Int. J. Damage Mech. 20 (4) (2011) 618–652.
[5] R. de Borst, C.V. Verhoosel, Gradient damage vs phase-field approaches for fracture: Similarities and differences, Comput. Methods Appl. Mech. Engrg. 312 (2016) 78–94.
[6] B. Bourdin, G.A. Francfort, J.-J. Marigo, The variational approach to fracture, J. Elasticity 91 (1–3) (2008) 5–148.
[7] C. Miehe, M. Hofacker, F. Welschinger, A phase field model for rate-independent crack propagation: Robust algorithmic implementation based on operator splits, Comput. Methods Appl. Mech. Engrg. 199 (45) (2010) 2765–2778.
[8] H. Amor, J.-J. Marigo, C. Maurini, Regularized formulation of the variational brittle fracture with unilateral contact: Numerical experiments, J. Mech. Phys. Solids 57 (8) (2009) 1209–1229.
[9] F. Freddi, G. Royer-Carfagni, Regularized variational theories of fracture: A unified approach, J. Mech. Phys. Solids 58 (8) (2010) 1154–1174.
[10] C. Steinke, M. Kaliske, A phase-field crack model based on directional stress decomposition, Comput. Mech. 63 (5) (2019) 1019–1046.
[11] M.J. Borden, Isogeometric Analysis of Phase-Field Models for Dynamic Brittle and Ductile Fracture (PhD thesis), 2012.
[12] C. Kuhn, A. Schlüter, R. Müller, On degradation functions in phase field fracture models, Comput. Mater. Sci. 108 (2015) 374–384.
[13] T. Gerasimov, L. De Lorenzis, A line search assisted monolithic approach for phase-field computing of brittle fracture, Comput. Methods Appl. Mech. Engrg. 312 (2016) 276–303.
[14] C. Kuhn, R. Müller, A continuum phase field model for fracture, Eng. Fract. Mech. 77 (18) (2010) 3625–3634.
[15] M. Ambati, T. Gerasimov, L. De Lorenzis, A review on phase-field models of brittle fracture and a new fast hybrid formulation, Comput. Mech. 55 (2) (2015) 383–405.
[16] M. Ambati, T. Gerasimov, L. De Lorenzis, Phase-field modeling of ductile fracture, Comput. Mech. 55 (5) (2015) 1017–1040.
[17] F.P. Duda, A. Ciarbonetti, P.J. Sánchez, A.E. Huespe, A phase-field/gradient damage model for brittle fracture in elastic-plastic solids, Int. J. Plast. 65 (2015) 269–296.
[18] R. Alessi, J.-J. Marigo, S. Vidoli, Gradient damage models coupled with plasticity: Variational formulation and main properties, Mech. Mater. 80 (2015) 351–367.
[19] M.J. Borden, T.J.R. Hughes, C.M. Landis, A. Anvari, I.J. Lee, A phase-field formulation for fracture in ductile materials: Finite deformation balance law derivation, plastic degradation, and stress triaxiality effects, Comput. Methods Appl. Mech. Engrg. 312 (2016) 130–166.
[20] B. Bourdin, C.J. Larsen, C.L. Richardson, A time-discrete model for dynamic fracture based on crack regularization, Int. J. Fract. 168 (2) (2011) 133–143.
[21] M.J. Borden, C.V. Verhoosel, M.A. Scott, T.J.R. Hughes, C.M. Landis, A phase-field description of dynamic brittle fracture, Comput. Methods Appl. Mech. Engrg. 217 (2012) 77–95.
[22] M. Hofacker, C. Miehe, A phase field model of dynamic fracture: Robust field updates for the analysis of complex crack patterns, Internat. J. Numer. Methods Engrg. 93 (3) (2012) 276–301.
[23] B. Li, C. Peco, D. Millán, I. Arias, M. Arroyo, Phase-field modeling and simulation of fracture in brittle materials with strongly anisotropic surface energy, Internat. J. Numer. Methods Engrg. 102 (3–4) (2015) 711–727.
[24] S. Teichtmeister, D. Kienle, F. Aldakheel, M.-A. Keip, Phase field modeling of fracture in anisotropic brittle solids, Int. J. Non-Linear Mech. 97 (Supplement C) (2017) 1–21.

[25] J.L. Boldrini, E.A. Barros de Moraes, L.R. Chiarelli, F.G. Fumes, M.L. Bittencourt, A non-isothermal thermodynamically consistent phase field framework for structural damage and fatigue, Comput. Methods Appl. Mech. Engrg. 312 (2016) 395–427.

[26] A. Mesgarnejad, A. Imanian, A. Karma, Phase-field models for fatigue crack growth, Theor. Appl. Fract. Mech. 103 (2012) 102282.

[27] P. Carrara, M. Ambati, R. Alessi, L. De Lorenzis, A framework to model the fatigue behavior of brittle materials based on a variational phase-field approach, Comput. Methods Appl. Mech. Engrg. 361 (2020) 112731.

[28] M. Seiler, T. Linse, P. Hantschke, M. Kästner, An efficient phase-field model for fatigue fracture in ductile materials, Eng. Fract. Mech. 224 (2020) 106807.

[29] A. Mesgarnejad, B. Bourdin, M.M. Khonsari, Validation simulations for the variational approach to fracture, Comput. Methods Appl. Mech. Engrg. 290 (2015) 420–437.

[30] K.H. Pham, K. Ravi-Chandar, C.M. Landis, Experimental validation of a phase-field model for fracture, Int. J. Fract. 205 (1) (2017) 83–101.

[31] T. Wu, A. Carpiuc-Prisacari, M. Poncelet, L. De Lorenzis, Phase-field simulation of interactive mixed-mode fracture tests on cement mortar with full-field displacement boundary conditions, Eng. Fract. Mech. 182 (2017) 658–688.

[32] E. Tanné, T. Li, B. Bourdin, J.-J. Marigo, C. Maurini, Crack nucleation in variational phase-field models of brittle fracture, J. Mech. Phys. Solids 110 (2018) 80–99.

[33] M. Ambati, R. Kruse, L. De Lorenzis, A phase-field model for ductile fracture at finite strains and its experimental verification, Comput. Mech. 57 (1) (2016) 149–167.

[34] M.J. Borden, T.J.R. Hughes, C.M. Landis, C.V. Verhoosel, A higher-order phase-field model for brittle fracture: Formulation and analysis within the isogeometric analysis framework, Comput. Methods Appl. Mech. Engrg. 273 (2014) 100–118.

[35] M.A. Msekh, J.M. Sargado, M. Jamshidian, P.M. Areias, T. Rabczuk, Abaqus implementation of phase-field model for brittle fracture, Comput. Mater. Sci. 96 (2015) 472–484.

[36] G. Liu, Q. Li, M.A. Msekh, Z. Zuo, Abaqus implementation of monolithic and staggered schemes for quasi-static and dynamic fracture phase-field model, Comput. Mater. Sci. 121 (2016) 35–47.

[37] G. Molnár, A. Gravouil, 2D and 3D Abaqus implementation of a robust staggered phase-field solution for modeling brittle fracture, Finite Elem. Anal. Des. 130 (Supplement C) (2017) 27–38.

[38] K. Seleš, T. Lesičar, Z. Tonković, J. Sorić, A residual control staggered solution scheme for the phase-field modeling of brittle fracture, Eng. Fract. Mech. (2018).

[39] M. Ambati, L. De Lorenzis, Phase-field modeling of brittle and ductile fracture in shells with isogeometric NURBS-based solid-shell elements, Comput. Methods Appl. Mech. Engrg. 312 (Supplement C) (2016) 351–373.

[40] J. Reinoso, M. Paggi, C. Linder, Phase field modeling of brittle fracture for enhanced assumed strain shells at large deformations: formulation and finite element implementation, Comput. Mech. 59 (6) (2017) 981–1001.

[41] P. Areias, T. Rabczuk, M.A. Msekh, Phase-field analysis of finite-strain plates and shells including element subdivision, Comput. Methods Appl. Mech. Engrg. 312 (2016) 322–350.

[42] F. Amiri, D. Millán, Y. Shen, T. Rabczuk, M. Arroyo, Phase-field modeling of fracture in linear thin shells, Theor. Appl. Fract. Mech. 69 (2014) 102–109.

[43] H. Ulmer, M. Hofacker, C. Miehe, Phase field modeling of fracture in plates and shells, Proc. Appl. Math. Mech. 12 (1) (2012) 171–172.

[44] J. Kiendl, M. Ambati, L. De Lorenzis, H. Gomez, A. Reali, Phase-field description of brittle fracture in plates and shells, Comput. Methods Appl. Mech. Engrg. 312 (2016) 374–394.

[45] K. Paul, C. Zimmermann, K.K. Mandadapu, T.J.R. Hughes, C.M. Landis, R.A. Sauer, An adaptive space-time phase field formulation for dynamic fracture of brittle shells based on LR NURBS, Comput. Mech. (2020).

[46] S. Burke, C. Ortner, E. Süli, An adaptive finite element approximation of a variational model of brittle fracture, SIAM J. Numer. Anal. 48 (3) (2010) 980–1012.

[47] M. Artina, M. Fornasier, S. Micheletti, S. Perotto, Anisotropic mesh adaptation for crack detection in brittle materials, SIAM J. Sci. Comput. 37 (4) (2015) B633–B659.

[48] G. Del Piero, G. Lancioni, R. March, A variational model for fracture mechanics: Numerical experiments, J. Mech. Phys. Solids 55 (12) (2007) 2513–2537.

[49] T. Wick, Goal functional evaluations for phase-field fracture using PU-based DWR mesh adaptivity, Comput. Mech. 57 (6) (2016) 1017–1035.

[50] T. Heister, M.F. Wheeler, T. Wick, A primal-dual active set method and predictor-corrector mesh adaptivity for computing fracture propagation using a phase-field approach, Comput. Methods Appl. Mech. Engrg. 290 (2015) 466–495.

[51] M. Klinsmann, D. Rosato, M. Kamlah, R.M. McMeeking, An assessment of the phase field formulation for crack growth, Comput. Methods Appl. Mech. Engrg. 294 (2015) 313–330.

[52] S. Nagaraja, M. Elhaddad, M. Ambati, S. Kollmannsberger, L. De Lorenzis, E. Rank, Phase-field modeling of brittle fracture with multi-level hp-FEM and the finite cell method, Comput. Mech. (2018).

[53] D.R. Forsey, R.H. Bartels, Hierarchical B-spline refinement, ACM Siggraph Comput. Graph. 22 (4) (1988) 205–212.

[54] A.-V. Vuong, C. Giannelli, B. Jüttler, B. Simeon, A hierarchical approach to adaptive local refinement in isogeometric analysis, Comput. Methods Appl. Mech. Engrg. 200 (49) (2011) 3554–3567.

[55] C. Giannelli, B. Jüttler, H. Speleers, THB-splines: The truncated basis for hierarchical splines, Comput. Aided Geom. Design 29 (7) (2012) 485–498.

[56] T.W. Sederberg, J. Zheng, A. Bakenov, A. Nasri, T-splines and T-NURCCs, ACM Trans. Graph. (TOG) 22 (3) (2003) 477–484.

[57] Y. Bazilevs, V.M. Calo, J.A. Cottrell, J.A. Evans, T.J.R. Hughes, S. Lipton, M.A. Scott, T.W. Sederberg, Isogeometric analysis using T-splines, Comput. Methods Appl. Mech. Engrg. 199 (5) (2010) 229–263.

[58] E.J. Evans, M.A. Scott, X. Li, D.C. Thomas, Hierarchical T-splines: Analysis-suitability, Bézier extraction, and application as an adaptive basis for isogeometric analysis, Comput. Methods Appl. Mech. Engrg. 284 (2015) 1–20.
[59] T. Dokken, T. Lyche, K.F. Pettersen, Polynomial splines over locally refined box-partitions, Comput. Aided Geom. Design 30 (3) (2013) 331–356.
[60] K.A. Johannessen, T. Kvamsdal, T. Dokken, Isogeometric analysis using LR B-splines, Comput. Methods Appl. Mech. Engrg. 269 (2014) 471–514.
[61] K.A. Johannessen, F. Remonato, T. Kvamsdal, On the similarities and differences between Classical Hierarchical, Truncated Hierarchical and LR B-splines, Comput. Methods Appl. Mech. Engrg. 291 (2015) 64–101.
[62] C. Zimmermann, R.A. Sauer, Adaptive local surface refinement based on LR NURBS and its application to contact, Comput. Mech. 60 (6) (2017) 1011–1031.
[63] M. Kästner, P. Hennig, T. Linse, V. Ulbricht, Phase-field modelling of damage and fracture–convergence and local mesh refinement, in: Advanced Methods of Continuum Mechanics for Materials and Structures, Springer, 2016, pp. 307–324.
[64] P. Hennig, S. Müller, M. Kästner, Bézier extraction and adaptive refinement of truncated hierarchical NURBS, Comput. Methods Appl. Mech. Engrg. 305 (2016) 316–339.
[65] P. Hennig, M. Ambati, L. De Lorenzis, M. Kästner, Projection and transfer operators in adaptive isogeometric analysis with hierarchical B-splines, Comput. Methods Appl. Mech. Engrg. 334 (2018) 313–336.
[66] J. Kiendl, K.-U. Bletzinger, J. Linhard, R. Wüchner, Isogeometric shell analysis with Kirchhoff-Love elements, Comput. Methods Appl. Mech. Engrg. 198 (49) (2009) 3902–3914.
[67] A.J. Herrema, E.L. Johnson, D. Proserpio, M.C.H. Wu, J. Kiendl, M.-C. Hsu, Penalty coupling of non-matching isogeometric Kirchhoff-Love shell patches with application to composite wind turbine blades, Comput. Methods Appl. Mech. Engrg. 346 (2019) 810–840.
[68] J.F. Caseiro, R.A.F. Valente, A. Reali, J. Kiendl, F. Auricchio, R.J. Alves de Sousa, On the Assumed Natural Strain method to alleviate locking in solid-shell NURBS-based finite elements, Comput. Mech. 53 (6) (2014) 1341–1353.
[69] P. Areias, J. Garção, E.B. Pires, J. Infante Barbosa, Exact corotational shell for finite strains and fracture, Comput. Mech. 48 (4) (2011) 385–406.
[70] P. Areias, T. Rabczuk, Finite strain fracture of plates and shells with configurational forces and edge rotations, Internat. J. Numer. Methods Engrg. 94 (12) (2013) 1099–1122.
[71] K. Weinberg, C. Hesch, A high-order finite deformation phase-field approach to fracture, Contin. Mech. Thermodyn. 29 (4) (2017) 935–945.

A.4 Paper 4

Davide Proserpio, Marreddy Ambati, Laura De Lorenzis, Josef Kiendl

Phase-field simulation of ductile fracture in shell structures

Submitted to Computer Methods in Applied Mechanics and Engineering

Phase-field simulation of ductile fracture in shell structures

Davide Proserpio[a,b,*], Marreddy Ambati[c], Laura De Lorenzis[d], Josef Kiendl[a,b]

[a]*Institute of Engineering Mechanics and Structural Analysis – Bundeswehr University Munich, Werner-Heisenberg-Weg 39, 85577 Neubiberg, Germany*
[b]*Department of Marine Technology – Norwegian University of Science and Technology, Otto Nielsens veg 10, 7052 Trondheim, Norway*
[c]*Institute of Solid Mechanics – TU Dresden, George-Bähr-Straße 3c, 01069 Dresden, Germany*
[d]*Department of Mechanical and Process Engineering – ETH Zürich, Tannenstraße 3, 8092 Zürich, Switzerland*

Abstract

In this paper, a computational framework for simulating ductile fracture in multipatch shell structures is presented. A ductile fracture phase-field model at finite strains is combined with an isogeometric Kirchhoff-Love shell formulation. For the application to complex structures, we employ a penalty approach for imposing, at patch interfaces, displacement and rotational continuity and C^0 and C^1 continuity of the phase-field, the latter required if a higher-order phase-field formulation is adopted. We study the mesh dependency of the numerical model and we show that mesh refinement allows for capturing important features of ductile fracture such as cracking along shear bands. Therefore, we investigate the effectiveness of a predictor-corrector algorithm for adaptive mesh refinement based on LR NURBS. Thanks to the adoption of time- and space-adaptivity strategies, it is possible to simulate the failure of complex structures with a reasonable computational effort. Finally, we compare the predictions of the numerical model with experimental results from indentation tests performed on stiffened steel panels.

Keywords: Phase-field model; Ductile fracture; Isogeometric; Shell; Multipatch; Adaptive refinement

---

1. Introduction

The numerical prediction of the fracture and post-failure behavior of shell structures constituted by ductile materials like metals requires sophisticated simulation tools. Adequate formulations for the description of ductility and fracture, in combination with structural models, are needed. The phase-field approach for the simulation of fracture has been the

---

[*] Corresponding author
Email address: `davide.proserpio@ntnu.no` (Davide Proserpio)

Preprint submitted to Computer Methods in Applied Mechanics and Engineering *December 17, 2020*

object of several studies in the last years. The formulation, stemming directly from Griffith's theory [1], is based on the description of brittle fracture in a variational framework by Francfort and Marigo [2], later regularized by Bourdin et al. [3]. The competition between the strain and the fracture surface energy controls the nucleation and growth of cracks, which are described by the smooth variation, between the intact and broken material states, of a continuous scalar parameter, the so-called phase-field. The formulation is now well established for the brittle fracture case thanks to various advances from the original formulation. Among others, we recall the different approaches for introducing a split in the strain energy in order to take into account the physical asymmetry of the fracture behavior in tension and compression [4–7], for employing alternative degradation functions for the tensile part of the elastic strain energy instead of the standard quadratic one [8, 9], for enforcing the irreversibility of fracture [5, 10], and for adopting a higher-order phase-field formulation [11], or a dissipation function capable of reproducing the initial linear elastic behavior of the material before fracture [12].

The phase-field simulation of fracture in ductile materials requires a more complex formulation that includes, in addition to the elastic and fracture energy contributions already present in the brittle fracture approach, an energy dissipation term related to plastic deformation. The main challenge of these models is represented by the interaction between the dissipative term related to plasticity and the fracture term, and how these contributions are coupled, taking into account the fact that usually, in ductile materials, the plastic flow precedes the crack growth. Miehe et al. [13] consider a classical formulation of the fracture energy contributions (i.e. the same used for brittle fracture) applied to thermo-elastic-plastic materials and investigate the experimentally observed transition between brittle and ductile fracture due to dynamic loading conditions. The work by Alessi et al. [14] reviews several phase-field approaches for ductile fracture. The formulation proposed by Duda et al. [15] can be considered as a "brittle fracture in elasto-plastic solids" since no coupling is assumed between the phase-field and the plasticity. In the model by Ambati et al., at first proposed for the small strains framework [16] and then extended to finite strains [17], the coupling between the two terms is included in the degradation function of the tensile part of the elastic strain energy, since this function depends on the accumulated plastic strain. In the formulations by Alessi et al. [18, 19], Borden et al. [9], Kuhn et al. [20], Huang et al. [21], Rodriguez et al. [22] and Miehe et al. [23], the damage-plastic coupling is based on the fact that a degradation function depending on the phase-field parameter is defined not only for the bulk elastic strain energy, but also for the hardening energy contribution and the plastic dissipated work. The latter two references include also a non-local gradient formulation for plasticity. Dittman and co-workers [24] adopt the higher-order phase-field formulation and couple the plasticity and fracture behaviors by degrading the critical fracture energy by a function depending on the equivalent plastic strain.

The phase-field method has been coupled with plate and shell models for simulating brittle fracture in thin-walled structures adopting different approaches [25–28]. The formulations by Kiendl et al. [29] and Paul et al. [30], based on the idea of performing the tension-compression split at various integration points through the shell thickness and then numerically integrating the strain energy contributions along these points, have been also extended to the case of multipatch structures with isogeometric analysis [31, 32]. A similar approach has been recently adopted by Kikis et al. [33] for modeling phase-field brittle fracture in Reissner-Mindlin shells and plates. Pillai et al. [34] also presented a formulation for phase-field brittle fracture in a MITC4+ Reissner-Mindlin degenerated shell element. Formulations for ductile fracture have only been applied to a solid shell model in the small strains setting [35].

Several works are focused on the validation of the phase-field fracture approach through the comparison of the results of numerical simulations with experimental tests, such as [36–40] for the brittle case. For ductile fracture, we recall the works by Wick et al. [41] and Borden et al. [9] which report qualitative results for the fracture of screws and of a bolted plate, respectively. A quantitative comparison, showing good agreement of the results of ductile fracture phase-field simulations and experiments, is reported by Ambati et al. [17].

The aim of this work is to present an isogeometric phase-field approach for simulating the ductile fracture of thin plates and shells and to test and validate the model through the comparison of numerical analyses with experimental benchmarks. In addition, we study how the mesh refinement influences the results of the model in terms of fracture path and load-displacement curves. The computational efficiency of the simulations is therefore improved by employing a predictor-corrector algorithm for the adaptive local refinement of the mesh only in the region where it is needed, i.e. in the vicinity of the cracked area. In view of simulating the behavior of real-world structures, we adopt a penalty formulation for patch coupling that allows the description of geometrically complex multipatch structures.

The paper is outlined as follows. Section 2 provides the details of the proposed approach. Firstly, the elasto-plasticity formulation and its combination with a rotation-free isogeometric Kirchhoff-Love shell model are reviewed. A phase-field approach for ductile fracture at finite strains, including its higher-order formulation, is then presented and a detailed explanation is provided about its coupling to the elasto-plastic shell model. In the same section, we introduce the penalty formulation for coupling the structural and phase-field behaviors of adjacent shells in multipatch structures and we briefly present the penalty contact formulation used for the simulation of the experimental tests. We also focus on the employed solution algorithm, especially on the staggering and on the adaptive step size schemes. Section 3 is devoted to the study of the effects of mesh refinement on the ductile fracture phase-field simulations through numerical experiments, and to the presentation and application of an adaptive local refinement procedure. In Section 4, the proposed approach is validated by the simulation and the comparison with the results of indentation tests on stiffened steel plates. The paper is closed by the conclusions in Section 5.

2. Formulation

This section presents the main features of the adopted phase-field ductile fracture approach and how this formulation is coupled with a model for shells and plates. Firstly, the main aspects of a Kirchhoff-Love shell formulation for elasto-plasticity are introduced, then a phase-field ductile fracture model valid in the finite strains regime is presented and combined with the structural model. Lastly, a penalty patch coupling and a penalty contact formulation, adopted for the numerical simulations of section 4, are briefly recalled.

2.1. Elasto-plasticity formulation for Kirchhoff-Love shells

We adopt a rotation-free Kirchhoff-Love shell formulation developed by Kiendl et al. [42] in the framework of isogeometric analysis (IGA). The main assumption for thin shell theories is that segments which are perpendicular to the midsurface in the undeformed configuration remain straight and normal to the midsurface during deformation, so that the transverse shear deformation can be neglected. Therefore, the description of the shell kinematics is reduced to the description of its middle surface.

In the shell governing equations, we use the curvilinear coordinates θ^1 and θ^2 for the midsurface and the coordinate $\theta^3 \in [-t/2, +t/2]$ for the thickness direction, with t indicating the shell thickness. Considering a point $\mathbf{r}(\theta^1, \theta^2)$ on the middle surface of the shell, the tangent base vectors $\mathbf{a}_\alpha$, constituting a covariant coordinate system, are defined as:

$$\mathbf{a}_\alpha = \frac{\partial \mathbf{r}}{\partial \theta^\alpha}. \tag{1}$$

According to the adopted index notation, Greek indices α and β assume the values $\{1, 2\}$ for indicating the in-plane components, while Latin indices i and j take the values $\{1, 2, 3\}$. Partial derivatives with respect to θ^α are indicated as $(\cdot)_{,\alpha} = \partial(\cdot)/\partial\theta^\alpha$, so that equation (1) can be written also as $\mathbf{a}_\alpha = \mathbf{r}_{,\alpha}$. The dual contravariant base vectors are defined by $\mathbf{a}^\alpha \cdot \mathbf{a}_\beta = \delta^\alpha_\beta$, with δ^α_β being the Kronecker delta, and they can be used for defining a contravariant coordinate system on the shell midsurface. The unit normal vector in thickness direction is defined as:

$$\mathbf{a}_3 = \frac{\mathbf{a}_1 \times \mathbf{a}_2}{\|\mathbf{a}_1 \times \mathbf{a}_2\|}. \tag{2}$$

Considering a point in the shell continuum and $\mathbf{x}$ being its position vector in the deformed configuration, the position of the vector can be described, due to the Kirchhoff assumption, by the corresponding point on the midsurface $\mathbf{r}$ and the fiber director $\mathbf{a}_3$:

$$\mathbf{x} = \mathbf{r} + \theta^3 \mathbf{a}_3. \tag{3}$$

Accordingly, the base vectors, defined at any point $\mathbf{x}$ in the shell continuum, are denoted as $\mathbf{g}_i = \mathbf{x}_{,i}$ and take the form:

$$\mathbf{g}_\alpha = \mathbf{a}_\alpha + \theta^3 \mathbf{a}_{3,\alpha}, \qquad \mathbf{g}_3 = \mathbf{a}_3. \tag{4}$$

The dual contravariant base vectors can be retrieved by the expression $\mathbf{g}^i \cdot \mathbf{g}_j = \delta^i_j$. As follows, the notation $\overset{\circ}{(\cdot)}$ indicates the undeformed configuration of the geometric variables. With these terms in hand, the covariant components of the deformation gradient $\mathbf{F} = d\mathbf{x}/d\mathring{\mathbf{x}}$, in the curvilinear reference system constituted by the contravariant bases in the undeformed configuration $\mathring{\mathbf{g}}^i \otimes \mathring{\mathbf{g}}^j$, can be computed as:

$$F_{ij} = \mathring{\mathbf{g}}_i \cdot \mathbf{g}_j. \tag{5}$$

Accordingly, the right Cauchy-Green deformation tensor $\mathbf{C} = \mathbf{F}^T\mathbf{F}$ covariant components can be defined as:

$$C_{ij} = \mathbf{g}_i \cdot \mathbf{g}_j. \tag{6}$$

The adopted approach for plasticity, based on the work from Simo [43], consists in a standard three-dimensional isochoric von-Mises $J2$ rate-independent plasticity theory at finite strains, which employs a multiplicative decomposition of the deformation gradient into its elastic and plastic parts:

$$\mathbf{F} = \mathbf{F}^e \mathbf{F}^p. \tag{7}$$

From the elastic deformation gradient, the elastic left Cauchy-Green deformation tensor $\mathbf{b}^e$ is computed as:

$$\mathbf{b}^e = \mathbf{F}^e \mathbf{F}^{eT}. \tag{8}$$

The determinant of the elastic deformation gradient tensor, which is a measure of the elastic change of volume, is designated as $J^e = \det[\mathbf{F}^e]$. We adopt a neo-Hookean constitutive law of decoupled type for describing the elastic behavior of the material. According to this approach, the strain energy density ψ_e can be additively decomposed into a volumetric (shape preserving) and a deviatoric (volume preserving) part:

$$\psi_e = \psi_e^{vol} + \psi_e^{dev}. \tag{9}$$

The two terms are computed as follows:

$$\psi_e^{vol} = \frac{\kappa_0}{2}\left(\frac{J^{e2}-1}{2} - \ln J^e\right), \tag{10}$$

$$\psi_e^{dev} = \frac{\mu}{2}\left(\bar{I}_b^e - 3\right), \tag{11}$$

with κ_0 and μ as the bulk and shear modulus of the material, respectively. In equation (11), $\bar{I}_b^e = \mathrm{tr}[\bar{\mathbf{b}}^e]$, with $\bar{\mathbf{b}}^e = J^{e-\frac{2}{3}}\mathbf{b}^e$. Further details regarding the plasticity model, including the formulation of the yield function, the associative flow rule, and the time-integration scheme required for the solution of the elasto-plastic constitutive equations can be found in Ambati et al. [44].

For the implementation of the elasto-plasticity model in the shell formulation, we adopt a stress-based approach consisting in defining integration points in the shell thickness direction where the validity of the three-dimensional material model is enforced. Consequently, the stress resultants are computed by the integration of the stress components through the thickness. In the finite strain context, it is important to point out that the considered shell formulation defines only the midsurface deformation, while the thickness deformation is neglected. In order to take into account the out-of-plane deformation, we follow the same approach as in Kiendl et al. [45] and Ambati et al. [44], and we correct the definition of the base vector in thickness direction:

$$\mathbf{g}_3 = \lambda_3\mathbf{a}_3, \tag{12}$$

where λ_3 is the thickness stretch. Accordingly, the change of $\mathbf{g}_3$ modifies the definition of the components of the deformation gradient:

$$F_{i\beta} = \mathring{\mathbf{g}}_i \cdot \mathbf{g}_\beta, \qquad F_{i3} = \lambda_3\, \mathring{\mathbf{g}}_i \cdot \mathbf{a}_3, \tag{13}$$

and also of the Cauchy-Green deformation tensor:

$$C_{\alpha\beta} = \mathbf{g}_{\alpha\beta}, \qquad C_{\alpha 3} = 0, \qquad C_{33} = {\lambda_3}^2. \tag{14}$$

However, the information about the thickness deformation cannot be retrieved directly from the shell kinematics, which is based only on the displacement field of the midsurface. For this purpose, we employ the plane stress condition as an additional constraint. This condition is expressed by the contravariant component $S^{33} = 0$ of the second Piola-Kirchhoff stress tensor $\mathbf{S} = S^{ij}\mathring{\mathbf{g}}_i \otimes \mathring{\mathbf{g}}_j$. According to the considered approach, the plane stress condition is enforced locally, in an iterative manner, at each thickness integration point. Without entering into the details, which can be found in [44], the process starts by choosing the value of λ_3 from the last converged load step ($\lambda_3 = 1$ for the first step), then the deformation gradient tensor is corrected as in equation (13) and the updated Cauchy-Green deformation tensor is computed as $\mathbf{C} = \mathbf{F}^T\mathbf{F}$. From the corrected $\mathbf{F}$, the stress tensor $\mathbf{S}$ and the elasto-plastic material tangent tensor $\mathbb{C}$ are computed according to $J2$ plasticity theory [43]. With these quantities in hand, the linearization of the plane stress conditions allows us to compute an updated value of C_{33} from the just obtained S^{33} and $\mathbb{C}^{3333}$. According to equation (14), the updated value of the thickness stretch is easily found as:

$$\lambda_3 = \sqrt{C_{33}}. \tag{15}$$

This value is used for obtaining again the corrected deformation gradient and Cauchy-Green deformation tensors, as in equations (13) and (14). From this point, the iterative process starts again and it is repeated until the plane stress condition is satisfied within a specific tolerance. With this procedure, the stress resultants and the material tensor can be computed at any point of the continuum, specifically in the considered thickness integration point. The strain tensor $\boldsymbol{\varepsilon}$, according to the Kirchhoff-Love formulation, can be defined at any location of the shell, based on the midsurface kinematics, as the sum of the membrane and bending parts as follows:

$$\boldsymbol{\varepsilon}(\theta^3) = \boldsymbol{\varepsilon}^m + \theta^3\boldsymbol{\kappa}, \tag{16}$$

where $\boldsymbol{\varepsilon}^m = \varepsilon^m_{\alpha\beta}\,\mathbf{a}^\alpha \otimes \mathbf{a}^\beta$ is the membrane strain tensor, whose covariant components can be expressed as:

$$\varepsilon^m_{\alpha\beta} = \frac{1}{2}\left(\mathbf{a}_\alpha \cdot \mathbf{a}_\beta - \mathring{\mathbf{a}}_\alpha \cdot \mathring{\mathbf{a}}_\beta\right). \tag{17}$$

The second term in equation (16) is related to bending and varies linearly with the thickness coordinate θ^3. The covariant components of the curvature change tensor $\boldsymbol{\kappa} = \kappa_{\alpha\beta}\,\mathbf{a}^\alpha \otimes \mathbf{a}^\beta$ are computed as:

$$\kappa_{\alpha\beta} = \mathring{\mathbf{a}}_{\alpha,\beta} \cdot \mathring{\mathbf{a}}_3 - \mathbf{a}_{\alpha,\beta} \cdot \mathbf{a}_3. \tag{18}$$

The presence of the second-order derivatives in the curvature expression in equation (18) requires at least C^1 continuity of the shape functions of the discretized model, making IGA a favorable choice for the discretization of the thin shell formulation.

The variational formulation used for the discretized model is based on the virtual work principle and corresponds to the weak form of the momentum equation:

$$\delta W = \delta W^{\text{int}} - \delta W^{\text{ext}} = 0. \tag{19}$$

In the definition of the internal virtual work:

$$\delta W^{\text{int}} = \int_A \left(\delta \boldsymbol{\varepsilon}^m : \boldsymbol{n} + \delta \boldsymbol{\kappa} : \boldsymbol{m}\right) dA, \tag{20}$$

$\delta \boldsymbol{\varepsilon}^m$ and $\delta \boldsymbol{\kappa}$ are computed according to equations (17), (18) and related ones, considering a virtual displacement field $\delta \mathbf{u}$. The effective stress resultants $\boldsymbol{n}$ and $\boldsymbol{m}$, for axial force and bending respectively, are computed employing numerical integration of the stresses through the thickness.

2.2. Higher order phase-field model for ductile fracture

In the phase-field fracture model, the nucleation and/or evolution of cracks are solely described through the minimization of an energy functional, as first proposed, for the case of brittle fracture, by Bourdin et al. [3]. For the ductile fracture case, we assume a regularized energy functional that includes elastic, plastic and fracture energy contributions, as in Ambati et al. [16, 17]:

$$E_\ell(\bar{\mathbf{b}}^e, J^e, \alpha, s) = \int_\Omega \left[\psi_e(\bar{\mathbf{b}}^e, J^e, p, s) + \psi_p(\alpha) + \psi_s(s)\right] dV. \tag{21}$$

The term $\psi_p(\alpha)$ represents the plastic strain energy density function, under the assumption of isotropic hardening, and α is the relative internal hardening variable corresponding to the equivalent accumulated plastic strain.

The fracture energy density function ψ_s, introduced by Bourdin et al. [3] in the regularized formulation of brittle fracture, can be expressed in its original form ("second-order phase-field model"):

$$\psi_{s,2}(s, \nabla s) = G_c \left[\frac{(1-s)^2}{4\ell} + \ell |\nabla s|^2\right], \tag{22}$$

or in the so-called "fourth-order phase-field model" form, as proposed by Borden et al. [11]:

$$\psi_{s,4}(s, \nabla s, \Delta s) = G_c \left[\frac{(1-s)^2}{4\ell} + \frac{\ell}{2}|\nabla s|^2 + \frac{\ell^3}{4}\left(\Delta s\right)^2\right]. \tag{23}$$

Choosing an expression of the fracture energy density as in equation (23) would lead to a higher-order formulation of the phase-field ductile fracture model, that has shown superior convergence rate with respect to the standard formulation [11, 31] and therefore will be adopted, whenever possible, in the numerical simulations present in this paper. As for the Kirchhoff-Love shell formulation, a discretization employing isogeometric analysis can provide the continuity required by the higher order derivatives present in the fourth-order model (C^1 continuity). For both formulations, ψ_s depends on the phase-field scalar variable s, whose smooth transition from 1, corresponding to intact material, to 0, corresponding to fully broken material, approximates the crack topology in the considered domain Ω. The scalar term ℓ is a length scale parameter that controls the width of the transition zone of the phase-field and G_c represents the fracture toughness of the material. Equations (22) and (23) employ a quadratic dissipation function in the form $(1-s)^2$, following the so-called "AT2 model" originally proposed by Ambrosio and Tortorelli [46] and later adopted by Bourdin et al. [3]. This formulation leads to a material model that does not show a perfectly linear elastic behavior, since the damage starts to accumulate from the beginning of the analysis. An alternative is represented by the "AT1 model", proposed by Pham et al. [12], which employs a linear dissipation function $(1-s)$ and according to which a linear elastic behavior of the material is obtained.

Intending to distinguish the different fracture behaviors of the material in tension and compression, we adopt an additive decomposition of the elastic strain energy ψ_e in its positive (tensile and shear, ψ_e^+) and negative (compressive, ψ_e^-) parts. Following the model adopted for the description of the $J2$ plasticity, the decomposition involves the volumetric and deviatoric contributions of the strain energy (see equations (10) and (11)), as in Borden et al. [9] (whose approach is based on the split, introduced in the small strains framework, by Amor et al. [4]), so that:

$$
\begin{aligned}
J^e < 1 &\begin{cases} \psi_e^+ = \psi_e^{dev}(\bar{\mathbf{b}}^e) \\ \psi_e^- = \psi_e^{vol}(J^e) \end{cases} \\
J^e \geq 1 &\begin{cases} \psi_e^+ = \psi_e^{dev}(\bar{\mathbf{b}}^e) + \psi_e^{vol}(J^e) \\ \psi_e^- = 0 \end{cases}
\end{aligned}
\tag{24}
$$

Accordingly, only the positive part of the elastic strain energy is degraded by the degradation function $g(s,p)$:

$$
\psi_e(\bar{\mathbf{b}}^e, J^e, p, s) = g(s,p)\ \psi_e^+(\bar{\mathbf{b}}^e, J^e) + \psi_e^-(J^e). \tag{25}
$$

The degradation function, which accounts for the deterioration of the material due to the nucleation and growth of microcracks, includes a positive small factor $\eta \approx 0$ for avoiding zero stiffness of the material in the fully cracked state, and takes the form:

$$g(s,p) = (1-\eta)s^{2p^m} + \eta, \tag{26}$$

with

$$p = \frac{\alpha}{\alpha_{crit}}. \tag{27}$$

In equation (26), the presence of p, which describes the localization and accumulation of the plastic strains, couples the plastic behavior of the material with the fracture process. The phase-field is dependent on the accumulation of the ductile damage, as the fracture can develop only in regions with significant (i.e. comparable with the critical value of the hardening variable α_{crit}) plastic strains. For elasto-plastic materials, this is in agreement with the observation that fracture occurs in areas that undergo high plastic strain. Additionally, the present formulation implies that, once the fracture starts evolving in a certain region, the plastic strain ceases to accumulate, so that the occurring deformations are totally elastic in that area. It is important to point out that, for $\alpha = \alpha_{crit}$, the standard quadratic degradation function is retrieved. The parameters α_{crit} and m can be considered as material parameters that need to be calibrated through the comparison with experimental results. The second one can assume the values $m = \{1, 2, 3, ...\}$ and controls the speed of the ductile fracture process. A higher value of m allows for a slower accumulation of the damage when $p < 1$, i.e. $\alpha < \alpha_{crit}$, and for a faster accumulation when the hardening values exceeds the critical threshold [16].

The stationarity condition of the energy functional in equation (21) with respect to s leads to the strong form of the phase-field evolution equation for ductile fracture which reads, for the second- and fourth-order formulations respectively,

$$\frac{2\,\ell}{G_c} g_{,s}\psi_e^+ + s - 4\,\ell^2\Delta s = 1, \tag{28}$$

$$\frac{2\,\ell}{G_c} g_{,s}\psi_e^+ + s - 2\,\ell^2\Delta s + \ell^4\Delta(\Delta s) = 1, \tag{29}$$

where:

$$g_{,s} = \frac{\partial g(s,p)}{\partial s} = (1-\eta)2p^m s^{(2p^m-1)}. \tag{30}$$

Unlike for the brittle fracture model, in this case, the phase-field evolution equation is non-linear.

The irreversibility of the fracture, meaning that cracks will not heal if the external loads are removed, is enforced by introducing in the phase-field model the following local history variable $\mathcal{H}^e$, defined as the maximum of the positive part of the elastic strain energy density up to the current pseudo-time T:

$$\mathcal{H}^e(T) := \max_{\tau\in[0,T]} \psi_e^+(\bar{\mathbf{b}}^e, J^e, \tau). \tag{31}$$

The history variable replaces ψ_e^+ in the phase-field evolution equation.

2.3. Phase-field ductile fracture modeling for thin shells and plates

The combination of the ductile fracture phase-field approach with the considered Kirchhoff-Love shell model is based on the methodology adopted by Kiendl et al. [29] for the brittle fracture case, which can be employed regardless of the specific shell formulation. Accordingly, the model is reduced to the behavior of the midsurface variables and we introduce the strain energy surface density Ψ_e, which expresses the elastic strain energy per unit area of the midsurface:

$$\Psi_e = \int_{-t/2}^{+t/2} \psi_e(\theta^3)\, d\theta^3. \tag{32}$$

Analogously, we can define the fracture energy surface density $\Psi_s(s)$, from the through-thickness integration of ψ_s, and the plastic energy surface density $\Psi_p(\alpha)$, based on the integration of $\psi_p(\alpha)$ along the thickness. Consequently, for the case of plates or shells, the energy functional in equation (21) can be rewritten in the following form:

$$E_\ell(\bar{\mathbf{b}}^e, J^e, \alpha, s) = \int_A \left[\Psi_e(\bar{\mathbf{b}}^e, J^e, s, p) + \Psi_p(\alpha) + \Psi_s(s)\right] dA. \tag{33}$$

Figure 1 shows how, due to the bending component related to the shell curvature change, the strain tensor linearly varies from tension to compression through the thickness (see also equation (16)). Moreover, as a consequence of the assumed plastic behavior of the material and of the degradation of the tensile part of the stress tensor due to the phase-field fracture formulation, the stress tensor itself can have a nonlinear distribution along the shell thickness. For this reason, numerical integration is employed for computing the integral in equation (32) and special attention is required for the tension-compression split, which is operated according to equation (24) at each thickness integration point. Since the correct strain tensor depends both on the membrane and on the bending components, the split needs to be computed on the total strain energy without separating the membrane and bending parts.

Unlike the formulation for brittle fracture, the adopted degradation function (see equation (26)) depends not only on the phase-field variable s, but also on the plasticity-related scalar parameter p that, according to the definition in equation (27), depends on the hardening parameter α. Since α can vary through the shell thickness, also the degradation function varies through the thickness. So, in this approach, we assume the phase-field parameter,

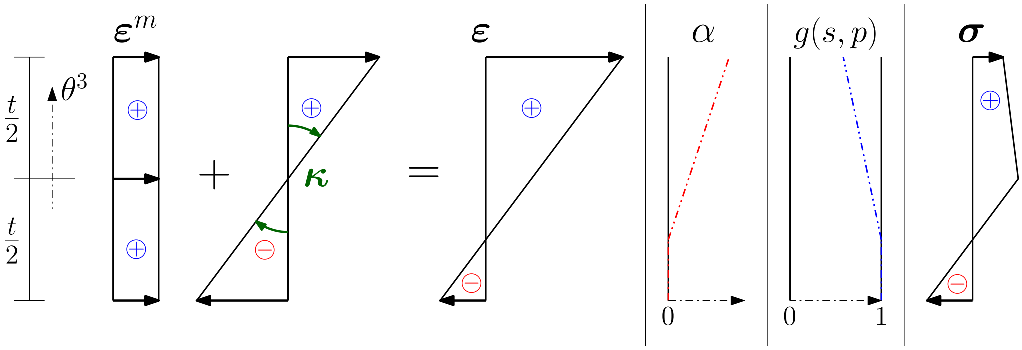

Figure 1: Combination of the contributions of membrane and bending strain and total strain $\boldsymbol{\varepsilon}$ over the thickness t for a shell subjected to bending and tension. Possible distributions of the hardening variable α and of the degradation function $g(s,p)$ along t. As a result, the through-thickness stress $\boldsymbol{\sigma}$ distribution after degradation of the positive (tensile) component is depicted.

which is defined only on the midsurface, to be constant through the thickness, but we obtain a non-constant degradation function and nonlinear distributions of the stresses (see again Figure 1). This means that, when the integral in equation (32) is computed taking into account the tension-compression split,

$$\Psi_e = \int_{-t/2}^{+t/2} \left[g(s,p)\psi_e^+(\bar{\mathbf{b}}^e, J^e) + \psi_e^-(J^e) \right] d\theta^3, \tag{34}$$

the degradation function term $g(s,p)$ needs to be included in the through-thickness numerical integration. As a consequence, the strong form of the phase-field ductile fracture evolution equation for shells, based on the stationarity condition of the energy functional (33) with respect to s, is:

$$\frac{2\,\ell}{tG_c}\int_t g_{,s}\psi_e^+ \, d\theta^3 + s - 4\,\ell^2 \Delta s = 1, \tag{35}$$

$$\frac{2\,\ell}{tG_c}\int_t g_{,s}\psi_e^+ \, d\theta^3 + s - 2\,\ell^2 \Delta s + \ell^4 \Delta(\Delta s) = 1, \tag{36}$$

with equation (35) valid for the second-order formulation and (36) for the higher-order model. The weak form of the two previous equations, including δs as a test function and considering the usual boundary conditions of the phase-field problem, read:

$$\int_A \left(\frac{2\,\ell}{tG_c}\int_t g_{,s}\mathcal{H}^e d\theta^3 + s - 1 \right) \delta s \, dA + 4\,\ell^2 \int_A \nabla s \cdot \nabla \delta s \, dA = 0, \tag{37}$$

$$\int_A \left(\frac{2\,\ell}{tG_c}\int_t g_{,s}\mathcal{H}^e d\theta^3 + s - 1 \right) \delta s \, dA + 2\,\ell^2 \int_A \nabla s \cdot \nabla \delta s \, dA + \ell^4 \int_A \Delta s \cdot \Delta \delta s \, dA = 0. \tag{38}$$

The previous equations employ the history field $\mathcal{H}^e$ for enforcing the irreversibility of the fracture and need to be solved by an iterative solver due to their nonlinearity. In the discretized framework, the variation of the expressions (37) and (38) with respect to the discrete value of the phase-field at the control points s_r leads to the expression of the residual phase-field vector $\mathbf{R}_{PF}$, whose linearization yields the tangent stiffness matrix $\mathbf{K}_{PF}$. So, the linearized version of the phase-field evolution equation, which is solved for an increment of the vector of the discrete phase-field values at control points $\Delta\mathbf{s}$, simply becomes:

$$\mathbf{K}_{PF}\,\Delta\mathbf{s} = \mathbf{R}_{PF}. \tag{39}$$

2.4. Penalty-based coupling of adjacent shell patches

In view of simulating the fracture behavior of complex multipatch shell structures, as done in Section 4, a penalty-based approach for coupling adjacent isogeometric patches is adopted. Both the structural and the phase-field behaviors across the patch interfaces are coupled and a single dimensionless penalty term $\alpha_{glob} = 10^3$, scaled by the problem parameters, is needed for all the coupling terms.

Considering two patches A and B that share an interface curve $\mathcal{L}$, the structural coupling consists in imposing displacement and rotational continuity across the patch connection by augmenting the virtual work formulation in equation (19) by adding the terms δW^{pd} and δW^{pr}. The first term imposes the displacement continuity:

$$\delta W^{\mathrm{pd}} = \int_{\mathcal{L}} \alpha_{\mathrm{d}} \left(\mathbf{u}^A - \mathbf{u}^B\right) \cdot \left(\delta\mathbf{u}^A - \delta\mathbf{u}^B\right) d\mathcal{L}, \tag{40}$$

while the second one preserves the rotational continuity:

$$\begin{aligned}\delta W^{\mathrm{pr}} = \int_{\mathcal{L}} \alpha_{\mathrm{r}} \Big(&\left(\mathbf{a}_3^A \cdot \mathbf{a}_3^B - \mathring{\mathbf{a}}_3^A \cdot \mathring{\mathbf{a}}_3^B\right)\left(\delta\mathbf{a}_3^A \cdot \delta\mathbf{a}_3^B - \delta\mathring{\mathbf{a}}_3^A \cdot \delta\mathring{\mathbf{a}}_3^B\right) + \\ &+ \left(\mathbf{a}_n^A \cdot \mathbf{a}_3^B - \mathring{\mathbf{a}}_n^A \cdot \mathring{\mathbf{a}}_3^B\right)\left(\delta\mathbf{a}_n^A \cdot \delta\mathbf{a}_3^B - \delta\mathring{\mathbf{a}}_n^A \cdot \delta\mathring{\mathbf{a}}_3^B\right)\Big) d\mathcal{L},\end{aligned} \tag{41}$$

where $\mathbf{a}_n^A$ is the unit vector lying in the plane of patch A and perpendicular to $\mathcal{L}$. For further details regarding the formulation, the reader is referred to the work by Herrema et al. [47], according to which the penalty terms α_{d} and α_{r} are computed by scaling the global penalty parameter $\alpha_{glob} = 10^3$ with the membrane and bending elastic stiffness values of the coupled shells. In our case, uniform isotropic materials are considered, so:

$$\alpha_{\mathrm{d}} = g(s,p)\;\alpha_{glob}\frac{E\,t}{h\,(1-\nu^2)}, \tag{42}$$

$$\alpha_{\mathrm{r}} = g(s,p)\ \alpha_{glob} \frac{E\,t^3}{12\,h\,(1-\nu^2)}, \tag{43}$$

with E as the Young's modulus, ν as the Poisson's ratio, and t as the shell thickness, while h is the average element length along the coupled edge having the finer discretization. The meaning of h needs to be specified, since the formulation can handle non-conforming meshes at the two sides of the coupled edge, thus it can be used in combination with adaptive mesh refinement technologies. The phase-field degradation function $g(s,p)$ ensures a consistent scaling between the structural and penalty stiffness in fractured patch interfaces.

In analogy with the methodology used for the structural coupling, the penalty approach is used also for enforcing continuity of the phase-field between the patch interfaces, as shown in Proserpio et al. [31]. Accordingly, the term

$$\int_{\mathcal{L}} \alpha_{PF}^{C^0} (s^A - s^B)(\delta s^A - \delta s^B)\ d\mathcal{L}, \tag{44}$$

which penalizes the difference of the phase-field at the two sides of $\mathcal{L}$, is added to the left-hand side of equations (37) and (38) for guaranteeing C^0 continuity of s. If the higher-order phase-field formulation is employed, also C^1 continuity of s needs to be imposed between smooth patch interfaces. This can be achieved by summing to the left-hand side of equation (38), in addition to the aforementioned term for C^0 continuity, the following expression:

$$\int_{\mathcal{L}} \alpha_{PF}^{C^1} (\nabla s^A \cdot \mathbf{a}_n^A - \nabla s^B \cdot \mathbf{a}_n^B)(\nabla \delta s^A \cdot \mathbf{a}_n^A - \nabla \delta s^B \cdot \mathbf{a}_n^B)\ d\mathcal{L}, \tag{45}$$

which penalizes the relative change in the directional derivative of s along $\mathbf{a}_n$ between the two patches. The penalty imposition of C^1 continuity of s can only be applied to smooth patch interfaces. For this reason, the higher-order phase-field formulation cannot be used for structures including patch connections forming a kink, and the second-order model needs to be adopted. Because of the nonlinearity of the phase-field evolution equation, the first variation of equation (44), and of equation (45) if applicable, with respect to the discrete value of the phase-field at the control points s_r, need to be added to the residual phase-field vector $\mathbf{R}_{PF}$:

$$\int_{\mathcal{L}} \alpha_{PF}^{C^0} (s^A - s^B)(s^A_{,r} - s^B_{,r})\ d\mathcal{L}, \tag{46}$$

$$\int_{\mathcal{L}} \alpha_{PF}^{C^1} (\nabla s^A \cdot \mathbf{a}_n^A - \nabla s^B \cdot \mathbf{a}_n^B)(\nabla s^A_{,r} \cdot \mathbf{a}_n^A - \nabla s^B_{,r} \cdot \mathbf{a}_n^B)\ d\mathcal{L}. \tag{47}$$

Analogously, the second variation expressions:

$$\int_{\mathcal{L}} \alpha_{PF}^{C^0}(s^A_{,s} - s^B_{,s})(s^A_{,r} - s^B_{,r})\, d\mathcal{L}, \tag{48}$$

$$\int_{\mathcal{L}} \alpha_{PF}^{C^1}(\nabla s^A_{,s} \cdot \mathbf{a}^A_n - \nabla s^B_{,s} \cdot \mathbf{a}^B_n)(\nabla s^A_{,r} \cdot \mathbf{a}^A_n - \nabla s^B_{,r} \cdot \mathbf{a}^B_n)\, d\mathcal{L}, \tag{49}$$

need to be added to the phase-field tangent stiffness matrix $\mathbf{K}_{PF}$. As for the structural case, the penalty terms for imposing phase-field continuity between patches ($\alpha_{PF}^{C^0}$ and $\alpha_{PF}^{C^1}$) are chosen by scaling the global penalty parameter $\alpha_{glob} = 10^3$ with terms that maintain dimensional consistency with the related equation. At the same time, the penalty parameters need to be large enough in order to guarantee the imposition of the required continuity of s, without creating ill-conditioning in $\mathbf{K}_{PF}$. The history field $\mathcal{H}^e$ is the driving force of the phase-field equation and the term in which it is included becomes numerically predominant in the regions where fracture develops. Additionally, in cracked areas, the plastic strains usually increase up to a level comparable to α_{crit}, thus implying that $p = 1$. Considering that, for $p = 1$, the quadratic degradation function considered for brittle fracture is retrieved, we adopt the same penalty terms as for the brittle fracture case:

$$\alpha_{PF}^{C^0} = \alpha_{glob}\left[\frac{4\ell(1-\eta)\mathcal{H}^e_{max}}{tG_c} + 1\right] h, \tag{50}$$

$$\alpha_{PF}^{C^1} = \alpha_{glob}\left[\frac{4\ell(1-\eta)\mathcal{H}^e_{max}}{tG_c} + 1\right] \ell^2 h. \tag{51}$$

The term $\mathcal{H}^e_{max}$ corresponds to the current maximum value of the history field in the structure.

As a final remark, we highlight that the penalty methodology presented in this section can be used also for weakly imposing clamping and symmetry boundary conditions.

2.5. Penalty-based frictionless contact formulation

In Section 4, we study a series of tests where different steel structures are penetrated by an indenter, simulating the consequences of ship grounding. For this reason, a frictionless penalty contact formulation suitable for large deformation problems is employed. We follow the approach outlined in Dimitri et al. [48], but instead of T-splines, LR NURBS (Locally Refined Non-Uniform Rational B-splines, see Section 2.6) are adopted for the discretization [49].

Two bodies, in this case two patches representing the shell midsurfaces, are assumed to be in contact. One of them is referred to as the *slave* surface and the other as the *master* surface. We assume that each point $\mathbf{x}^s$ on the slave surface can have only one partner contact

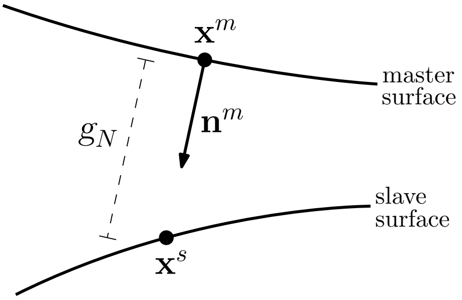

Figure 2: Contact formulation, definition of the normal gap.

point $\mathbf{x}^m$ on the master surface, whose position is computed by a closest point projection [50] of $\mathbf{x}^s$ over the master surface. The normal gap between the two surfaces is computed as:

$$g_N = (\mathbf{x}^s - \mathbf{x}^m) \cdot \mathbf{n}^m, \tag{52}$$

where $\mathbf{n}^m$ is defined as the normal unit vector at $\mathbf{x}^m$, with direction pointing towards the slave surface when no contact occurs, see Figure 2. The direction of $\mathbf{x}^m$ remains constant during the analysis, even in case if the surfaces come into contact. According to the definition in equation (52), the normal gap is positive if the contact is open, while $g_N < 0$ in case of penetration. For thin shells and plates, instead of defining the contact between the midsurfaces, it is possible to describe the contact between the shell faces by taking into account the slave and master thicknesses, t^s and t^m respectively. In this case, $\mathbf{x}^s$ and $\mathbf{x}^m$ and the relative quantities continue to be defined at the midsurfaces, but contact starts occurring when $g_N < (t^s + t^m)/2$. Denoting with $\mathbf{T}$ the Piola traction vector, its normal component is the normal contact traction T_N:

$$\mathbf{T} = \mathbf{T}^m = -\mathbf{T}^s = T_N \mathbf{n}^m, \qquad T_N = \mathbf{T} \cdot \mathbf{n}^m. \tag{53}$$

The Kuhn-Tucker conditions for impenetrability are defined as follows:

$$g_N \geq 0, \qquad T_N \leq 0, \qquad g_N T_N = 0. \tag{54}$$

These contact constraints can be regularized by adopting the penalty formulation, and thus assume the form:

$$T_N = \alpha_N \langle g_N \rangle^-, \qquad \langle g_N \rangle^- = \begin{cases} g_N & \text{if} \quad g_N < 0 \\ 0 & \text{otherwise} \end{cases} \tag{55}$$

with α_N as the penalty parameter related to contact. Accordingly, the contribution of the frictionless contact formulation to the virtual work of the structure is defined as:

$$\delta W^{\mathrm{N}} = \int_{A^s} T_N \delta g_N \; dA = \alpha_N \int_{A^s} g_N \delta g_N \; dA, \tag{56}$$

with the integral evaluated on the slave surface in the reference configuration and δg_N representing the variation of the normal gap. For details regarding the variation and the linearization of the gap function and of the contact virtual work, and their discretization, the reader is referred to De Lorenzis et al. [51].

This contact formulation is denoted as "Gauss-point-to-surface", since the contribution to the virtual work δW^{N} is computed at each integration point of the slave surface. Contact between patches having non conforming meshes can be managed without any problem, as the master contact point $\mathbf{x}^m$ does not need to be a quadrature point. We adopt a pre-search algorithm that allows excluding, from the computation of the integral (56), slave elements which are sufficiently far from the master patch so that they are not affected by penetration, i.e. they do not contribute to δW^{N}. For each element on the slave surface, we identify the closest element on the master patch, whose center will be the starting point of the search algorithm for finding the contact point $\mathbf{x}^m$ of each integration point belonging to the considered slave element. This pre-computation makes the point search algorithm more efficient and prevents it from diverging, i.e. not finding the correct contact point. At this stage, we also compute the normal unit vector at $\mathbf{x}^m$ and we make sure that it is oriented in the correct way by inverting its direction if necessary, so that it can correctly represent $\mathbf{n}^m$. Once the direction of $\mathbf{n}^m$ is determined as the one pointing towards the slave surface (before contact occurs at $\mathbf{x}^m$), it is kept constant for the rest of the analysis.

In order to guarantee a scaling between the structural and the contact penalty stiffness when the penalty contact formulation is combined with the phase-field fracture approach, the effect of the phase-field degradation function is added into equation (56) by the term $g^{s,m}$, which takes the minimum value of the degradation function between the master and the slave contact points. The elements in the cracked zones have degraded material properties but still contribute to the contact penalty terms and, therefore, they provide resistance against penetration. In order to avoid this numerical problem and to remove fully broken elements from the contact computations, zero contact stiffness is guaranteed by imposing $g^{s,m} = 0$ if $s < 0.05$ at $\mathbf{x}^s$ or $\mathbf{x}^m$. So, the virtual work formulation in equation (19) is augmented by adding the following term:

$$\delta W^{\mathrm{N}} = \alpha_N \int_{A^s} g^{s,m} g_N \delta g_N \; dA. \tag{57}$$

2.6. Discretization of the geometry with LR NURBS

Thanks to the smoothness of the basis functions, IGA represents a favorable choice for the discretization of the geometry, because it allows for an efficient implementation of the rotation-free Kirchhoff-Love shell model and of the fourth-order phase-field formulation. In the context of the numerical simulation of contact, IGA allows for considering the exact geometry of the surfaces. Additionally, the higher continuity of the basis functions contributes to improving the performance of the contact algorithms, with respect to the traditional finite element implementations, thanks to the well-posedness of the closest-point projection problems [51].

In phase-field fracture analyses, the steep gradient of the smeared crack profile, whose width depends on the (often small) length scale parameter ℓ, requires a mesh having fine elements at least in the vicinity of the crack region. Due to their tensor product properties, the NURBS basis functions used in standard isogeometric analysis allow only a global refinement of the geometry. For this reason, we adopt a local refinement technology by employing LR NURBS [52], an extension of LR B-splines [53], for the discretization of the geometry. In this work, a ductile fracture formulation that employs a local plasticity theory is presented. Since mesh refinement is well known to be critical for local plasticity formulations [54], its influence is studied in Section 3.

2.7. Aspects related to the solution algorithm

From the stationarity condition of the energy functional (see equation (33)) with respect to the displacement field $\mathbf{u}$ and the phase-field s, the two governing equations of the coupled problem, i.e. the momentum and the phase-field evolution equations, are obtained. According to the staggered approach proposed by Bourdin et al. [3] and Miehe et al. [5], the two equations are solved separately at each pseudo-time step of the analysis, keeping frozen the field which the equation is not solved for. In order to guarantee that the structure is in equilibrium at end of each load step, we check the convergence of the solution after each staggered iteration and we repeat the process until the convergence is reached. It is important to point out that both the momentum and the phase-field equilibrium equations are nonlinear, so that they require an iterative solver. A classical approach, which will be called “loosely coupled” staggering scheme, would require, for each staggered iteration, first the iterative solution of the equilibrium equation for $\mathbf{u}$ and then the iterative solution of the phase-field equation for s. In order to improve the efficiency of the numerical simulation, we adopt the ”strongly coupled” scheme, used in [31] for brittle fracture problems (where the phase-field equation is linear), according to which, in each staggered iteration, a single iteration of each of the two governing equation is performed, until convergence of the staggering process is reached (both for the momentum and the phase-field equation) with an adequately low tolerance for the residual. Box 1 outlines a comparison of the two approaches. The strong staggered coupling scheme is employed for all the numerical simulations of this paper.

Box 1: Loosely and strongly coupled staggering schemes. In case the convergence conditions are not satisfied, the iterations are repeated.

Loosely coupled staggering scheme

```
Load step $i$
  Staggered iterations:
  | Iterative solution of momentum eq.:
  | | Iteration of momentum eq.
  | |            ↓
  | | Check convergence of momentum eq.
  |        ⇓
  | Iterative solution of phase-field eq.:
  | | Iteration of phase-field eq.
  | |            ↓
  | | Check convergence of phase-field eq.
  |        ⇓
  | Check convergence of stagg. iterations
Load step $i+1$
  ...
```

Strongly coupled staggering scheme

```
Load step $i$
  Staggered iterations:
  | Iteration of momentum eq.
  |        ⇓
  | Iteration of phase-field eq.
  |        ⇓
  | Check convergence of stagg. iterations
Load step $i+1$
  ...
```

As observed by Gerasimov et al. [10] for phase-field brittle fracture analyses, when the staggering process is repeated until convergence in each step, the use of relatively large pseudo-time steps does not affect the results accuracy and even reduces the computational time, with respect to smaller steps. In order to improve the efficiency of the simulations, the use of quite large increments between the steps is possible in the initial part of the simulations or when the pure elastic regime dominates. On the other hand, large steps cannot be used when the plasticity starts evolving in the structure, otherwise no convergence of the momentum equation, and so of the staggered iterations, can be achieved. The same applies to the contact formulation, which cannot handle too large step increments that would lead to penetration at the beginning of the steps too large for allowing the convergence of the equilibrium equation. For these reasons, we adopt a simple adaptive step size procedure that will be briefly exposed. The initial step size is chosen as relatively large and represents the maximum possible step increment for the analyses. When a load step does not reach convergence, the step is recomputed with an increment reduced by a factor of 2, until convergence is reached. In order to improve the efficiency of the simulations, we strive to have increments as large as possible. So, each time a step converges, we increase the step size by a factor 1.5 (we observed that an increase factor equal to the one for step reduction would often lead to non-convergence). The increment cannot, anyway, be larger than the maximum one set at the beginning of the analyses. This approach allows relatively large steps in the initial part of the analyses, while the increment size is reduced when complex deformations occur (for example the buckling of stiffeners in Section 4) or contact and phase-field ductile fracture effects dominate the simulation.

3. Adaptive local refinement for ductile fracture simulations

The $J2$ plasticity formulation (see Section 2.1) employed in this work is a local plasticity model, meaning that the plastic constitutive equation of the material is evaluated at the integration points of the structure, without including any information about the size of the zone where plastic strains localize, because no length scale parameter is present in the model. As a consequence, the results of the simulations may be sensitive to the mesh size in the plastic region, which can localize differently and change dimension in case the mesh is refined [54].

3.1. Influence of the mesh size on the phase-field modeling of ductile fracture

In order to evaluate the effect of the mesh size on the considered local plasticity model combined with the phase-field fracture approach, we consider two numerical examples, a rectangular flat specimen and a hollow cylinder, under tensile loading caused by the imposed displacement of the top edge. Geometry and boundary conditions are shown in Figure 3 (the thickness is $t = 1$ mm for both specimens). For the cylinder example, only one quarter of the model is simulated due to symmetry, employing symmetric boundary conditions imposed by penalty, according to the formulation in Section 2.4. The same $J2$ plasticity model as in [44] with the following material parameters is considered in this work, i.e. $E = 189 \times 10^3$ N/mm^2 and $\nu = 0.29$ for elasticity. A nonlinear hardening law in the following form is assumed [17]:

$$R(\alpha) = \sigma_y + H_m \alpha + \left(\sigma_\infty - \sigma_y\right)\left(1 - e^{-\delta\alpha}\right), \tag{58}$$

with yielding stress $\sigma_y = 343$ MPa, ultimate tensile strength $\sigma_\infty = 680$ MPa, hardening modulus $H_m = 300$ MPa, and saturation coefficient $\delta = 16.93$. The parameters required for the phase-field ductile fracture model are chosen as follows: fracture toughness $G_c = 1000$ N/mm, critical value of the hardening variable $\alpha_{crit} = 0.50$, $m = 1$, and $\ell = 0.50$ mm. The

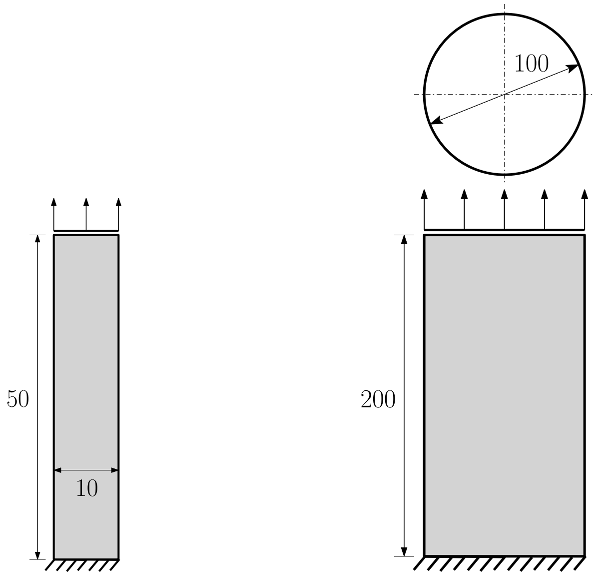

(a) Rectangular flat specimen (b) Hollow cylinder specimen

Figure 3: Setup of the tensile problems (dimensions in mm).

simulations are performed firstly only considering the elasto-plastic material model, then also including the phase-field ductile fracture formulation. Different mesh sizes are considered by employing local mesh refinement in the central region of the specimen, where necking, plastic strain concentration and fracture are expected to take place. For the rectangular flat specimen, we consider $h = \{0.500,\ 0.250,\ 0.125\}$ mm, where h indicates the minimum characteristic element size in the mesh. For the cylindrical geometry, $h = \{2.00,\ 1.00,\ 0.50\}$ mm is taken. In both cases, these minimum element sizes correspond to one, two or three levels of pre-refinement, respectively. For these and all the simulations in this paper, we use quadratic LR NURBS having 3 through-thickness integration points for each of the 3×3 Gauss points per element.

Figures 4 and 5 show the results of the simulations involving phase-field fracture for the two specimens and the different meshes used. From the plots of the equivalent plastic strain α it is possible to notice that the plasticity accumulates in different ways as the mesh is refined. By using smaller elements, the concentration of the plasticity in shear bands can be captured. Since, according to the adopted phase-field formulation, the fracture starts evolving only in zones that undergo plastic strains, also the cracks will change shape and will start following the orientation of the shear bands as the mesh is refined. Figures 6 and 7 show the load-displacement curves for the two specimens, both with only elasto-plasticity

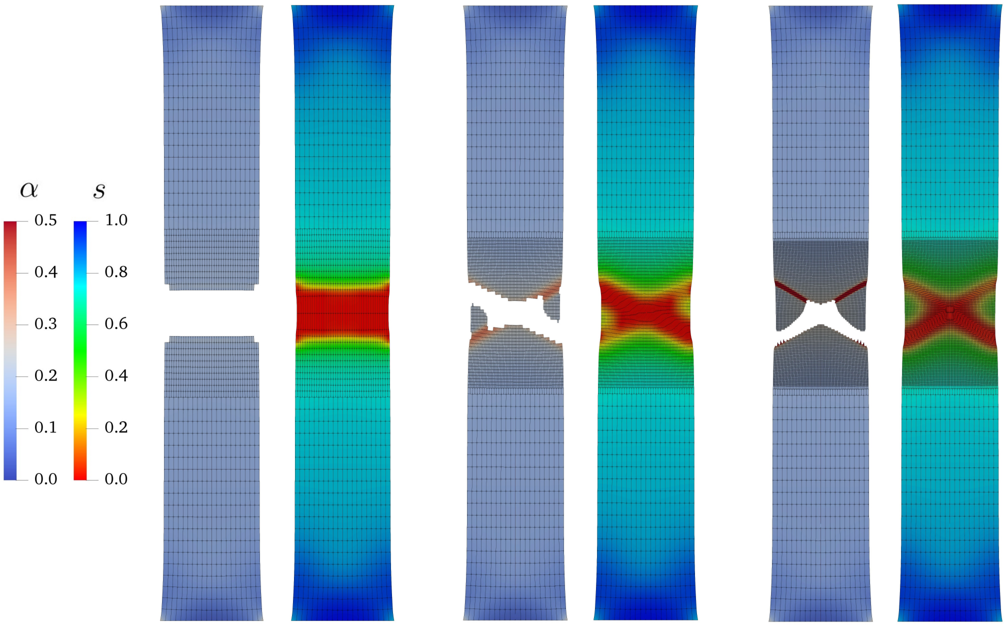

(a) $h = 0.500$ (b) $h = 0.250$ (c) $h = 0.125$

Figure 4: Results of the phase-field ductile fracture simulations for the rectangular flat specimen with pre-refined mesh. The colormaps indicate the values of the hardening variable α and of the phase-field s. For visualization purposes, in the equivalent plastic strain plots, elements considered broken ($s < 0.05$) are removed.

and with ductile fracture, for the considered element sizes. The results of the elasto-plastic simulations with and without phase-field fracture are the same until the points when the cracks start initiating and the curves of the phase-field simulations show a drop. Considering the simulations involving only $J2$ plasticity, it is clear that the mesh refinement does not lead to convergence in the results. Even if all the curves are coincident in the first part of the analysis, after the occurrence of necking, finer meshes cause larger localization of the plastic strains in the necking region (following shear bands), leading to a softening behavior and to load-displacement curves showing less load-carrying capacity. The simulations involving phase-field fracture in addition to elasto-plasticity show instead load-displacement curves not too sensitive to mesh refinement, and convergence can be observed as the element size is reduced. It is important to recall that, according to the adopted phase-field ductile fracture model, plastic strains cease to concentrate when the fracture starts developing (only elastic deformation can take place in the fractured region). This means that, unlike for the pure elasto-plastic simulations, the plasticity cannot increasingly localize as the phase-field ductile

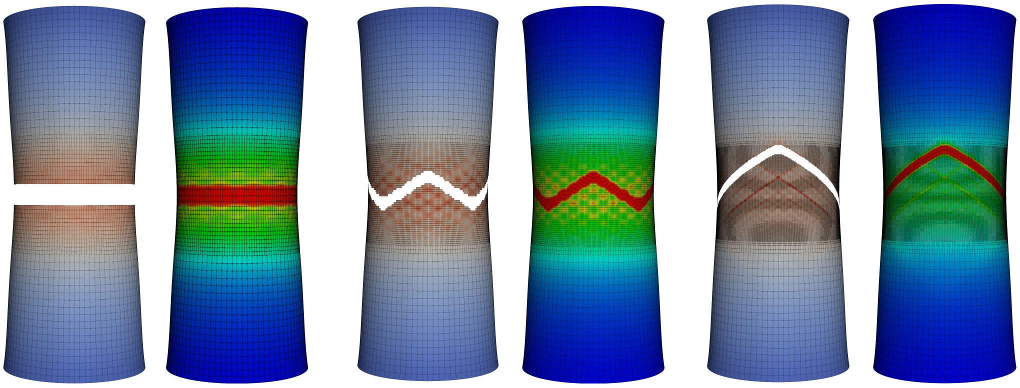

(a) $h = 2.00$ (b) $h = 1.00$ (c) $h = 0.50$

Figure 5: Results of the phase-field ductile fracture simulations for the hollow cylinder specimen with pre-refined mesh. The colormaps indicate the values of the hardening variable α and of the phase-field s. For visualization purposes, in the equivalent plastic strain plots, elements considered broken ($s < 0.05$) are removed.

fracture simulations proceed, thus alleviating the mesh dependency of the elasto-plastic model, even without adopting a non-local gradient formulation for plasticity. A possible interpretation of these results can also be related to the fact that the gradient term present in the phase-field model reduces the need of adopting a gradient plasticity formulation. In conclusion, we can assume that a local pre-refinement of the mesh can influence the direction and the shape of the fracture, but affects the simulated load-displacement curves of the specimens only up to a limited extent.

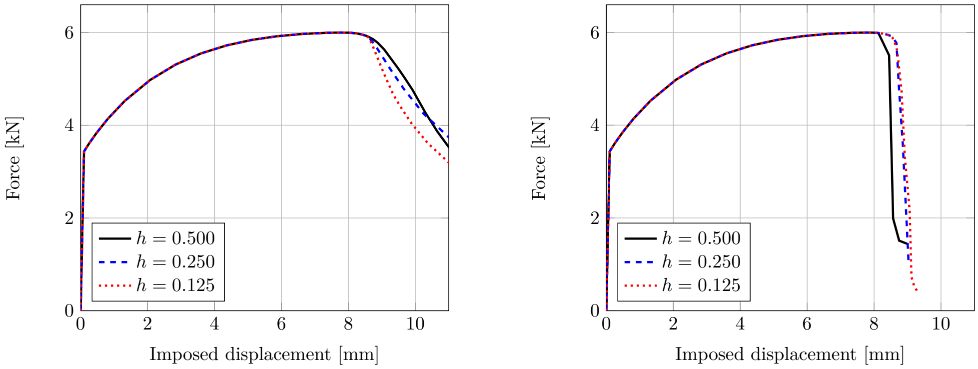

(a) Elasto-plasticity (b) Phase-field ductile fracture

Figure 6: Load-displacement curves of the elasto-plastic simulations with and without phase-field fracture formulation for the rectangular flat specimen with pre-refined mesh.

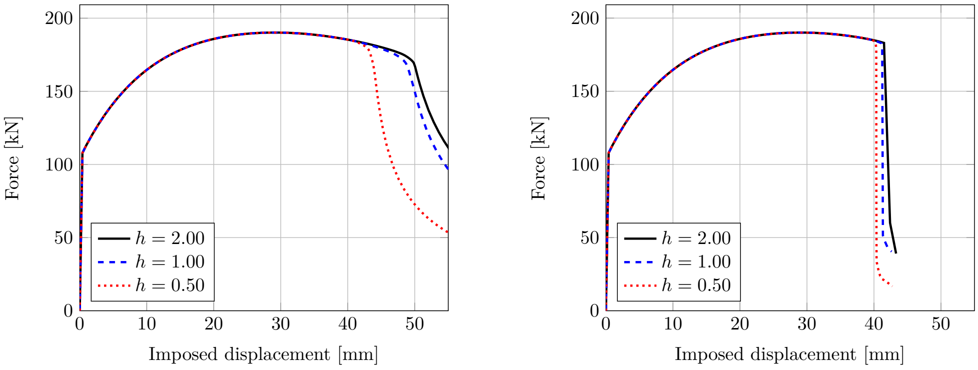

(a) Elasto-plasticity

(b) Phase-field ductile fracture

Figure 7: Load-displacement curves of the elasto-plastic simulations with and without phase-field fracture formulation for the hollow cylinder specimen with pre-refined mesh.

3.2. Adaptive local refinement strategy and validation

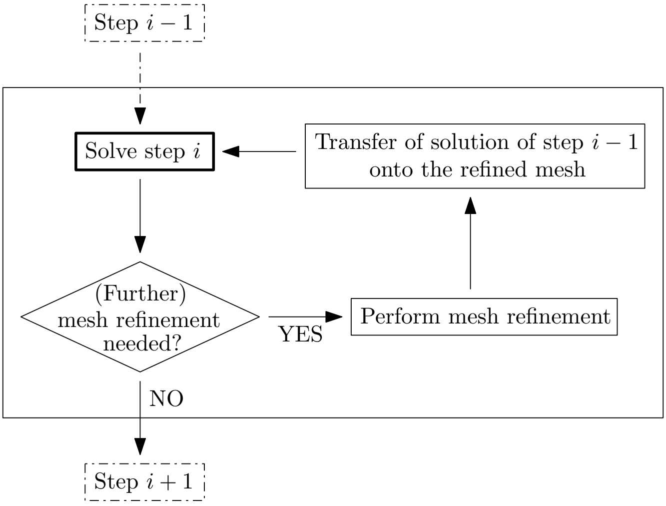

Figure 8: Adaptive local refinement algorithm.

The use of an adaptive local mesh refinement scheme is crucial for performing phase-field fracture simulations on complex structures with a reasonable computational cost. In this section, we adopt the approach used in Proserpio et al. [31] for brittle fracture, and we test its validity in the framework of ductile fracture. The method consists in a predictor-corrector algorithm that allows refining the mesh only where needed, i.e. in the regions where the fracture is evolving, without knowing *a priori* where the cracks are going to nucleate and/or grow. According to the algorithm, which is summarized in Figure 8, at the end of each step we evaluate whether the mesh needs to be refined. If this is the case, the mesh refinement is performed, the solution of the precedent step is transferred to the refined mesh and the considered step is recomputed with the new mesh. Unlike for the brittle fracture case, in ductile fracture simulations cracks often grow during several steps, meaning that the evolution of the fracture during a single step is relatively limited (even when the convergence of the staggered iterations is achieved). Nevertheless, it may happen that, at the end of a recomputed step, the crack has grown outside of the region just refined. In this case, the load step needs to be recomputed again, and the process is repeated until there is no need for further refinement.

The need for refinement is evaluated according to the fact that ductile fracture is preceded by a concentration of the plastic strain, which is measured by the hardening variable α. For this reason, we choose the equivalent plastic strain α as the indicator for the refinement and, at the end of each load step (including recomputed ones), we mark for refinement all the elements that are larger than the prescribed minimum element size and in which the value of the hardening parameter is higher than a threshold value, i.e. $\alpha > \alpha_t$ at least in one integration point. Since we want to be able to capture the localization of plasticity, that can potentially lead to cracks following shear bands (see Section 3.1), we adopt a conservative approach so that the mesh is refined before the onset of fracture. Therefore, the value $\alpha_t = 0.25\,\alpha_{crit}$ is chosen and used in all the simulations of this paper including adaptive mesh refinement. The refinement is performed according to the ”structured mesh” strategy [53], which consists in splitting all the knot spans of the support of a certain basis function. This approach provides a regular mesh, with a good transition between zones having different element sizes, and keeps the aspect ratio of the elements in parametric space constant.

For each refinement round, it is necessary to transfer all the state variables from the coarse to the refined mesh. The field quantities defined at the control points (displacement $\mathbf{u}$ and phase-field s, which are also the unknowns of the coupled problem) are projected according to the same algorithms used for determining the coordinates of the control points corresponding to split basis functions [53]. The history field $\mathcal{H}^e$, the hardening variable α, the thickness stretch λ_3, and the plastic right Cauchy-Green deformation tensors $\mathbf{C}^p = \mathbf{F}^{p^T}\mathbf{F}^p$ are instead quantities defined at each thickness integration point. The transfer of these quantities, from the integration points of the coarse element to the ones of the refined elements having the same position across the thickness, is performed for each scalar variable according to a local Bézier-element-based interpolation [31, 55]. For the right Cauchy-Green deformation tensor, the transfer is operated separately for each component.

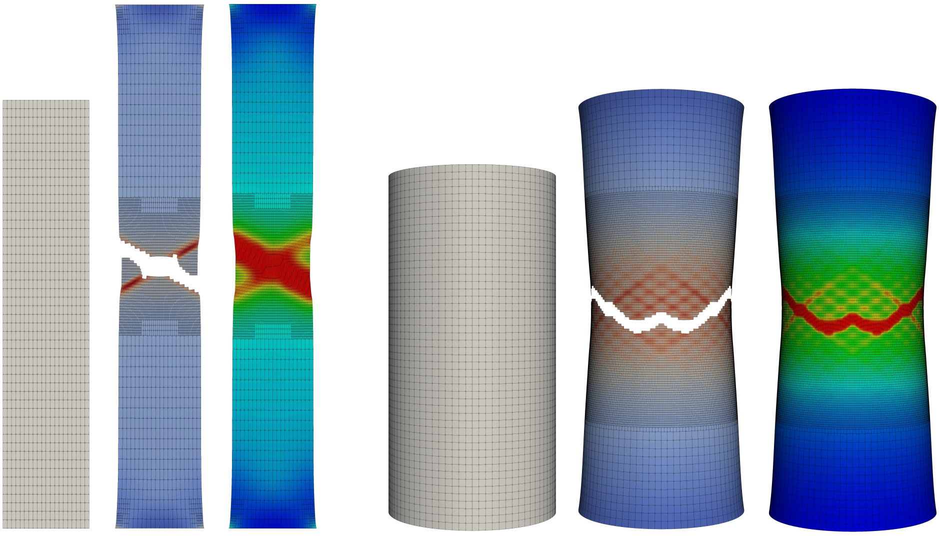
(a) Rectangular flat specimen, $h = 0.250$ mm

(b) Hollow cylinder specimen, $h = 1.00$ mm

Figure 9: Results of the phase-field ductile fracture simulations employing adaptive mesh refinement for the tensile specimens in the terms of hardening variable and phase-field. The colormaps indicate the values of the hardening variable α and of the phase-field s. For visualization purposes, in the equivalent plastic strain plots, elements considered broken ($s < 0.05$) are removed.

We test the effectiveness of the adaptive local refinement procedure on the two numerical examples previously run for verifying the effect of the mesh pre-refinement (see Section 3.1). In both cases, two levels of adaptive mesh refinement are employed, for a minimum mesh size $h = 0.250$ mm for the rectangular flat specimen and $h = 1.00$ mm for the hollow cylinder example. Figure 9 shows the initial mesh and the final results of the simulations for the two geometries, which can be compared with the ones from the simulations with pre-refinement of the mesh (Figures 4b and 5b). The mesh refinement is performed early enough in order to capture the localization of the plastic strains and therefore the cracking develops along the shear bands. In the rectangular flat specimen, some local refinement occurs also at the corners due to plasticity localization, but this does not lead to fracture in those locations. Figure 10 shows a good agreement of the load-displacement curves between the simulations employing adaptive local refinement and the corresponding ones performed with a pre-refined mesh. For the examples presented in this section, the reduction of the computational cost due to the adoption of the adaptive refinement is limited by the fact that a large portion of the mesh needs to be refined. The examples in Section 4 will show the importance of adaptive refinement for structures where the cracked area covers only a small part of the total domain.

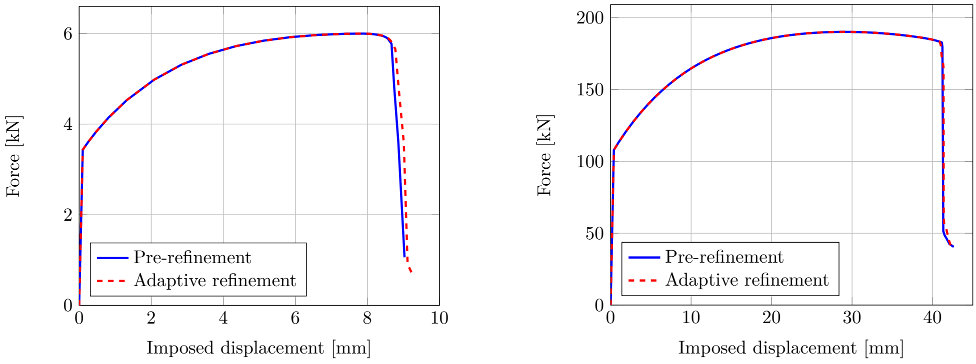

(a) Rectangular flat specimen, $h = 0.250$ mm (b) Hollow cylinder specimen, $h = 1.00$ mm

Figure 10: Comparison of the load-displacement curves from the phase-field ductile fracture simulations with and without adaptive mesh refinement for the tensile specimens.

4. Application to complex structures with experimental validation

We now validate our method by simulating a series of experimental indentation tests on steel panels performed by Alsos et al. [56]. The experimental campaign was conducted in order to evaluate the resistance of stiffened plates from ship hulls in case of events like ship grounding. Section 4.1 presents the setup of the problem, while in Section 4.2 the results of the simulations are compared with the experimental ones and then discussed.

4.1. Problem definition and setup of the simulations

The experimental campaign from which we extract the experimental benchmarks consists in a series of indentation tests performed on rectangular steel panels. The experimental setup is shown in Figure 11. Different plate configurations are considered: unstiffened panel (US), panel with one flat bar stiffener (1-FB), and panel with two flat bar stiffeners (2-FB). For both the 1-FB and 2-FB case, the stiffeners are welded to the plate. In the experimental setup, the panel and the ends of the stiffeners are welded to a strong frame consisting of massive steel boxes. We choose to include in the simulations only the plates and the stiffeners, and we model their connections to the frames employing clamped boundary conditions (imposed by penalty, see Section 2.4), as it can be assumed that the surrounding girder webs are stiff enough to represent a rigid support [56]. The dimensions and geometry of the panels and of the indenter are depicted in Figure 12. The thickness of the plate is 5 mm, while the thickness of the stiffeners is 6 mm.

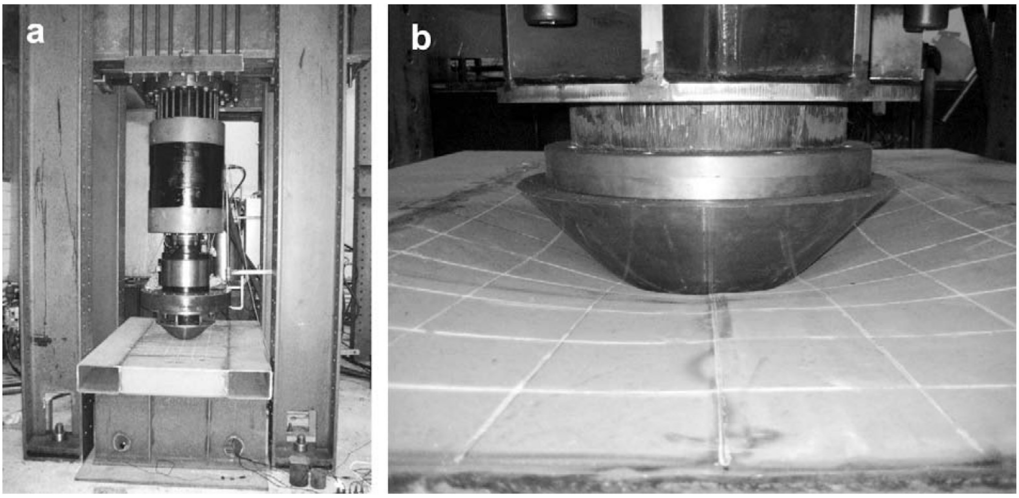

Figure 11: Experimental setup for the indentation test. (a) shows a tested panel with its box beam frame in the experimental rigging, that includes a hydraulic jack mounted on a crosshead and the indenter. (b) shows the interaction between the indenter and the plate during the test. [56]§

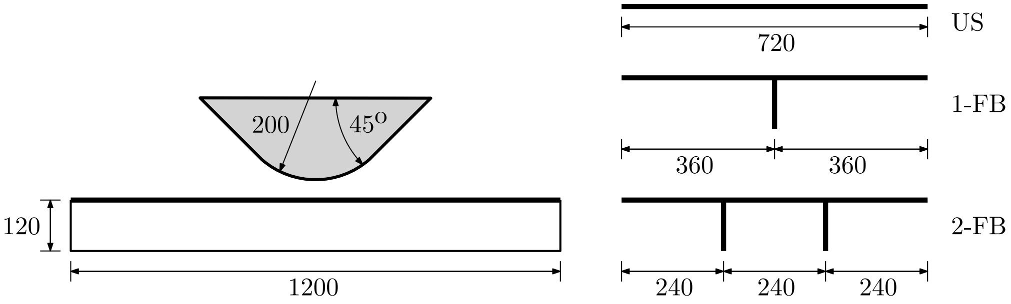

Figure 12: Longitudinal view of a stiffened plate with the indenter and transversal view of the three panel configurations (dimensions in mm).

The material of the plate and of the stiffeners consists in rolled mild steel, namely S235JR EN10025. Stress-strain curves, resulting from tensile tests performed on samples extracted from the same batch from which the tested structure was manufactured, are published [56]. The tensile tests have been performed in directions both parallel and perpendicular to the rolling direction. From the average of the two responses, the experimental curve shown in Figure 13 is obtained. Apart from the elastic properties, which are taken as the well known ones for mild steel ($E = 210 \times 10^3$ N/mm^2, $\nu = 0.30$), numerical simulations of the tensile tests are necessary in order to determine, by comparison with the available experimental curve, the plasticity and fracture parameters of the material. The elasto-plasticity model without phase-field fracture employing a nonlinear hardening law as in equation (58) is adopted for the quantification of the plasticity properties, which result in yielding stress $\sigma_y = 285$ MPa, ultimate tensile strength $\sigma_\infty = 395$ MPa, hardening modulus $H_m = 550$ MPa, and saturation coefficient $\delta = 25.00$. Once these values are set, ductile fracture simulations are performed for determining the fracture toughness as $G_c = 35$ kN/mm, the critical value of the hardening variable as $\alpha_{crit} = 2.0$, and $m = 1$. Figure 13 shows the stress-strain curves from the simulations employing these parameters, in comparison with the one obtained from the experiments on the specimens. The material parameters determined in this section will be used as input for the numerical modeling and for predictions of the results of the indentation tests.

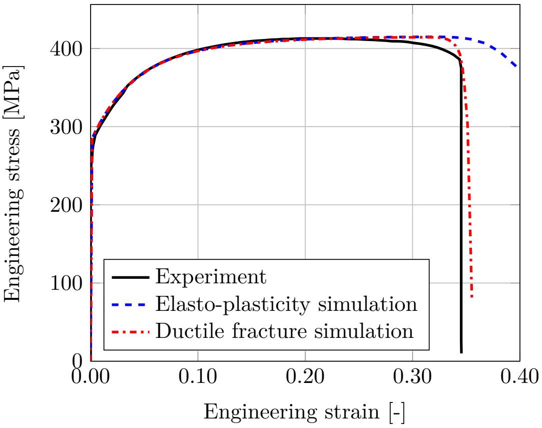

Figure 13: Stress-strain curves for the tensile test and simulations used for evaluating the material properties, according to the adopted computational model, of the mild steel rolled plates employed in the indentation test.

The simulations of the indentation tests are performed in displacement control, imposing the displacement of the indenter in the direction perpendicular to the plate. In the experimental campaign, the displacement rate of the cylinder was set to 10 mm/min in order to minimize the strain rate effects, which can be considered negligible as they are supposed to account for an increase in loads of $2-4$ % with respect to the static scenario [56]. For this reason, the analyses are performed in the quasi-static regime. Despite the better efficiency of the fourth-order phase-field model, especially in connection with adaptive local refinement [31], the higher-order formulation can be employed only for the US analysis, where no patch connections with kinks are present. The second-order phase-field model is used instead for the 1-FB and 2-FB cases, because of the non-smooth patch connections between the panel and the stiffener, which prevent the imposition of the C^1 continuity of s (see Section 2.4).

The length scale parameter for the phase-field model is taken as $\ell = 6$ mm. Adaptive local mesh refinement according to the strategy explained in Section 3.2 is adopted, with three levels of refinement leading to a minimum element size $h = 3$ mm, so that $h = \ell/2$. Due to the symmetry of the setup and considering that the experimental results showed a symmetric behavior, only half of the geometry is simulated, with the symmetry plane passing at the transverse center line of the plate. Since the model involves another symmetry plane (corresponding to the panel center line, in the longitudinal direction), the perfectly symmetric setup makes the nucleation of localized cracks difficult, in the simulations. For this reason, we introduce an imperfection in the model in the form of a small pre-crack located along the transversal symmetry plane. In addition, the indenter tip is supposed to hit the center of the panels, but assuming that some offset between the indenter position and the target center is present in the testing, the indenter position is shifted by 5 mm from the panel center, along the transversal symmetry plane, in the simulations setup. Patch coupling, symmetry and clamping boundary conditions are applied by employing the penalty formulation (Section 2.4). In the experimental setup, the indenter is milled out from a solid piece of steel, therefore, in the simulations, only its lower surface is modeled and it is considered as a rigid shell. Contact conditions are simulated according to the frictionless penalty formulation exposed in Section 2.5. In addition to the plate-indenter and the plate-stiffeners interactions, due to the possibility of penetration caused by the damage of the panel elements involved in the contact, the contact between the indenter and the stiffeners has to be taken into account as well. Shell thickness is considered in the contact computations for the panel and the stiffeners. The contact penalty parameter is set as $\alpha_N = 10^3$.

4.2. Simulation results and discussion

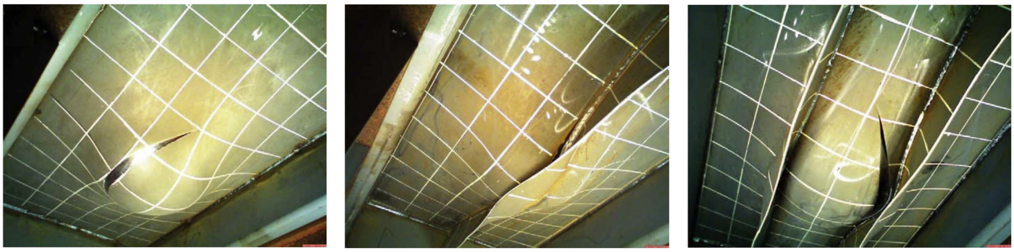

(a) US (b) 1-FB (c) 2-FB

Figure 14: Results of the indentation tests on the three panel configurations. [56]§

Figure 15 shows the result of the simulation for the unstiffened plate in the undeformed and deformed configuration. The fracture starts at approximately 100 mm from the center

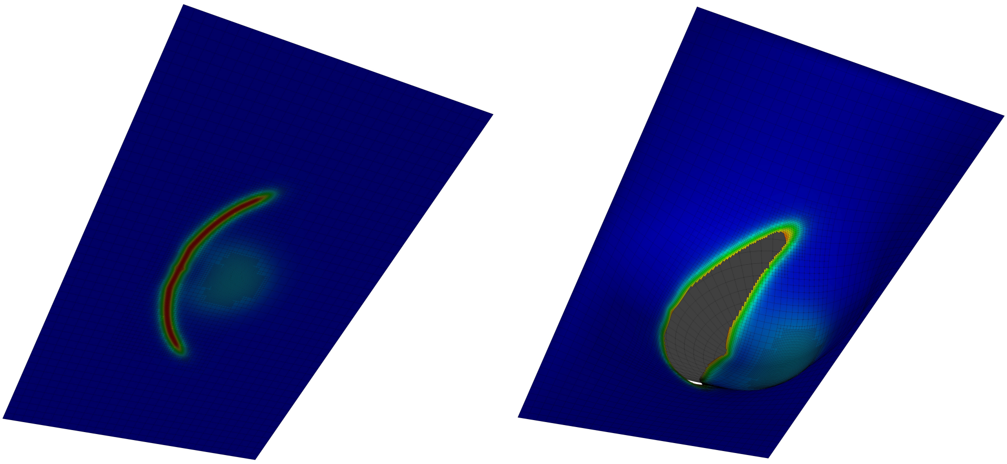

(a) Undeformed configuration

(b) Deformed configuration. For visualization purposes, the fully broken elements are removed from the plate.

Figure 15: Result of the simulation of the indentation test on the US panel.

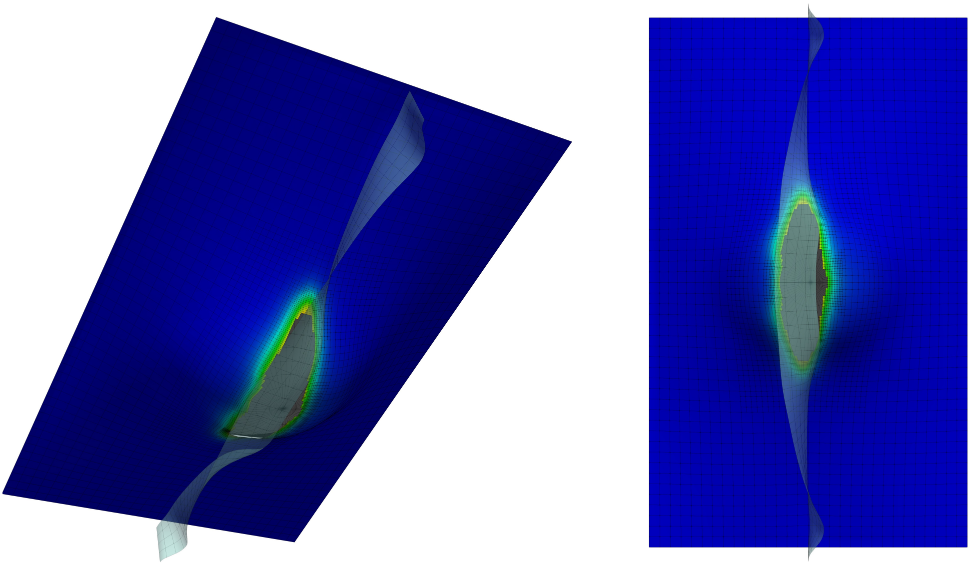

Figure 16: Result of the simulation of the indentation test on the 1-FB panel from two different viewpoints. For visualization purposes, the fully broken elements are removed from the plate. The indenter and the stiffener are represented with different colormaps.

line in the longitudinal direction (referring to the undeformed configuration) and evolves with a shape similar to the one observed during the benchmark experimental tests (Figure 14a).

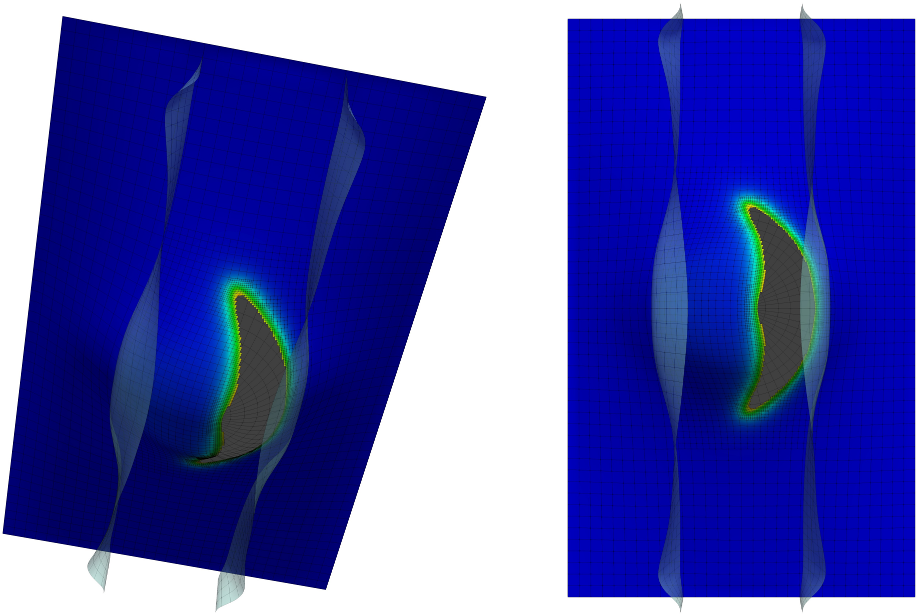

Figure 17: Result of the simulation of the indentation test on the 2-FB panel from two different viewpoints. For visualization purposes, the fully broken elements are removed from the plate. The indenter and the stiffeners are represented with different colormaps.

It can be noted that some mesh refinement occurs around the plate center due to the increase of the plastic strain in that region. Nevertheless, this does not lead to fracture, showing that the refinement of the mesh does not necessarily imply the onset of cracks. In the 1-FB case (Figure 16), the stiffener, which is placed in the middle of the panel, is initially subjected to bending and shear action, until buckling and consequent folding occur. Therefore, the stiffener does not break, while the fracture happens in the plate, close to the connection with the stiffener itself, as observed in the tests (Figure 14b). For the 2-FB geometry, the fracture occurs in the area between the two stiffeners and evolves in a way similar to the unstiffened case. No stiffeners failure is again observed, nor in the experiments neither in the simulations, as shown in Figures 14c and 17. The comparison of the load-displacement curves resulting from the indentation tests and the simulations performed for this paper is shown in Figures 18 and 19. In the experimental setup, the force and the displacement were measured on the crosshead of the hydraulic jack that acts on the movement of the indenter. Since the simulations are conducted in (increasing) displacement control, we removed from the experimental curves the part referring to the retraction of the indenter. There is good agreement between the curves in the first part of the analyses, which includes the initial elastic deformation, the onset and development of plasticity, and the buckling of the stiffeners (if present). The simulations predict the failure moment with reasonable precision in the US and 1-FB cases, and with good estimates of the peak load with respect to the experimental curves. The two-stiffeners panel simulation, instead, overestimates the maximum load carried by the structure and predicts a too late fracture.

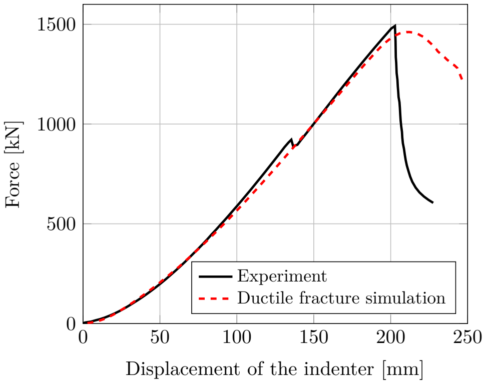

Figure 18: Comparison of the load-displacement curves for the indentation test on the US panel.

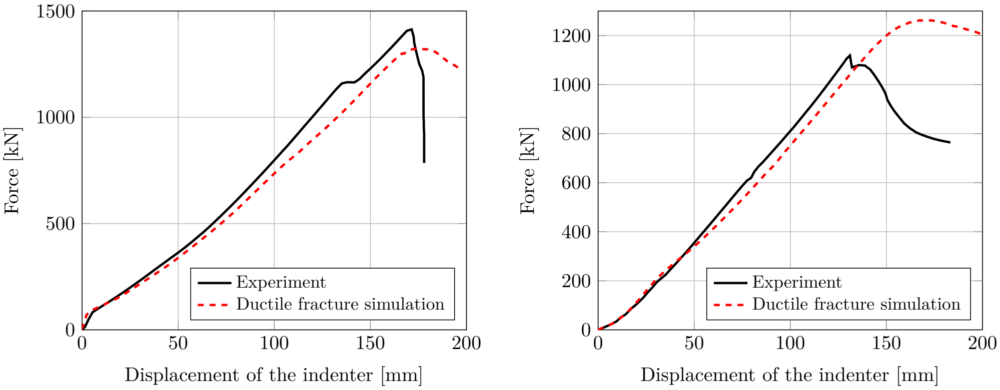

(a) 1-FB

(b) 2-FB

Figure 19: Comparison of the load-displacement curves for the indentation tests on the stiffened panels.

Among the factors that influence the not perfect matching of the curves, we recall that a frictionless contact formulation is employed, while the presence of static friction should be assumed between the steel surfaces of the indenter and of the plate. Moreover, the larger difference between the experimental and the simulation curves of the 1-FB and 2-FB cases compared with the unstiffened case can be related to the fact that the simulations do not include the modeling of the stiffeners weld bead. Fracture was never experimentally observed in the weld material, but the modeling of the weld bead would make the simulated structure stiffer. After fracture development, the curves resulting from the simulations show more post-cracking ductility than the experimental ones. This behavior is more evident than in the results from the analyses performed on the tensile specimens, see Figure 13, where it is possible to describe the drop of the load-displacement curve. The adoption of an enriched model could be useful for replicating this behavior also for the considered structure. However, considering the complexity of the model, the numerical simulations provide satisfactory predictions of the behavior of the stiffened plates both in terms of crack path and load-displacement curves. The result is relevant, especially taking into account the fact that the material parameters of the model have been determined only from the results of the tensile tests performed on the specimens of the material considered in the experiments. Considerations similar to the ones after the experimental campaign can be drawn from the performed simulations. First of all, the initiation of fracture does not imply a total loss of the resistance of the structure. Moreover, the presence of one or more stiffeners obviously increases the initial stiffness of the panels and reduces their flexibility, at the price of earlier fracture and less maximum carried load.

5. Conclusion

We have presented an approach for the simulation of ductile fracture in shell structures. An isogeometric rotation-free Kirchhoff-Love shell formulation was combined with an elasto-plasticity material model and with a phase-field ductile fracture formulation at finite strains, here extended to the higher-order version. According to this approach, it is possible to describe, with a single value of the phase-field defined at the midsurface, a nonlinear distribution of the stress tensor and a degradation function varying through the shell thickness.

In order to simulate the failure of geometrically complex multipatch structures, we adopted a penalty formulation for coupling the structural and the phase-field fracture behaviors across the patch interfaces. A penalty formulation has been also employed for the simulation of frictionless contact conditions. Being used in phase-field fracture simulations, both the penalty formulations had their terms scaled by the phase-field degradation function, in order to maintain the numerical proportion between structural and penalty stiffness during the analyses and in order the relax the penalty constraints in the fractured zones. Additionally, we found that fractured elements have to be removed from the contact algorithms for enabling penetration. The adequate choice of the penalty terms was suggested by the stability and convergence of the numerical analyses performed.

Despite the strong mesh dependency of the local plasticity model, the mesh sensitivity of the ductile failure simulations is reduced by the fact that the localization of the plastic strains ceases at the occurrence of fracture. At the same time, the use of fine meshes allows capturing characteristic features of ductile fracture, such as cracking along shear-bands or cup-and-cone fracture. In view of improving the numerical efficiency of the analyses, a predictor-corrector algorithm for adaptive local refinement employing LR NURBS was adopted, so that a fine mesh can be employed only in the vicinity of the crack, without the need of knowing in advance the fracture pattern.

The effectiveness of the numerical approach has been tested through the comparison with results from experimental indentation tests performed on steel stiffened panels for simulating the consequences of grounding on ship hulls. The material parameters for the simulations have been determined only according to the available results of tensile tests operated on specimens from the same plates used in the experiments. The qualitative (crack patterns) and quantitative (load-displacement curves) agreement of the results of the simulations and of the tests highlights the potential and the flexibility of the phase-field method also for ductile fracture, and its possible application to the prediction of the failure of real-world structures.

Acknowledgments

The authors gratefully acknowledge the support from the European Research Council through the ERC Consolidator Grant *FDM* ^{2}, grant number 864482, along with the support from the Research Council of Norway, NFR, and the German Academic Exchange Service, DAAD, through the project *FATIKA - Isogeometric phase-field modeling of fatigue in slender structures*, project number 281247.

§ Figures 11 and 14 reproduced from International Journal of Impact Engineering, Vol. 36, H. S. Alsos, J. Amdahl, On the resistance to penetration of stiffened plates, Part I-Experiments, Pages 799-807, Copyright (2009), with permission from Elsevier.

References

[1] A. A. Griffith, The phenomena of rupture and flow in solids, Philosophical Transactions of the Royal Society of London. Series A, Containing Papers of a Mathematical or Physical Character 221 (1921) 163–198.

[2] G. A. Francfort, J.-J. Marigo, Revisiting brittle fracture as an energy minimization problem, Journal of the Mechanics and Physics of Solids 46 (8) (1998) 1319–1342.

[3] B. Bourdin, G. A. Francfort, J.-J. Marigo, Numerical experiments in revisited brittle fracture, Journal of the Mechanics and Physics of Solids 48 (4) (2000) 797–826.

[4] H. Amor, J.-J. Marigo, C. Maurini, Regularized formulation of the variational brittle fracture with unilateral contact: Numerical experiments, Journal of the Mechanics and Physics of Solids 57 (8) (2009) 1209–1229.

[5] C. Miehe, M. Hofacker, F. Welschinger, A phase field model for rate-independent crack propagation: Robust algorithmic implementation based on operator splits, Computer Methods in Applied Mechanics and Engineering 199 (45) (2010) 2765–2778.

[6] F. Freddi, G. Royer-Carfagni, Regularized variational theories of fracture: A unified approach, Journal of the Mechanics and Physics of Solids 58 (8) (2010) 1154–1174.

[7] C. Steinke, M. Kaliske, A phase-field crack model based on directional stress decomposition, Computational Mechanics 63 (5) (2019) 1019–1046.

[8] C. Kuhn, A. Schlüter, R. Müller, On degradation functions in phase field fracture models, Computational Materials Science 108 (2015) 374–384.

[9] M. J. Borden, T. J. R. Hughes, C. M. Landis, A. Anvari, I. J. Lee, A phase-field formulation for fracture in ductile materials: Finite deformation balance law derivation, plastic degradation, and stress triaxiality effects, Computer Methods in Applied Mechanics and Engineering 312 (2016) 130–166.

[10] T. Gerasimov, L. De Lorenzis, A line search assisted monolithic approach for phase-field computing of brittle fracture, Computer Methods in Applied Mechanics and Engineering 312 (2016) 276–303.

[11] M. J. Borden, T. J. R. Hughes, C. M. Landis, C. V. Verhoosel, A higher-order phase-field model for brittle fracture: Formulation and analysis within the isogeometric analysis framework, Computer Methods in Applied Mechanics and Engineering 273 (2014) 100–118.

[12] K. Pham, H. Amor, J.-J. Marigo, C. Maurini, Gradient damage models and their use to approximate brittle fracture, International Journal of Damage Mechanics 20 (4) (2011) 618–652.

[13] C. Miehe, M. Hofacker, L.-M. Schänzel, F. Aldakheel, Phase field modeling of fracture in multi-physics problems. Part II. Coupled brittle-to-ductile failure criteria and crack

propagation in thermo-elastic-plastic solids, Computer Methods in Applied Mechanics and Engineering 294 (2015) 486–522.

[14] R. Alessi, M. Ambati, T. Gerasimov, S. Vidoli, L. De Lorenzis, Comparison of phase-field models of fracture coupled with plasticity, in: Advances in Computational Plasticity: A Book in Honour of D. Roger J. Owen, Springer International Publishing, Cham, 2018, pp. 1–21.

[15] F. P. Duda, A. Ciarbonetti, P. J. Sánchez, A. E. Huespe, A phase-field/gradient damage model for brittle fracture in elastic-plastic solids, International Journal of Plasticity 65 (2015) 269–296.

[16] M. Ambati, T. Gerasimov, L. De Lorenzis, Phase-field modeling of ductile fracture, Computational Mechanics 55 (5) (2015) 1017–1040.

[17] M. Ambati, R. Kruse, L. De Lorenzis, A phase-field model for ductile fracture at finite strains and its experimental verification, Computational Mechanics 57 (1) (2016) 149–167.

[18] R. Alessi, J.-J. Marigo, S. Vidoli, Gradient damage models coupled with plasticity and nucleation of cohesive cracks, Archive for Rational Mechanics and Analysis 214 (2) (2014) 575–615.

[19] R. Alessi, J.-J. Marigo, S. Vidoli, Gradient damage models coupled with plasticity: Variational formulation and main properties, Mechanics of Materials 80 (2015) 351–367.

[20] C. Kuhn, T. Noll, R. Müller, On phase field modeling of ductile fracture, GAMM-Mitteilungen 39 (1) (2016) 35–54.

[21] C. Huang, X. Gao, Development of a phase field method for modeling brittle and ductile fracture, Computational Materials Science 169 (2019) 109089.

[22] P. Rodriguez, J. Ulloa, C. Samaniego, E. Samaniego, A variational approach to the phase field modeling of brittle and ductile fracture, International Journal of Mechanical Sciences 144 (2018) 502–517.

[23] C. Miehe, S. Teichtmeister, F. Aldakheel, Phase-field modelling of ductile fracture: a variational gradient-extended plasticity-damage theory and its micromorphic regularization, Philosophical Transactions of the Royal Society A: Mathematical, Physical and Engineering Sciences 374 (2066) (2016) 20150170.

[24] M. Dittmann, F. Aldakheel, J. Schulte, P. Wriggers, C. Hesch, Variational phase-field formulation of non-linear ductile fracture, Computer Methods in Applied Mechanics and Engineering 342 (2018) 71–94.

[25] H. Ulmer, M. Hofacker, C. Miehe, Phase field modeling of fracture in plates and shells, Proc. Appl. Math. Mech. 12 (1) (2012) 171–172.

[26] F. Amiri, D. Millán, Y. Shen, T. Rabczuk, M. Arroyo, Phase-field modeling of fracture in linear thin shells, Theoretical and Applied Fracture Mechanics 69 (2014) 102–109.

[27] P. Areias, T. Rabczuk, M. A. Msekh, Phase-field analysis of finite-strain plates and shells including element subdivision, Computer Methods in Applied Mechanics and Engineering 312 (2016) 322–350.

[28] J. Reinoso, M. Paggi, C. Linder, Phase field modeling of brittle fracture for enhanced assumed strain shells at large deformations: formulation and finite element implementation, Computational Mechanics 59 (6) (2017) 981–1001.

[29] J. Kiendl, M. Ambati, L. De Lorenzis, H. Gomez, A. Reali, Phase-field description of brittle fracture in plates and shells, Computer Methods in Applied Mechanics and Engineering 312 (2016) 374–394.

[30] K. Paul, C. Zimmermann, K. K. Mandadapu, T. J. R. Hughes, C. M. Landis, R. A. Sauer, An adaptive space-time phase field formulation for dynamic fracture of brittle shells based on LR NURBS, Computational Mechanics (2020).

[31] D. Proserpio, M. Ambati, L. De Lorenzis, J. Kiendl, A framework for efficient isogeometric computations of phase-field brittle fracture in multipatch shell structures, Computer Methods in Applied Mechanics and Engineering 372 (2020) 113363.

[32] K. Paul, C. Zimmermann, T. X. Duong, R. A. Sauer, Isogeometric continuity constraints for multi-patch shells governed by fourth-order deformation and phase field models, Computer Methods in Applied Mechanics and Engineering 370 (2020) 113219.

[33] G. Kikis, M. Ambati, L. De Lorenzis, S. Klinkel, Phase-field model of brittle fracture in Reissnmoder-Mindlin plates and shells, Computer Methods in Applied Mechanics and Engineering 373 (2021) 113490.

[34] U. Pillai, S. P. Triantafyllou, I. Ashcroft, Y. Essa, F. M. de la Escalera, Phase-field modelling of brittle fracture in thin shell elements based on the MITC4+ approach, Computational Mechanics 65 (6) (2020) 1413–1432.

[35] M. Ambati, L. De Lorenzis, Phase-field modeling of brittle and ductile fracture in shells with isogeometric NURBS-based solid-shell elements, Computer Methods in Applied Mechanics and Engineering 312 (Supplement C) (2016) 351–373.

[36] M. Ambati, T. Gerasimov, L. De Lorenzis, A review on phase-field models of brittle fracture and a new fast hybrid formulation, Computational Mechanics 55 (2) (2015) 383–405.

[37] A. Mesgarnejad, B. Bourdin, M. M. Khonsari, Validation simulations for the variational approach to fracture, Computer Methods in Applied Mechanics and Engineering 290 (2015) 420–437.

[38] K. H. Pham, K. Ravi-Chandar, C. M. Landis, Experimental validation of a phase-field model for fracture, International Journal of Fracture 205 (1) (2017) 83–101.

[39] T. Wu, A. Carpiuc-Prisacari, M. Poncelet, L. De Lorenzis, Phase-field simulation of interactive mixed-mode fracture tests on cement mortar with full-field displacement boundary conditions, Engineering Fracture Mechanics 182 (2017) 658–688.

[40] E. Tanné, T. Li, B. Bourdin, J.-J. Marigo, C. Maurini, Crack nucleation in variational phase-field models of brittle fracture, Journal of the Mechanics and Physics of Solids 110 (2018) 80–99.

[41] D. Wick, T. Wick, R. J. Hellmig, H.-J. Christ, Numerical simulations of crack propagation in screws with phase-field modeling, Computational Materials Science 109 (2015) 367–379.

[42] J. Kiendl, K.-U. Bletzinger, J. Linhard, R. Wüchner, Isogeometric shell analysis with Kirchhoff–Love elements, Computer Methods in Applied Mechanics and Engineering 198 (49) (2009) 3902–3914.

[43] J. C. Simo, A framework for finite strain elastoplasticity based on maximum plastic dissipation and the multiplicative decomposition: Part I. Continuum formulation, Computer Methods in Applied Mechanics and Engineering 66 (2) (1988) 199–219.

[44] M. Ambati, J. Kiendl, L. De Lorenzis, Isogeometric Kirchhoff-Love shell formulation for elasto-plasticity, Computer Methods in Applied Mechanics and Engineering 340 (2018) 320–339.

[45] J. Kiendl, M.-C. Hsu, M. C. H. Wu, A. Reali, Isogeometric Kirchhoff-Love shell formulations for general hyperelastic materials, Computer Methods in Applied Mechanics and Engineering 291 (2015) 280–303.

[46] L. Ambrosio, V. Tortorelli, On the approximation of free discontinuity problems, Bollettino Unione Matematica Italiana B 6 (1992) 105–123.

[47] A. J. Herrema, E. L. Johnson, D. Proserpio, M. C. H. Wu, J. Kiendl, M.-C. Hsu, Penalty coupling of non-matching isogeometric Kirchhoff-Love shell patches with application to composite wind turbine blades, Computer Methods in Applied Mechanics and Engineering 346 (2019) 810–840.

[48] R. Dimitri, L. De Lorenzis, M. A. Scott, P. Wriggers, R. L. Taylor, G. Zavarise, Isogeometric large deformation frictionless contact using T-splines, Computer Methods in Applied Mechanics and Engineering 269 (2014) 394–414.

[49] E. L. Holten, Isogeometric contact analysis implementation of a penalty-based algorithm, Master's thesis, NTNU (2019).

[50] L. Piegl, W. Tiller, The NURBS book, Springer Science & Business Media, 2012.

[51] L. De Lorenzis, P. Wriggers, C. Weißenfels, Computational Contact Mechanics with the Finite Element Method, American Cancer Society, 2017, pp. 1–45.

[52] C. Zimmermann, R. A. Sauer, Adaptive local surface refinement based on LR NURBS and its application to contact, Computational Mechanics 60 (6) (2017) 1011–1031.

[53] K. A. Johannessen, T. Kvamsdal, T. Dokken, Isogeometric analysis using LR B-splines, Computer Methods in Applied Mechanics and Engineering 269 (2014) 471–514.

[54] J. Besson, Continuum models of ductile fracture: A review, International Journal of Damage Mechanics 19 (1) (2010) 3–52.

[55] J. F. Caseiro, R. A. F. Valente, A. Reali, J. Kiendl, F. Auricchio, R. J. Alves de Sousa, On the Assumed Natural Strain method to alleviate locking in solid-shell NURBS-based finite elements, Computational Mechanics 53 (6) (2014) 1341–1353.

[56] H. S. Alsos, J. Amdahl, On the resistance to penetration of stiffened plates, Part I–Experiments, International Journal of Impact Engineering 36 (6) (2009) 799–807.

Figures 11 and 14 reproduced from International Journal of Impact Engineering, Vol. 36, H. S. Alsos and J. Amdahl, On the resistance to penetration of stiffened plates, Part I-Experiments, Pages 799-807, Copyright (2009), with permission from Elsevier.

Previous PhD theses published at the Department of Marine Technology

Previous PhD theses published at the Department of Marine Technology (earlier: Faculty of Marine Technology)
NORWEGIAN UNIVERSITY OF SCIENCE AND TECHNOLOGY

Report No.	Author	Title
	Kavlie, Dag	Optimization of Plane Elastic Grillages, 1967
	Hansen, Hans R.	Man-Machine Communication and Data-Storage Methods in Ship Structural Design, 1971
	Gisvold, Kaare M.	A Method for non-linear mixed -integer programming and its Application to Design Problems, 1971
	Lund, Sverre	Tanker Frame Optimalization by means of SUMT-Transformation and Behaviour Models, 1971
	Vinje, Tor	On Vibration of Spherical Shells Interacting with Fluid, 1972
	Lorentz, Jan D.	Tank Arrangement for Crude Oil Carriers in Accordance with the new Anti-Pollution Regulations, 1975
	Carlsen, Carl A.	Computer-Aided Design of Tanker Structures, 1975
	Larsen, Carl M.	Static and Dynamic Analysis of Offshore Pipelines during Installation, 1976
UR-79-01	Brigt Hatlestad, MK	The finite element method used in a fatigue evaluation of fixed offshore platforms. (Dr.Ing. Thesis)
UR-79-02	Erik Pettersen, MK	Analysis and design of cellular structures. (Dr.Ing. Thesis)
UR-79-03	Sverre Valsgård, MK	Finite difference and finite element methods applied to nonlinear analysis of plated structures. (Dr.Ing. Thesis)
UR-79-04	Nils T. Nordsve, MK	Finite element collapse analysis of structural members considering imperfections and stresses due to fabrication. (Dr.Ing. Thesis)
UR-79-05	Ivar J. Fylling, MK	Analysis of towline forces in ocean towing systems. (Dr.Ing. Thesis)
UR-80-06	Nils Sandsmark, MM	Analysis of Stationary and Transient Heat Conduction by the Use of the Finite Element Method. (Dr.Ing. Thesis)
UR-80-09	Sverre Haver, MK	Analysis of uncertainties related to the stochastic modeling of ocean waves. (Dr.Ing. Thesis)
UR-81-15	Odland, Jonas	On the Strength of welded Ring stiffened cylindrical Shells primarily subjected to axial Compression
UR-82-17	Engesvik, Knut	Analysis of Uncertainties in the fatigue Capacity of

		Welded Joints
UR-82-18	Rye, Henrik	Ocean wave groups
UR-83-30	Eide, Oddvar Inge	On Cumulative Fatigue Damage in Steel Welded Joints
UR-83-33	Mo, Olav	Stochastic Time Domain Analysis of Slender Offshore Structures
UR-83-34	Amdahl, Jørgen	Energy absorption in Ship-platform impacts
UR-84-37	Mørch, Morten	Motions and mooring forces of semi submersibles as determined by full-scale measurements and theoretical analysis
UR-84-38	Soares, C. Guedes	Probabilistic models for load effects in ship structures
UR-84-39	Aarsnes, Jan V.	Current forces on ships
UR-84-40	Czujko, Jerzy	Collapse Analysis of Plates subjected to Biaxial Compression and Lateral Load
UR-85-46	Alf G. Engseth, MK	Finite element collapse analysis of tubular steel offshore structures. (Dr.Ing. Thesis)
UR-86-47	Dengody Sheshappa, MP	A Computer Design Model for Optimizing Fishing Vessel Designs Based on Techno-Economic Analysis. (Dr.Ing. Thesis)
UR-86-48	Vidar Aanesland, MH	A Theoretical and Numerical Study of Ship Wave Resistance. (Dr.Ing. Thesis)
UR-86-49	Heinz-Joachim Wessel, MK	Fracture Mechanics Analysis of Crack Growth in Plate Girders. (Dr.Ing. Thesis)
UR-86-50	Jon Taby, MK	Ultimate and Post-ultimate Strength of Dented Tubular Members. (Dr.Ing. Thesis)
UR-86-51	Walter Lian, MH	A Numerical Study of Two-Dimensional Separated Flow Past Bluff Bodies at Moderate KC-Numbers. (Dr.Ing. Thesis)
UR-86-52	Bjørn Sortland, MH	Force Measurements in Oscillating Flow on Ship Sections and Circular Cylinders in a U-Tube Water Tank. (Dr.Ing. Thesis)
UR-86-53	Kurt Strand, MM	A System Dynamic Approach to One-dimensional Fluid Flow. (Dr.Ing. Thesis)
UR-86-54	Arne Edvin Løken, MH	Three Dimensional Second Order Hydrodynamic Effects on Ocean Structures in Waves. (Dr.Ing. Thesis)
UR-86-55	Sigurd Falch, MH	A Numerical Study of Slamming of Two-Dimensional Bodies. (Dr.Ing. Thesis)
UR-87-56	Arne Braathen, MH	Application of a Vortex Tracking Method to the Prediction of Roll Damping of a Two-Dimension Floating Body. (Dr.Ing. Thesis)

UR-87-57	Bernt Leira, MK	Gaussian Vector Processes for Reliability Analysis involving Wave-Induced Load Effects. (Dr.Ing. Thesis)
UR-87-58	Magnus Småvik, MM	Thermal Load and Process Characteristics in a Two-Stroke Diesel Engine with Thermal Barriers (in Norwegian). (Dr.Ing. Thesis)
MTA-88-59	Bernt Arild Bremdal, MP	An Investigation of Marine Installation Processes – A Knowledge - Based Planning Approach. (Dr.Ing. Thesis)
MTA-88-60	Xu Jun, MK	Non-linear Dynamic Analysis of Space-framed Offshore Structures. (Dr.Ing. Thesis)
MTA-89-61	Gang Miao, MH	Hydrodynamic Forces and Dynamic Responses of Circular Cylinders in Wave Zones. (Dr.Ing. Thesis)
MTA-89-62	Martin Greenhow, MH	Linear and Non-Linear Studies of Waves and Floating Bodies. Part I and Part II. (Dr.Techn. Thesis)
MTA-89-63	Chang Li, MH	Force Coefficients of Spheres and Cubes in Oscillatory Flow with and without Current. (Dr.Ing. Thesis
MTA-89-64	Hu Ying, MP	A Study of Marketing and Design in Development of Marine Transport Systems. (Dr.Ing. Thesis)
MTA-89-65	Arild Jæger, MH	Seakeeping, Dynamic Stability and Performance of a Wedge Shaped Planing Hull. (Dr.Ing. Thesis)
MTA-89-66	Chan Siu Hung, MM	The dynamic characteristics of tilting-pad bearings
MTA-89-67	Kim Wikstrøm, MP	Analysis av projekteringen for ett offshore projekt. (Licenciat-avhandling)
MTA-89-68	Jiao Guoyang, MK	Reliability Analysis of Crack Growth under Random Loading, considering Model Updating. (Dr.Ing. Thesis)
MTA-89-69	Arnt Olufsen, MK	Uncertainty and Reliability Analysis of Fixed Offshore Structures. (Dr.Ing. Thesis)
MTA-89-70	Wu Yu-Lin, MR	System Reliability Analyses of Offshore Structures using improved Truss and Beam Models. (Dr.Ing. Thesis)
MTA-90-71	Jan Roger Hoff, MH	Three-dimensional Green function of a vessel with forward speed in waves. (Dr.Ing. Thesis)
MTA-90-72	Rong Zhao, MH	Slow-Drift Motions of a Moored Two-Dimensional Body in Irregular Waves. (Dr.Ing. Thesis)
MTA-90-73	Atle Minsaas, MP	Economical Risk Analysis. (Dr.Ing. Thesis)
MTA-90-74	Knut-Aril Farnes, MK	Long-term Statistics of Response in Non-linear Marine Structures. (Dr.Ing. Thesis)
MTA-90-75	Torbjørn Sotberg, MK	Application of Reliability Methods for Safety Assessment of Submarine Pipelines. (Dr.Ing.

		Thesis)
MTA-90-76	Zeuthen, Steffen, MP	SEAMAID. A computational model of the design process in a constraint-based logic programming environment. An example from the offshore domain. (Dr.Ing. Thesis)
MTA-91-77	Haagensen, Sven, MM	Fuel Dependant Cyclic Variability in a Spark Ignition Engine - An Optical Approach. (Dr.Ing. Thesis)
MTA-91-78	Løland, Geir, MH	Current forces on and flow through fish farms. (Dr.Ing. Thesis)
MTA-91-79	Hoen, Christopher, MK	System Identification of Structures Excited by Stochastic Load Processes. (Dr.Ing. Thesis)
MTA-91-80	Haugen, Stein, MK	Probabilistic Evaluation of Frequency of Collision between Ships and Offshore Platforms. (Dr.Ing. Thesis)
MTA-91-81	Sødahl, Nils, MK	Methods for Design and Analysis of Flexible Risers. (Dr.Ing. Thesis)
MTA-91-82	Ormberg, Harald, MK	Non-linear Response Analysis of Floating Fish Farm Systems. (Dr.Ing. Thesis)
MTA-91-83	Marley, Mark J., MK	Time Variant Reliability under Fatigue Degradation. (Dr.Ing. Thesis)
MTA-91-84	Krokstad, Jørgen R., MH	Second-order Loads in Multidirectional Seas. (Dr.Ing. Thesis)
MTA-91-85	Molteberg, Gunnar A., MM	The Application of System Identification Techniques to Performance Monitoring of Four Stroke Turbocharged Diesel Engines. (Dr.Ing. Thesis)
MTA-92-86	Mørch, Hans Jørgen Bjelke, MH	Aspects of Hydrofoil Design: with Emphasis on Hydrofoil Interaction in Calm Water. (Dr.Ing. Thesis)
MTA-92-87	Chan Siu Hung, MM	Nonlinear Analysis of Rotordynamic Instabilities in Highspeed Turbomachinery. (Dr.Ing. Thesis)
MTA-92-88	Bessason, Bjarni, MK	Assessment of Earthquake Loading and Response of Seismically Isolated Bridges. (Dr.Ing. Thesis)
MTA-92-89	Langli, Geir, MP	Improving Operational Safety through exploitation of Design Knowledge - an investigation of offshore platform safety. (Dr.Ing. Thesis)
MTA-92-90	Sævik, Svein, MK	On Stresses and Fatigue in Flexible Pipes. (Dr.Ing. Thesis)
MTA-92-91	Ask, Tor Ø., MM	Ignition and Flame Growth in Lean Gas-Air Mixtures. An Experimental Study with a Schlieren System. (Dr.Ing. Thesis)
MTA-86-92	Hessen, Gunnar, MK	Fracture Mechanics Analysis of Stiffened Tubular Members. (Dr.Ing. Thesis)

MTA-93-93	Steinebach, Christian, MM	Knowledge Based Systems for Diagnosis of Rotating Machinery. (Dr.Ing. Thesis)
MTA-93-94	Dalane, Jan Inge, MK	System Reliability in Design and Maintenance of Fixed Offshore Structures. (Dr.Ing. Thesis)
MTA-93-95	Steen, Sverre, MH	Cobblestone Effect on SES. (Dr.Ing. Thesis)
MTA-93-96	Karunakaran, Daniel, MK	Nonlinear Dynamic Response and Reliability Analysis of Drag-dominated Offshore Platforms. (Dr.Ing. Thesis)
MTA-93-97	Hagen, Arnulf, MP	The Framework of a Design Process Language. (Dr.Ing. Thesis)
MTA-93-98	Nordrik, Rune, MM	Investigation of Spark Ignition and Autoignition in Methane and Air Using Computational Fluid Dynamics and Chemical Reaction Kinetics. A Numerical Study of Ignition Processes in Internal Combustion Engines. (Dr.Ing. Thesis)
MTA-94-99	Passano, Elizabeth, MK	Efficient Analysis of Nonlinear Slender Marine Structures. (Dr.Ing. Thesis)
MTA-94-100	Kvålsvold, Jan, MH	Hydroelastic Modelling of Wetdeck Slamming on Multihull Vessels. (Dr.Ing. Thesis)
MTA-94-102	Bech, Sidsel M., MK	Experimental and Numerical Determination of Stiffness and Strength of GRP/PVC Sandwich Structures. (Dr.Ing. Thesis)
MTA-95-103	Paulsen, Hallvard, MM	A Study of Transient Jet and Spray using a Schlieren Method and Digital Image Processing. (Dr.Ing. Thesis)
MTA-95-104	Hovde, Geir Olav, MK	Fatigue and Overload Reliability of Offshore Structural Systems, Considering the Effect of Inspection and Repair. (Dr.Ing. Thesis)
MTA-95-105	Wang, Xiaozhi, MK	Reliability Analysis of Production Ships with Emphasis on Load Combination and Ultimate Strength. (Dr.Ing. Thesis)
MTA-95-106	Ulstein, Tore, MH	Nonlinear Effects of a Flexible Stern Seal Bag on Cobblestone Oscillations of an SES. (Dr.Ing. Thesis)
MTA-95-107	Solaas, Frøydis, MH	Analytical and Numerical Studies of Sloshing in Tanks. (Dr.Ing. Thesis)
MTA-95-108	Hellan, Øyvind, MK	Nonlinear Pushover and Cyclic Analyses in Ultimate Limit State Design and Reassessment of Tubular Steel Offshore Structures. (Dr.Ing. Thesis)
MTA-95-109	Hermundstad, Ole A., MK	Theoretical and Experimental Hydroelastic Analysis of High Speed Vessels. (Dr.Ing. Thesis)
MTA-96-110	Bratland, Anne K., MH	Wave-Current Interaction Effects on Large-Volume Bodies in Water of Finite Depth. (Dr.Ing. Thesis)
MTA-96-111	Herfjord, Kjell, MH	A Study of Two-dimensional Separated Flow by a Combination of the Finite Element Method and

		Navier-Stokes Equations. (Dr.Ing. Thesis)
MTA-96-112	Æsøy, Vilmar, MM	Hot Surface Assisted Compression Ignition in a Direct Injection Natural Gas Engine. (Dr.Ing. Thesis)
MTA-96-113	Eknes, Monika L., MK	Escalation Scenarios Initiated by Gas Explosions on Offshore Installations. (Dr.Ing. Thesis)
MTA-96-114	Erikstad, Stein O., MP	A Decision Support Model for Preliminary Ship Design. (Dr.Ing. Thesis)
MTA-96-115	Pedersen, Egil, MH	A Nautical Study of Towed Marine Seismic Streamer Cable Configurations. (Dr.Ing. Thesis)
MTA-97-116	Moksnes, Paul O., MM	Modelling Two-Phase Thermo-Fluid Systems Using Bond Graphs. (Dr.Ing. Thesis)
MTA-97-117	Halse, Karl H., MK	On Vortex Shedding and Prediction of Vortex-Induced Vibrations of Circular Cylinders. (Dr.Ing. Thesis)
MTA-97-118	Igland, Ragnar T., MK	Reliability Analysis of Pipelines during Laying, considering Ultimate Strength under Combined Loads. (Dr.Ing. Thesis)
MTA-97-119	Pedersen, Hans-P., MP	Levendefiskteknologi for fiskefartøy. (Dr.Ing. Thesis)
MTA-98-120	Vikestad, Kyrre, MK	Multi-Frequency Response of a Cylinder Subjected to Vortex Shedding and Support Motions. (Dr.Ing. Thesis)
MTA-98-121	Azadi, Mohammad R. E., MK	Analysis of Static and Dynamic Pile-Soil-Jacket Behaviour. (Dr.Ing. Thesis)
MTA-98-122	Ulltang, Terje, MP	A Communication Model for Product Information. (Dr.Ing. Thesis)
MTA-98-123	Torbergsen, Erik, MM	Impeller/Diffuser Interaction Forces in Centrifugal Pumps. (Dr.Ing. Thesis)
MTA-98-124	Hansen, Edmond, MH	A Discrete Element Model to Study Marginal Ice Zone Dynamics and the Behaviour of Vessels Moored in Broken Ice. (Dr.Ing. Thesis)
MTA-98-125	Videiro, Paulo M., MK	Reliability Based Design of Marine Structures. (Dr.Ing. Thesis)
MTA-99-126	Mainçon, Philippe, MK	Fatigue Reliability of Long Welds Application to Titanium Risers. (Dr.Ing. Thesis)
MTA-99-127	Haugen, Elin M., MH	Hydroelastic Analysis of Slamming on Stiffened Plates with Application to Catamaran Wetdecks. (Dr.Ing. Thesis)
MTA-99-128	Langhelle, Nina K., MK	Experimental Validation and Calibration of Nonlinear Finite Element Models for Use in Design of Aluminium Structures Exposed to Fire. (Dr.Ing. Thesis)
MTA-99-	Berstad, Are J., MK	Calculation of Fatigue Damage in Ship Structures.

129		(Dr.Ing. Thesis)
MTA-99-130	Andersen, Trond M., MM	Short Term Maintenance Planning. (Dr.Ing. Thesis)
MTA-99-131	Tveiten, Bård Wathne, MK	Fatigue Assessment of Welded Aluminium Ship Details. (Dr.Ing. Thesis)
MTA-99-132	Søreide, Fredrik, MP	Applications of underwater technology in deep water archaeology. Principles and practice. (Dr.Ing. Thesis)
MTA-99-133	Tønnessen, Rune, MH	A Finite Element Method Applied to Unsteady Viscous Flow Around 2D Blunt Bodies With Sharp Corners. (Dr.Ing. Thesis)
MTA-99-134	Elvekrok, Dag R., MP	Engineering Integration in Field Development Projects in the Norwegian Oil and Gas Industry. The Supplier Management of Norne. (Dr.Ing. Thesis)
MTA-99-135	Fagerholt, Kjetil, MP	Optimeringsbaserte Metoder for Ruteplanlegging innen skipsfart. (Dr.Ing. Thesis)
MTA-99-136	Bysveen, Marie, MM	Visualization in Two Directions on a Dynamic Combustion Rig for Studies of Fuel Quality. (Dr.Ing. Thesis)
MTA-2000-137	Storteig, Eskild, MM	Dynamic characteristics and leakage performance of liquid annular seals in centrifugal pumps. (Dr.Ing. Thesis)
MTA-2000-138	Sagli, Gro, MK	Model uncertainty and simplified estimates of long term extremes of hull girder loads in ships. (Dr.Ing. Thesis)
MTA-2000-139	Tronstad, Harald, MK	Nonlinear analysis and design of cable net structures like fishing gear based on the finite element method. (Dr.Ing. Thesis)
MTA-2000-140	Kroneberg, André, MP	Innovation in shipping by using scenarios. (Dr.Ing. Thesis)
MTA-2000-141	Haslum, Herbjørn Alf, MH	Simplified methods applied to nonlinear motion of spar platforms. (Dr.Ing. Thesis)
MTA-2001-142	Samdal, Ole Johan, MM	Modelling of Degradation Mechanisms and Stressor Interaction on Static Mechanical Equipment Residual Lifetime. (Dr.Ing. Thesis)
MTA-2001-143	Baarholm, Rolf Jarle, MH	Theoretical and experimental studies of wave impact underneath decks of offshore platforms. (Dr.Ing. Thesis)
MTA-2001-144	Wang, Lihua, MK	Probabilistic Analysis of Nonlinear Wave-induced Loads on Ships. (Dr.Ing. Thesis)
MTA-2001-145	Kristensen, Odd H. Holt, MK	Ultimate Capacity of Aluminium Plates under Multiple Loads, Considering HAZ Properties. (Dr.Ing. Thesis)
MTA-2001-146	Greco, Marilena, MH	A Two-Dimensional Study of Green-Water

		Loading. (Dr.Ing. Thesis)
MTA-2001-147	Heggelund, Svein E., MK	Calculation of Global Design Loads and Load Effects in Large High Speed Catamarans. (Dr.Ing. Thesis)
MTA-2001-148	Babalola, Olusegun T., MK	Fatigue Strength of Titanium Risers – Defect Sensitivity. (Dr.Ing. Thesis)
MTA-2001-149	Mohammed, Abuu K., MK	Nonlinear Shell Finite Elements for Ultimate Strength and Collapse Analysis of Ship Structures. (Dr.Ing. Thesis)
MTA-2002-150	Holmedal, Lars E., MH	Wave-current interactions in the vicinity of the sea bed. (Dr.Ing. Thesis)
MTA-2002-151	Rognebakke, Olav F., MH	Sloshing in rectangular tanks and interaction with ship motions. (Dr.Ing. Thesis)
MTA-2002-152	Lader, Pål Furset, MH	Geometry and Kinematics of Breaking Waves. (Dr.Ing. Thesis)
MTA-2002-153	Yang, Qinzheng, MH	Wash and wave resistance of ships in finite water depth. (Dr.Ing. Thesis)
MTA-2002-154	Melhus, Øyvin, MM	Utilization of VOC in Diesel Engines. Ignition and combustion of VOC released by crude oil tankers. (Dr.Ing. Thesis)
MTA-2002-155	Ronæss, Marit, MH	Wave Induced Motions of Two Ships Advancing on Parallel Course. (Dr.Ing. Thesis)
MTA-2002-156	Økland, Ole D., MK	Numerical and experimental investigation of whipping in twin hull vessels exposed to severe wet deck slamming. (Dr.Ing. Thesis)
MTA-2002-157	Ge, Chunhua, MK	Global Hydroelastic Response of Catamarans due to Wet Deck Slamming. (Dr.Ing. Thesis)
MTA-2002-158	Byklum, Eirik, MK	Nonlinear Shell Finite Elements for Ultimate Strength and Collapse Analysis of Ship Structures. (Dr.Ing. Thesis)
IMT-2003-1	Chen, Haibo, MK	Probabilistic Evaluation of FPSO-Tanker Collision in Tandem Offloading Operation. (Dr.Ing. Thesis)
IMT-2003-2	Skaugset, Kjetil Bjørn, MK	On the Suppression of Vortex Induced Vibrations of Circular Cylinders by Radial Water Jets. (Dr.Ing. Thesis)
IMT-2003-3	Chezhian, Muthu	Three-Dimensional Analysis of Slamming. (Dr.Ing. Thesis)
IMT-2003-4	Buhaug, Øyvind	Deposit Formation on Cylinder Liner Surfaces in Medium Speed Engines. (Dr.Ing. Thesis)
IMT-2003-5	Tregde, Vidar	Aspects of Ship Design: Optimization of Aft Hull with Inverse Geometry Design. (Dr.Ing. Thesis)
IMT-	Wist, Hanne Therese	Statistical Properties of Successive Ocean Wave

2003-6		Parameters. (Dr.Ing. Thesis)
IMT-2004-7	Ransau, Samuel	Numerical Methods for Flows with Evolving Interfaces. (Dr.Ing. Thesis)
IMT-2004-8	Soma, Torkel	Blue-Chip or Sub-Standard. A data interrogation approach of identity safety characteristics of shipping organization. (Dr.Ing. Thesis)
IMT-2004-9	Ersdal, Svein	An experimental study of hydrodynamic forces on cylinders and cables in near axial flow. (Dr.Ing. Thesis)
IMT-2005-10	Brodtkorb, Per Andreas	The Probability of Occurrence of Dangerous Wave Situations at Sea. (Dr.Ing. Thesis)
IMT-2005-11	Yttervik, Rune	Ocean current variability in relation to offshore engineering. (Dr.Ing. Thesis)
IMT-2005-12	Fredheim, Arne	Current Forces on Net-Structures. (Dr.Ing. Thesis)
IMT-2005-13	Heggernes, Kjetil	Flow around marine structures. (Dr.Ing. Thesis
IMT-2005-14	Fouques, Sebastien	Lagrangian Modelling of Ocean Surface Waves and Synthetic Aperture Radar Wave Measurements. (Dr.Ing. Thesis)
IMT-2006-15	Holm, Håvard	Numerical calculation of viscous free surface flow around marine structures. (Dr.Ing. Thesis)
IMT-2006-16	Bjørheim, Lars G.	Failure Assessment of Long Through Thickness Fatigue Cracks in Ship Hulls. (Dr.Ing. Thesis)
IMT-2006-17	Hansson, Lisbeth	Safety Management for Prevention of Occupational Accidents. (Dr.Ing. Thesis)
IMT-2006-18	Zhu, Xinying	Application of the CIP Method to Strongly Nonlinear Wave-Body Interaction Problems. (Dr.Ing. Thesis)
IMT-2006-19	Reite, Karl Johan	Modelling and Control of Trawl Systems. (Dr.Ing. Thesis)
IMT-2006-20	Smogeli, Øyvind Notland	Control of Marine Propellers. From Normal to Extreme Conditions. (Dr.Ing. Thesis)
IMT-2007-21	Storhaug, Gaute	Experimental Investigation of Wave Induced Vibrations and Their Effect on the Fatigue Loading of Ships. (Dr.Ing. Thesis)
IMT-2007-22	Sun, Hui	A Boundary Element Method Applied to Strongly Nonlinear Wave-Body Interaction Problems. (PhD Thesis, CeSOS)
IMT-2007-23	Rustad, Anne Marthine	Modelling and Control of Top Tensioned Risers. (PhD Thesis, CeSOS)
IMT-2007-24	Johansen, Vegar	Modelling flexible slender system for real-time simulations and control applications
IMT-2007-25	Wroldsen, Anders Sunde	Modelling and control of tensegrity structures.

		(PhD Thesis, CeSOS)
IMT-2007-26	Aronsen, Kristoffer Høye	An experimental investigation of in-line and combined inline and cross flow vortex induced vibrations. (Dr. avhandling, IMT)
IMT-2007-27	Gao, Zhen	Stochastic Response Analysis of Mooring Systems with Emphasis on Frequency-domain Analysis of Fatigue due to Wide-band Response Processes (PhD Thesis, CeSOS)
IMT-2007-28	Thorstensen, Tom Anders	Lifetime Profit Modelling of Ageing Systems Utilizing Information about Technical Condition. (Dr.ing. thesis, IMT)
IMT-2008-29	Refsnes, Jon Erling Gorset	Nonlinear Model-Based Control of Slender Body AUVs (PhD Thesis, IMT)
IMT-2008-30	Berntsen, Per Ivar B.	Structural Reliability Based Position Mooring. (PhD-Thesis, IMT)
IMT-2008-31	Ye, Naiquan	Fatigue Assessment of Aluminium Welded Box-stiffener Joints in Ships (Dr.ing. thesis, IMT)
IMT-2008-32	Radan, Damir	Integrated Control of Marine Electrical Power Systems. (PhD-Thesis, IMT)
IMT-2008-33	Thomassen, Paul	Methods for Dynamic Response Analysis and Fatigue Life Estimation of Floating Fish Cages. (Dr.ing. thesis, IMT)
IMT-2008-34	Pákozdi, Csaba	A Smoothed Particle Hydrodynamics Study of Two-dimensional Nonlinear Sloshing in Rectangular Tanks. (Dr.ing.thesis, IMT/ CeSOS)
IMT-2007-35	Grytøyr, Guttorm	A Higher-Order Boundary Element Method and Applications to Marine Hydrodynamics. (Dr.ing.thesis, IMT)
IMT-2008-36	Drummen, Ingo	Experimental and Numerical Investigation of Nonlinear Wave-Induced Load Effects in Containerships considering Hydroelasticity. (PhD thesis, CeSOS)
IMT-2008-37	Skejic, Renato	Maneuvering and Seakeeping of a Singel Ship and of Two Ships in Interaction. (PhD-Thesis, CeSOS)
IMT-2008-38	Harlem, Alf	An Age-Based Replacement Model for Repairable Systems with Attention to High-Speed Marine Diesel Engines. (PhD-Thesis, IMT)
IMT-2008-39	Alsos, Hagbart S.	Ship Grounding. Analysis of Ductile Fracture, Bottom Damage and Hull Girder Response. (PhD-thesis, IMT)
IMT-2008-40	Graczyk, Mateusz	Experimental Investigation of Sloshing Loading and Load Effects in Membrane LNG Tanks Subjected to Random Excitation. (PhD-thesis, CeSOS)
IMT-2008-41	Taghipour, Reza	Efficient Prediction of Dynamic Response for Flexible amd Multi-body Marine Structures. (PhD-

		thesis, CeSOS)
IMT-2008-42	Ruth, Eivind	Propulsion control and thrust allocation on marine vessels. (PhD thesis, CeSOS)
IMT-2008-43	Nystad, Bent Helge	Technical Condition Indexes and Remaining Useful Life of Aggregated Systems. PhD thesis, IMT
IMT-2008-44	Soni, Prashant Kumar	Hydrodynamic Coefficients for Vortex Induced Vibrations of Flexible Beams, PhD thesis, CeSOS
IMT-2009-45	Amlashi, Hadi K.K.	Ultimate Strength and Reliability-based Design of Ship Hulls with Emphasis on Combined Global and Local Loads. PhD Thesis, IMT
IMT-2009-46	Pedersen, Tom Arne	Bond Graph Modelling of Marine Power Systems. PhD Thesis, IMT
IMT-2009-47	Kristiansen, Trygve	Two-Dimensional Numerical and Experimental Studies of Piston-Mode Resonance. PhD-Thesis, CeSOS
IMT-2009-48	Ong, Muk Chen	Applications of a Standard High Reynolds Number Model and a Stochastic Scour Prediction Model for Marine Structures. PhD-thesis, IMT
IMT-2009-49	Hong, Lin	Simplified Analysis and Design of Ships subjected to Collision and Grounding. PhD-thesis, IMT
IMT-2009-50	Koushan, Kamran	Vortex Induced Vibrations of Free Span Pipelines, PhD thesis, IMT
IMT-2009-51	Korsvik, Jarl Eirik	Heuristic Methods for Ship Routing and Scheduling. PhD-thesis, IMT
IMT-2009-52	Lee, Jihoon	Experimental Investigation and Numerical in Analyzing the Ocean Current Displacement of Longlines. Ph.d.-Thesis, IMT.
IMT-2009-53	Vestbøstad, Tone Gran	A Numerical Study of Wave-in-Deck Impact usin a Two-Dimensional Constrained Interpolation Profile Method, Ph.d.thesis, CeSOS.
IMT-2009-54	Bruun, Kristine	Bond Graph Modelling of Fuel Cells for Marine Power Plants. Ph.d.-thesis, IMT
IMT 2009-55	Holstad, Anders	Numerical Investigation of Turbulence in a Sekwed Three-Dimensional Channel Flow, Ph.d.-thesis, IMT.
IMT 2009-56	Ayala-Uraga, Efren	Reliability-Based Assessment of Deteriorating Ship-shaped Offshore Structures, Ph.d.-thesis, IMT
IMT 2009-57	Kong, Xiangjun	A Numerical Study of a Damaged Ship in Beam Sea Waves. Ph.d.-thesis, IMT/CeSOS.
IMT 2010-58	Kristiansen, David	Wave Induced Effects on Floaters of Aquaculture Plants, Ph.d.-thesis, CeSOS.

IMT 2010-59	Ludvigsen, Martin	An ROV-Toolbox for Optical and Acoustic Scientific Seabed Investigation. Ph.d.-thesis IMT.
IMT 2010-60	Hals, Jørgen	Modelling and Phase Control of Wave-Energy Converters. Ph.d.thesis, CeSOS.
IMT 2010- 61	Shu, Zhi	Uncertainty Assessment of Wave Loads and Ultimate Strength of Tankers and Bulk Carriers in a Reliability Framework. Ph.d. Thesis, IMT/ CeSOS
IMT 2010-62	Shao, Yanlin	Numerical Potential-Flow Studies on Weakly-Nonlinear Wave-Body Interactions with/without Small Forward Speed, Ph.d.thesis,CeSOS.
IMT 2010-63	Califano, Andrea	Dynamic Loads on Marine Propellers due to Intermittent Ventilation. Ph.d.thesis, IMT.
IMT 2010-64	El Khoury, George	Numerical Simulations of Massively Separated Turbulent Flows, Ph.d.-thesis, IMT
IMT 2010-65	Seim, Knut Sponheim	Mixing Process in Dense Overflows with Emphasis on the Faroe Bank Channel Overflow. Ph.d.thesis, IMT
IMT 2010-66	Jia, Huirong	Structural Analysis of Intect and Damaged Ships in a Collission Risk Analysis Perspective. Ph.d.thesis CeSoS.
IMT 2010-67	Jiao, Linlin	Wave-Induced Effects on a Pontoon-type Very Large Floating Structures (VLFS). Ph.D.-thesis, CeSOS.
IMT 2010-68	Abrahamsen, Bjørn Christian	Sloshing Induced Tank Roof with Entrapped Air Pocket. Ph.d.thesis, CeSOS.
IMT 2011-69	Karimirad, Madjid	Stochastic Dynamic Response Analysis of Spar-Type Wind Turbines with Catenary or Taut Mooring Systems. Ph.d.-thesis, CeSOS.
IMT - 2011-70	Erlend Meland	Condition Monitoring of Safety Critical Valves. Ph.d.-thesis, IMT.
IMT – 2011-71	Yang, Limin	Stochastic Dynamic System Analysis of Wave Energy Converter with Hydraulic Power Take-Off, with Particular Reference to Wear Damage Analysis, Ph.d. Thesis, CeSOS.
IMT – 2011-72	Visscher, Jan	Application of Particla Image Velocimetry on Turbulent Marine Flows, Ph.d.Thesis, IMT.
IMT – 2011-73	Su, Biao	Numerical Predictions of Global and Local Ice Loads on Ships. Ph.d.Thesis, CeSOS.
IMT – 2011-74	Liu, Zhenhui	Analytical and Numerical Analysis of Iceberg Collision with Ship Structures. Ph.d.Thesis, IMT.
IMT – 2011-75	Aarsæther, Karl Gunnar	Modeling and Analysis of Ship Traffic by Observation and Numerical Simulation. Ph.d.Thesis, IMT.

Imt – 2011-76	Wu, Jie	Hydrodynamic Force Identification from Stochastic Vortex Induced Vibration Experiments with Slender Beams. Ph.d.Thesis, IMT.
Imt – 2011-77	Amini, Hamid	Azimuth Propulsors in Off-design Conditions. Ph.d.Thesis, IMT.
IMT – 2011-78	Nguyen, Tan-Hoi	Toward a System of Real-Time Prediction and Monitoring of Bottom Damage Conditions During Ship Grounding. Ph.d.thesis, IMT.
IMT-2011-79	Tavakoli, Mohammad T.	Assessment of Oil Spill in Ship Collision and Grounding, Ph.d.thesis, IMT.
IMT-2011-80	Guo, Bingjie	Numerical and Experimental Investigation of Added Resistance in Waves. Ph.d.Thesis, IMT.
IMT-2011-81	Chen, Qiaofeng	Ultimate Strength of Aluminium Panels, considering HAZ Effects, IMT
IMT-2012-82	Kota, Ravikiran S.	Wave Loads on Decks of Offshore Structures in Random Seas, CeSOS.
IMT-2012-83	Sten, Ronny	Dynamic Simulation of Deep Water Drilling Risers with Heave Compensating System, IMT.
IMT-2012-84	Berle, Øyvind	Risk and resilience in global maritime supply chains, IMT.
IMT-2012-85	Fang, Shaoji	Fault Tolerant Position Mooring Control Based on Structural Reliability, CeSOS.
IMT-2012-86	You, Jikun	Numerical studies on wave forces and moored ship motions in intermediate and shallow water, CeSOS.
IMT-2012-87	Xiang ,Xu	Maneuvering of two interacting ships in waves, CeSOS
IMT-2012-88	Dong, Wenbin	Time-domain fatigue response and reliability analysis of offshore wind turbines with emphasis on welded tubular joints and gear components, CeSOS
IMT-2012-89	Zhu, Suji	Investigation of Wave-Induced Nonlinear Load Effects in Open Ships considering Hull Girder Vibrations in Bending and Torsion, CeSOS
IMT-2012-90	Zhou, Li	Numerical and Experimental Investigation of Station-keeping in Level Ice, CeSOS
IMT-2012-91	Ushakov, Sergey	Particulate matter emission characteristics from diesel enignes operating on conventional and alternative marine fuels, IMT
IMT-2013-1	Yin, Decao	Experimental and Numerical Analysis of Combined In-line and Cross-flow Vortex Induced Vibrations, CeSOS

IMT-2013-2	Kurniawan, Adi	Modelling and geometry optimisation of wave energy converters, CeSOS
IMT-2013-3	Al Ryati, Nabil	Technical condition indexes doe auxiliary marine diesel engines, IMT
IMT-2013-4	Firoozkoohi, Reza	Experimental, numerical and analytical investigation of the effect of screens on sloshing, CeSOS
IMT-2013-5	Ommani, Babak	Potential-Flow Predictions of a Semi-Displacement Vessel Including Applications to Calm Water Broaching, CeSOS
IMT-2013-6	Xing, Yihan	Modelling and analysis of the gearbox in a floating spar-type wind turbine, CeSOS
IMT-7-2013	Balland, Océane	Optimization models for reducing air emissions from ships, IMT
IMT-8-2013	Yang, Dan	Transitional wake flow behind an inclined flat plate-----Computation and analysis, IMT
IMT-9-2013	Abdillah, Suyuthi	Prediction of Extreme Loads and Fatigue Damage for a Ship Hull due to Ice Action, IMT
IMT-10-2013	Ramìrez, Pedro Agustìn Pèrez	Ageing management and life extension of technical systems- Concepts and methods applied to oil and gas facilities, IMT
IMT-11-2013	Chuang, Zhenju	Experimental and Numerical Investigation of Speed Loss due to Seakeeping and Maneuvering. IMT
IMT-12-2013	Etemaddar, Mahmoud	Load and Response Analysis of Wind Turbines under Atmospheric Icing and Controller System Faults with Emphasis on Spar Type Floating Wind Turbines, IMT
IMT-13-2013	Lindstad, Haakon	Strategies and measures for reducing maritime CO2 emissons, IMT
IMT-14-2013	Haris, Sabril	Damage interaction analysis of ship collisions, IMT
IMT-15-2013	Shainee, Mohamed	Conceptual Design, Numerical and Experimental Investigation of a SPM Cage Concept for Offshore Mariculture, IMT
IMT-16-2013	Gansel, Lars	Flow past porous cylinders and effects of biofouling and fish behavior on the flow in and around Atlantic salmon net cages, IMT
IMT-17-2013	Gaspar, Henrique	Handling Aspects of Complexity in Conceptual Ship Design, IMT
IMT-18-2013	Thys, Maxime	Theoretical and Experimental Investigation of a Free Running Fishing Vessel at Small Frequency of Encounter, CeSOS
IMT-19-2013	Aglen, Ida	VIV in Free Spanning Pipelines, CeSOS

IMT-1-2014	Song, An	Theoretical and experimental studies of wave diffraction and radiation loads on a horizontally submerged perforated plate, CeSOS
IMT-2-2014	Rogne, Øyvind Ygre	Numerical and Experimental Investigation of a Hinged 5-body Wave Energy Converter, CeSOS
IMT-3-2014	Dai, Lijuan	Safe and efficient operation and maintenance of offshore wind farms ,IMT
IMT-4-2014	Bachynski, Erin Elizabeth	Design and Dynamic Analysis of Tension Leg Platform Wind Turbines, CeSOS
IMT-5-2014	Wang, Jingbo	Water Entry of Freefall Wedged – Wedge motions and Cavity Dynamics, CeSOS
IMT-6-2014	Kim, Ekaterina	Experimental and numerical studies related to the coupled behavior of ice mass and steel structures during accidental collisions, IMT
IMT-7-2014	Tan, Xiang	Numerical investigation of ship's continuous- mode icebreaking in leverl ice, CeSOS
IMT-8-2014	Muliawan, Made Jaya	Design and Analysis of Combined Floating Wave and Wind Power Facilities, with Emphasis on Extreme Load Effects of the Mooring System, CeSOS
IMT-9-2014	Jiang, Zhiyu	Long-term response analysis of wind turbines with an emphasis on fault and shutdown conditions, IMT
IMT-10-2014	Dukan, Fredrik	ROV Motion Control Systems, IMT
IMT-11-2014	Grimsmo, Nils I.	Dynamic simulations of hydraulic cylinder for heave compensation of deep water drilling risers, IMT
IMT-12-2014	Kvittem, Marit I.	Modelling and response analysis for fatigue design of a semisubmersible wind turbine, CeSOS
IMT-13-2014	Akhtar, Juned	The Effects of Human Fatigue on Risk at Sea, IMT
IMT-14-2014	Syahroni, Nur	Fatigue Assessment of Welded Joints Taking into Account Effects of Residual Stress, IMT
IMT-1-2015	Bøckmann, Eirik	Wave Propulsion of ships, IMT
IMT-2-2015	Wang, Kai	Modelling and dynamic analysis of a semi-submersible floating vertical axis wind turbine, CeSOS
IMT-3-2015	Fredriksen, Arnt Gunvald	A numerical and experimental study of a two-dimensional body with moonpool in waves and current, CeSOS
IMT-4-2015	Jose Patricio Gallardo Canabes	Numerical studies of viscous flow around bluff bodies, IMT

IMT-5-2015	Vegard Longva	Formulation and application of finite element techniques for slender marine structures subjected to contact interactions, IMT
IMT-6-2015	Jacobus De Vaal	Aerodynamic modelling of floating wind turbines, CeSOS
IMT-7-2015	Fachri Nasution	Fatigue Performance of Copper Power Conductors, IMT
IMT-8-2015	Oleh I Karpa	Development of bivariate extreme value distributions for applications in marine technology,CeSOS
IMT-9-2015	Daniel de Almeida Fernandes	An output feedback motion control system for ROVs, AMOS
IMT-10-2015	Bo Zhao	Particle Filter for Fault Diagnosis: Application to Dynamic Positioning Vessel and Underwater Robotics, CeSOS
IMT-11-2015	Wenting Zhu	Impact of emission allocation in maritime transportation, IMT
IMT-12-2015	Amir Rasekhi Nejad	Dynamic Analysis and Design of Gearboxes in Offshore Wind Turbines in a Structural Reliability Perspective, CeSOS
IMT-13-2015	Arturo Jesùs Ortega Malca	Dynamic Response of Flexibles Risers due to Unsteady Slug Flow, CeSOS
IMT-14-2015	Dagfinn Husjord	Guidance and decision-support system for safe navigation of ships operating in close proximity, IMT
IMT-15-2015	Anirban Bhattacharyya	Ducted Propellers: Behaviour in Waves and Scale Effects, IMT
IMT-16-2015	Qin Zhang	Image Processing for Ice Parameter Identification in Ice Management, IMT
IMT-1-2016	Vincentius Rumawas	Human Factors in Ship Design and Operation: An Experiential Learning, IMT
IMT-2-2016	Martin Storheim	Structural response in ship-platform and ship-ice collisions, IMT
IMT-3-2016	Mia Abrahamsen Prsic	Numerical Simulations of the Flow around single and Tandem Circular Cylinders Close to a Plane Wall, IMT
IMT-4-2016	Tufan Arslan	Large-eddy simulations of cross-flow around ship sections, IMT

IMT-5-2016	Pierre Yves-Henry	Parametrisation of aquatic vegetation in hydraulic and coastal research,IMT
IMT-6-2016	Lin Li	Dynamic Analysis of the Instalation of Monopiles for Offshore Wind Turbines, CeSOS
IMT-7-2016	Øivind Kåre Kjerstad	Dynamic Positioning of Marine Vessels in Ice, IMT
IMT-8-2016	Xiaopeng Wu	Numerical Analysis of Anchor Handling and Fish Trawling Operations in a Safety Perspective, CeSOS
IMT-9-2016	Zhengshun Cheng	Integrated Dynamic Analysis of Floating Vertical Axis Wind Turbines, CeSOS
IMT-10-2016	Ling Wan	Experimental and Numerical Study of a Combined Offshore Wind and Wave Energy Converter Concept
IMT-11-2016	Wei Chai	Stochastic dynamic analysis and reliability evaluation of the roll motion for ships in random seas, CeSOS
IMT-12-2016	Øyvind Selnes Patricksson	Decision support for conceptual ship design with focus on a changing life cycle and future uncertainty, IMT
IMT-13-2016	Mats Jørgen Thorsen	Time domain analysis of vortex-induced vibrations, IMT
IMT-14-2016	Edgar McGuinness	Safety in the Norwegian Fishing Fleet – Analysis and measures for improvement, IMT
IMT-15-2016	Sepideh Jafarzadeh	Energy effiency and emission abatement in the fishing fleet, IMT
IMT-16-2016	Wilson Ivan Guachamin Acero	Assessment of marine operations for offshore wind turbine installation with emphasis on response-based operational limits, IMT
IMT-17-2016	Mauro Candeloro	Tools and Methods for Autonomous Operations on Seabed and Water Coumn using Underwater Vehicles, IMT
IMT-18-2016	Valentin Chabaud	Real-Time Hybrid Model Testing of Floating Wind Tubines, IMT
IMT-1-2017	Mohammad Saud Afzal	Three-dimensional streaming in a sea bed boundary layer
IMT-2-2017	Peng Li	A Theoretical and Experimental Study of Wave-induced Hydroelastic Response of a Circular Floating Collar
IMT-3-2017	Martin Bergström	A simulation-based design method for arctic maritime transport systems

IMT-4-2017	Bhushan Taskar	The effect of waves on marine propellers and propulsion
IMT-5-2017	Mohsen Bardestani	A two-dimensional numerical and experimental study of a floater with net and sinker tube in waves and current
IMT-6-2017	Fatemeh Hoseini Dadmarzi	Direct Numerical Simualtion of turbulent wakes behind different plate configurations
IMT-7-2017	Michel R. Miyazaki	Modeling and control of hybrid marine power plants
IMT-8-2017	Giri Rajasekhar Gunnu	Safety and effiency enhancement of anchor handling operations with particular emphasis on the stability of anchor handling vessels
IMT-9-2017	Kevin Koosup Yum	Transient Performance and Emissions of a Turbocharged Diesel Engine for Marine Power Plants
IMT-10-2017	Zhaolong Yu	Hydrodynamic and structural aspects of ship collisions
IMT-11-2017	Martin Hassel	Risk Analysis and Modelling of Allisions between Passing Vessels and Offshore Installations
IMT-12-2017	Astrid H. Brodtkorb	Hybrid Control of Marine Vessels – Dynamic Positioning in Varying Conditions
IMT-13-2017	Kjersti Bruserud	Simultaneous stochastic model of waves and current for prediction of structural design loads
IMT-14-2017	Finn-Idar Grøtta Giske	Long-Term Extreme Response Analysis of Marine Structures Using Inverse Reliability Methods
IMT-15-2017	Stian Skjong	Modeling and Simulation of Maritime Systems and Operations for Virtual Prototyping using co-Simulations
IMT-1-2018	Yingguang Chu	Virtual Prototyping for Marine Crane Design and Operations
IMT-2-2018	Sergey Gavrilin	Validation of ship manoeuvring simulation models
IMT-3-2018	Jeevith Hegde	Tools and methods to manage risk in autonomous subsea inspection,maintenance and repair operations
IMT-4-2018	Ida M. Strand	Sea Loads on Closed Flexible Fish Cages
IMT-5-2018	Erlend Kvinge Jørgensen	Navigation and Control of Underwater Robotic Vehicles

IMT-6-2018	Bård Stovner	Aided Intertial Navigation of Underwater Vehicles
IMT-7-2018	Erlend Liavåg Grotle	Thermodynamic Response Enhanced by Sloshing in Marine LNG Fuel Tanks
IMT-8-2018	Børge Rokseth	Safety and Verification of Advanced Maritime Vessels
IMT-9-2018	Jan Vidar Ulveseter	Advances in Semi-Empirical Time Domain Modelling of Vortex-Induced Vibrations
IMT-10-2018	Chenyu Luan	Design and analysis for a steel braceless semi-submersible hull for supporting a 5-MW horizontal axis wind turbine
IMT-11-2018	Carl Fredrik Rehn	Ship Design under Uncertainty
IMT-12-2018	Øyvind Ødegård	Towards Autonomous Operations and Systems in Marine Archaeology
IMT-13-2018	Stein Melvær Nornes	Guidance and Control of Marine Robotics for Ocean Mapping and Monitoring
IMT-14-2018	Petter Norgren	Autonomous Underwater Vehicles in Arctic Marine Operations: Arctic marine research and ice monitoring
IMT-15-2018	Minjoo Choi	Modular Adaptable Ship Design for Handling Uncertainty in the Future Operating Context
MT-16-2018	Ole Alexander Eidsvik	Dynamics of Remotely Operated Underwater Vehicle Systems
IMT-17-2018	Mahdi Ghane	Fault Diagnosis of Floating Wind Turbine Drivetrain- Methodologies and Applications
IMT-18-2018	Christoph Alexander Thieme	Risk Analysis and Modelling of Autonomous Marine Systems
IMT-19-2018	Yugao Shen	Operational limits for floating-collar fish farms in waves and current, without and with well-boat presence
IMT-20-2018	Tianjiao Dai	Investigations of Shear Interaction and Stresses in Flexible Pipes and Umbilicals
IMT-21-2018	Sigurd Solheim Pettersen	Resilience by Latent Capabilities in Marine Systems
IMT-22-2018	Thomas Sauder	Fidelity of Cyber-physical Empirical Methods. Application to the Active Truncation of Slender Marine Structures
IMT-23-2018	Jan-Tore Horn	Statistical and Modelling Uncertainties in the Design of Offshore Wind Turbines

IMT-24-2018	Anna Swider	Data Mining Methods for the Analysis of Power Systems of Vessels
IMT-1-2019	Zhao He	Hydrodynamic study of a moored fish farming cage with fish influence
IMT-2-2019	Isar Ghamari	Numerical and Experimental Study on the Ship Parametric Roll Resonance and the Effect of Anti-Roll Tank
IMT-3-2019	Håkon Strandenes	Turbulent Flow Simulations at Higher Reynolds Numbers
IMT-4-2019	Siri Mariane Holen	Safety in Norwegian Fish Farming – Concepts and Methods for Improvement
IMT-5-2019	Ping Fu	Reliability Analysis of Wake-Induced Riser Collision
IMT-6-2019	Vladimir Krivopolianskii	Experimental Investigation of Injection and Combustion Processes in Marine Gas Engines using Constant Volume Rig
IMT-7-2019	Anna Maria Kozlowska	Hydrodynamic Loads on Marine Propellers Subject to Ventilation and out of Water Condition.
IMT-8-2019	Hans-Martin Heyn	Motion Sensing on Vessels Operating in Sea Ice: A Local Ice Monitoring System for Transit and Stationkeeping Operations under the Influence of Sea Ice
IMT-9-2019|	Stefan Vilsen	Method for Real-Time Hybrid Model Testing of Ocean Structures – Case on Slender Marine Systems
IMT-10-2019	Finn-Christian W. Hanssen	Non-Linear Wave-Body Interaction in Severe Waves
IMT-11-2019	Trygve Olav Fossum	Adaptive Sampling for Marine Robotics
IMT-12-2019	Jørgen Bremnes Nielsen	Modeling and Simulation for Design Evaluation
IMT-13-2019	Yuna Zhao	Numerical modelling and dyncamic analysis of offshore wind turbine blade installation
IMT-14-2019	Daniela Myland	Experimental and Theoretical Investigations on the Ship Resistance in Level Ice
IMT-15-2019	Zhengru Ren	Advanced control algorithms to support automated offshore wind turbine installation
IMT-16-2019	Drazen Polic	Ice-propeller impact analysis using an inverse propulsion machinery simulation approach
IMT-17-2019	Endre Sandvik	Sea passage scenario simulation for ship system performance evaluation

IMT-18-2019	Loup Suja-Thauvin	Response of Monopile Wind Turbines to Higher Order Wave Loads
IMT-19-2019	Emil Smilden	Structural control of offshore wind turbines – Increasing the role of control design in offshore wind farm development
IMT-20-2019	Aleksandar-Sasa Milakovic	On equivalent ice thickness and machine learning in ship ice transit simulations
IMT-1-2020	Amrit Shankar Verma	Modelling, Analysis and Response-based Operability Assessment of Offshore Wind Turbine Blade Installation with Emphasis on Impact Damages
IMT-2-2020	Bent Oddvar Arnesen Haugaløkken	Autonomous Technology for Inspection, Maintenance and Repair Operations in the Norwegian Aquaculture
IMT-3-2020	Seongpil Cho	Model-based fault detection and diagnosis of a blade pitch system in floating wind turbines
IMT-4-2020	Jose Jorge Garcia Agis	Effectiveness in Decision-Making in Ship Design under Uncertainty
IMT-5-2020	Thomas H. Viuff	Uncertainty Assessment of Wave-and Current-induced Global Response of Floating Bridges
IMT-6-2020	Fredrik Mentzoni	Hydrodynamic Loads on Complex Structures in the Wave Zone
IMT-7-2020	Senthuran Ravinthrakumar	Numerical and Experimental Studies of Resonant Flow in Moonpools in Operational Conditions
IMT-8-2020	Stian Skaalvik Sandøy	Acoustic-based Probabilistic Localization and Mapping using Unmanned Underwater Vehicles for Aquaculture Operations
IMT-9-2020	Kun Xu	Design and Analysis of Mooring System for Semi-submersible Floating Wind Turbine in Shallow Water
IMT-10-2020	Jianxun Zhu	Cavity Flows and Wake Behind an Elliptic Cylinder Translating Above the Wall
IMT-11-2020	Sandra Hogenboom	Decision-making within Dynamic Positioning Operations in the Offshore Industry – A Human Factors based Approach
IMT-12-2020	Woongshik Nam	Structural Resistance of Ship and Offshore Structures Exposed to the Risk of Brittle Failure
IMT-13-2020	Svenn Are Tutturen Værnø	Transient Performance in Dynamic Positioning of Ships: Investigation of Residual Load Models and Control Methods for Effective Compensation
IMT-14-2020	Mohd Atif Siddiqui	Experimental and Numerical Hydrodynamic Analysis of a Damaged Ship in Waves
IMT-15-2020	John Marius Hegseth	Efficient Modelling and Design Optimization of Large Floating Wind Turbines

IMT-16-2020	Asle Natskår	Reliability-based Assessment of Marine Operations with Emphasis on Sea Transport on Barges
IMT-17-2020	Shi Deng	Experimental and Numerical Study of Hydrodynamic Responses of a Twin-Tube Submerged Floating Tunnel Considering Vortex-Induced Vibration
IMT-18-2020	Jone Torsvik	Dynamic Analysis in Design and Operation of Large Floating Offshore Wind Turbine Drivetrains
IMT-1-2021	Ali Ebrahimi	Handling Complexity to Improve Ship Design Competitiveness
IMT-2-2021	Davide Proserpio	Isogeometric Phase-Field Methods for Modeling Fracture in Shell Structures